UNIVERSITÀ DEGLI STUDI DI MILANO

Scuola di Dottorato in Fisica, Astrofisica e Fisica Applicata

Dipartimento di Fisica

Corso di Dottorato in Fisica, Astrofisica e Fisica Applicata

Ciclo XXX

Probing electron correlation dynamics: a multi-technique study applied to the half-metallic oxide $La_{1-x}Sr_xMnO_3$

Settore Scientifico Disciplinare Fis/03

Supervisore: Professor Giorgio ROSSI

Coordinatore: Professor Marco BERSANELLI

Tesi di Dottorato di:

Tommaso Pincelli

Anno Accademico 2016-2017

Commission of the final examination:

External Referees:
Prof. P. Postorino & Prof. D. Pescia

External Members:
Prof. G. Ghiringhelli & Prof. M. Nisoli

Internal Member:
Prof. G. Rossi

Final examination:

19 December 2017

Università degli Studi di Milano, Dipartimento di Fisica, Milano, Italy

To freedom and adventure

Cover illustration:

T. Pincelli

Internal illustrations:

T. Pincelli

Design:

A.D. Copia, Copiae

MIUR subjects:

FIS/03

PACS:

75.78.Jp, 78.47.D, 75.47.Lx, 79.60.-i,

Contents

Abstract

This thesis completes my work as doctoral student of the Scuola di Dottorato in Fisica, Astrofisica e Fisica Applicata at the Università degli Studi di Milano that has been carried out, starting in November 2014, mostly at the Laboratorio TASC of IOM-CNR[1] in the premises of the Elettra - Sincrotrone Trieste and FERMI@Elettra infrastructures[2], in the framework of the NFFA and APE-beamline facilites[3], as well as by accessing international large scale infrastructures and laboratories.

The activity has addressed the development of experimental methodologies and novel instrumentation oriented to the study of the dynamical properties of highly correlated materials after high energy excitation. The science programme has been carried out by exploiting ultrafast femtosecond probes from the optical regime (Ti-Sa lasers, fibre laser oscillators) to the extreme UV-soft X rays at FERMI, to the picosecond hard X-rays from the SPring-8 and Diamond synchrotron radiation source. The sample synthesis of correlated oxides and its characterization has been performed within the NFFA facility and APE-group collaboration in Trieste as well as the design and construction of the all new laser High Harmonic Generation beam line NFFA-SPRINT and its end station for time resolved vectorial electron spin polarimetry.

This report concentrates on the main scientific concern of my work that has been the relaxation of external perturbations in a correlated electron material both in the time and space domain.

I have employed Photoelectron Spectroscopy (PES) mostly in the Hard X-ray regime (HAXPES), pushing the boundaries of its application to achieve a coherent perspective. The material I have mainly focused on is $La_{0.67}Sr_{0.33}MnO_3$ (LSMO), of high interest for spintronics. This system is prototypical, yielding the highest simplicity in the class of transition metal oxides.

In the spatial investigation, I have controlled with high precision the PES probing depth and I have observed the evolution of one spectral feature. I have identified it as

[1] IOM website.
[2] Elettra website.
[3] NFFA-Trieste website.

probe of electronic hybridization and long-range ordering. I have studied LSMO films of 40 nm in three substrate-induced strain states (1% tensile in-plane, relaxed, 1% compressive in-plane) and a 18 nm film of (Ga,Mn)As (GMA), a well-studied diluted magnetic semiconductor. I have found that the electronic properties to be modified at significant distances from the surface, 4 nm for LSMO and 1.2 nm for GMA, while strain had no detectable effects.

In the temporal study, I have employed HAXPES in pump-probe mode (TR-HAXPES) to observe the evolution of the electronic structure after intense optical excitation. A detailed dynamical characterization with optical techniques has allowed me to identify the characteristic time of the collapse of long-range magnetic order to be significantly longer than the one of elemental transition metals. I have ascribed this effect to the half-metallic character of LSMO. With TR-HAXPES I have observed that the whole electronic band-structure evolution is bottlenecked by the slow response of the magnetization, proceeding on hundreds of picoseconds timescales.

Finally, I have described the techniques and the instrumentation that can be used to push these investigations to shorter spatial and temporal scales. This has been realized in the form of the NFFA-SPRINT laboratory, a facility open to users, which I participated in designing and developing.

Introduction

> [...] τὴν λίθον ἔφη ψυχὴν ἔχειν, ὅτι τὸν σίδηρον κινεῖ.
> [Thales of Miletus] says that the lodestone must have a soul, because it moves iron.
>
> Aristotle, *De Anima*, IV century b.C.

Magnetism has been known to the mankind since the prehistoric times. Yet, the understanding of this phenomenon requires such a deep comprehension of the profound nature of solids that even today, standing at the edge of a millennial wave of progress, our picture is far from complete. Nonetheless, the peculiar qualities of magnetism are now pervasive and their application, especially in the field of digital data recording and manipulation, is a powerful drive towards further advancements.

Despite the spectacular progress undergone until today, the demand for ever increasing high performance electronics is far from evening out. The future panorama of data usage will likely (Reinsel *et al.*, 2017) not only face a tenfold increase in its dimension (from 16 ZB in 2016 to 163 ZB expected for 2025), but also a vast rearrangement of its modalities. With the increased mobility and connectivity of our devices, the generation and request of information will move away from data centres in a myriad of peripheral small units.

The networking of advanced devices will result in automated generation, access and processing of information, therefore increasing the need for continuous access. It is estimated that up to 25% of the whole datasphere will be used in real time. A significant portion of these data will be considered "hypercritical", meaning that a failure in its storage would directly harm humans. It is thus of fundamental importance that systems designed to cheaply and reliably preserve information not only further increase the spatial density of storage, but also accelerate significantly the speed of access.

The central point of this thesis ultimately gravitates around this issue: the development of methods to experimentally address the physical processes arising when materials

at the forefront of technological development are limited either temporally or spatially. The following discussion will thus be carried out along this two-fold theme.

The trilemma and the gap

From the spatial point of view, the exploitation of magnetic media to record information has been struggling with the so-called *superparamagnetic trilemma*. As the size of the area dedicated to one bit nears the nanometre scale, the strength of the anisotropy produced by the crystal decreases, and the magnetization is no longer pinned to a precise orientation. Being subject to thermally triggered directional fluctuations, it averages to zero. Smaller magnetic grains would then not perform as switchable two-state bits. Yet, choosing materials with higher anisotropies requires larger switching fields. Electromagnets thus need higher currents to reverse them, which in turn necessitate larger read/write heads, with higher power consumption and less controlled stray fields.

The importance of speed, on the other hand, is related to what is called *the memory gap*. It refers to the difference between the frequency at which the information is processed and the one at which it is stored. Aside from non-volatile memory, mainly tied to sequential access until recently, even the volatile memories such as the *dynamical random access memory* (DRAM) have latencies about three orders of magnitude longer than the CPU clock. High throughput computing (HTC) where large amounts of data undergo relatively simple computational operations in a multi-iteration approach, is severely limited by the data input-output to storage.

The need for compactness, faster access and reduced power consumption is however urgently emerging also for long-term, non-volatile memory. This is shown by the increased use of flash memory, even at the expense of a reduction in storage density, cost and long term stability with respect to hard disk drives (HDD). Despite its yet unbeaten[4] areal density and cost per bit, the HDD is likely to become increasingly relegated to large data centres.

Spintronics

Since the observation of the injection of spin-polarized currents in 1985 (Johnson and Silsbee, 1985), and of giant magneto resistance in metallic multilayers in 1988 (Baibich *et al.*, 1988; Binasch *et al.*, 1989), the manipulation of electron spin simultaneously to currents and voltages has been considered as a viable path towards increased miniaturization and efficiency. These separate, high impact studies rapidly evolved in the very active research topic named *spintronics*. Grünberg and Fert were awarded the Nobel prize for having planted its seeds, and magneto-resistance enjoyed one of the shortest discovery-to-applications times and revolutionised the hard disks read/write heads. The spintronics

[4] At present, one of the few media that can spectacularly surpass the HDD density is non-magnetic: DNA has recently proven to hold up to 214 Pb/g (Erlich and Zielinski, 2017), with full recovery of the encoded data and potentially millions of years long retention.

tango (Sinova and Žutić, 2012) started to play, material science and condensed matter physics closely pirouetting in successive triggering of new waves of interest.

A wealth of complex mechanisms were discovered or revamped. We begun to actively seek after interactions allowing spin control, such as proximity effects, spin-transfer torque, the family of spin Hall effects, the Sebeeck effect and topological spin-momentum locking. Itinerant forms of magnetism, such as superexchange, double exchange, RKKY-interaction and DM-interaction, offered a new playground for the realization of advanced devices. The spectrum of the materials of interest for electronics widened from traditional semiconductors to the ones doped with magnetic impurities, of which one of the most interesting is (Ga,Mn)As. Magnetic metals evolved to complex alloys such as the half-metallic Heusler compounds.

Thanks to advanced development in the realization of metallic, semiconducting and insulating heterostructures, it became possible to realize devices such as the magnetic tunnel junction (MTJ) , which displays up to one order of magnitude change in resistivity when the one of the two ferromagnetic layers has its magnetization reversed. Further progress came with the spin-transfer torque magnetic tunnel junction (STT-MTJ) (Ralph and Stiles, 2008; Fong *et al.*, 2016), that could be switched without the application of an external field. This unlocked fast random access in a non-volatile, long retention time memory.

Today, the quest still advances. There are even faster mechanisms taking place at even shorter length scales that can be controlled, as suggested by Fig. 1. Exchange itself, electronic correlation and the absorption of a photon are interactions of high characteristic energies, and thus define the response of the material on extremely short timescales, that can be estimated with Heisenberg uncertainty relationship.

Ultrafast magnetism

The field of research that aims at deepening the understanding of the fastest magnetic processes was opened by the discovery, in 1996, of a quench in the magneto-optic response of Ni thin films optically excited with 100 femtoseconds (fs) long infrared laser pulses. Implementing the pump-probe experimental scheme, a rapid decrease of the Kerr signal was observed to complete within few hundred fs, followed by a recovery in tens of picoseconds (ps). Such a short time was interpreted as suggesting the possibility of manipulating magnetic materials on timescales almost three orders of magnitude shorter than the typical hundreds of picoseconds of the spin-lattice effects, linked to spin-orbit coupling.

The development of research in ultrafast magnetism resulted in several compelling results, such as the demonstration of all-optical magnetic reversal in ferrimagnetic alloys and in transparent garnets (Stupakiewicz *et al.*, 2017), or the increasing theoretical (Battiato *et al.*, 2010) and experimental (Melnikov *et al.*, 2011) evidence of transient, short-lived pure spin currents that ensue after optical excitation. Both of these highlights stimulate the research to explore the possibilities for new spintronics applications, with devices acting on extremely short timescales (Walowski and Münzenberg, 2016).

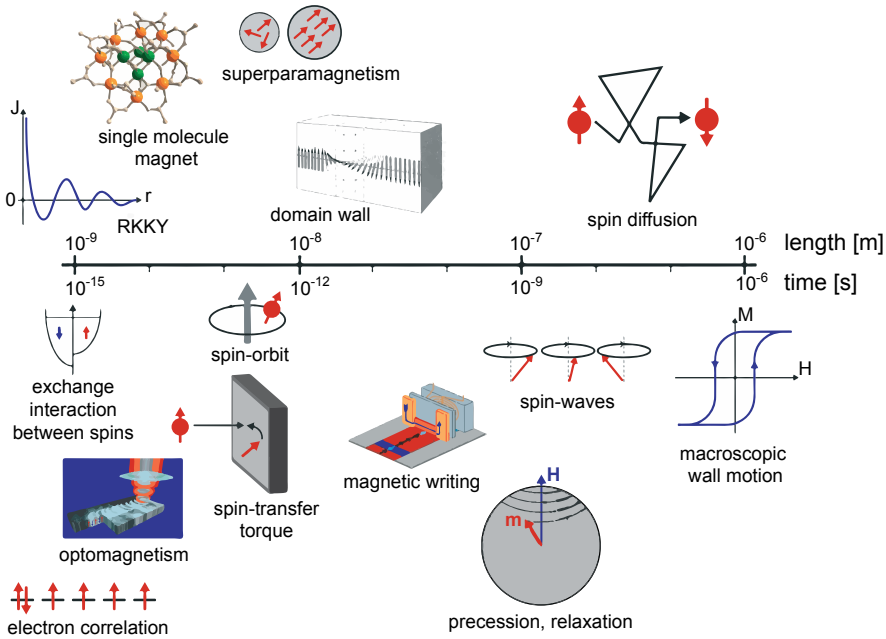

Figure 1: Length and timescales of the most relevant magnetic interactions. From the Swiss FEL science case (Patterson *et al.*, 2010).

Our instruments to cope with the complexity of magnetic systems strongly out of equilibrium are, however, still in their infancy both experimentally and theoretically.

On the theoretical side, going out of equilibrium deprives most of the models of a fundamental pillar on which they rely. A plethora of individual mechanisms that can describe relevant many-body interactions have been proposed and can be handled at the shortest timescales. At longer timescales, when the degrees of freedom of the solid can be considered at internal equilibrium and only the energy flux between them is relevant, advanced forms of rate equations have been established (Koopmans *et al.*, 2010). In the intermediate region between these two ranges, however, the emergence of highly non-equilibrium microscopic mechanisms in macroscopic phenomena still largely defies understanding.

The concepts of "transient" phases of the collective ground states, like ferromagnetism, antiferromagnetism or superconductivity have been introduced in the literature, short of having better descriptive tools of the excited states. We are just beginning to cope with these definitions, and sometimes the necessary simplification still does not preserve sufficient depth, overlooking critically important notions, and at times leading to confusion.

Experimental techniques also struggle: until now, the exploration of ultrafast magnetic processes has been performed mostly by optical means. A formidable progress has been obtained in the construction of ultrashort intense sources of EM radiation, like lasers reaching the atto-second, single or fractional optical cycle, IR sources. Yet, being

sensitive to the whole electronic structure of the solid, it is difficult to retrieve the desired information. Indeed, when the material is driven strongly out of equilibrium, the measured response can be mixed in with the evolution of the optical constants.

Optical spectroscopy yields an enormous wealth of information, and it certainly offers valuable information on the state of a solid, but it is only a one-sided piece of information in the exploration of such complex processes. It is clear that other techniques, based on higher energy interactions and thus more focused on precise mechanisms, need to complement the current experimental results.

The challenge, in this case, lies in the control of high energy probes at such short timescales. This requires large scale facilities, with 100 M€ to 1 B€ sources that are being built and put on-line for experiments with soft and hard X-ray ultra-brilliant pulses of 10-100 fs duration.

Transition metal oxides

In the constant research of larger responses to smaller external stimuli to boost energetic efficiency, spintronics is now arching over several exotic processes and materials. One class of compounds that has increasingly gained relevance is the one of strongly correlated oxides. In these materials, the presence of the oxygen between the transition metal or rare earth ions drives the chemical bond towards an ionic character, favouring electronic localization. Yet the extension and the symmetry of the cations d orbitals tend to allow electrons to hop between the d or f element sites across the oxygen, thus extending the wavefunctions of the carriers and minimizing their kinetic energy.

It is this competition between extended and localized character that makes the electronic structure of transition metal oxides extraordinarily delicate and sensitive to external perturbations. The ground state of these materials can cross over from being metallic to insulating due to different effects. Electron-electron repulsion produces the Mott-Hubbard insulating state. The distortion of the lattice results in Peierls insulators. The effects of disorder produce localization in Anderson insulators. In charge transfer insulators, finally, the most relevant role is played by the p bands of the ligand (Yang *et al.*, 2011).

Eager of delocalizing their carriers, these insulators can recover their metallic character (metal-insulator transition or MIT) if their electronic structure is perturbed by changing the width or the filling of the bands, the temperature, electromagnetic fields, or at symmetry lowering defects as the surface or artificial interfaces. In the quantum critical phase that emerges in such conditions, the system is driven towards high instability by the competition of configurations defining a ground state. Owing to the progress in the techniques of epitaxial growth and of control of the stoichiometry that have been achieved in the last years, these materials offer a unique playground to study sophisticated emerging phenomena, with great fascination for the physicist's curiosity.

From the applicative point of view, they allow to tune materials with highly sought-after properties, among which many are of interest for spintronics (Bibes and Barthelemy, 2007). Materials capable of undergoing magnetically, electrically or thermally controlled MIT offer very large contrast in the flow of current, and perfectly half-metallic band-

structures allow for highly spin-polarised current injection. Direct magnetic control of the resistivity within a single material is made possible by the colossal magnetoresistance effect (CMR).

In spite of these advantages, however, the exploitation of such sensitivity of the electronic structure comes at a price. The response of materials close to quantum criticality is highly complex: even the simplest theoretical models are challenging to solve exactly, and approximate solutions may fail to capture the criticality of some concurring parameters. The dominant interaction giving rise to the fundamental ordered state might be difficult to resolve in a landscape of closely concurring energies.

This last energetic problem can be mapped into a temporal one. Indeed, by driving a TMO out of equilibrium, we can understand how the difference in the energy of ordering mechanisms leads to re-establishment of the ground state on different timescales. Such a question can also be reversed, leaning more on the applicative side: is it possible to tailor the electronic structure in order to control the frequency of operation? What are the characteristic timescales of the dominant interactions in the oxides of interest for spintronics? The search for an answer highlights once again the need of techniques that are capable of addressing specific features even in the bandstructure of a material evolving critically out of equilibrium. Encouraging results (Zhang *et al.*, 2016; Yang *et al.*, 2011), show that ultrafast-MIT processes are indeed possible and that a high degree of control over them can be achieved.

On the other hand, the length scales at which order is established are also very important and difficult to address. Indeed, the frail electronic structure of these materials makes the interruption of the crystal in surfaces or interfaces a considerable perturbation. This can be controlled to achieve new functionalities such as the recently discovered 2DEG at the LAO/STO interface (Ohtomo and Hwang, 2004), but it often is uncontrolled, as a result of requirements of spatial confinement.

Either way, it is necessary to understand what the length required to the solid to re-establish the intrinsic characteristics is. This presents us with the challenge of non-destructively resolving not only the the chemical composition, but also some specific features of the electronic structure as a function of the distance from the surface within the same material.

Development of high-energy techniques

It is clear that the need of an effective technique, that could provide a coherent information both in the spatial and temporal domain, is not only of interest for a more complete understanding of these materials, but also for the advancement of spintronics. An outstanding example of the movement of the community in this direction is, for example, the recent work of Baumgartner et al. on Co nanodots (Baumgartner *et al.*, 2017).

At present, we are witnessing the appearance of numerous sharply pulsed sources of X-rays: several free electron lasers are now operating, synchrotrons are upgrading to low-α modes, and the technology of sharply pulsed X-ray laser sources based on laser harmonics generation from gas (HHG) is rapidly progressing. Numerous techniques whose

effectiveness was proven in equilibrium studies are now being transferred to time-resolved investigations.

Among them, some the most relevant techniques for the exploration of the electronic structure of magnetic solids are X-ray Magnetic Circular Dichroism (XMCD), which has gradually moved to FELs (Higley *et al.*, 2016) after being developed in synchrotrons (Radu *et al.*, 2010; Bobowski *et al.*, 2017; Rini *et al.*, 2009; Ünal *et al.*, 2017), time-resolved Resonant Inelastic Scattering (Dean *et al.*, 2016), time resolved X-ray magnetic diffraction (Beaud *et al.*, 2014; Esposito *et al.*, 2017). X-ray magnetic scattering has recently been demonstrated in a rather advanced X-ray pump and X-ray probe, resonantly exciting one of the components of $Ni_{1-x}Fe_x$ and probing the other, thus investigating the magnetic interactions in alloys with chemical resolution (Ferrari *et al.*, 2016).

However, at present, most of these techniques lack the precise tuning of the probing depth that is necessary to envision intrinsic spatial variations of the electronic properties. This thesis focuses on the application of photoelectron spectroscopy (PES) as a technique to explore the electronic properties of complex spintronic materials in the spatial and time domain.

PES has established as a powerful method to explore the electronic structure of complex materials (Hüfner, 2003), and gives the possibility of precisely measuring band energies, dispersion and lifetime of quasi-particles, surface states, elastic and inelastic scattering processes. PES is mostly considered as a technique strictly limited to the extreme surface (<1 nm) of solids. In recent years it has nonetheless proven its ability to retrieve invaluable information originating also from significantly deeper regions, when realized with hard X-ray primary photons (Woicik, 2016).

In particular Hard X-ray Photoelectron Spectroscopy (HAXPES) has demonstrated to be effective in addressing materials whose cross-over thickness is above the nanometre, such as strongly correlated oxides and diluted magnetic semiconductors. The large variability of electrons inelastic mean free path as a function of the photon energy allows for a probe of unique specificity, with finely tunable intrinsic probing depth. An accurate exploitation of its potentialities allows us to assess the spatial extension of electronic properties without resorting to spatial confinement of materials, that can result in further complications arising from the presence of multiple close-by interfaces.

Furthermore, photoemission is an extremely fast process. HHG based experiments that border on metrology have recently been assessing the effective timing of the photoemission phenomenon itself. Typical timescales are in the tens of of attoseconds (as) for the formation of the electronic wavepacket, and less than one femtosecond for its emission from the solid. Even more interestingly, the delay of the satellite peaks originating from electronic correlations has been measured in gas samples to be around 6 as (Ossiander *et al.*, 2017), while the photoemission lines arising from different angular momentum orbitals are separated by few tens as (Siek *et al.*, 2017).

It is therefore possible to say that photoemission constitutes a sharp event in time, much shorter than any many-body interaction in the solid. It can thus be used to capture a snapshot of the electronic structure referring to a precise instant. The clear picture

of the electronic structure that it is able to retrieve allows us to target the dynamics of specific features, even in presence of complex dynamical behaviour.

Approach and structure of this thesis

In this thesis I addressed, with the use of soft and hard X-ray photoelectron spectroscopy, the problem of how the electronic structure of a correlated material relaxes subsequently to external perturbations. From the spatial point of view, I studied the spatial cross-over thickness of relaxation of the surface perturbation. On the temporal side, instead, I measured the characteristic timescales of relaxation of optical energy, pumped-in by means of a shortly pulsed laser.

I focus on a material of interest for spintronics $La_{1-x}Sr_xMnO_3$ (LSMO). I challenge the complexity of the manganite response by choosing the approach of maximum simplicity. Indeed, LSMO is the manganite with the widest band and with the highest Curie temperature: it represents the most schematic double exchange model, where competition among different order parameters and electronic disorder are reduced to the minimum. This strive for clearness allows for a more solid interpretation of the experimental evidence.

As any experimental physicist knows, however, moving a real experiment towards ideality is none but an easy task. The realization of such a coherent study required pushing the limits of the established techniques and largely building new approaches to the experimental methods, as well as choosing the most appropriate experimental set-up that are available worldwide. The main experiments are thus supported by the most accurate characterization I could achieve, ensuring that both statically and dynamically the samples did indeed show the response I expected from the current understanding of the properties of this solid.

This thesis is composed of 11 chapters, which are grouped in three parts.

In **Part I** (Chap. 1-4), I employ HAXPES and PES to demonstrate highly precise spatial control of the distance from the surface at which the spectral information is retrieved, measuring the cross-over thickness in LSMO and the diluted magnetic semiconductor (Ga,Mn)As (GMA). In Chap. 1 I briefly introduce the grand picture of the problem of correlated electron materials, and sketch out the relevance of photoelectron spectroscopy in addressing it experimentally. In Chap. 2. I present LSMO within the landscape of correlated electron materials and discuss the mechanisms proposed to explain its properties.

In Chap. 3 I show the experimental results of experiments in which I measured the Mn 2p and the valence band of LSMO changing the photon energy (1-6 keV) and the temperature (140-415 K). For GMA I measured the Mn 2p lineshape as a function of the photon energy (0.8-6 keV). Dividing it in three sections, methods, results and discussion, I first expose the details of the experimental approach and of sample characterization. Then I proceed to display the gathered data, with a commentary on the immediately understandable features. A sharp satellite at lower binding energies appears in both materials at high photon energies and low temperatures. In the same conditions, the valence band shows shifts of spectral weight towards the Fermi energy. Measurements of

circular dichroism show a large magnetic asymmetry on the satellite. I measured three samples in different strain states (1% tensile, relaxed, 1% compressive), but found no significant differences in their core-level spectra.

Finally in the discussion, a more complex analysis is carried out. The temperature evolution shows that the largest variation of the satellite follows the decrease of the magnetization, confirming the circular dichroism measurements. Modelling with the ECM allows to describe the satellite peak as arising from high mobility states with large delocalization of the carriers, allowing for a screening of the core hole charge more effective than charge transfer from the ligand (that produces the main line). By using the dependence of the probing depth from the photon energy, I can apply a modified overlayer model to calculate the cross-over thickness at which the hybridization is reduced. By a reliable confrontation with the calculated spectra I can define a scale of the hybridization with increasing depth in the solid. I find largely different scales that however relate closely to other results in the literature. Finally in Chap. 4 I draw detailed conclusions and present the perspectives of this work.

In **Part II** (Chap. 5-9), I extend the investigation of $La_{1-x}Sr_xMnO_3$ to the time domain. In Chap. 5 I introduce the motivations and the methods to probe the dynamics of correlated electron materials. In particular, I address the relevance of high energy techniques and the strategies to efficiently implement HAXPES in a stroboscopic fashion. In Chap. 6, instead, I line out the results of the field of ultrafast magnetism that are needed to interpret the dynamical behaviour of LSMO. We indeed choose our system to be essentially dominated by the double exchange interaction, which, in absence of phase competition, gives a behaviour close to that of an Heisenberg ferromagnet. I furthermore focus on the effects of half-metallic bandstructure on the dynamics.

In Chap. 7, I describe the Time Resolved MOKE characterization of the dynamics of two LSMO samples in two strain states (strain relaxed and 1% tensile). I present reflectivity curves that show a rapid (τ =160 fs) thermalization of the electrons with the lattice, followed by a long lived dynamical rearrangement of the spectral weight due to the approaching to the phase transition. Kerr ellipsometry shows that at the shortest delays, the optical probe is significantly affected by the large changes in the optical constants that happen when LSMO is moved out of equilibrium. The Kerr signal no longer probes long range magnetic order in these conditions. This prevents us from clearly observing a magnetic dynamics at the femtosecond timescale in this material by TR-MOKE.

On the other hand, I demonstrate, by combining measurements at different initial temperatures and ellipsometric analysis, that Kerr traces at long ($> 50ps$) timescales are instead sensitive to the magnetic order. I observe a slow dynamics that I can attribute to the bottleneck effect of the half-metallic band-structure, that thermally isolates the spin system by suppressing spin-flip scattering. The collapse of magnetization proceeds by weak spin-lattice anisotropy coupling, leading to $> 200ps$ timescales required to complete demagnetization. The variation of the characteristic time of demagnetization shows a critical behaviour, and its critical exponent is consistent with that of a double exchange three dimensional ferromagnet.

In Chap. 8 I directly address the dynamics of electronic correlation in LSMO by performing pump-probe TR-HAXPES experiments on strain relaxed LSMO. I introduce the experimental methods I employed. I worked in a synchrotron radiation source, with 130 fs IR pump and 40 ps hard X-ray probe (8 keV). In lack of non-equilibrium theoretical models, the discussion can only be qualitative. I observe that the variation of the lineshape at the shortest delays ("0 ps") is not reproducible by diffrences between equilibrium configurations at different temperature. At longer delays ($> 100ps$), instead, the shifts of spectral weight correspond to the ones observable between equilibrium states. I thus conclude that the "0 ps" line shows an out-of equilibrium band-structure. The Kerr data confirm that large rearrangements of spectral weight indeed take place at tens of picoseconds timescales and are detectable also by the synchrotron pulse, averaging over 40 ps. I can then conclude, in Chap. 9, that electronic bandstructure evolution is slowed down by the bottleneck of the half-metallicity, and it reaches a new equilibrium configuration only when the magnetization has relaxed. Finally I present the perspectives of this work.

In **Part III** (Chap. 10-11) I described how I developed a new facility for the realization of advanced photoemission experiments at hundreds of femtoseconds time resolution, with the use of an HHG UV/soft X-ray source. In Chap. 10 I describe the long term strategy behind the development of this laboratory and its design, in which I provided a relevant contribution. I especially focus on the design choices of an apparatus for the measurement of the spin polarization of the total quantum (electron) yield from solid surfaces in high probe photon density regime, where multi-hit events have to be detected efficiently. In Chap. 11 I show the test runs of such instrument and some preliminary measurements that offer promising perspectives.

Building novel experimental tools to address with an original approach the physics problem of the dynamical evolution towards equilibrium, or metastable, order parameters is a fil-rouge that I have followed throughout this doctor thesis, building also on the work previously started during the master thesis. This approach is a classical one in physics research and creates the conditions for the future development of my activity, as well as for a general understanding of the data actually obtained in a given experiment run. The scientific environment of the NFFA and APE group and the access I could exploit to the international user large scale facilities have enabled the fulfilment of this approach.

Part I

Cross-over thickness of electronic correlation

Chapter 1

Correlated electrons in photoelectron spectroscopy

> It is quite possible that the electrostatic interaction between the electrons prevents them from moving at all.
>
> Rudolf Peierls, 1937

During the early and enthusiastic years of the dawn of quantum mechanics, the newly derived ideas were immediately applied to the description of solids, moving from the old Drude theory of metals to the Drude-Sommerfeld Free Electron model (Bethe, 1928; Sommerfeld, 1928) and the connected Nearly Free Electron model (Mott and Jones, 1945), which converged with the Tight Binding method (Bloch, 1928; Kronig and Penney, 1931) to give the picture of the Band Theory of solids. Yet, it became quickly clear that the assumption of non-interacting electrons laying below these models leads to paradoxically wrong predictions in the case of several transition metal oxides (de Boer and Verwey, 1937).

Indeed, the oxides of the 4th period metals have an half filled 3d band, which would lead, in the free or nearly free electron approximation, to a completely metallic character. Resistivity measurements, however, demonstrated the exact opposite with extremely low conductivities at low temperatures, indicating a semiconducting or even insulating character.

The microscopic origin of the insulating or semiconducting character of the oxides of Ti, V, Cr, Mn, Fe, Co, Ni and Cu was correctly individuated by N. F. Mott and R. Peierls (Mott and Peierls, 1937) in the localization of the charge carriers due to Coulomb repulsion between them. Transition metal oxides (TMOs) have indeed a peculiar combination of distances between their ions and balance of electronegativity between their chemical components, giving rise, in a tight-binding picture, to rather narrow 3d bands, strongly localized on the TM ion. The localization acts as a barrier, as the energy cost of two electrons occupying the same site exceeds the bandwidth, resulting in a band-gap.

This idea gave rise to the concept of *electronic correlation*, i.e. the interaction of electrons in solids with the electronic structure itself. The plethora of possible influences on electron dispersion is even larger than the simple charge correlation effects. Orbital

correlations, for example, appear when the effect of orbital degeneracy or the presence of orbitals of atoms of different species comes into play. Spin correlations, on the other hand, become relevant when the occupation of different spin states drastically influences the bandstructure.

Nowadays the concept of an insulating state of matter arising from strong electronic correlations is called *Mott insulator*, and is considered, to all intents, as a non-trivial quantum phase of matter. As the chemical composition of a material brings it near to the quantum critical region it acquires the character of *strongly correlated electrons material*, and its properties become extremely sensitive to a wide range of parameters. Such kind of materials often display peculiar and interesting behaviours such as high temperature superconductivity, colossal magnetoresistance, antiferromagnetism, superxchange interactions, charge ordering and others.

It is the fact that several correlation effects compete very closely that leads to macroscopic effects emerging from small (on the meV scale) energy differences; and it is this delicate equilibrium that is relentlessly sought after, as it enables the simultaneous control of several degrees of freedom with external (and as small as possible) stimuli such as electric or magnetic fields, temperature, doping and strain.

As the description of the quantum critical behaviour in the vicinity of the transition requires the handling of a many-body problem near a phase transition, where quantum fluctuations become very large, the task of treating it quantitatively has proven to be extremely hard. Since Mott and Peierl's intuition in 1937, the problem has been tackled with a large number of techniques both theoretical and experimental (Imada *et al.*, 1998). Nonetheless, a full picture has still to be found.

One of the most successful models, that allowed to describe at least a part of the range of phenomena that develop in presence of correlated electrons is the Hubbard model.

1.1 Hubbard model

Proposed by Anderson and Hubbard (Anderson, 1959; Hubbard, 1963), the model is the simplest member of the class of model Hamiltonian approaches. It arises from a tight binding picture of the solid and assumes only two interactions.

$$t = \int \mathrm{d}\mathbf{r}\varphi^*_{i\sigma}(\mathbf{r})\frac{1}{2m}\nabla^2\varphi_{j\sigma}(\mathbf{r}) \tag{1.1}$$

is the kinetic term operator. It is also defined *hopping term* because it arises from the overlap between the two Wannier orbitals $\varphi_{i\sigma}(\mathbf{r})$ on the lattice site i and $\varphi_{j\sigma}(\mathbf{r})$ on site j. m is the electron mass and $\hbar$ is set to unity.

$$U = \int \mathrm{d}\mathbf{r}\mathrm{d}\mathbf{r}'\varphi^*_{i\sigma}(\mathbf{r})\varphi_{i\sigma}(\mathbf{r})\frac{e^2}{|\mathrm{r}-\mathrm{r}'|}\varphi^*_{i-\sigma}(\mathbf{r}')\varphi_{i-\sigma}(\mathbf{r}') \tag{1.2}$$

this represents the electrostatic repulsion term that prevents electrons from residing on the same site, even when complying with the exclusion principle by occupying opposite

spin states. The Hamiltonian in the second quantized form then reads:

$$\mathfrak{H} = -t \sum_{\langle ij \rangle} c^{\dagger}_{i\sigma} c_{j\sigma} + H.C. + U \sum_{i} (n_{i\uparrow} - \frac{1}{2})(n_{i,\downarrow} - \frac{1}{2}) - \mu \sum_{i\sigma} n_{i\sigma} \tag{1.3}$$

the last term shifts the total energy as a function of the band occupation.

In the construction of this model, a large number of assumptions have been done. Indeed, only the nearest neighbour hopping is considered, t is assumed to be identical for every site, together with strong screening of the Coulomb repulsion, making t and U parameters with no indexes. Finally, multiband effects are neglected and only one band with s character is considered.

It must be stressed that in this model the only relevant parameter here is the ratio U/t, as t only defines the energy scale. It is rather straightforward to imagine the behaviour of this model in the case of half-filling (i.e. the presence of exactly one electron per site) at the two extrema of the parameter U/t. Indeed, in what is called the *weak coupling limit*, for $U = 0$, only the kinetic term will be retained, resulting in the free electron Hamiltonian. The ground state for $U = 0$ is therefore formed by sites either non-occupied or occupied by a doublet of electrons with opposing spins, and the electrons fill up the band up to the Fermi energy that crosses it in the middle. The solid is therefore in a paramagnetic metallic phase, with gapless spin and charge excitations.

In the opposite, strong coupling case, the situation is slightly more complex. If t is simply set to zero, the ground state has infinite degeneracy as each possible configuration with one electron per site has zero energy. A charge excitation requires the energy U, so the system is in an insulating state with an highly degenerate spin arrangement. If the value of t is finite, but small, it is possible to calculate the energy of the system by defining the ground state as a linear combination of all singly occupied states with different spin configurations and applying the second order term of perturbation theory. It is nonetheless possible to individuate a simple kind of low-energy excitation: the flipping of spins of electrons located at neighbouring lattice points. It is indeed possible to map the problem (approximated at the second order) onto the spin-only Heisenberg hamiltonian, that gives an antiferromagnetic coupling between neighbouring spins. Therefore, the ground state of the solid is that of an insulator (gapped charge excitations), with antiferromagnetic ordering. This implies that in between these two extrema, at half-filling, a radical change of the ground state must have happened and the model must have crossed a quantum critical point.

Despite its simplicity, the Hubbard model displays quantum critical behaviour, which makes it interesting in order to fully comprehend the behaviour of strongly correlated electron materials, but at the same time extremely difficult to treat mathematically. Indeed, an exact solution of the three dimensional Hubbard model has not yet been found. It is fascinating to mention that very recently the technical advancements in optical manipulation of atoms have advanced so significantly that it possible to create the idealized conditions of the Hubbard model in an actual experiment, to the point that it can actually be used to explore the Hubbard model phase diagram (Jürgensen, 2015).

Several other model Hamiltonians have been designed to improve the description of real materials: it is worth mentioning a few of them, as they simply relate microscopic interactions to complex behaviours that will be relevant in the following discussion.

- The introduction of degeneracy of 3d levels leads to strong anisotropies in the strong-coupling limit of the model, resulting in a periodic modulation of the preferentially occupied orbitals in the ground state, a condition termed *orbital ordering*.
- The introduction of exchange interaction might lift considerably the density of states for majority spin with respect to the minority ones. The shift can be so large that the minority band is not occupied and the atom is in a high spin state. This gives rise to complex itinerant ferromagnetic interactions that go under the name of *double exchange* (de Gennes, 1960; Kubo and Ohata, 1972; Kubo, 1972; Ohata, 1973; Irkhin and Katsnelson, 1994).
- The introduction of a term accounting for the hybridization between the d orbital of the transition metal ion and the p orbital of oxygen (*ligand*). This, defined the *d-p model*, gives evidence to an important process, called *charge transfer*.

The last point evidences the existence of a further subdivision of materials whose insulating character emerges from electronic correlation, identified after long experimental and theoretical effort in the understanding of the characteristics of NiO (Zaanen *et al.*, 1985). Indeed, let Δ be the energy distance (in absolute value) between the centre of the transition metal ion (TMI) 3d band and the centre of the ligand 2p band. Then, depending on how Δ compares to U, the 2p band can be in the middle between the two Hubbard bands. The lowest energy charge excitations are then not obtained as transition between bands with the same orbital symmetry, but between 2p and 3d states, as shown in fig. 1.1(b). The class of materials in which such condition is verified are called *Charge-transfer insulators* and show significantly different properties than the strictly termed *Mott-Hubbard insulators* shown in fig. 1.1(a). Examples of Mott-Hubbard insulators are V_2O_3, Ti_2O_3, Cr_2O_3. Examples of Charge-transfer insulators are NiO, FeO, $LaMnO_3$.

Despite the powerful insight and the numerous exact and approximate results achieved by model Hamiltonian approaches, their capability of describing the complexity of real systems, where several mechanisms are at play, is rather limited. However, other approaches have been developed, that treat in a more schematic way the many-body interaction, but allow to account for much more realistic characteristic of the crystal. One of the most successful of these approaches is the Dynamical Mean Field Theory (DMFT).

1.2 Dynamical mean field theory

The development of this theory relies on two important turning points (Kotliar and Vollhardt, 2004): the first is the assumption of an infinite dimensional crystal, i. e. the description of the system in the limit of infinitely many neighbouring atoms. Despite this might seem a quite odd assumption, it is needed to model the quantum fluctuations of

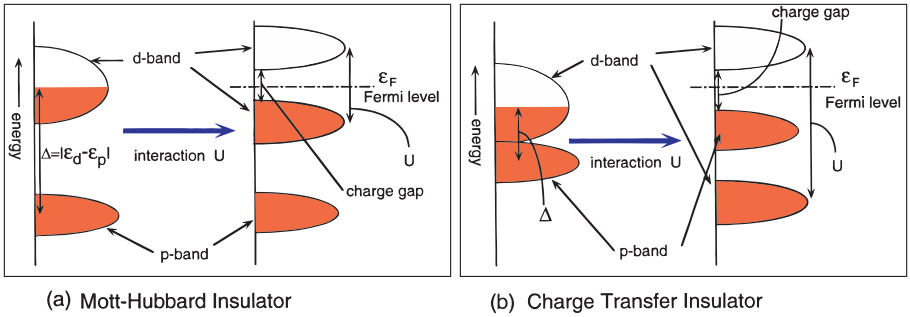

Figure 1.1: a. Density of states of a Mott-Hubbard insulator when the correlation is considered. Note that the gap is between the two split parts of the 3d band, called Lower and Upper Hubbard band. b. Density of states of a Charge transfer insulator. Note that the gap is between the Upper Hubbard Band and the hybridized oxygen 2p band. From (Imada *et al.*, 1998).

the crystal with a mean field, freezing out the spatial oscillations due to the periodicity of the lattice. Only temporal fluctuations are considered, and this is the reason why the theory is defined as *dynamic*. The density of atoms in a solid makes this assumption not too far from truth, and DMFT has been proven to be applicable even in two dimensions. The second crucial element of the theory is the use of an auxiliary impurity hamiltonian.

The *impurity model* was developed by P. W. Anderson (Anderson, 1961) to treat magnetic impurities in a host crystal, by the use of the hamiltonian:

$$\mathfrak{H} = \sum_l \left(\varepsilon_l d^\dagger_{l\sigma} d_{l\sigma} + V_l c^\dagger_{0\sigma} d_{l\sigma} + V_l^* d^\dagger_{l\sigma} c_{0\sigma} \right) + U n_{0\uparrow} n_{0\downarrow} \tag{1.4}$$

It sketches the system as a bath with l degrees of freedom, each with energy ε_l, which interacts with the impurity (labelled with 0 and operators $c, c^\dagger$) through single particle operators $d, d^\dagger$. The amplitude of such interaction is V_l, the *hybridization parameter*.

The dynamical mean field theory reinterprets this approach by considering the impurity as representative of each lattice site, and treating its interaction with the rest of the solid as a mean field. When applied to a single band Hubbard model, the interactions consist in a single electron hopping on the central atom, singly or doubly occupying it at different instants in time, as shown in fig. 1.2(a). The V_l parameters then become an *hybridization function* $\Delta(E)$ which is function of the energy of the charge excitation, describing the degree at which the external electronic bath can transfer or remove electrons from the site. The condition that all equivalent sites behave identically allows to impose a self-consistency condition that ties down the hybridization function. In this way, it is possible to extract the spectral function of the problem, describing the density of states of the solid.

The DMFT approach has given a good insight on the behaviour of correlated electrons. First of all, it allowed to follow, at zero temperature, the evolution of the bandstructure as the strength of the interaction is increased with respect to the bandwidth, as shown

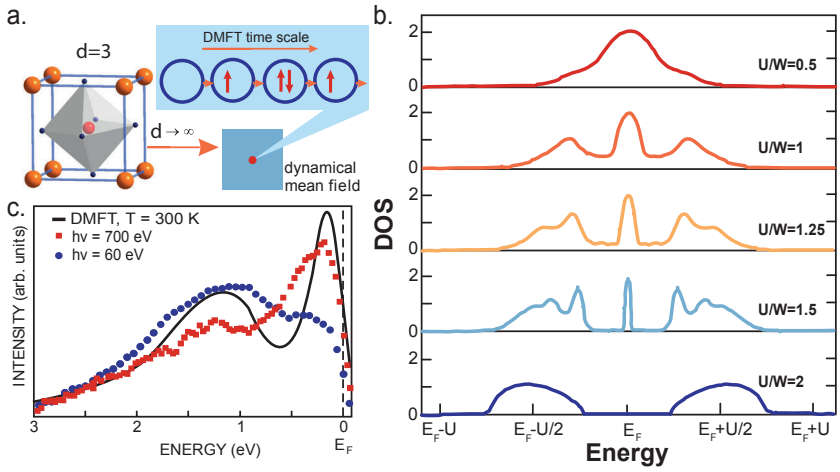

Figure 1.2: a. Schematic representation of the DMFT concept. From (Vollhardt *et al.*, 2012) b. Density of states of the Hubbard model at half-filling and zero temperature obtained with the dynamical mean field theory. Each curve represents a different U/W ratio across the Mott transition. (Imada *et al.*, 1998) c. Comparison between the DOS calculated with DMFT at finite temperature for metallic V_2O_3 and photoemission experiments at two photon energies. From (Kotliar and Vollhardt, 2004)

in fig. 1.2(b). Starting from a semicircular density of states (DOS) of width W, when U is equal to zero the solid behaves as a simple metal. When the interaction is turned on, but it's weak (U/W=0.5), the basics for the *Fermi liquid theory* are still valid: the interaction can be considered as a perturbation adiabatically turned on, and the carriers can be described as non-interacting dressed particles, the *quasi-particles*. Tails appear around the central peak at the Fermi energy that can be described, among the others, by the density functional theory. When the interaction is strong (U/W=1), the DOS has a three peak structure, with a central band that retains the coherent properties of the quasi-particle metal, and two bands that originate from local excitations, but are broadened by the hopping of electrons from the atom. As the intensity of the interaction is increased (U/W=1.25-1.5), the quasi-particle peak becomes narrower and more isolated, finally resulting in its disappearance and the formation of a Mott-Hubbard insulator (U/W=2).

The DMFT picture ultimately shows that the Mott transition can be seen as a transfer of spectral weight from the quasi-particle peak to the Hubbard bands. The DMFT also allowed to explore a wider range of parameters, demonstrating that the transfer of spectral weight can be triggered by pressure, doping or temperature. The possibility of accounting for characteristics closer to the ones of real materials ultimately resulted in a more direct confrontation with experiments. In particular, strong connections were created with photoemission experiments (see fig. 1.2(c)), as they allow to measure, with extremely high precision, the bandstructure of the solids.

Fig. 1.2(c) already hints at a point that will be thoroughly discussed in what follows, as

it is clear that DMFT qualitatively reproduces the features of the photoemission spectrum measured at higher photon energy, while it is much different from the other. The questions that naturally arise are: why there is such a difference, and how comparison can be made quantitative? The attempt to answer the first question gave rise to a whole new branch of the photoemission technique, and the main result described in this Part is that it now enters the quantitative realm, and is able to answer to the second question.

1.3 Correlated electrons in core-level photoemission

One of the most interesting aspects of photoelectron spectroscopy is that it intrinsically probes many-body effects. Indeed, with the exception of monoatomic hydrogen, any atom, molecule or condensed material has a sufficiently large number of degrees of freedom to configure itself in a relaxed state. In this condition, the material rearranges in order to screen the positive charge produced by photoionization, at least to some degree.

By using the terminology of the perturbation theory, the initial state of the experiment is formed by the impinging X-ray photon wave and the solid in the ground state. After the interaction, the photoelectron is detached from the atom, and the ionized solid can project over several possible final states. Each mechanism of relaxation of the solid yields a different efficiency in screening the photohole, corresponding to different gains in binding energy of the atom. Since in the whole process the total energy must be conserved, the different relaxation mechanisms will result in the presence of spectral weight at different final kinetic energies, producing the so called *satellite structures*. The photoelectron, in the three-step picture of photoemission, will then have to travel through the solid and cross the surface barrier before being finally detected.

The satellite features can therefore be divided in two classes:

- the *extrinsic* features arise from interactions of the electron detached from the atom as it travels through the solid. They are observed most clearly in simple metals where the small energy needed to produce charge excitation leads to continuous energy losses of the photoelectron, resulting in an asymmetric lineshape, or in the form of excitation of plasmons.

- the *intrinsic* features are due to the possibility of the ionized atom to relax in different final states. They appear most significantly in strongly correlated materials, as the vicinity in energy between several configurations generates strong hybridization between the ground and multiple final states.

The intrinsic satellites of core-level lines are an ideal testing ground for both the theoretical description and the experimental study of new strongly correlated materials. Indeed, the core-levels lines do not show k dispersion, that complicates the modelling and the realization of measurements. Furthermore, as it will be discussed in Sect. 1.5, core-level photoemission can be performed with high resolution up to very high photon energy, therefore allowing to span a wide range of probing depths. In the following, the

most relevant schemes necessary to understand the modelling of intrinsic satellites in transition metal oxides are reviewed.

1.4 Intrinsic satellites in transition metal oxides

The first attempts to describe the structure of the core level satellites were developed by Kotani and Toyozawa (Hüfner, 2003). The model is highly simplified, but it correctly individuates the origin of the satellites in charge transfer processes between the re-arranged energy levels of the ionized atom. The core-hole charge, indeed acts as a positive potential added to the atomic nucleus, acting on the whole electronic band-structure. This ultimately leads to a lowering of unoccupied states below the Fermi energy, where they become available for charge transfer processes.

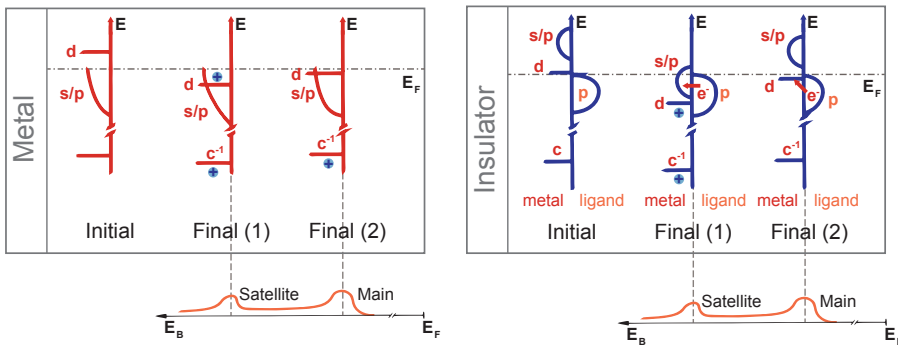

Figure 1.3: Schematic representation of the Kotani-Toyozawa model for PES from a core level in a metal and an insulator. In the initial state the metal *d* level is above the Fermi energy; in the insulator it is above the ligand *p* band. In the final state the *d* level is pulled down below the Fermi energy and can now accommodate an additional *d* electron. Screening in this situation can be achieved by *sp* conduction electrons (final (1), *satellite line*) or if the d-hole is filled by an electron, whereby the ground state is attained (final (2), *main line*). From (Hüfner, 2003).

The model yields the simplest picture if we consider a metal with a partially filled s or p band and a single unoccupied d state above the Fermi energy, as sketched in Fig. 1.3. When the core-hole is created, the d state is pulled below the Fermi energy, and the system can screen the core-hole charge in two ways: either rearranging the s/p band charges, or transferring one charge to the d state. As the d state is significantly more localized than the s/p band, its charge density is higher and it will screen more efficiently the core-hole. This results in a larger binding energy of the atom and therefore higher kinetic energy of the photoelectron. This peak is termed the *well-screened peak*, while the satellite is defined *poorly-screened satellite*.

A similar picture can be applied also to insulators having an occupied ligand p band, a metal ion unoccupied d state, and a metal ion unoccupied s/p band. When the core hole is created, both the d and the s/p band are pulled below the Fermi energy. The charge

transfer can then happen between the filled p band and the s/p band (*poorly-screened satellite*) and between the filled p band and the d state (*well-screened satellite*). By finding an appropriate way to represent the electronic structure of the solid, this model has been successful in describing the characteristics of Copper dihalide compounds (Hüfner, 2003).

The notation for the electronic states usually puts the number of electrons in the TM ion as a superscript to the band labelling, while for the ligand states a simple L is used, with a superscript -1 if a hole is transferred to it. The KT model can anyway mapped on a more broad scheme of TM compounds, allowing us to build the terminology that is still in use today. In this case, the lowest energy excitations are a charge transfer from a TM ion to another TM ion, which has a positive energy cost U. A second possibility is the transfer of a charge from the ligand state onto the TM atom, of energy cost Δ. Finally, a third parameter comes into play, the core hole potential shift U_{cd}. Depending on the relationship between Δ and U_{cd}, the final state with the lowest energy might be the unscreened configuration $d^n L$ or the screened configuration $d^{n+1}L^{-1}$, as shown in Fig. 1.4.

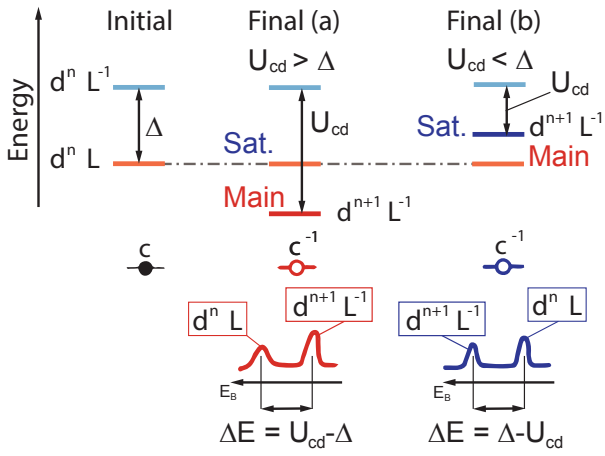

Figure 1.4: Valence configurations used to interpret the core-level photoemission in a TM charge transfer insulator neglecting metal-ligand coupling. The core-hole (c^{-1}) on the metal ion lowers the energy of the d^{n+1} configuration with respect to the d^n configuration. This lowering is described by U_{cd}. Depending on the relative magnitude of U_{cd} and Δ either the $d^{n+1}L^{-1}$ configuration is the lowest final state ($U_{cd} > \Delta$) or the d^nL configuration is the lowest ($U_{cd} < \Delta$). From (Hüfner, 2003).

This model is anyway extremely sketchy and phenomenological. Despite giving a picture of the main mechanisms behind core-level satellite formation, it however cannot account for the complex correlation mechanisms that come from the interplay between the ionized atom and the rest of the solid, and even more, it introduces only a weak hybridization between the ligand and the TM ion by allowing charge transfer, but neglecting the correlation effects.

The attempt to implement the hybridization in the modelling of core level satellites resulted in the Gunnarson-Schönhammer model. This model utilizes the framework of the Anderson impurity model to describe the interaction of the ionized atom with the crystal. The hybridization is now included as a parameter that can be controlled, describing the interaction between the localized and delocalized elements of the band-structure that give rise to the satellites. With the adoption of this model, several important results were achieved, and in

particular a correct description of the relevance of the poorly- and well-screened features in as a function of the change in amplitude of the screening peak in Fig. 1.5.

Building on the successes of the Gunnarson-Schönhammer model, more refined descriptions of the electronic structure of the solid were implemented, leading to the Configuration Interaction Cluster Model (CM). In this approach, the immediate surroundings of the TM atom are described in a Molecular Orbital framework, then adding the intra atomic multiplet effects and the splitting associated to the crystal field. The Anderson impurity approach then rules the interaction between the single cluster and the ligands. The CM approach is extremely effective in reproducing the experimental results in situations where all the relevant interactions in the solid can be considered local.

However, in systems in which highly non-local effects arise, such as strongly correlated materials, the intrinsic limitation of the CM appear evident. For example, as can be seen in Fig. 1.6, the use of a simple NiO_6 cluster in the CM leads to the definition of three lines: a mainly $3d^9L^{-1}$ line, here set at zero energy; a $3d^{10}L^{-2}$ satellite with a two hole configuration located 6 eV higher in binding energy; and the poorly-screened satellite arising from the rigid shift of the $3d^8L$ configuration. As can be clearly seen from the experimental data in panel Fig. 1.6(a), the double edged shape of the main line is not reproduced. In order to account for non local charge-transfer effects, the CM has been extended to the Multiple Cluster Model (MCM), in which several clusters are taken into account. In the case of NiO, a 7-cluster system has been sufficient to give the good agreement presented in Fig. 1.6(a). However, the computational cost of accounting for a large number of cluster forces to use strong approximations, either in terms of "freezing" of some mobile charges (van Veenendaal and Sawatzky, 1993), or in the use of a more sketchy representation of the ligand orbitals (van Veenendaal, 2006).

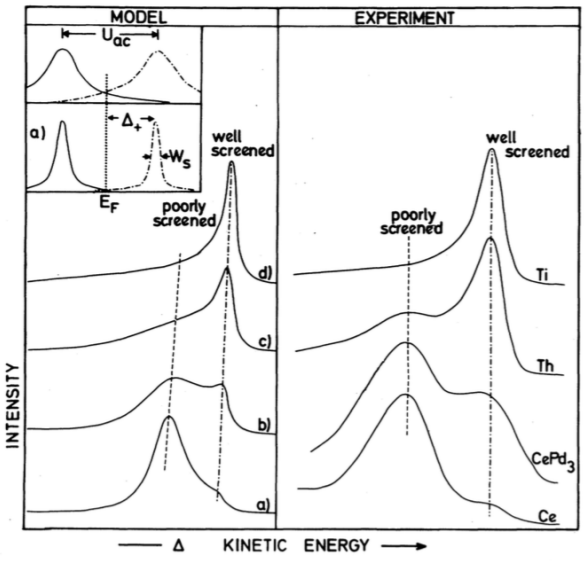

Figure 1.5: Comparison of photoemission spectra from core levels of metals (Ce $3d^5$=2, Th $4f^7$=2 and Ti $2p^3$=2) with theoretical results obtained by applying the Gunnarson-Schönhammer model. From (Fuggle *et al.*, 1980).

The description of correlated electron systems, however, requires one further step. As it has been discussed in Fig. 1.2(b), when close to the Mott transition, the correlated electron systems at half-filling show a three-fold peaked DOS, with one narrow band at

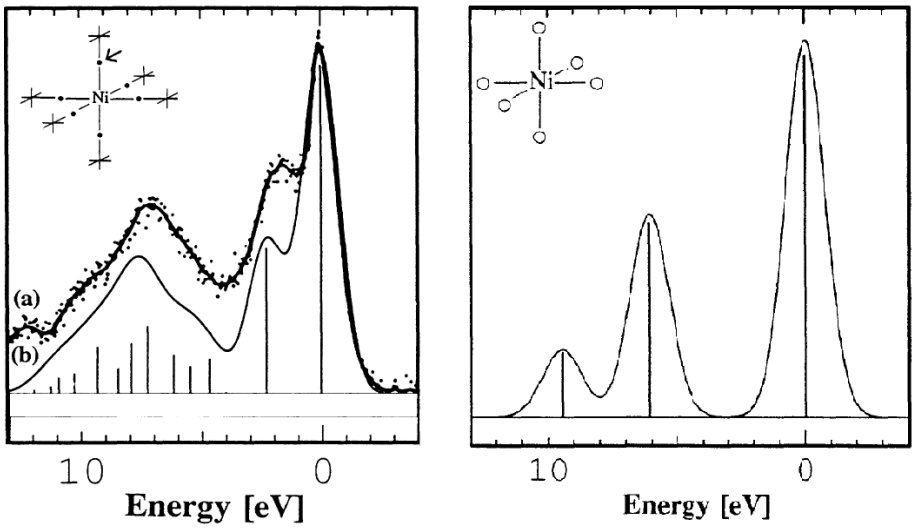

Figure 1.6: Left panel: comparison of experimental Ni 2p spectrum from a NiO single crystal (a) and the result of MCM calculations using Ni_7O_{36} system (b); the main line double peak structure is due to nonlocal screening. In the inset, a scheme of the Ni_7O_{36} system is shown. Right panel: Ni 2p spectrum calculated for a single NiO_6 cluster, also sketched in the inset. Considering a single octahedron does not allow to retrieve the correct shape of the main line. From (van Veenendaal and Sawatzky, 1993).

the Fermi energy. Following the conceptual scheme of the KT-model, it is clear that such a band must give rise to satellites in the core-level photoemission lineshapes. Nonetheless, the emergence of a coherent peak is a collective phenomenon that arises in the solid when it is in a quantum critical condition, making it difficult to describe such system with the use of intrinsically limited models such as the CM or the MCM. An Extended Cluster Model (ECM), which adds the Coherent Band as a separate term in the Hamiltonian has proved effective in the description of bulk sensitive spectra of colossal magnetoresistive oxides, nichelates and several strongly correlated oxides.

Very recently, relying on the fact that both pivot on the Anderson impurity model, the DMFT and the CM have been combined, by treating the crystal with the DMFT and then calculating the hybridization between the TM+ligand states and the DOS of the crystal. This yielded some interesting results such as the description with one framework of 3d doublet and its satellites in the rutenates, or the description of the bulk-only feature in $LaMnO_3$ and $La_{1-x}Sr_xMnO_3$ that will be discussed in Sect. 3.3.2.

It must anyway be stressed that the agreement shown by application of DMFT to the photoemission spectroscopy from real correlated materials must be considered carefully. The functional dependence of the hybridization function gives it a significantly larger number of degrees of freedom than extended models that simply add one term to the CM Hamiltonian, therefore laying themselves open to extrapolations of the model beyond the

limits of its simplified picture.

1.5 Hard X-ray Photoelectron Spectroscopy

Since the effects of electronic correlation are particularly evident in the bandstructure of transition metal oxides, photoelectron spectroscopy has always been regarded as a very powerful technique in the experimental investigation of this kind of materials. Nonetheless, a large number of XPS investigations, both addressing the direct valence band measurement or the satellite structures of the core levels, found puzzling results when addressing even materials with a very clear Mott-Hubbard character, displaying a sharp Mott transition such as V_2O_3, or the doped compound $(V_{1-x}Cr_x)O_3$. Analogous difficulties were met when trying to address *f*-electron materials giving rise to heavy fermion behaviour (Zimmermann *et al.*, 1998).

The contradicting experimental results were clarified by the realization of the first high resolution Hard X-ray Photoelectron Spectroscopy (HAXPES) experiments i.e. photoemission experiments in which the primary photon energy was larger than 5 keV. In these conditions, the probing depth of PES is extended from the 5-15 Å of UV-Soft X-ray PES to 50-100 Å, therefore probing the effective bulk characteristics of the examined solid. In a flourishing of exciting results, the HAXPES studies of transition metal oxides demonstrated large deviation from the surface sensitive measurement, displaying high intensity features close to the Fermi energy (Sekiyama *et al.*, 2000; Mo *et al.*, 2003; Panaccione *et al.*, 2006). The sharp structure close to the Fermi energy was quickly recognized as a coherent feature, followed closely by the Hubbard bands at higher binding energy, more and more defined as the material was closer to the Mott transition.

It became then clear that the surface of a correlated electron material represents a region characterized by larger electronic localization than the bulk. The microscopic mechanism that produces larger correlation at the surface has clearly proven to go beyond the roughness and stoichiometric quality of the surface, beyond the intrinsic lattice reconstruction and reduced coordination, but unfold for lengths significantly larger than the relaxation length of the electronic structure in a metal. The argument is still under active debate, with several models proposed. Some studies even suggest that the large region of suppressed hybridization observed in strongly correlated systems might indeed be an intrinsic property (Borghi *et al.*, 2009). HAXPES has, since then, become a technique of extremely high interest for the study of correlated electron materials, and, as the technology progresses making measurements more precise and efficient, it has a fundamental role in shedding new light in the complex phenomena that characterize such systems.

The HAXPES technique boasts an active an rapidly growing community of users and is now branching in several advanced techniques that go far beyond the investigation of strongly correlated materials (Fadley, 2016); to mention just a few: Hard X-ray Angularly Resolved PES (HARPES), Hard X-ray Photoelectron Diffraction, Time-Resolved HAXPES, Hard X-ray Pohotoelectron Microscopy, Standing Wave HAXPES. Without the ambition of giving on overview of the field, I will try to sum up the most relevant

characteristics of the technique addressing the main focus of this part.

1.5.1 Cross sections, experimental geometries and electron escape depths

The significantly larger primary photon energy of the HAXPES has, as a main outcome, a much larger kinetic energy of the photoemitted electrons. As can be seen in Fig. 1.7(a), the inelastic mean free path (IMFP) of electrons in solids is increased significantly when it has large kinetic energies. While it is true that long IMFPs are also observed in very low energy electrons, it is also clear from the scatter of curves that the IMFP value is, in that range, strongly material dependent[1], and spans more than one order of magnitude. At high kinetic energies (> 2keV), the IMFP increases more significantly and with a weaker material dependence. The IMFP is the parameter that has the largest influence on the PES probing depth, making HAXPES a reliable way to probe, with a good control on the depth of the probed region, buried interfaces, heterostructures, or in general the electronic structure of complex materials far away from the surface perturbation.

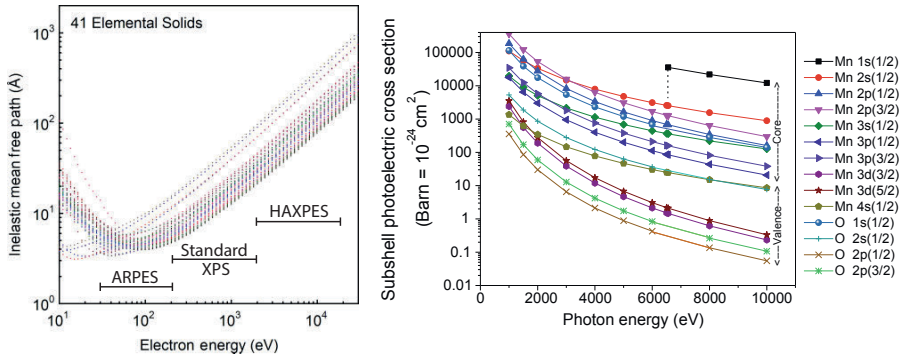

Figure 1.7: a. Energy dependence of the IMFP calculated up to 30 keV from optical data in 41 elements, that lead to the much used TPP-2M formula to estimate the IMFP (Tanuma *et al.*, 2011). Each different colour corresponds to a different material. b. Relativistic subshell cross sections for Mn and O as a function of the photon energy between 1-10 keV (Fadley, 2016).

Nonetheless, several consequences are connected to the use of larger photon energies. The first is the strong decrease in the photoionization cross section, shown for Mn and oxygen in Fig. 1.7(b). It is blatant how the photoionization of each subshell drops more than two orders of magnitude when going from 1 to 6 keV. Despite the fact that new core levels with larger binding energies become accessible with large cross sections (see the Mn 1s appearing at 6.5 keV), most of the interest remains devoted to the outer subshells and the valence band, as they are often more sensitive to the chemical surrounding of the atom. Such a decrease in the cross sections de facto translates in a strong reduction of the signal, especially towards the low binding energy part of the spectrum. For this

[1] in particular is sensitive to the presence of an optical bandgap

reason a careful optimization of all the involved parameters was needed for HAXPES to fully express its potential.

The first is the technical difficulty arising from the high spectral resolution needed for the X-rays in order to achieve sufficiently high energy resolution combined with a large photon flux. This has limited the realization of HAXPES experiments to synchrotron radiation facilities for the last 15 years. Only very recently, high energy monochromatized X-ray lamps have been developed (Kobayashi, 2016). The development of high resolution channel-cut monochromators, allowing for energy resolution lower than 50 meV, combined with high brilliance undulator sources maintaining photon fluxes in excess of 10^{11} ph/s has been the basis of the development of modern HAXPES (Ishikawa *et al.*, 2005).

A precise monochromatization of X-rays had to be combined with an improvement in the technology of electron energy analysers, as the resolving power had to be improved significantly, in order to achieve a final photoelectron energy resolution in the tens of meV range (Kobayashi *et al.*, 2003; Torelli *et al.*, 2005). Furthermore, an accurate evaluation of the experimental geometry had to be carried out. Indeed it was found that positioning the impinging photon beam with a very low (2°-3°) grazing angle, collecting the electrons at normal emission and orienting the X-ray polarization in the direction of the analyser increased the intensity of the signal more than 30 times. This is due to a combination of increased illuminated area and the exploitation of a maximum in the asymmetry in the distribution of photoemitted electrons (Takata *et al.*, 2005).

Despite the technical challenges associated with the realization of experiments, HAXPES carries a wealth of significant benefits besides the sought after bulk-sensititvity. This is due to the fact that at higher kinetic energy several approximations employed in the modelling of photoemission spectra are more closely verified: the sudden approximation holds more precisely (giving a stronger basis to the analysis of satellite peaks), the elastic and inelastic effects of crossing the potential barrier of the surface are suppressed, the smearing of the lineshape due to elastic scattering of the photoelectron in the solid is decreased, and a simpler decomposition of the valence band structure is possible. Furthermore, the inelastic backgrounds are smaller and Auger lines rarely overlap with the HAXPES lines (Fadley, 2016).

Due to the advancements of the recent years in terms of statistics and resolution of HAXPES measurements, it has now become possible to study with high precision the fine structures of the line-shape, addressing satellite peaks and their connection to the many-body interactions in the solid.

1.5.2 Bulk-only satellites

The study of the 2p peaks of strongly correlated materials has presented a significant amount of experimental evidence of the presence of low-binding energy satellite structures which appear only when the probing depth reaches the bulk. Besides the appearance of such structures in the vanadates (Panaccione *et al.*, 2006) in correspondence of the shift of spectral weight in the valence band with the appearance of a coherent band close to the Fermi energy, such structures have been observed in Cuprates, in Nichel Oxide, in

Manganites and in the diluted magnetic semiconductor (Ga,Mn)As (GMA).

The first study of this kind of structures was performed in 2004 by the group of Horiba (Horiba *et al.*, 2004), who studied the Mn 2p lineshape in $LaMnO_3$ (LMO) and $La_{1-x}Sr_xMnO_3$ (LSMO). As shown in Fig. 1.8, the $Mn2p_{3/2}$ line was measured both with standard photoemission (with photon energy 800 eV), and with HAXPES, at two different off-normal emission angles, showing unambiguously that the peak appears only when the maximum bulk sensitivity is reached.

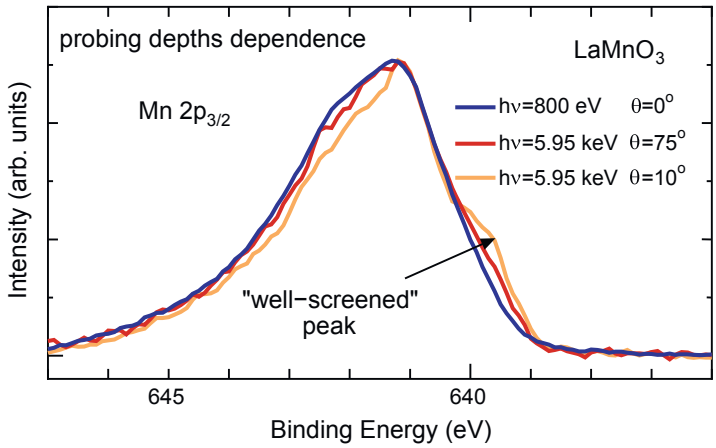

Figure 1.8: Bulk-only high binding energy satellite in $LaMnO_3$. From (Horiba *et al.*, 2004).

The measurements performed on LSMO also showed a low binding energy satellite (LBES) that proved to evolve with doping and temperature. The LBES was shown to appear in correspondence of the magnetic ordering transition of the hole-doped manganite, and to reach the maximum amplitude when the "optimal doping" (corresponding to the maximum value of the Curie temperature).

These features cannot be explained by the simple Anderson Impurity Model, which, given the electronic structure of such materials, does not allow the presence of low-binding energy structures. If one considers the picture given in Sect. 1.2 and fig. 1.2(b) of the bandstructure of strongly correlated materials, in which doping, temperature, lattice or orbital reconfiguration can drive the system closer or further from the quantum critical behaviour, it appears sensible that a good agreement between with the data has been obtained by adding to the cluster model hamiltonian an additional term, representing the screening effects produced by a narrow delocalized structure. This is the basis of the so-called extended cluster model put forward by Taguchi et al. (Taguchi and Panaccione, 2016), which will be employed and discussed in more detail in Sect. 3.3.2.

The fascinating question that emerges from the wide body of experimental results on 3d TMOs is why, in this class of materials, it is necessary to reach bulk sensitivity to observe the non-local satellites. Addressing it involves a deeper comprehension of the

effect of surface on electronic correlation, and the experimental investigation needs to take a step further and evaluate quantitatively the depth dependence of such structures. Our effort has been in aimed in this direction as we performed a quantitative study of the depth dependence of the bulk-only features described in Sect. 3.3.3. We focussed on LSMO as a material which is prototypical in two ways: it is of high interest for spintronic applications, and it is one of the most widely investigated 3d TMOs presenting bulk-only features.

Chapter 2

A correlated electron material for spintronics: $La_{1-x}Sr_xMnO_3$

> Manganites are like good wine. The longer they age, the more they express their complexity.
>
> Giancarlo Panaccione, 2017

Two of the practical ways in which electronic correlation can be changed are either by changing the electronic bandwidth or by varying the band filling. The bandwidth is modified by tuning the lattice parameter of the system while maintaining the same lattice structure. In this case, the on-site or inter-site Coulomb repulsion remains constant with good approximation, while the transfer integral t is changed, giving raise to a modification of the bandwidth W. Besides the direct application of hydrostatic pressure, which results rather limited in terms of applicability, the most used method consists in modifying the chemical composition in a ionic crystal (chemical pressure effect).

To achieve this, it is necessary to find a crystal structure in which the atoms of the desired oxides can be arranged together with another ion. It must then be possible to combine the oxide (in the same valence state) with several different ionic species and still grow crystals with the same lattice structure, although distorted. This can be done, for a very large number of transition metal oxides, with a perovskitic crystal structure, indicated by the formula ABO_3. In this configuration, the 3d TM ions (B) sit at the vertexes of a cube, while the A site is occupied by a larger ionic radius element, an alkaline earth or rare earth, positioned at the centre of the cube. The oxygen atoms are disposed in an octahedral arrangement around each TM ion.

Usually, the *tolerance factor* parameter is defined as:

$$f = \frac{r_A + r_O}{\sqrt{2}\,(r_B + r_O)} \tag{2.1}$$

Where r_i is the ionic radius of each element. If this parameter is one, the perovskite has a cubic structure and the unit cell contains only one chemical formula. If f decreases, the structure is distorted and the B-O-B angle (θ) is no longer 180°. This results in

an alternate tilting of the oxygen octahedra (fig. 2.1). The unit cell assumes several different geometries with reduced symmetry, including a larger number of atoms. The cubic structure containing only one formula unit, with the tilted octahedra, is called the *pseudocubic unit cell*.

The electron bandwidth changes because the hopping mainly happens through the *supertransfer* process in which one electron hops from a B site to an O 2p site while simultaneously from the O 2p site an electron is transferred to the successive B' ion (Zener, 1951). In the strong-ligand field approximation the transfer coefficient has a dependence from $\cos(\pi - \theta)$ (Imada *et al.*, 1998). This allows to change the bandwidth by 30-40% by changing the A site ion. As long as the A site ion has the same valence, substituting it does not affect significantly the electronic bandstructure beyond the discussed variation of W.

The filling control is also easily realized in perovskitic structures, and consist in artificially changing the occupation number of the transition metal 3d states. If, instead of a single species of rare earth or alkaline earth, a calculated mixture of different valence ions is used, the oxide can be electron- or hole-doped. The different occupation reduces on average the on-site repulsion U, reducing the correlation. The change in occupation, however, induces significant modifications not only in the band-structure, but also in the mechanisms with which electrons interact between each other.

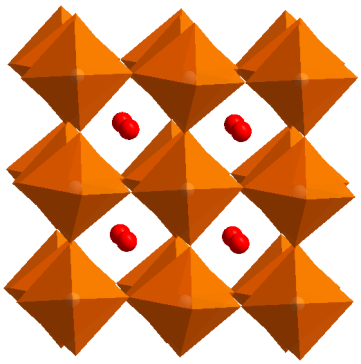

Figure 2.1: Several pseudocubic unit cells of LSMO. The Mn ion is at the centre of each octahedron, while at the edges sit oxygen atoms.La/Sr atoms are marked by the red spheres. The slight tilting of the octahedra leads to a much larger effective unit cell, with trigonal symmetry.

Combining the presence of bandwidth control in the form of a perovskite distorted structure with the filling control, it is possible to fine tune the value of U/W, obtaining compounds which are extremely close to the metal insulator phase transition, where the energy scales are very close, and slight external variations can produce very large effects. The Strontium doped Lanthanum manganite is a compound that is obtained by substituting x tetravalent Strontium ions to the trivalent Lanthanum per chemical formula unit, both of which are residing in the A site of the perovskitic structure (fig. 2.1), therefore giving a chemical formula $La_{1-x}Sr_xMnO_3$.

The parent compound $LaMnO_3$ (LMO) is classified as a wide-band charge-transfer insulator. In LMO the occupation number of the 3d band is 4, making it a system with half-filling of the 3d band. The partial filling (and in particular half) of the 3d band makes the on-site and inter-site spin interactions also very important, together with the effects on the electronic structure of the perovskitic lattice geometry. The substitution of Sr reduces the value of

U, making the system metallic at all temperatures for concentrations $0.2 > x > 0.5$. Higher values of Sr concentration drive the system towards the parent compound $SrMnO_3$ (SMO), a wide-band (even wider than LMO as the Sr ionic radius is smaller) charge-transfer insulator. In LSMO, the holes created by Sr doping have a strong ligand 2p character, so both types of charge excitations have to be considered (Saitoh *et al.*, 1995). In fig. 2.2 is shown a diagram that contextualizes LSMO within the landscape of several perovskitic TMOs.

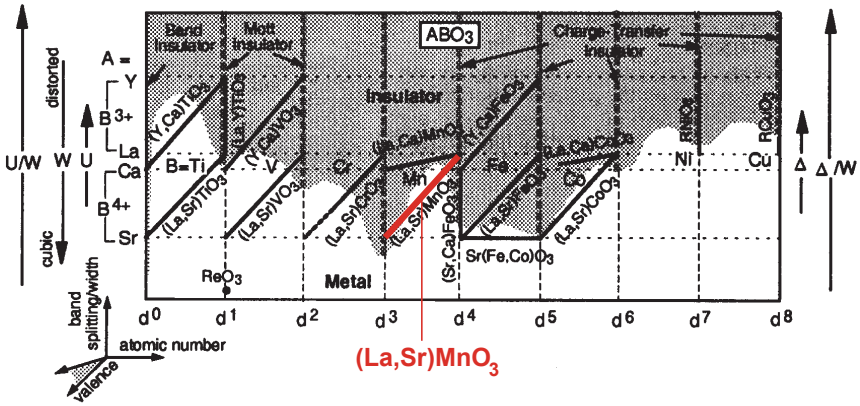

Figure 2.2: Schematic diagram identifying the insulating and metallic regions in 3d transition metal oxides with perovskitic structure. From (Fujimori, 1992).

The high interest in LSMO stems from the fact that the control of electronic correlation allows to drive it very close to the metal-insulator transition. For a material in this condition, the presence of further degrees of freedom capable of creating long range order leads to complex behaviours: when these dominate, they are capable of rendering the material metallic. When, increasing the temperature, the long range order collapses, the material crosses the metal-insulator transition. However, the transport migh not disappear completely, but just be strongly reduced as weaker, more localized interactions dominate the crystal energy minimization. The transition often passes through to a nanoscale disordered phase (Dagotto *et al.*, 2001; Salamon and Jaime, 2001) in which percolative processes are at play. In the case of LSMO, the long range ordering is produced by magnetic interactions, giving rise to the phenomenon of Colossal Magnetoresistance and half-metallicity, two properties that are of high interest for the application to spintronics, as mentioned in the Introduction. To understand how these properties emerge, and how to explore them with photoemission spectroscopy, a deeper insight on the details of the electronic structure is needed.

2.1 Electronic structure of LSMO

The first effect that must be considered in the description of the electronic bandstructure of manganites is the presence of the *crystal field*. Indeed, as the Mn atom is surrounded

by the oxygen nearest neighbours and the second nearest neighbours (La,Sr), the presence of the electrostatic field of the crystal breaks the spherical symmetry that makes the 3d states five-fold degenerate. From the group theory (Pavarini *et al.*, 2012) it is found that in a perovskitic structure produces a splitting of the 3d states in a doublet (e_g) and a triplet (t_{2g}).

The energy position of the system is usually built by keeping in mind the atom symmetric state: when the atom is surrounded by a spherically symmetric negative field, the 3d state energy is increased from the zero field value. If the crystal symmetry is added, the e_g states will be lifted in energy while the t_{2g} will be lowered, so as to keep the average energy of the system in the same position. The Δ_{e_g} and the $\Delta_{t_{2g}}$ are therefore in a 3/2 ratio, and the energy difference is customarily indicated with the symbol $10Dq$. In a schematic picture, the e_g orbitals have higher energy because their charge distribution is oriented towards the negatively charged oxygen, while the t_{2g} states are oriented in directions that minimize electrostatic repulsion, as shown in fig. 2.3. For LSMO, $10Dq$ is around 1.5 eV.

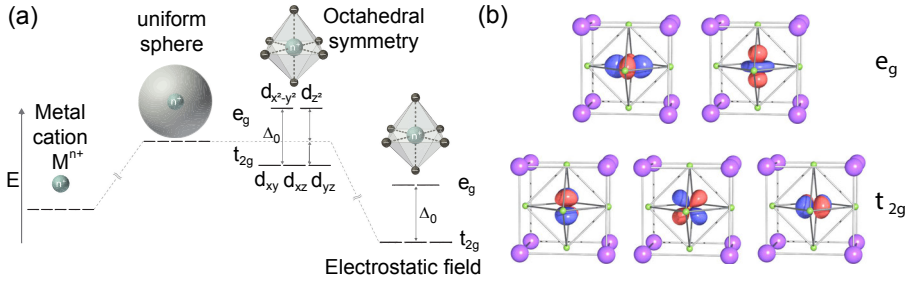

Figure 2.3: a. Scheme of the levels involved in the crystal field splitting of the 3d bands in perovskites. From (Awan *et al.*, 2017). b. Surfaces of equiprobability of the 3d orbitals in the e_g and t_{2g} levels. Note the orientation of the lobes, towards the oxygen atoms in e_g, in the farthest angular direction in t_{2g}. From (Pavarini *et al.*, 2012).

LSMO is magnetic, and it therefore has a strong Hund exchange shift (J_H) of the 3d bands between spin majority and spin minority states. For LSMO J_H is in excess of 2.5 eV, leading to a configuration in which the majority t_{2g} and e_g bands are below the lowest t_{2g} minority state. When populating the 3d band then, the first three electrons are then placed in the majority t_{2g} state. The electrons in the t_{2g} states are not playing a significant role in the delocalization mechanisms, and, from the point of view of magnetic interactions, they are assumed to generate what is called the *core spin*, i.e. a momentum **S** of amplitude S=3/2 that can be treated as localized on each manganese ion.

The single electron added by the presence of Mn^{3+} ions must then be placed in the majority e_g band, and that defines the Fermi energy and the low-temperature metallic character. The majority e_g band is indeed less than half filled as part of the ions are Mn^{4+}. The Mn ions, in both valence states, are therefore in the high spin state. As it can be seen in fig. 2.4 a, the Fermi surface lies completely within the majority e_g,

giving rise to a completely spin-polarized transport in LSMO. This has proven to be a characteristic of this material that, combined with the persistence of ferromagnetic order above room temperature, makes it extremely interesting from the application point of view. This schematic picture is sufficient to describe broadly the characteristics of the real bandstructure of LSMO, as can be seen in the results of DMFT calculations in fig. 2.4 b.

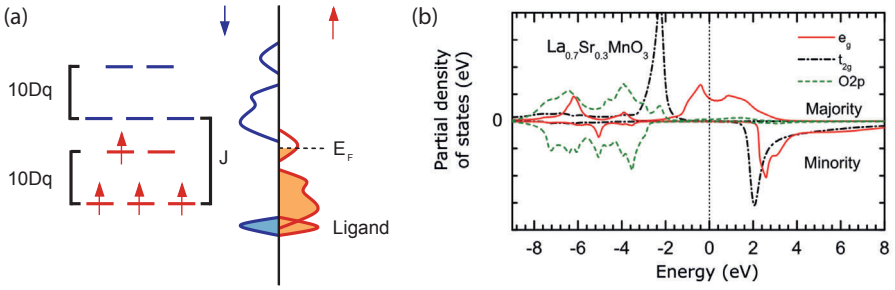

Figure 2.4: a. Scheme describing the position of the electronic energy levels in combined presence of a large exchange splitting and crystal field. On the right a cartoon figure shows that how these result in the electronic structure of LSMO, when atomic levels are broadened in bands. b. The electronic bandstructure of LSMO as results from DMFT calculations (Hariki *et al.*, 2016), isolating the contributing subshells of the Mn and ligand.

2.1.1 Double exchange and Jahn-Teller interaction

In order to have a complete picture of the interactions at play in this system, it is important to identify the two of them that dominate the low temperature metallic phase and the weaker one that mainly drives the high temperature, paramagnetic high-resistivity state.

In the case of LSMO, since the t_{2g} produce a large localized magnetic momentum, it is possible to treat the magnetic system as a lattice of localized spins interacting through the hopping of the mobile electrons. In the case of LSMO, relevant mechanism can be reduced to the hopping between Mn^{3+} and Mn^{4+}. In this case the hopping is favoured when the core spins of the atoms are aligned, because the Mn^{4+} has an empty majority e_g to accommodate the hopping electron (fig. 2.5 a). This process, called *double exchange* (Zener, 1951) is fundamentally different from the process known as *superexchange* in which the initial and final atom of the supertransfer process have the same valence. In the latter case, the alignment tends to be antiferromagnetic, although geometrical factors can favour hopping between perpendicular orbitals of Oxygen, resulting in a weak ferromagnetic order (Pavarini *et al.*, 2012).

The concept by Zener was transformed in a model by Anderson and Hasegawa (Anderson and Hasegawa, 1955), who treated the core spins classically and the tunnelling electron quantum mechanically: they found that the effective transfer integral of the su-

pertransfer process is $\propto \cos(\vartheta/2)$, where ϑ is the angle between the core spins. The picture that emerges is that, in order to minimize the energy of the crystal by delocalizing the electrons, the alignment between the core spins must be ferromagnetic, and the hopping electron must also have spin majority character. When the temperature is sufficiently large to produce a large enough disalignment of the core spins, the charge transport is also suppressed, and the system assumes an insulating character.

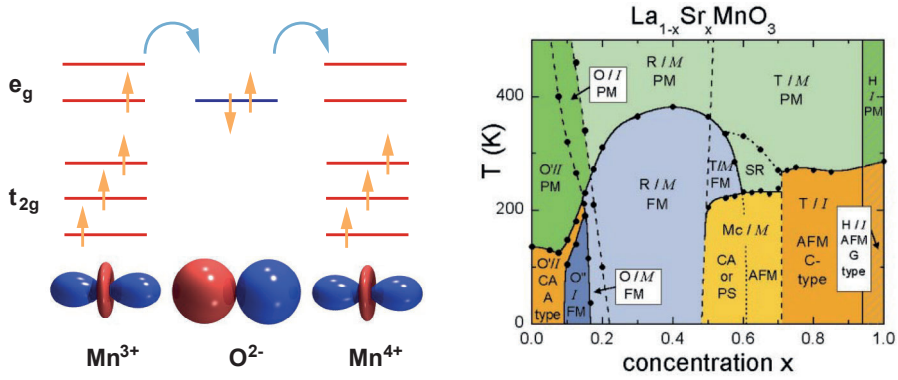

Figure 2.5: **a**. Schematic picture of the double exchange mechanism. **b**. Phase diagram of LSMO. The labelling is as follows. **Crystal structure**: Jahn-Teller distorted orthorhombic (**O'**), orthorhombic (**O**), orbital-ordered orthorhombic (**O"**), rhombohedral (**R**), tetragonal (**T**), monoclinic (**Mc**), and hexagonal (**H**). Magnetic structure: paramagnetic (**PM**), short-range order (**SR**), canted (**CA**), A-type antiferromagnetic (**AFM**), ferromagnetic (**FM**), phase separated (**PS**, C-type antiferromagnetic (**AFM C-type**. Electronic state: insulating (***I***) and metallic (***M***). From (Hemberger *et al.*, 2002).

The double exchange model satisfactorily explains the low temperature ferromagnetic phase that is observed in the $0.2 < x < 0.5$ region of Strontium doping, and the dome with the maximum Curie temperature at the optimal doping $x = 0.33$. However, when applying this schematic picture to the full complexity of LSMO phase diagram, as is seen in fig. 2.5 b, several difficulties arose: for example, it does not explain why at low temperature antiferromagnetic phases appear for $x < 0.1$ and $x > 0.6$. Progress in the understanding of double exchange process has been made first by treating it in a semiclassical way in the presence of an antiferromagnetic background (de Gennes, 1960), and then finally developing an effective double exchange hamiltonian (Kubo and Ohata, 1972) that gave a fully quantum mechanical description of the double exchange magnet.

But even a fully quantum-mechanical description based solely on double exchange leaves some questions unanswered. The most relevant is the character of the high temperature phase. Above the Curie temperature, indeed, thermal fluctuations reach the threshold energy, and are sufficient to destroy the magnetic ordering. The system crosses a second order phase transition to a paramagnetic state. Taken away the advantage of supertransfer hopping, the ideal system should behave like a badly conducting metal,

with single electron charge transfer processes across the oxygen orbitals.

Confusingly, a large number of LSMO crystals, together with several other compounds of the manganite family such as LCMO, LBMO or PCMO, show instead resistivity curves with negative slopes, fingerprint of emergent insulating behaviour, or, more rigorously, of semiconducting character.

This has been explained as an effect of Jahn-Teller (JT) interaction. Such process consists of a dynamical distortion of the octahedral symmetry triggered by the presence of a carrier in a degenerate e_g state. The distortion removes the degeneracy and reduces the energy of the crystal by setting the electron in a lower energy state.

In a crystal this effect tends to localize the charge carriers, as the electron in a Jahn-Teller lowered e_g state needs to hop into higher energy empty e_g states. The electron propagating in the crystal together with such a lattice distortion is called a *polaron*, and can be treated as a quasi-particle (Holstein, 1959). Charge transport can then be seen as happening by thermally activated hopping of the polarons, from one lattice site to the next, which requires a specific activation energy, retrievable in the slope of resistivity vs. temperature curves (Salamon and Jaime, 2001).

Millis and coworkers (Millis *et al.*, 1996) developed a model to include polaronic effects in the double exchange hamiltonian, describing phonons as eigenstates of an oscillator of stiffness k, appearing in the total Hamiltonian with a JT-coupling constant g. Solution of the model with DMFT gives an effective polaron coupling constant $\lambda = g^2/kt$, which also depends on the bandwidth via the kinetic term t. This model suggests that the polaron trapping energy becomes larger in narrower bandwidth compounds.

When the bandwidth is the largest, i.e. in optimally doped LSMO, λ is the lowest, and JT interaction does not produce self-trapping. The Curie temperature is thus maximal and close to the value predicted by double exchange alone. Above it, the system has simple high-resistivity metallic behaviour. On the other hand, when the bandwidth is decreased by changing the alkaline metal or the lanthanide, the self-trapping threshold is crossed and above T_C a sharp but continuous transition drives the system in an insulating state. Also the changing of dimensionality via perovskite layering (another form of bandwidth control) gives rise to polaronic self-trapping as observed recently by appearance of a proper quasiparticle peak (Massee *et al.*, 2011).

Bandwidth control via doping can be understood within a similar picture, although it is more complicated because the effects of phase competition are also at play. Within a similar theoretical framework, indeed, it was also demonstrated that in the parent insulator LMO the Jahn-Teller effect can be cooperative, and produce a macroscopic ordered phase, defined as *orbital ordered* (Millis, 1996). The combined presence of superexchange and orbital ordering produces an insulating antiferromagnetic state at low temperatures, that evolves in a paramagnetic insulating state above 140 K. The orbitally ordered phase persists up to very high temperatures (>500 K).

In the doping range between $x = 0$ and $x = 0.3$, and similarly on the other end between $x = 0.45$ and $x = 1$, the system is in a crossover region, where the competition between orbital order and ferromagnetic order gives rise to a complex sequence of phases in the low-

temperature ground state. At finite temperature, and in particular in the vicinity of Néel or Curie temperatures, phase competition gives rise to electronically disordered phases, with spatially heterogeneous bandstructure that have been interpreted in the framework of nanoscale phase separation (Dagotto *et al.*, 2001) and Griffiths phases (Salamon and Jaime, 2001; Krivoruchko, 2014).

In presence of extrinsic structural disorder, such as cation disorder (Salafranca and Brey, 2006), crystalline defects or inclusion of impurities (Dagotto *et al.*, 2001), Anderson localization of the carriers adds a further tendency towards an insulating character. The effect of oxygen vacancies, which can be easily created by non-optimal oxygenation during growth, or annealing in vacuum, plays both effects, introducing crystalline distortions and reducing the valence of Mn (i.e. contrary to the effect of Sr doping) (Schlueter *et al.*, 2012).

2.1.2 Surface effects

In the perspective of the previous discussion, where competition between interactions in the few eV to hundred of meV range give the complex phase diagram of fig. 2.5 b, it becomes clear that the perturbation produced by the creation of a surface must have a strong impact on electron mobility. As a rule of thumb, it is clear that reduced symmetry and coordination (not to mention the introduction of disorder due to surface roughness and lattice reconstruction) tend to localize electrons, hindering the ordering processes that lower the energy of the crystal sufficiently to make electrons mobile.

This effect came as a rather disappointing realization in the case of LSMO, as its promising colossal magnetoresistence properties (Jin *et al.*, 1994), that were shown to be present at low temperatures (Lu *et al.*, 1996; Bowen *et al.*, 2003), could not be maintained up to room temperature, regardless of the crystalline quality of the material (Rodriguez-Martinez and Attfield, 1996). Despite the recent realization of a few devices operating at room temperature (Brivio *et al.*, 2010; Yajima *et al.*, 2011), big difficulties are still encountered when interfacing LSMO with other oxides.

It was quickly acknowledged (Park *et al.*, 1998b), by pioneering work combining spin-resolved photoemission (SPES), XMCD and SQUID magnetometry that the surface of LSMO shows a particularly large region in which electronic and magnetic properties are different with respect to those of the bulk. This is often addressed to as *dead layer behaviour*. Such term indicates the presence of a region, in correspondence of the crystal interruption, in which the magnetic and transport properties are strongly suppressed. As a short-hand definition we will use this term, although it is important to keep in mind that the difference from the bulk is a pervasive characteristic of surfaces, and that skilful surface engineering has often proven the capability of finding new functionalities in regions with modified properties.

The effect of vertical confinement in the properties of complex oxides has proven to be relevant also in other systems, such as the interface between insulating Lanthanum Aluminate ($LaAlO_3$, LAO) and insulating Strontium Titanate ($SrTiO_3$, STO). This heterostructure presents us with a problem similar to LSMO dead-layer behaviour: below a certain thickness of the LAO layer, the interface is insulating, while above it a two dimen-

sional conductive electron system is formed, with very peculiar characteristics (Ohtomo and Hwang, 2004; Berner *et al.*, 2013). Also in this case, a description accounting for every experimental evidence has not yet been agreed upon. It thus appears that in several complex oxides there is a thickness, often called *critical* in the literature, above which the sought-after properties are attained. However, this term might create some confusion with the critical length scales that arise in correspondence of a phase transition in the presence of an order parameter, in particular for magnetic materials. In the following, we will thus indicate with the term *cross-over thickness* the distance from the surface in the vertical direction at which the electronic properties appear to be strongly modified.

For LSMO, Park and coworkers individuated a temperature dependence of the metallicity (evaluated as the spectral weight close to the Fermi edge) and the magnetization (measured as the spin polarization of e_g and t_{2g} electrons) way faster than the bulk of the film, as shown in a combined technique study in fig. 2.6.

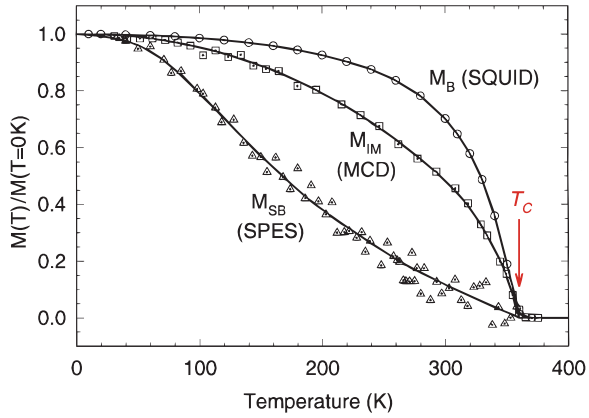

Figure 2.6: a. Magnetization vs. temperature curve for LSMO epitaxial layers (190 nm thick) on $SrTiO_3$ substrate. Spin-resolved photoelectron spectroscopy (SPES) has an estimated probing depth of 5Å, Magnetic Circular Dichroism in x-ray absorption (MCD) has a probing depth of 50Å, while SQUID magnetometry probes the bulk magnetization of the system. From (Park *et al.*, 1998b).

The observed curve obtained by SPES can be compared to the ones observed in Fe by LMDAD (Sirotti *et al.*, 1995), that show an almost linear relationship with temperature ($\vec{M}_S \propto (1 - T/T_C)^{\beta_S}$ with $\beta_S = 0.81 \pm 0.01$, where T_C is the bulk Curie temperature). This is explained by statistical mechanics considering the effects of surfaces in the Ginzburg-Landau theory of second order phase transitions (Domb, 1986). The striking feature of Park observations is, however, that a large discrepancy from the bulk trend is also observed in the XMCD measurement, with a probing depth close to 50 Å, signalling that the region characterized by reduced magnetic interactions is rather large.

This triggered a significant effort, still ongoing today, to understand the physics of electronic correlation at the surface of LSMO, with the aim of controlling it with the powerful instruments at our disposal such as the inclusion in heterostructures, the exploitation of proximity effects, the interfacing with multiferroics and many others. Initially, the issue was attributed to the presence of defects in the films either due to effective impurities arising for non-optimal growth, or to effects of oxygen disproportionation, which is known to have significant effects in LSMO properties (Schlueter *et al.*, 2012).

However, with the refinement of the growth technology and the realization of extremely high quality thin films by Ozone assisted Molecular Beam Epitaxy (Werner *et al.*, 2011) and Pulsed Laser Deposition, the former hypotesis was gradually ruled out. The rejection of the latter required even further progress, with the realization of in-vacuum sample transfers for the measurement of free surfaces (Bertacco *et al.*, 2008), and more recently also for buried interfaces, with the development of High Resolution Transmission Electron Microscopy (HRTEM) methods combined with Electron Energy Loss Spectroscopy (EELS) (Mundy *et al.*, 2014; Spurgeon *et al.*, 2015), it became clear that the dead layer must arise from intrinsic mechanisms.

It is possible to divide the large body of literature on the topic in two main directions: the study of the dead layer appearing when the system is interfaced with other materials, and the study of free surfaces.

For what concerns interfacing, the model of the *charge catastrophe* has recently been proposed (Nakagawa *et al.*, 2006) and seems to yield a promising consistency. Indeed, both LSMO and the materials that are usually interfaced with it are generally perovskitic polar solids, in which the neutrality of the bulk crystal is guaranteed by matching of the opposite charges of the forming AO and BO_2 layers. When such a configuration is interrupted, an unbalanced charge is accumulated at the interface. In presence of atomically sharp transitions, this can result in very large effective fields at the interface: in a material with mobile carriers, this triggers a screening redistribution of charges, that locally alters the occupation of the TM sites. Following this concept, interesting results have been obtained by tuning the Sr doping layer-by-layer in order to compensate the charge accumulation (Peng *et al.*, 2014).

Nonetheless, when turning to the study of the free surface, charge accumulation seems to be only part of the picture. A large number of different mechanisms have been proposed: nanoscale phase separation (Bibes *et al.*, 2001), the redistribution of orbital occupancies (Pesquera *et al.*, 2012, 2016) and magnetic reconstruction (Bruno *et al.*, 2011), to mention a few. It has even been suggested that the dead layer behaviour might stem from a more fundamental level such as the limited dimensionality effects on the double exchange interaction (Brey, 2007).

The scatter in the proposed mechanisms partly arises from the complexity of the material, but also from the contrasting results of experiments, which struggle to capture the fine details of the electronic structure within the same material and nanometric control of the depth. Indeed, it has become clear that the simple variation of the film thickness cannot be easily used as a way to explore the dead layer behaviour. The distinct scales at which the interactions are established, indeed, give radically diverse properties to films of slightly different thickness. On the other hand, the combination of techniques with different probing depth often requires the changing of a large number of experimental parameters, of which some cannot always be controlled.

Our effort, demonstrated here in this interesting system, sets in the direction of developing a quantitative method to study the electronic structure with high precision in the probing depth, chemical selectivity and maintaining identical experimental conditions.

Chapter 3

Experimental results

> Here's one thing you have to know.
> We only measure spectra with good statistics.
>
> Giancarlo Panaccione, 2014

Part of the results presented in this chapter have been published in (Pincelli et al., 2017b). The results presented in that paper are the accomplishment of a work initiated by V. Lollobrigida and in part described in (Lollobrigida, 2016), which we developed together and to which we contributed equally.

In the next chapter is collected a summary of the experimental results on the characteristics of the Bulk-only Low Binding Energy Structure observed in LSMO, in the effort of giving a coherent picture of its features. The knowledge achieved in this way will then be applied to quantification of the the spatial extension of the region with altered transport and magnetic properties.

3.1 Methods

With the aim of giving quantitative information on the depth at which transport and magnetic properties are recovered, we chose to measure the manganite in three different strain states. Indeed, as will be discussed in Sect. 3.1.3, we had the possibility of making sure that the films had a high degree of stoichiometric purity and structural order: we therefore chose to probe the electronic structure of a strain-relaxed film, and then to introduce a controlled structural perturbation by means of controlled compressive or tensile strain due to lattice mismatch between the substrate and the epitaxial film.

We also addressed a diluted magnetic semiconductor sample, (Ga,Mn)As. In this material, as mentioned in Sect. 1.5, a low binding energy feature, associated with the mobility of charges and the magnetic ordering also been observed (Fujii *et al.*, 2011, 2013). Also this material, being of great interest for spintronic applications, has been object of large body of theoretical and experimental work dedicated to the understanding of its properties. Despite the efforts, however, the temperatures at which the magnetic order collapses remain extremely low. In this material a carrier depletion zone up to 1 nm has

been observed (Sawicki *et al.*, 2010), with modified magnetic ordering. It was nonetheless proven to be a region whose characteristics can be modified by the application of external electric fields (Sawicki *et al.*, 2010) or the exploitation of magnetic proximity effect (Maccherozzi *et al.*, 2008) by a Fe overlayer. The latter result represented a significant achievement since it allowed to retain ferromagnetic alignment well above room temperature in a 2 nm region of the (Ga,Mn)As underlayer.

Due to the fact that in this system the spectroscopic fingerprint that we use to track the depth of the electronic relaxation is present, and the transport and magnetic properties are also deeply intertwined, but rely on completely different mechanisms (Dobrowolska *et al.*, 2012; Jungwirth *et al.*, 2014), we were interested in quantifying possible differences between this material and LSMO.

A key point in the strategy we envisioned relies on the exploitation of the new capabilities of state-of-the-art beamline facilities at medium and high energy synchrotron radiation facilities. In particular, I09 at the Diamond Lightsource, UK, is capable of delivering tunable soft x-rays in the 230-2000 eV range and hard x-rays up to 18 keV essentially in the same position and with the same energy resolution. On the other hand, BL19LXU at SPring-8, Japan, relies on an extremely long undulator to achieve a high photon flux ($2\text{x}10^{14} ph/s$) at large photon energies, allowing for the realization of more complex experiments such as the use of circularly polarized light or time-resolved experiments. In the following, the key traits of these facilities will be discussed in detail.

For the sake of the fluidity of the discussion, the characteristics of the instrumentation used for time-resolved experiments at BL19LXU will be deferred to Sect. 7.1. For the same reason, we leave out a discussion of the nature and properties of synchrotron radiation. The historical perspective and the technological progress that has brought to the third generation machines, albeit extremely instructive for the understanding of important choices in the technical solutions, will be also left out and circumstantially mentioned only when needed. The interested reader is referred to (Mobilio *et al.*, 2015), which treats the subject in detail and covers topics which are way beyond the limits of this thesis.

3.1.1 Beamline I09

As mentioned before, the main concept of this beamline, for which it is considered to be the first of the *next-generation* in the HAXPES community (Pianetta and Lindau, 2016), is to deliver to the same point soft and hard x-rays with comparable spot size and energy resolution, so as to perform PES experiments with varying probing depth maintaining all the other experimental conditions unchanged. This concept raises several technical challenges: two different sources need to be used and the x-ray optics for the two beams is completely different. The realization of high energy resolution, high flux and small spot size transport is individually for soft or hard x-ray hardly a simple task. The combination of the two adds geometrical constraints that need to be carefully accounted for.

Beamline I09 (fig. 3.1) uses as x-ray sources two undulators hosted in the straight section of the 3 GeV U.K. national synchrotron, Diamond Light Source. The first one

is a 27 mm period, 5 mm minimum gap in-vacuum undulator, two meter long. It spans an energy range of 2-18 keV, and it feeds the hard x-ray branch, called *branch I*. The undulator whitelight is transmitted through the front-end slits (HS1) to the first monochromator, a double crystal fixed-exit system using the Bragg (111) reflection of silicon. The first crystal sustains the largest heat load (up to 30 W/mm²) and is therefore efficiently cooled with liquid nitrogen to keep a stable temperature on the optics. The double cystal monochromator reaches a relative energy resolution in the range of $\Delta E/E \approx 10^{-4}$, leading to a photon energy broadening $\Delta E \approx 0.6eV$ at $h\nu = 6000eV$, a value too large for high resolution HAXPES.

A channel-cut monochromator can then be introduced in the beam. This geometry allows to use high Bragg index reflections yielding very small relative energy resolutions while maintaining positional stability and relatively high flux (Ishikawa *et al.*, 2005). For the case of the Si (004) reflection used in these experiments, it results in a photon energy broadening of about 250 meV at the sample position. A set of mirrors focus the beam down to a 15 μm $\times$ 30 μm spotsize and reject the harmonics of the monochromator crystals. The branch I serves an endstation in EH1 where it is the only probe, and one in EH2, which can also receive the soft x-rays.

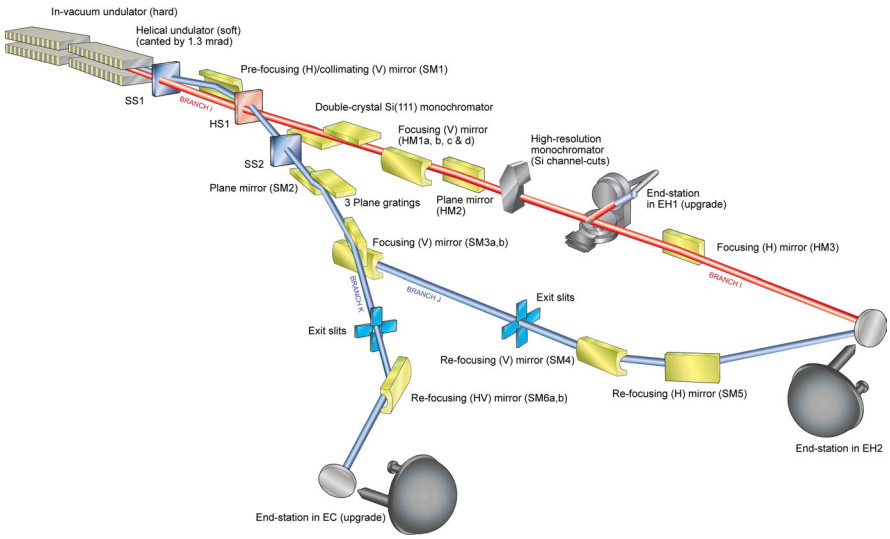

Figure 3.1: Scheme of beamline I09. Details in text. From I09 Webpage.

The soft x-ray source is a 2.3 m APPLE II helical undulator, allowing polarization control (Sasaki, 1994). Since soft x-rays allow for larger angle reflections on the optics without large flux losses, this branch has a more complicated path. The undulator is canted 1.3 mrad outwards with respect to the ring. The white beam crosses the I branch as it is reflected by a mirror producing horizontal focussing and vertical collimation to optimize the performance of the grating monochromator. A pair of entrance slits (SS1 & SS2) shapes the whitelight beam and reduces the heat load on the optics.

The monochromator features a system of 3 gratings of 300, 400 and 800 lines/mm that, combined with an appropriate opening of the exit slits, allows to achieve hundred meV energy resolution in the whole energy range covered (200-2000 eV). The vertical focussing mirror (SM3) further divides the soft x-ray branch in *branch K* which serves a purely soft x-ray endstation (EC) and *branch J* which with a final refocussing is steered back to the endstation in EH2. Also in this case the final spotsize is 15 μm $\times$ 30 μm in focussed configuration. In defocussed configuration both I and J branches have a 300 μm $\times$ 300 μm spotsize.

The experimental endstation features a state of the art VG Scienta EW4000 electron energy analyser with a large acceptance angle, with nominal resolution below 100 meV at 10 keV, which is the maximum electron kinetic energy accepted. The manipulator, with 5 degrees of freedom (X,Y,Z,Θ), allows for the grazing angle geometry mentioned in Sect. 1.5.1, is cryocooled down to $<$ 50K and can be heated up to 1500 K. The manipulator can be retracted into the preparation chamber positioned above, allowing for surface preparation and overlayer deposition on the same manipulator. All the photon energy dependent experiments and the temperature dependent experiments were performed in this beamline in the endstation in EH2.

3.1.2 Beamline BL19LXU

BL19LXU (fig. 3.2 a), attached to the large 8 GeV accumulation ring of SPring-8 in Japan, relies on a completely different strategy. Based on one of the longest undulators in the world employed at a synchrotron (Hara *et al.*, 2002), a 25 meters long 781 periods array, this beamline covers only the hard x-ray (7-18 keV) range, but it does so with an extremely large photon flux. In this case the radiation power, which peaks at 35 kW, is a serious issue: the off-axis part of it is handled by the front-end, but still the first double crystal monochromator using Si (111) reflection receives more than 500 W/mm^2 and required special design of the nitrogen cooling system.

A double Pd mirror system 40 m downstream allows to focus the beam down to millimeter size and to reject the higher harmonics. The photon flux delivered to the hutches is about 2 2 $\times$ 10^{14} ph/s. The large intensity available allows to use a high Bragg index channel cut monochromator, Si(444), with nominal ΔE/E = 6.5 $\times$ 10^{-6}. Indeed, an energy broadening of ΔE $\approx$ 60meV at 8 keV was achieved.

The beam then crosses a diamond crystal that acts as a phase retarder (fig. 3.2 b). Indeed considering the dynamical theory of x-ray diffraction, the wave transmitted through a perfect crystal can be decomposed into two waves of perpendicular σ and π polarization. The emerging wave is in a polarization state that depends on the accumulated phase difference between the two components. As the phase deviation depends on the deviation from the Bragg angle $\Delta\theta$, it is possible to control the polarization state of the transmitted beam (Hirano *et al.*, 1991). In fig. 3.2 c the degree of polarization as a function of the offset from the Bragg angle is measured by evaluating the x-ray magnetic circular dichroism (XMCD) of a powder of $CoPt_3$ alloy, demonstrating very high values around $\Delta\theta$ = 30 arcsec.

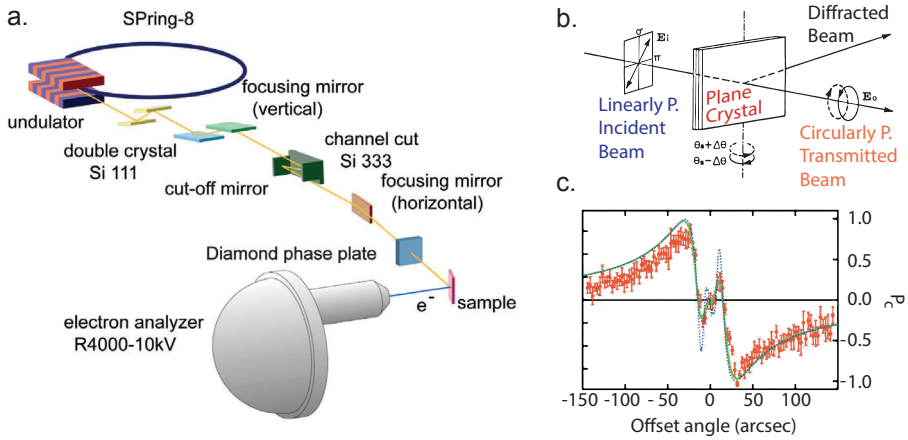

Figure 3.2: a. Scheme of beamline BL19LXU. b. Scheme describing the mechanism by which a hard x-ray beam is polarized by diffraction through a perfect crystal from (Hirano *et al.*, 1991). c. Recent measurement of the transmitted beam degree of circular polarization as a function of the offset angle (Suzuki *et al.*, 2014). The red dots are measured by XMCD contrast in transmission from a $CoPt_3$ sample. The continuous and dashed lines are obtained from calculations considering different relative energy resolutions ($\Delta E/E = 1.1 \times 10^{-4}$ and $\Delta E/E = 0.5 \times 10^{-4}$ respectively).

At the present day, thin diamond crystals are used for their crystalline quality and resistance to radiation damage, achieving circular polarization values as high as $P = 0.97$ (Suzuki *et al.*, 2014). The use of this technique to produce circular polarization has the advantage of being relatively easily implemented, as it requires the precise positioning of a single small object. It is easily reproducible, as the Bragg diffracted beam can be used as a monitor of the position of the crystal and the polarization state of light. This method also allows to quickly switch the polarization between horizontal, vertical and circular and it has been demonstrated in the kHz regime (Suzuki *et al.*, 2003, 2014).

However, with respect for example to the use of helical undulators, it implies the introduction of an object in the beam, and therefore a reduction of the flux of at least a factor of two. If one considers also the fact that, when performing HAXPES with polarization configuration other than the one defined in Sect. 1.5.1, the photoelectron yield is further reduced by a factor of about two, it becomes clear why an high flux beamline is needed to efficiently perform this kind of experiment.

After crossing the polarizing crystal the beam enters the first two hutches. The first one, EH1, was left empty during our experiments. The second, EH2, hosts the femtosecond laser system and synchronization apparatus that is described in Sect. 7.1. Finally, after reaching the third hutch EH3, 77 m downstream, the beam enters the experimental endstation.

The endstation used for this experiment has a rather historical relevance, as it was the first one with which the modern form of HAXPES was demonstrated (Takata *et al.*,

2005). It is mounted on wheels and has a frame that allows positioning with high precision and a large number of degrees of freedom, that allowed to deploy it on several different beamlines in the campus, including the free-electron laser SACLA. The UHV chamber features a 5 degrees of freedom (X,Y,Z,Θ) manipulator designed for grazing incidence geometry, that allows cryocooling down to 15 K. The electrons are detected by a R4000-10kV (VG SCIENTA) hemispherical analyzer, with hundred meV resolution at 10 keV.

3.1.3 Sample growth and characterization

In order to draw reliable conclusions on the physical characteristics of the free surface, films of extremely high structural and chemical quality need to be used. Indeed, a large body of literature has demonstrated that even small modifications of the crystal can produce large modifications in the electronic structure (Tebano *et al.*, 2008; Pesquera *et al.*, 2016). On the other hand it is also known that stoichiometric disproportionation, especially in the case of oxygen vacancies, can have a rather profound impact (Orgiani *et al.*, 2012; Schlueter *et al.*, 2012) on magnetic and transport properties. Even theoretically, it has been demonstrated that the presence of extrinsic structural disorder can affect the characteristics and dynamics of the intrinsic electronic disorder appearing at the crossing of the phase transition (Dagotto *et al.*, 2001).

For this reason we fabricated our samples by ozone assisted Molecular Beam Epitaxy (OxMBE), employing the alternating shutter method pioneered by Schlom and coworkers (Schlom *et al.*, 2001). This technique consists in depositing the manganite AO and BO_3 planes separately by alternately exposing the substrate to the vapours of La and Sr or Mn emitted by shuttered Knudsen cells in an highly oxidizing Ozone atmosphere. When the optimal conditions for the growth are achieved ($T_{substrate}$=1000°C, P_{Ox}=5 x 10^{-5} mbar), the grown films have extremely high structural and stoichiometric purity (Petrov *et al.*, 2013).

The OxMBE has been monitored in-operando with in-situ reflection high energy electron diffraction (RHEED) in the sample growth instrument we employed (MBE-Cluster Growth), now available for users as part of the Nanofoundries and Fine Analysis (NFFA) facility hosted at the beamline APE (Advanced Photoelectric Effect) in Elettra Synchrotron, Trieste (NFFA-Trieste). The combination of OxMBE with RHEED allows to monitor the growth of each perovskite layer in real time, allowing for feedback control on the evaporators shutters, thus guaranteeing the realization of smooth films with good stoichiometry.

The transport and magnetization characteristics of films grown with this method are comparable with those of pure LSMO crystals. Such good quality films allows to investigate the intrinsic qualities of the manganite, yet having it in the form of a film, in which a large number of parameters can be controlled such as strain and thickness, and therefore paving the way for future applications. For the experiment discussed in the following, we used optimally doped ($x = 0.33$) LSMO thin films, unless specified. They were grown on three different substrates:

- Strontium Titanate ($SrTiO_3$, STO), which produces a 1% tensile strain in LSMO.
- Lanthanum aluminate - strontium aluminium tantalate or $(LaAlO_3)_{0.3}$ $(Sr_2TaAlO_6)_{0.7}$ (LSAT), which has a negligible lattice mismatch with LSMO and we considered to leave the manganite film relaxed.
- Strontium lanthanum aluminate ($SrLaAlO_4$, SLAO), which produces a 3% compressive strain in LSMO.

All the films were 100 unit cells thick (i.e. about 40 nm), well above the cross-over film thickness at which the transport and magnetic qualities are changed, and well below the thickness at which LSMO starts to relax the substrate strain (more than 120 u.c.).

Besides the RHEED monitoring during growth, the structure of the films has been characterized with the full plethora of the possible techniques allowed by the instrumentation of the NFFA facility in Trieste. In particular, with the use of the X'pert x-ray diffractometer (XRD):

- low angle x-ray reflectivity, shown in fig. 3.3 b, that allowed to verify the high surface and interface smoothness and to evaluate the thickness of the films to be consistent with the expected one.
- reciprocal space mapping that allowed to verify the fact that the LSMO film is completely strained and that only the vertical lattice parameter is different from the one of the substrate (fig. 3.3 d).
- Simple 2θ-ω scans that allowed to observe the substrate peak and, with sufficiently high index reflections (fig. 3.3 e and f), to resolve the film peak, quantifying the strain state.

Furthermore, microscopy techniques were used to verify the smoothness of the surface, employing the ZEISS Field Emission (FE) SEM Supra 40 of the NFFA facility to evaluate surface roughness which resulted below the detection threshold of 0.8 nm rms (fig. 3.3 a). This work was realized with the help of Dr. P. Orgiani and Dr. R. Ciancio. Thanks to the collaboration with Dr. Cavallini of the CNR-INSM institute of Bologna, we could use atomic force microscopy to determine that no significant outgrowths (very rare and below 5nm in size) are present and the samples have only large, extremely smooth terraces (0.32 nm roughness rms) of unit cell height (fig. 3.3 c).

Advantaging from the availability of techniques at the NFFA Facility APE beamline, a chemical characterization was also performed by measuring the near edge absorption spectrum fig. 3.4 a, which demonstrated that the manganese valence is between 3+ and 4+, as no significant structure corresponding to a 2+ valence was observed. This was complemented by the confirmation of good stoichiometry and correct positioning of the ions in the lattice coming from Rutherford backscattering.

Absorption spectroscopy was used to measure the magnetic signal with x-ray magnetic circular dichroism (XMCD) which demonstrated (fig. 3.4 a and b) the presence of

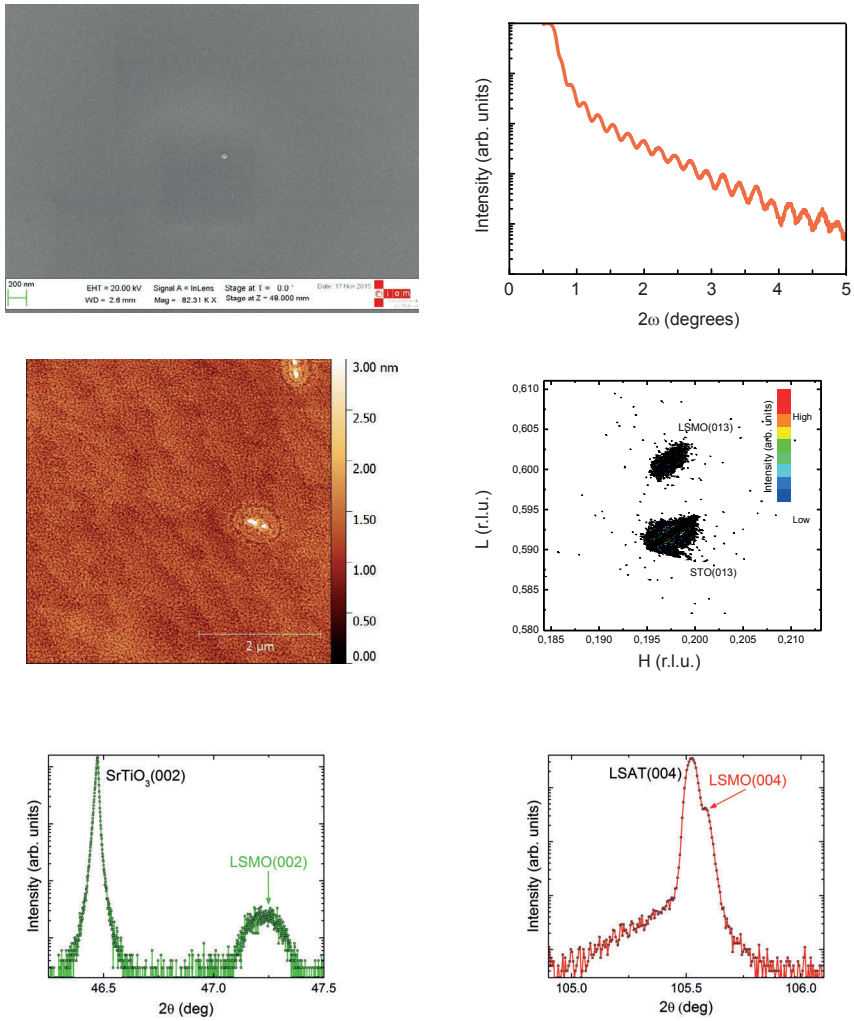

Figure 3.3: a. Secondary electron microscopy image of a LSMO/STO (001) surface. The high signal to noise ratio of the in-lens detector allows to evaluate a root-mean-square roughness below 0.8 nm. b. Low angle reflectivity of the film. The large number of fringes evidences a smooth upper surface and a sharp LSMO/STO interface. c. Atomic Force Microscope topographic image of the LSMO/STO upper surface. The rms roughness 0.6 ± 0.15nm, which goes down to 0.32 ± 0.1nm when measured between the terraces. d. Reciprocal space map around the asymmetric diffraction peak STO (013), the alignment along the H axis shows that the film is fully strained in plane. e. 2θ-ω XRD measurements of the LSMO/STO (001) film. f. 2θ-ω XRD measurements of the LSMO/LSAT (001) film.

magnetization at room temperature with a significant signal (6%). The spectral lineshape both of the absorption edges with opposite magnetization and of the difference dichroic

signal is in agreement with results observed in crystals. At room temperature, hysteresis loop were measured by magneto-optical Kerr effect (MOKE) on the reflection of a 400 nm laser beam, showing a square, low coercive field single domain response.

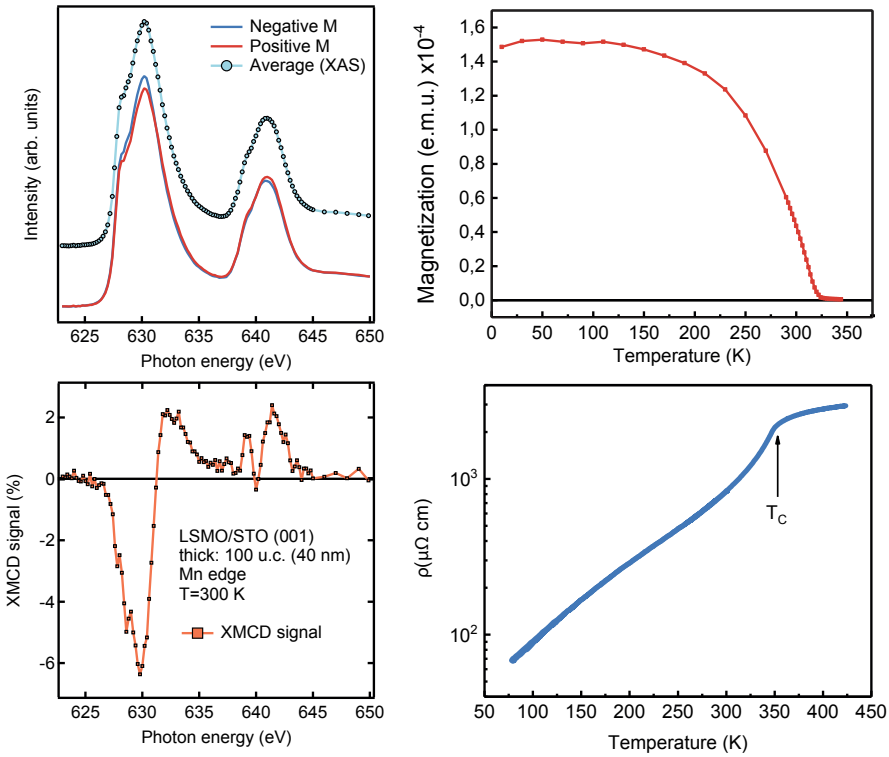

Figure 3.4: a. X-ray absorption spectra of LSMO/STO (001) 100 u.c. The solid curves are obtained by scanning the circularly polarized light collected by the undulator of APE beamline HE branch across the Mn $L_{2,3}$ edge, magnetizing the film in opposite directions in plane. The curve with circle symbols is the XAS spectrum obtained by averaging the two solid curves, and has been shifted vertically for clarity. b. X-ray magnetic circular dichroism signal at room temperature obtained as the difference between the two solid curves in a. It has been divided by the XAS peak height and expressed in percentage. c. Magnetization versus temperature of the film as obtained by SQUID measurements. d. Resistivity versus temperature, as measured by the four probe method in the van der Pauw configuration.

We also measured the resistivity as a function of temperature, by the standard four probe dc method in the van der Pauw configuration (fig. 3.4 d). In the low temperature magnetic phase, the curve follows the behaviour of high-purity optimally doped samples: at the lowest temperatures it is fitted by a power law $\rho - \rho_0 \propto T^\alpha$ with $\alpha < 2.2$, sign of half-metallic character (Schlueter *et al.*, 2012). In the vicinity of the phase transition it rapidly increases, until it reaches a cusp where a linear behaviour starts. This is the temperature

which defines the collapse of magnetization and double exchange supertransfer processes. The OxMBE films therefore show a behaviour analogous to that of high purity crystals, demonstrating the highest degree of structural and stoichiometric order (Petrov *et al.*, 2013).

Collaboration with the university of Regensburg (Lehrstuhl C. H. Back) allowed us to characterize one of our films during zero field cooling, by the use of a Superconducting Quantum Interference Device (SQUID) magnetometer. The M(T) curve (fig. 3.4 c) shows spontaneous magnetization and a Curie temperature slightly lower than the one individuated by the resistivity cusp. This may be due to the fact that the two samples of LSMO/STO (001) used for the resistivity measurement and the one used for the SQUID measurement have been grown in two different depositions.

The(Ga,Mn)As films were grown by low temperature molecular beam epitaxy (Ohno *et al.*, 1996). Mn inclusion in GaAs is indeed a highly non-equilibrium configuration. Only the high stoichiometric control allowed by MBE allows to synthesize this material. Moreover, it is even necessary to constrain the mean free paths of atoms by keeping the substrate at low temperatures. The film used for these experiments had a high concentration of Mn ($13 \pm 0.7\%$) and the highest Curie temperature (80 K). The films are grown on a GaAs wafer after deposition of a GaAs buffer layer. In-situ RHEED monitoring allowed to guarantee 2D growth and to control the thickness which was determined to be 18 nm. Post-growth annealing has been avoided in order to prevent the risk of MnAs segregation at the surface or in general to produce stoichiometric changes in the region probed by PES. The resistivity at low (5 K) and room temperature was measured in the four probes van der Pauw configuration, together with the SQUID zero field cooling magnetization, and have been found in agreement with previously grown samples (Wurstbauer *et al.*, 2008).

The (Ga,Mn)As film required chemical etching in order to display an unambiguous XPS peak lineshape (Maccherozzi *et al.*, 2006). The procedure consists in washing in ultrasonic bath of ultrapure ethanol, followed by immersion in a concentrated HCl solution (37 %) for one minute and a half. The film is then rinsed in ultrapure ethanol. After the measurements a topographic characterization by AFM denoted the presence of a large number of outgrowths of thickness between 3 and 12 nm. The RMS roughness of the surface is $1.05 \pm 0.2nm$ which reduces to $0.4 \pm 0.1nm$ between the outgrowths. The measurement of As 3d and Ga 3d peaks by Synchrotron PES at low energies ($h\nu = 800\,eV$) shows no detectable oxide satellites, demonstrating the efficiency of the etching in removing the As_2O_x and Ga_2O_x contamination (Lollobrigida, 2016).

For the LSMO samples, instead, no surface cleaning procedure was used. Indeed, it is almost impossible to perform successful procedures to clean the surface of LSMO without producing stoichiometric disproportionation, especially in the form of oxygen vacancies or cation site disordering. The only way in which good metallic and magnetic properties have been observed by surface sensitive techniques is by in vacuum cleavage of crystals or by in-situ growth (Park *et al.*, 1998a; Bertacco *et al.*, 2008). The surface of LSMO, however, is chemically inert: it is therefore expected that the pure crystal with correct

stoichiometry is found below a very thin layer of adsorbates such as Carbon compounds.

With fully characterized films, it was possible to address the features observed in photoemission by having a rather reliable knowledge of the quality of the materials, and in particular of the absence of several sources of extrinsic effects that can hinder the delicate mechanisms arising at the free surface.

3.2 Results

The measurements were performed in two beamtimes at I09, and one at BL19LXU. In the first beamtime at I09 the LSMO and GMA samples were measured at four photon energies, between 800 and 6000 eV. In the second one, only LSMO was measured at different temperatures across the phase transition (140-415K). In the beamtime at BL19LXU, the dichroism at room temperature and at 80 K was evaluated.

In all experiments, a polycrystalline Au foil was mounted on the manipulator, in good electrical contact with the samples and the chamber ground. At each modification of the parameters of the experiment, the Fermi edge of the Au reference was measured. Indeed, minimal variation of the geometry of the monchromators, due to thermal effects or backlash of the movimentation system can lead to small differences in the energy of the primary photon, thus shifting the resulting binding energy scale. Such drifts can be critical especially when dealing with valence band analysis.

The monitoring of the reference Fermi edge allows also to ensure consistency of the experimental resolution. At each temperature, energy and geometry configuration, indeed, we performed Fermi edge fitting with Gaussian broadening. In all experiments, the resolution has been maintained around $\Delta E = 250meV$. At several photon energies, the beamlines and spectrometers used could indeed achieve significantly higher resolutions. Nonetheless, since both the LBES and the features of the Valence Band could be clearly resolved, consistency was privileged. Where the resolution could have been higher, the slits were purposefully opened (both in the beamline and the spectrometer) to increase the statistics and obtain smoother lineshapes.

Except where otherwise stated, namely in Sect 3.2.3, the LSMO samples were measured at low temperature, by cryogenically cooling the experimental chamber manipulator with liquid nitrogen to 200 K, in order to guarantee that the manganite was well into its metallic and magnetic state. Indeed, as it will be discussed more rigorously in Sect 3.2.3, the LBES of LSMO shows a strong dependence on the temperature, almost disappearing when the phase transition is crossed. In GMA, the LBES structure does display a critical change in intensity when the ordering temperature is crossed, but it remains clearly measurable also well above T_C (Fujii *et al.*, 2011). The measurements were therefore performed at room temperature for GMA.

3.2.1 Photon energy

In discussing the measurements at different photon energies, it is interesting to dedicate some attention to the survey spectra taken at the maximum (Fig. 3.5 a) and minimum

(Fig. 3.5 b) photon energies, i.e. respectively at $h\nu = 6000\,eV$ and $h\nu = 1000\,eV$, as they allow to point out some of the features of HAXPES discussed in Sect. 1.5.1.

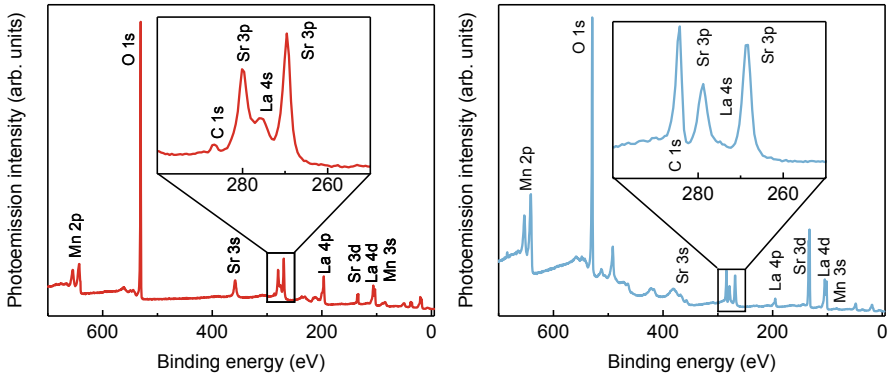

Figure 3.5: a. Survey spectrum of the strain-relaxed $La_{1-x}Sr_xMnO_3/SrTiO_3$ sample with a primary photon energy of $h\nu = 6000\,eV$. In the inset, an enlargement of the region between 300 and 250 eV of binding energy is shown. This range encompasses a La peak, a Sr doublet and the 1s peak of adventitious Carbon. b. Survey spectrum of LSMO/STO with a primary photon energy of $h\nu = 1000\,eV$. In the inset the same binding energy region is zoomed in as in a, showing a much larger C 1s peak due to increased surface sensitivity.

It is indeed clear, by inspecting the general shape of the spectra, that the HAXPES one has a step like-background with rather flat regions between the peaks. This is due to the small relative differences in the inelastic mean free paths of the secondaries arising from each particular line. The effect of the reduction of the cross section is also evident, as the relative intensity of the Mn 2p line with respect, for example, to the Sr 3p line, is significantly smaller in the HAXPES spectrum. This is a consequence of the fact that the photon energy of the PES spectrum is much closer to the resonance of the Mn 2p subshell (around 642 eV), and the cross-section is therefore significantly larger than that of Sr 3p. Further from the resonance, the relative difference is smaller.

What is most important, however, is the amplitude of Carbon 1s peak. As mentioned in Sect. 3.1.3, it is safe to assume that the Carbon peak arises from a thin layer of adsorbates. The strong reduction seen in HAXPES demonstrates how little is the contribution of the superficial layers to the signal. In this case, considering that the electron escape depth is of 70 Å, the first 5 Å only contribute to about 5% of the signal.

In Fig. 3.5 **a**, the Mn 2p doublet is shown as measured at three different photon energies. A Tougaard background (Tougaard, 1997) has been subtracted from each doublet, to account for the different secondary scattering rates.

In panel **a** is evident the presence of the LBES that emerges at higher photon energies: it consists of a sharp feature observable around 639 eV, at the low binding energy side of the the main $2p_{3/2}$ peak. At about 652 eV a somewhat more smudged feature is also

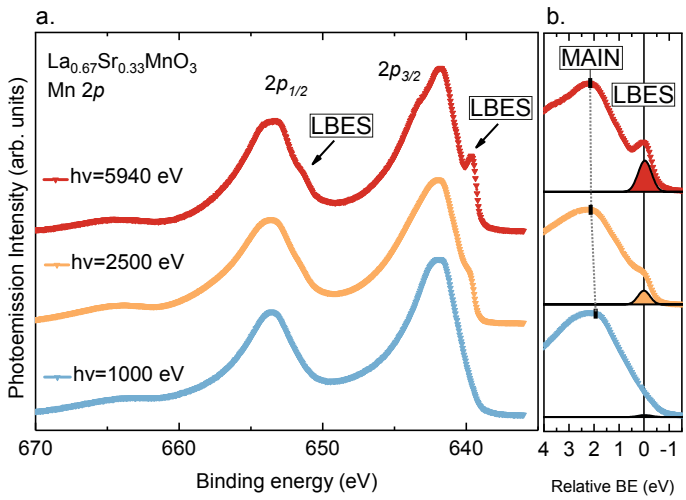

Figure 3.6: a. Mn 2p core-level spectra at three different primary photon energies with linear polarization. The sample is the strain relaxed LSMO/LSAT, held at $T = 200K$. b. Detail of the low binding energy satellite and the main line of the Mn $2p_{3/2}$ spin-orbit component. The position and shape of the satellite have been individuated by the fitting procedure described in Sect. 3.3.3. The binding energy has been shifted to place the satellite at zero. Slight variations in the position of the main-line maximum are indicated by the black ticks and grey dashed lines. In both panels the curves have been shifted vertically for clarity.

present in the $2p_{1/2}$ peak. As explained in Sect. 1.5.2, in a correlated electron material such as LSMO, the presence of bulk-only LBES can be attributed to the presence of an efficient screening of the core-hole: the largest peak at 642 eV (653 eV) of the Mn$2p_{3/2}$ (Mn $2p_{1/2}$) line is hence labelled as poorly-screened, or main peak. The LBES is therefore a well-screened state: in LSMO it is significantly smaller than the poorly-screened feature, an indication that the states giving raise to it have limited hybridization with the system ground state. The last characteristic is also suggested by the sharpness of the structure, indicating a long lifetime.

At 1000 eV the LBES is almost below the detection limit and it is not observable at lower energies. A charge-transfer satellite, due to the creation of a hole in the ligand band is observed at 665 eV, as a satellite of the $2p_{1/2}$ line. The change in the lineshape observable around 643 eV, on the high binding energy, poorly-screened part of the peak, is a rather subtle one. We will define this the high binding energy feature (HBEF). It shows, just as the LBES a significant evolution as a function of temperature and probing depth. As will be shown in Sect. 3.2.4, it yields a significant dichroic contrast too. It is a bit more complicated to extract the information that it yields than in the case of the LBES, as the HBEF overlaps to the broad poorly screened peak, where crystal field, multiplet effects and the presence of two valence states (Mn^{3+} and Mn^{4+}) are simultaneously at

play (see Appendix B).

In panel **b**, the fitting that will be used in Sect. 3.3.3 is shown in order to better resolve the LBES position. The peaks have been shifted to place the maximum of the LBES at zero relative BE, in order to appreciate small shifts in the relative position of the poorly-screened edge, indicated by the black ticks and grey dashed lines.

Another feature of the spectrum that shows significant variation across the primary photon energy variation is the valence band, shown in Fig. 3.7. The curves are normalised to the total area, and no background subtraction has been performed.

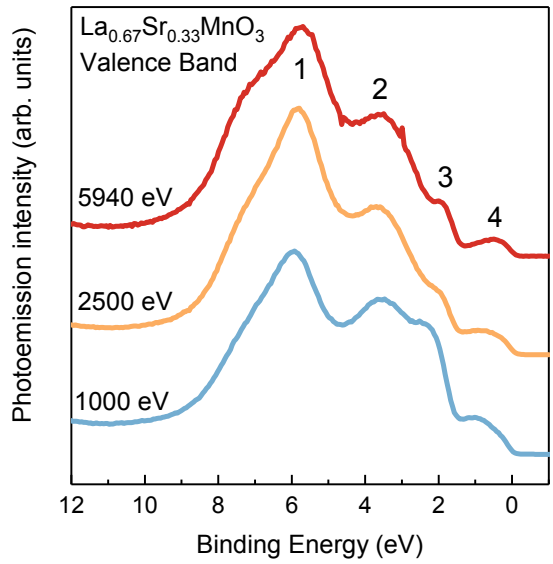

Figure 3.7: Valence band spectra at three different primary photon energies with linear polarization. The sample is the strain relaxed LSMO/LSAT, held at $T = 200K$. The curves have been shifted vertically for clarity.

Significant information can be obtained by looking at the redistribution of the spectral weight between the features of the valence band. Following previous combined experimental and theoretical studies (Picozzi *et al.*, 2007), we individuate:

1. At about 5.5-6 eV, a structure arising from ligand states, due to the O 2p orbital.
2. Around 3.5 eV, a broad peak arising from the strong hybridization of the O 2p states with the Mn 3d band.
3. At 2 eV, the t_{2g} band is clearly resolved.
4. At 0-1 eV, the narrow e_g band.

By comparing the different curves, it is clear that there is a shift of structure 1 towards lower binding energies, and a significant increase of the spectral weight of structure 2. Also in structure 4 the spectral weight shifts towards lower binding energies. This clearly indicates that when moving towards the surface, the system is driven towards a strong localization of the charges, with enhanced spectral weight in the localized t_{2g} structure and reduction close to the valence band edge. Similar effects, in particular the shift of structure 1 to lower binding energies and the shift of spectral weight towards the bottom of the e_g band has been observed in presence of controlled oxygen vacancy, which is known

to drive the optimally doped system towards a more insulating state (Schlueter *et al.*, 2012).

Finally, we turn to GMA. In the case of this material, the LBES is labelled as a well-screened satellite arising from a screening mechanism due to the narrow band of doped-in Mn 3d states. The peak is more robust than in LSMO, appearing well above the Curie temperature and even to lower photon energies, as it is detectable down to $h\nu = 800\,eV$. The Mn 2p doublet for the four photon energies used ($h\nu = 800, 1000, 2500, 6000\,eV$) is shown in Fig. 3.8. As in Fig. 3.6, the spectra have been positioned in BE by using the Au EF measurement and a Tougaard background has been removed.

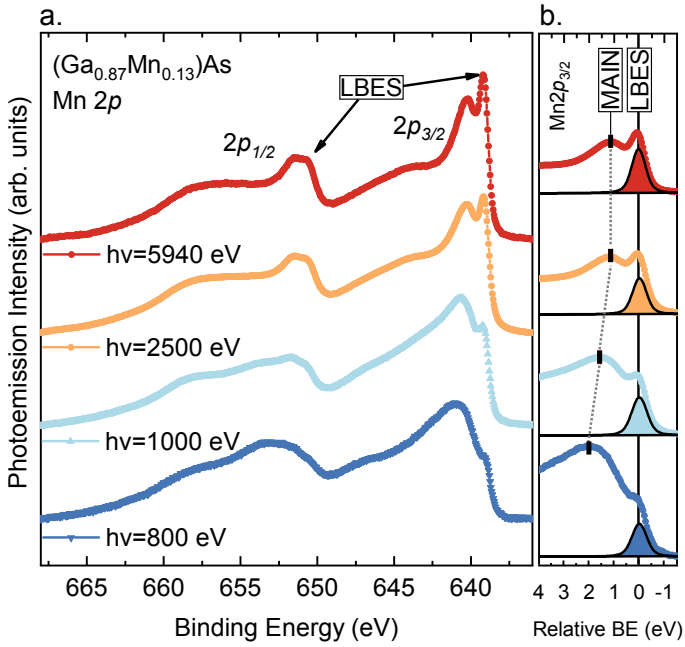

Figure 3.8: a. Mn 2p core-level spectra at four different primary photon energies with linear polarization. The sample is the etched ($Ga_{0.87}$,$Mn_{0.13}$)As, held at $T = 300K$. b. Detail of the low binding energy satellite and the main line of the Mn $2p_{3/2}$ spin-orbit component. The position and shape of the satellite have been individuated by the fitting procedure described in Sect. 3.3.3. The binding energy has been shifted to place the satellite at zero. Slight variations in the position of the main-line maximum are indicated by the black ticks and grey dashed lines. In both panels the curves have been shifted vertically for clarity.

At 640-641 eV (651-653 eV), the poorly-screened main line of the Mn $2p_{3/2}$ (Mn $2p_{1/2}$) can be seen to switch from dominating the PES (800 eV, 1000 eV) to being smaller than the LBES in HAXPES (2500 eV, 6000 eV). Both the poorly-screened lines are followed, at higher binding energies, by broad features arising from the hybridization of the As 4p ligand with the Mn 3d states (Fujii *et al.*, 2011; Okabayashi *et al.*, 1998).

These states are extremely sensitive and show sizeable shifts in their BE position across the different energies. This, combined with previous accurate HAXPES studies of the valence band (Fujii *et al.*, 2013), draw a picture of reduced hybridization at the surface and with increasing temperature.

In Fig. 3.8 b, the Mn $2p_{3/2}$ region is zoomed in and shifted to align the LBES maxima, in order to appreciate the variation of the relative energy position, that here translates in a shift of the poorly-screened edge, marked by black ticks and connected by grey dashed lines.

3.2.2 Strain

It is an interesting finding (Pesquera *et al.*, 2012, 2016) that in LSMO, both optimally doped and half-doped ($La_{0.5}Sr_{0.5}MnO_3$), a significant rearrangement of the occupation of the e_g orbitals occurs at the out-most layer of the crystal, due to the absence of the apical oxygen and consequently of its repulsive force on the out-of-plane ($3z^2$-r^2) orbital. It has been observed by X-ray Linear Dichroism in absorption in the high temperature region above the Curie temperature, where magnetic effects are not at play.

It was also demonstrated that, by controlling the strain applied to the LSMO film, it was possible to shift the energy position of the in-plane (x^2-y^2) e_g orbital. Control was achieved to such extent that the effect of the surface could be compensated, obtaining for the surface orbitals the same occupancy as that of the bulk system. Due to such intriguing possibility of controlling the electronic properties, and the suggestion of a mechanism driving the system towards the localization at the surface, we applied our technique also to samples in different strain states as mentioned in Sect. 3.1.3.

The results of our measurements are shown in Fig. 3.9. The three curves for 6 keV photon energy, no significant differences can be seen between the three films, the relaxed one (LSMO/LSAT), the one under tensile strain (LSMO/STO) and the one under compressive strain (LSMO/SLAO). Only the LSMO/SLAO sample shows a slightly reduced relative amplitude of the LBES, but this has been attributed to the fact that this film showed a Curie temperature 10 K lower than the others, as observed in resistivity measurements. The same similarity is observed at the other three energies.

Even performing the quantitative analysis of the cross-over thickness that will be discussed in detail in Sect. 3.3.3 for LSMO/LSAT, the values obtained are equal within the error bar. The effect of strain is thus not reflected in high energy spectroscopy at the resolution of our data and in these experimental conditions. We cannot discuss this point further basing on experimental evidence. It is possible that further investigation, encompassing a wider range of strain states, may bring different results.

3.2.3 Temperature

As mentioned in the previous sections, the LBES of LSMO is extremely sensitive to temperature. The exploration of the evolution of the LBES across the metal-insulator phase transition can give relevant information on the rearrangement of the electronic structure.

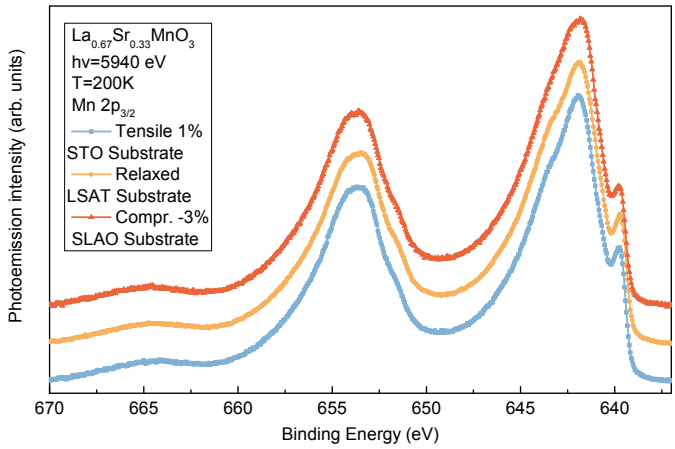

Figure 3.9: Mn 2p core-level doublet measured with 6 keV primary photon energy and linear polarization, at $T = 200K$. The curves are obtained from LSMO in the three different strain states due to the growth on different substrates. The spectra have been shifted for clarity.

In particular, we decided to venture in ranges of temperatures significantly above T_C in order to verify, with high resolution measurements, the complete disappearance of the LBES.

The results of high resolution measurements of the Mn 2p peak of a LSMO strain relaxed sample, at $h\nu = 6\,keV$, for five different temperatures (140-415 K), are shown in Fig. 3.10. The limits of the temperature range are due to a series of constraints: the liquid nitrogen cooling worked rather inefficiently unless a part of the manipulator was mechanically moved (which would have made it very difficult to maintain a consistent geometrical configuration throughout the data set) reaching at minimum 140 K. At the other end of the range, 415 K was the highest safe temperature to avoid oxygen disproportionation during the measurement. After the high temperature measurements, the room temperature measurements were repeated, to ensure that no stoichiometric disproportionation had occurred during the measurement.

The curves have been normalized to the area. In the insets **a**. and **b**. the poorly-screened HBEF and the LBES are zoomed in, respectively. What is striking, and arises from the high resolution and good counting statistics of the measurement, is that both the LBES and the HBEF show a significant evolution well above the Curie temperature. Furthermore, the LBES is still present at the maximum temperature measured (415 K), in the form of a very small shoulder. It is interesting to notice that the large changing of spectral weight in the HBEF is not completely compensated by the one in the LBEF (which is opposite): it is spread in a small difference over the large region where the charge-transfer satellites appear at higher binding energy. The evolution of the Mn 2p

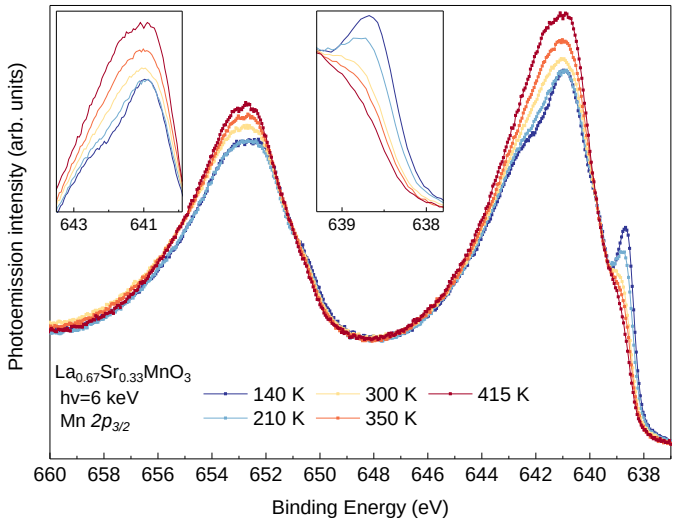

Figure 3.10: Evolution of the Mn 2p doublet as a function of temperature in the range 140-415K for the strain-relaxed LSMO/LSAT sample, measured at 6 keV primary photon energy. In the insets the detail of the high binding energy feature on the main line and the LBES are shown.

satellites with temperature is further analysed in Sect. 3.3.1.

To complete the picture, of the temperature dependence of the LSMO electronic structure, we present in Fig. 3.11 the confrontation between the valence band measured at the extreme temperatures: 140 K and 415 K. The curves have been normalized by area and positioned in binding energy according to the measured Fermi edge of the Au reference.

It is interesting to compare panel **a** to Fig. 3.7. Indeed, while the general variation of the features of the VB across the phase transition is analogous to the one observed by passing from $h\nu = 6000\,eV$ and $h\nu = 2500\,eV$, nowhere in the range of temperature variation explored we could observe the large shifts of $h\nu = 1000\,eV$. This suggests that there is something radically different in the electronic structure of LSMO surface which cannot be fully explained just as an exchange interaction weakened by the reduction of coordination, with increasingly lower T_C towards the surface. In panel **b**, the enhanced region close to the Fermi energy allows to observe a significant shift of spectral weight towards the Fermi edge when entering the low temperature metallic phase. A difference spectrum is shown in panel b to highlight such redistribution.

The study of the LBES as a function of temperature, therefore, sums up in a clear picture. As expected due to the sensitivity of the peak to the mobility of charges, the largest variations follow the magnetic behaviour, i.e. the interaction driving metallic transport and long range order. Nonetheless, owing to the increased resolution and the high S/N ratio, it is now possible to notice the presence of the LBES structure also above

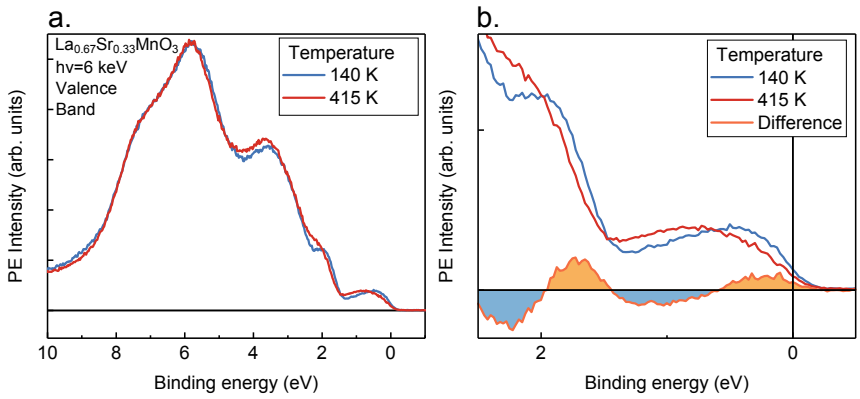

Figure 3.11: a. Valence band of strain relaxed LSMO/LSAT measured with linear polarization at 6 keV photon energy. The two extrema of the temperature range explored, well above and below the Curie temperature, are shown. b. Expanded view of the region close to the Fermi energy. A difference spectrum has been added to appreciate the shifts of spectral weight.

T_C. The inspection of the valence band shows clear shift of spectral weight towards higher binding energies when T_C is crossed. Finally, comparison with the VB measured at various photon energies gives strong hints that the electronic structure at the surface cannot be treated as the same of the bulk but with lowered T_C.

3.2.4 Dichroism

A further evidence that the LBES is strictly intertwined with magnetism in LSMO is the measurement of dichroism in HAXPES. The measurements, shown in Fig. 3.12 and Fig. Fig. 3.13 have been performed on the same sample, at a low temperature of 80 K and at room temperature.

The photon energy was $h\nu = 8000\,eV$, where we could achieve a resolution of about $\Delta E = 250\,meV$, analogous to the previous experiments. The diamond phase retarders allowed for ± 0.98 circular polarization of the light. The measurements were performed by reversing the helicity of light and measuring the sample with fixed magnetization orientation in the direction of the photon k-vector.

The curves have been normalized to the area, and no background removal was applied. The LBES shows an extremely large dichroic contrast, as opposed to the poorly-screened main line, indicating that the delocalized states from which it arises must have an highly spin-polarized character.

Also the magnetic origin of the HBEF is unveiled by the large contrast (with opposite sign) appearing at those energies. Despite tempting, it is not possible to infer the presence of a magnetic and non-magnetic parts of the peak from simple sums and differences, as dichroism in photoemission results from a combination of detection geometry and selction

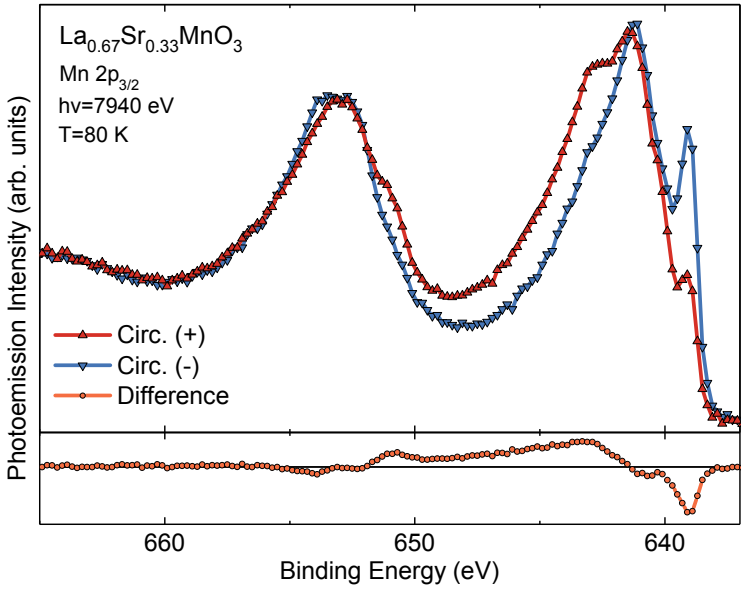

Figure 3.12: Mn 2p doublet of strain-relaxed LSMO measured with circularly polarized light of opposite helicity at cryogenic temperature (80 K). The photon energy is, here, 8 keV. In the lower inset, the difference spectrum is shown.

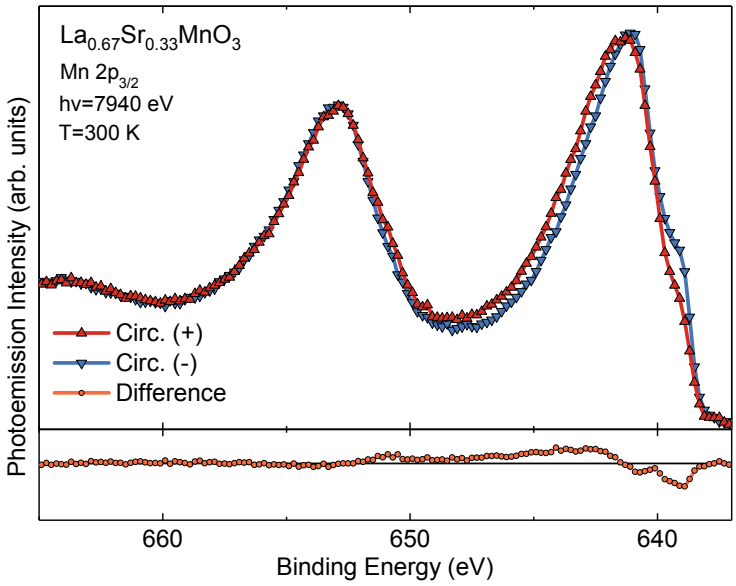

Figure 3.13: Mn 2p doublet dichroism at room temperature (300 K). The difference spectrum (Circ⊖-Circ⊕) is plotted with the same vertical scale of Fig. 3.12.

rules in the interaction (van der Laan, 2015): to have reliable insight on the details of the dichroic features, precise modelling accounting for the detection geometry and the characteristics of the band-structure must be used.

3.3 Discussion

The measurements presented in Sect. 3.2 yield a great deal of information on the spectroscopic features of the manganite and how they are affected by external parameters. In this section we will illustrate how, by building up a detailed model for the origin of the LBES, it is possible to link them to very precise parameters of the model describing the electronic structure, and how it is possible to quantify the influence of the interruption of the crystal on such parameters.

3.3.1 Temperature

The quality of the measurements in Fig. 3.10 allows to carry out a simple analysis by direct subtraction of the spectra, without the need for multipeak fitting. The result of subtraction of the spectrum at 415 K to the spectra at all other temperatures is shown for the region of the Mn $2p_{3/2}$ in Fig. 3.14.

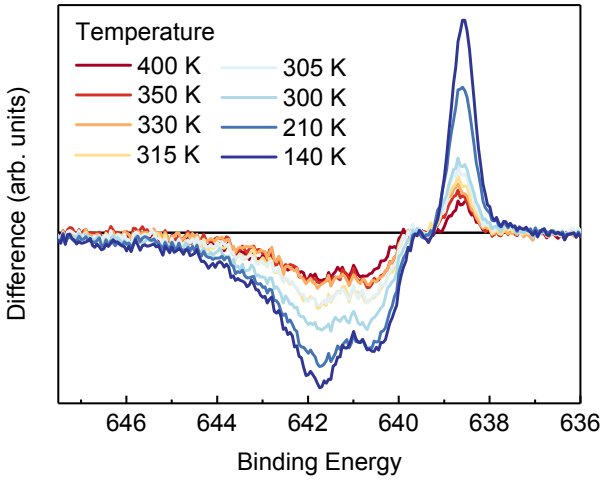

Figure 3.14: Difference spectra between the maximum recorded temperature $T = 451\ K$ and all the other measured spectra, in the region of the Mn $2p_{3/2}$ spin-orbit component.

If we assume that the spectrum at 415 K is the one representing the high temperature phase, we can integrate the difference spectrum in the range of energies, in order to evaluate the evolution of the lineshape driven by magnetic effects. In Fig. 3.15 the area as a function of temperature is reported (coloured squares), and compared with a Magneto-Optical Kerr Effect measurement[1] of the same sample (light grey circles). The curve obtained by HAXPES has been divided by the maximum value because, as can be seen in Fig. 3.4 **c** (on a sample that has an even slightly lower T_C), it is

[1]MOKE is a good comparison to explore the magnetic component of the LBES, because it probes a region of comparable distance from the surface (the extinction length of the optical light reflected at the surface, of the order of few tens of nm).

safe to assume that at 140 K the spontaneous magnetization has reached the maximum value.

The curve clearly shows a strong similarity with the trend of the magnetic signal, in particular close to T_C, where a sharp step is evident. When the temperature is increased above the Curie temperature, however, we can see a continuing gradual evolution of the LBES area, with a long tail declining much more slowly than the MOKE signal. By looking at Fig. 3.10, it is clear that variations of the LBES cannot reduce the spectral weight much further, as it is already very close to vanishing.

Due to the unexpected long tail of the LBES evolution, the curve in Fig. 3.15 suffers of a ill definition of the zero of the Y axis. For this reason it is difficult to further perfect the analysis along the lines of the previous studies of the LBES across the phase transition on LBMO (Tanaka *et al.*, 2006), where it is the square root of the area that is compared with the magnetic signal. It is clear that, to push this preliminary analysis further, measurements at higher temperatures need to be performed. Increasing the temperature would anyway require the realization of a different kind of experiment, i.e. HAXPES in gas: stoichiometric disproportionation is avoided only if significant pressures of oxygen or ozone are present at the surface.

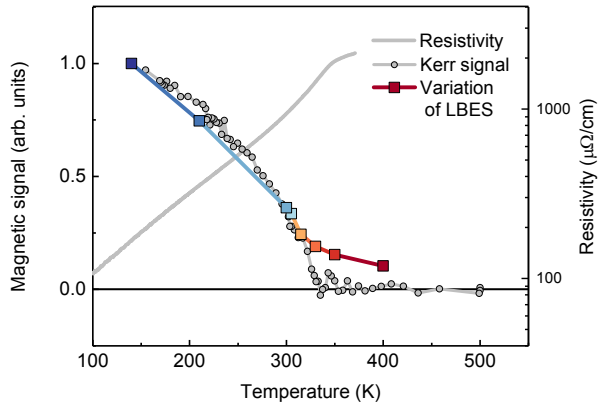

Figure 3.15: Area of the difference spectra in Fig. 3.14 between 639 eV and 636 eV compared with the MOKE signal from the same sample.

It is nonetheless possible to suggest a picture of the mechanisms that lead to such evolution above T_C by considering the resistivity curve, also reported in Fig. 3.15, plotted against the right logarithmic axis. When T_C is crossed, LSMO is left in a state of high resistivity by the absence of long range mechanisms for delocalization. However, charge transfer processes can still happen, as confirmed by the persistance of a metallic character. As temperature is further increased, the mean free path of the carriers increasingly reduces and the resistivity slowly grows, with a positive derivative of $\rho(T)$.

It is thus possible to individuate two regimes of variation of the LBES. The regime at temperatures lower than T_C, in which the double exchange is active, long range order is present, the mobility of charges is high and the peak is very intense. Here, its amplitude is sensitive to the modulus of magnetization, as suggested by the dichroic measurements and the first part of the curve in Fig. 3.15. It is in this regime that the peak will be used as a probe of the long-range hybridization as a function of the distance from

the surface. Above T_C only a small structure remains, which must be sensitive to the mobility at shorter ranges, and evolves more slowly with temperature. Our distinction of two regimes of lineshape evolution is supported by similar conclusions of methodical studies of the doping dependence (Hishida *et al.*, 2013b,a).

Whether the transition from long range hybridization to short range mobility proceeds in a phase separated manner[2] or in a single particle picture, is an information that cannot be extracted from these data. However, we would lean more towards the latter, as the former arises in presence of strong phase competition, and is invoked to explain significant deviations from the critical behaviour of a classical ferromagnet. We instead aimed at realizing the simplest double exchange ferromagnet with the lowest electronic disorder, and across this thesis we will gather further evidence that this objective has indeed been reached.

3.3.2 Modelling

The LBES in LSMO falls in the category of the bulk-only features that cannot be described by the simple Cluster-Interaction Model calculations, as discussed in Sect. 1.5.2. Historically, the first model that successfully reproduced this feature is the extended cluster model (Horiba *et al.*, 2004). It is developed (Taguchi and Panaccione, 2016) starting from the classical Cluster-Interaction model Hamiltonian:

$$H_{CI} = H_{Eig} + H_{Intra} + H_{Inter} \tag{3.1}$$

Where:

$$H_{Eig} = \sum_{\Gamma\sigma} \epsilon_{3d}(\Gamma) d^\dagger_{\Gamma\sigma} d_{\Gamma\sigma} + \sum_{\Gamma\sigma} \epsilon_p(\Gamma) a^\dagger_{\Gamma\sigma} a_{\Gamma\sigma} + \sum_{m\sigma} \epsilon_{2p} p^\dagger_{m\sigma} p_{m\sigma} \tag{3.2}$$

represents the eigenenergies of the Mn 3d band, O 2p band and Mn 2p states. Γ indicates the irreducible representation of the local symmetry around the TM atom, while m and σ are the orbital spin states. The intra-site interaction Hamiltonian includes the TM atomic multiplet term (H_{mult}), which describes the intra-band single atom interactions in the 3d band and the inter-band effects between the Mn 3d band and the 2p states, and the ligand-Mn 3d interaction with hybridization parameter $V(\Gamma)$:

$$H_{Intra} = H_{mult} + \sum_{\Gamma\sigma} V(\Gamma)(d^\dagger_{\Gamma\sigma} a_{\Gamma\sigma} + a^\dagger_{\Gamma\sigma} d_{\Gamma\sigma}) \tag{3.3}$$

The inter-site Hamiltonian includes the on-site coulomb repulsion (with constant parameter U_{dd}) and the attractive core-hole effect (with parameter U_{dc}):

$$H_{Inter} = U_{dd} \sum_{\Gamma\sigma \neq \Gamma'\sigma'} d^\dagger_{\Gamma\sigma} d_{\Gamma\sigma} d^\dagger_{\Gamma'\sigma'} d_{\Gamma'\sigma'} - U_{dc} \sum_{\Gamma m\sigma\sigma'} d^\dagger_{\Gamma\sigma} d_{\Gamma\sigma} (1 - p^\dagger_{m\sigma'} p_{m\sigma'}) \tag{3.4}$$

[2] Nanoscale phase separation, suggested by E. Dagotto (Dagotto *et al.*, 2001) to play an important role in the physics of manganites, is here intended as the appearance, in correspondence of the phase transition, of spatially inhomogeneous electronic properties.

To this Hamiltonian, Taguchi and coworkers (Horiba *et al.*, 2004) added two terms, to describe the screening processes arising from the states emerging close to the Fermi energy in the metallic state of correlated electron materials, labelled C:

$$H_{Ex} = H_{CI} + \sum_{\Gamma\sigma} \epsilon_C(\Gamma) c^\dagger_{\Gamma\sigma} c_{\Gamma\sigma} + \sum_{\Gamma\sigma} V^*(\Gamma)(d^\dagger_{\Gamma\sigma} c_{\Gamma\sigma} + c^\dagger_{\Gamma\sigma} d_{\Gamma\sigma}) \tag{3.5}$$

As can be seen, a new hybridization parameter $V^*(\Gamma)$ had to be introduced. The emerging states are treated as a separate band, as can be seen by the similarity between the new term and the one introduced to model the charge transfer effects with the ligand states. A second parameter that arises from the first new term is the Δ^*, i.e. the charge transfer energy, defined as the energy difference between the configuration averaged energies: $E(3d^{n+1}C^{-1}) - E(3d^n)$. Also this parameter is built in analogy with the charge transfer energy Δ due to the ligand states, evaluated as the difference $E(3d^{n+1}L^{-1}) - E(3d^n)$. The resolution of the Hamiltonian, using an appropriately constructed set of basis states, leads to the individuation of a large number of final states which are then convolved with a Lorentzian to reproduce lifetime effects and, eventually, with a Gaussian to simulate experimental resolution.

The photoemission process can then be depicted following the scheme in Fig. 3.16, where the broadening due to multiplet, crystal field and hybridization have been left out for clarity. In the initial state the core-hole is not present, and the ground state largest contribution comes from the $3d^4$ state. Δ^* is generally smaller than Δ, and when both the levels are shifted by the Coulomb potential of the core-hole, the state $3d^{n+1}C^{-1}$ is brought to lower binding energies than the $3d^{n+1}L^{-1}$, resulting in the LBES (Fig. 3.16). The V^* describes how much the $3d^{n+1}C^{-1}$ state is hybridized with the initial fundamental state of the crystal, and is therefore linked to the intensity of the LBES. The Δ^* is linked to its energy position.

The success of this model consists in the fact that by a clearly defined addition to the CM Hamiltonian, not only the LBES is explained, but a better general agreement of the overall lineshape is achieved. This model has been successfully applied to a large number of correlated electron compounds such as Titanates, Vanadates, Cuprates and Nichelates (Taguchi and Panaccione, 2016).

The ECM has, however, its shortcomings. Indeed, it introduces the coherent states phenomenologically, and a connection with some specific features of the bandstructure has been devised in a case-by-case fashion. In particular, the observation of the LBES in the parent compound $LaMnO_3$, which is an insulator, has been explained in the framework of the ECM as due to the presence of states arising from oxygen vacancies, which appears as a particularly weak argumentation.

The application of the multi-cluster model to this issue (van Veenendaal, 2006) seemed to hint at the fact that non-local screening mechanisms can describe more clearly the behaviour of the LBES as a function of doping and temperature. More specifically, it was shown that the LBES survives even in the parent compound, and that it is sensitive to the orbital ordering that characterizes LMO up to very high temperatures. Nonetheless, the necessary simplifications in the description of the orbitals involved in the photoemission

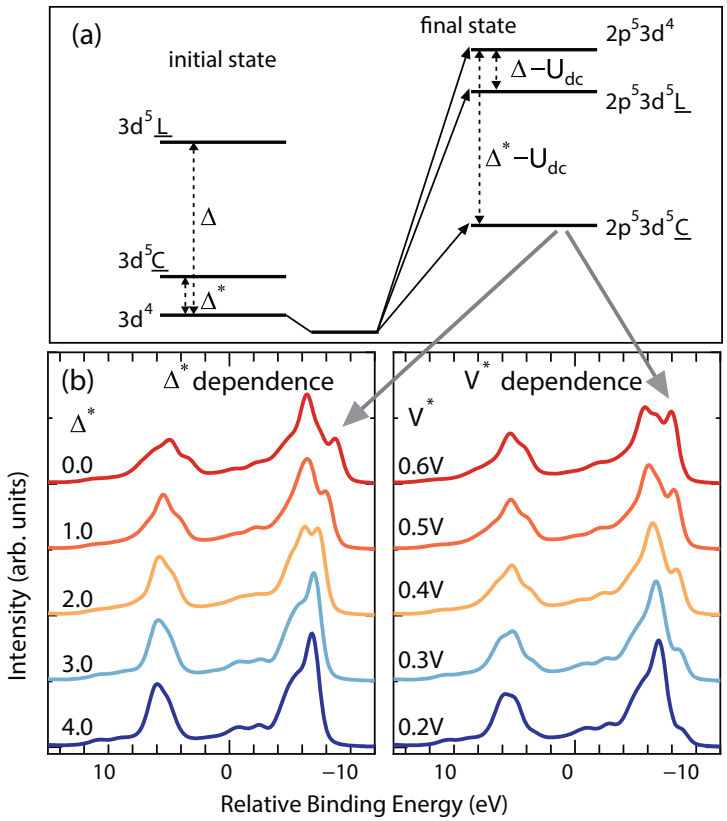

Figure 3.16: a. Schematic digram of the energy levels participating to the HAX-PES multiplet structure of LSMO. The number of configurations included in the real calculation (6) has been reduced for clarity to the three dominants one, and the broadening effects of crystal field, hybridization and intra-atomic multiplet have been neglected for the sake of simplicity. b. Dependence of the resulting calculated spectra from the parameter Δ^* (left) and V^* (right). From (Taguchi and Panaccione, 2016).

process, combined with the difficulty of ruling out boundary conditions issues, made confrontation between the MCM and experiments rather difficult.

Finally, very recently the combination of DMFT with the Cluster-Interaction framework (Hariki *et al.*, 2016), has strengthened the thesis that the mechanism giving rise to LBES is the magnetic ordering in LSMO and the orbital ordering (due to a cooperative Jahn-Teller effect) in LMO. A peak in the hybridization function close to the Fermi energy has been identified and its microscopic character linked to the dominant interactions in the two materials. This seems to add strength to the concept that the screening process producing the LBES arises from non-local process, differently from the mechanisms that were speculatively attributed to the ECM C-band.

The machinery of the ECM is, nonetheless, not invalidated by the recent results.

Conversely, the ECM can be interpreted as a schematic picture in which the dominant features of the DMFT hybridization function are separately introduced as single scalar parameters. From this point of view, the DMFT results relabel the microscopic origin of the introduction of the C-band.

We therefore chose the ECM approach to quantify the hybridization of the coherent states as a function of the probing depth, as it is the modelling approach that, while giving good agreement with the experimental data, yields the smallest number of parameters that can be adjusted. The functional dependence of the hybridization function of the DMFT+CM would give too many degrees of freedom to obtain a meaningful quantification with the small number of photon energies we could use.

Initial state	Energy	Final state	Energy
$3d^4$	$-\Delta + U = 3\ eV$	$2p^5 3d^4$	$-\Delta + U + Q = 8\ eV$
$3d^5$	$0\ eV$	$2p^5 3d^5$	$0\ eV$
$3d^6$	$\Delta = 1\ eV$	$2p^5 3d^6$	$\Delta - Q = -4\ eV$

Table 3.1: Energy position of the initial and final configurations of (Ga,Mn)As bandstructure in the photoemission process.

The modelling of GMA is somewhat less subtle, as it is reproduced within the standard cluster model calculations: the delocalized states giving rise to the LBES are indeed the doped-in 3d bands of the Mn atom themselves, so it is sufficient to consider an appropriate number of initial configurations, in our case the $3d^4$, $3d^5$ and $3d^6$. By using the customary (Fujii *et al.*, 2011) parameter set $\Delta = 1\ eV$ (ligand-Mn 3d charge transfer energy), $U = 4eV$ (On site Coulomb repulsion) and $Q = 5\ eV$ (Core-hole Coulomb attraction), one finds for the initial and final states the values described in Tab. 3.1. The final state of the lowest energy arises from the $3d^6$ state, which, in turn, has an energy larger than the $3d^5$ before the photoionization. The ground state has mainly a $3d^5$ character, giving rise to the poorly-screened feature, while the $3d^6$ component is hybridized with it by an amount quantified by a parameter V.

3.3.3 Quantitative analysis

In order to proceed to a quantitative analysis, four further steps are needed:

1. The experimental spectra must be fitted to individuate the position and amplitude of the LBES.

2. The probing depth corresponding to the different photon energies must be quantified as accurately as possible.

3. A reliable parameter must be used to compare the spectra observed in experiments with the theoretical ones, in order to find the corresponding hybridization value.

4. A fitting law must be established to disentangle the evolution of the hybridization from attenuation effects.

For point 1, we choose to fit only the Mn $2p_{3/2}$ peak both in LSMO and GMA samples. Even limiting the fit to only one spin-orbit component can lead to an enormous complexity, especially in systems with a not well defined valence: if the number of subpeaks were to be the sum of the ones used in literature for Mn^{3+} and Mn^{4+}, it would result in 11 independent components (Biesinger *et al.*, 2011). However, we are interested only in separating the weight of the LBES from the rest. Therefore we fitted the broad structures of the poorly-screened line with the minimum number of Gaussian components that reliably allows to reproduce the shape at all photon energies, five for both LSMO and GMA. For the LBES, given its sharp nature, we used a Gaussian in LSMO, but a Voigt lineshape in GMA. We then evaluated the relative weight of the LBES normalizing it to the area of the Mn $2p_{3/2}$.

As for point 2, we multiplied the IMFP values obtained from the recently optimized TPP-2M formula (Tanuma *et al.*, 2011) for GaAs and LSMO by the cosine between the sample surface and the photoelectron direction, to correctly evaluate the effective geometrical path of the electron in the solid. We added a 10 % uncertainty. The results are shown in Tab. 3.2.

Photon energy	IMFP in LSMO	IMFP in GMA
800 eV	N. M.	7 ± 1 Å
1000 eV	9 ± 1 Å	11 ± 1 Å
2500 eV	30 ± 3 Å	36 ± 4 Å
6000 eV	70 ± 7 Å	86 ± 9 Å

Table 3.2: TPP-2M calculated IMFP at three photon energies for LSMO and GMA.

For point 3, we individuated, besides an overall qualitative analysis of the spectra, the relative distance between the poorly screened peak and the LBES to be the parameter that identified the value of V^* or V in the theoretical spectra that matched the experimental values. Note that the parameter responsible of the largest variations of the relative energy position is Δ^* for LSMO and Δ for GMA. These were either obtained from literature values (GMA) or from comparison with the bulk ($h\nu = 6000\,eV$) spectrum (LSMO), and left unchanged across the probing depth scan. The best agreeing theoretical spectra are shown in Fig. 3.17 a. (LSMO) and b. (GMA), with the corresponding values of V^* and V respectively.

In Fig. 3.18, we plot the evolution of the relative distance between the poorly-screened main line and the LBES (abscissa) as a function of the IMFP of the electrons in the solid (left ordinate), and at the same time of the corresponding hybridization value (right ordinate, note the non-linear axis). It is clear that the trend is well reproduced, although

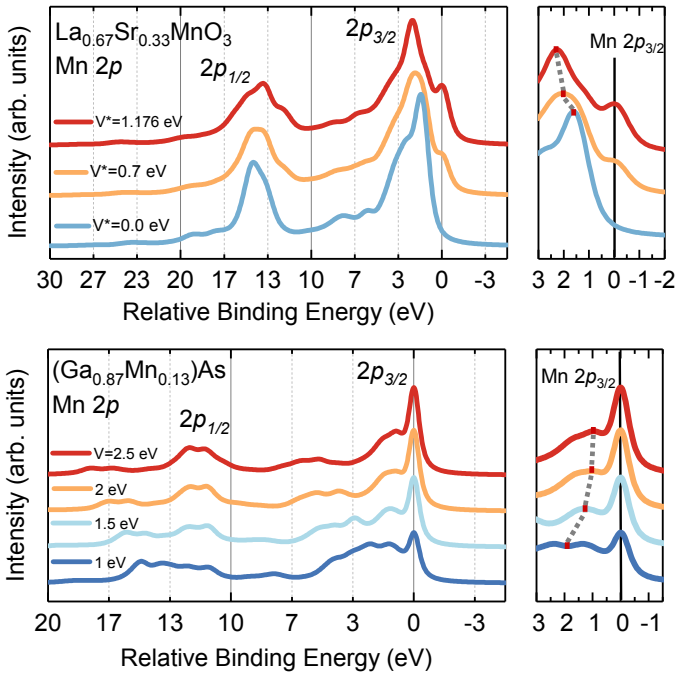

Figure 3.17: a. Best fitting theoretical spectra of LSMO as calculated with the Extended Cluster Model. Δ^* was obtained by confrontation with the highest photon energy spectrum. The reported values of V^* were obtained by the relative energy position criterion. In the right sub-panel, the Mn $2p_{3/2}$ region is zoomed in, and the relative energy shifts are observed as variations in the position of the main line analogously to what it is done in Fig. 3.6. b. Same as in panel a. but for the theoretical spectra of (Ga,Mn)As obtained within the standard cluster model calculation. In this case, Δ was obtained from literature values and only V needed to be defined by the energy position criterion. In the right panel, to be compared with Fig. 3.8, are presented the relative energy shifts.

in both cases there is a larger discrepancy towards the surface.

Finally (point 4), a fitting function is needed to define a numerical value for the cross-over thickness. It can be derived assuming that there are two extrema: SPECTRUM A (at the surface) and SPECTRUM B (in the bulk). Now, what will be measured in a photoemission measurement will always be a linear superposition of the two spectra:

$$\text{REAL SPECTRUM}(\lambda) = \text{a}(\lambda) \cdot \text{SPECTRUM A} + \text{b}(\lambda) \cdot \text{SPECTRUM B} \qquad (3.6)$$

Where $\lambda = \lambda(E_{hv})$ is the Inelastic Mean Free Path of the Mn 2p electrons, function of their kinetic energy (and therefore of the photon energy), and of the material. $a(\lambda)$ and $b(\lambda)$ add to unity for every λ. If $SPECTRUM\ B$ has a feature not present in $SPECTRUM\ A$, its measured evolution will be that of $b(\lambda)$.

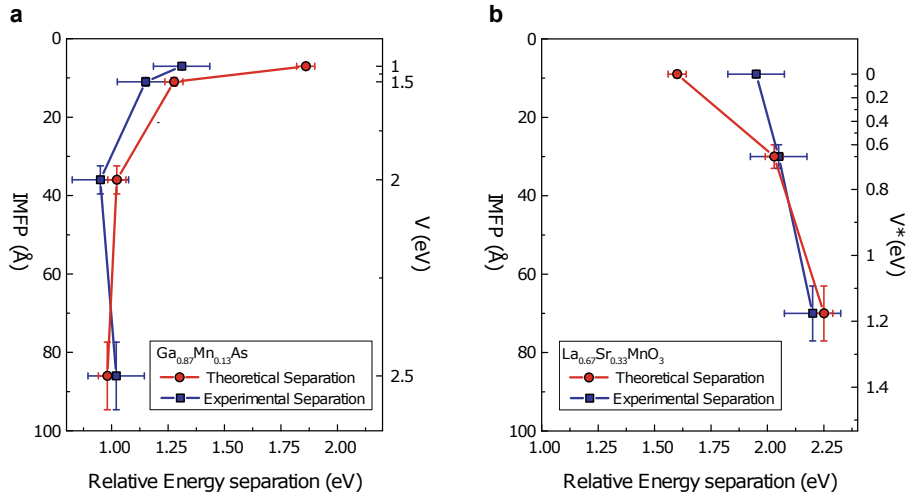

Figure 3.18: Comparison between experimental and theoretical data regarding the energy separation between well-screened and main peaks. The experimental data of (Ga,Mn)As (blue filled squares, panel a. and LSMO (blue filled squares, panel b. are plotted vs. the calculated inelastic mean free path (left vertical axis) and compared with the theoretical data (red filled circles in both panels) corresponding to the value of the hybridization parameter V and V^* (right vertical axis in eV). Lines through the points are guides for the eye. The horizontal error is estimated as the measured experimental energy resolution, which is always larger than the positioning uncertainty of the fitting functions. The separation between the peaks follows the trend predicted by theory.

$b(\lambda)$ is given by the integral of the (normalized) law that defines the contribution of each layer as a function of its depth times a "mask" function ($M(z)$) that is 0 at the depths at which we have no $SPECTRUM\ B$, and 1 in the bulk (where we do have $SPECTRUM\ B$). The depth-contribution normalized law (excluding angles for simplicity), is:

$$I(x,\lambda) = \frac{e^{(-z/\lambda)}}{\lambda} \tag{3.7}$$

The real depth evolution, disentangled from attenuation effects is therefore given by $M(z) \cdot SPECTRUM\ B$. However, we have to assume the simplest expression for the mask function, an abrupt Heaviside step from zero to one at depth k:

$$M(z) = \Theta(z-k) \tag{3.8}$$

Where k is the depth at which $SPECTRUM\,B$ appears. Clearly this is an non-physically simplistic assumption, as it is very hard to believe that the electronic structure presents such an abrupt step. With three-four data points it is not reasonable to extract more than one fitting parameter,and any smoother mask function would introduce further parameters. However, we can argue that the k parameter that we use, even in presence of

a smoother mask function, will approximately correspond to the quote of the inflection point, where the properties start changing radically.

Calculating:

$$b(\lambda) = \int_0^\infty \frac{e^{(-z/\lambda)}}{\lambda} \cdot \Theta(z-k)dz = e^{(-k/\lambda)} \tag{3.9}$$

Gives us the overlayer attenuation function, that has been used to study the evolution of PES signal from an underlayer while an overlayer is evaporated on it. In normal PES during evaporation, however, λ is fixed and k increases with the overlayer thickness, giving a simple exponential attenuation. In this case, instead, the free variable is λ and k is a fit parameter. If we assume that $SPECTRUM\ A$ has no extra-peak contribution, we can fit the the relative contribution of the LBES in the two materials obtained from point 1 as a function of the depth scale obtained at point 2.

The fitting function is, therefore:

$$b(z) = A \cdot e^{(-B/z)} \tag{3.10}$$

Where A is a pre-factor accounting for the different relative weights of the LBES in the two materials, B is the thickness of the region in which the peak is assumed to be negligible (the cross-over thickness), and z is the inelastic mean free path corresponding to the different photon energies. By using a least-squares routine to find the best values of B, we find (12 ± 1)Å for GMA and (40 ± 2)Å for the strain relaxed sample LSMO/LSAT. The application of the same procedure to the LSMO films in the other strain states did not yield significant differences within the error bar.

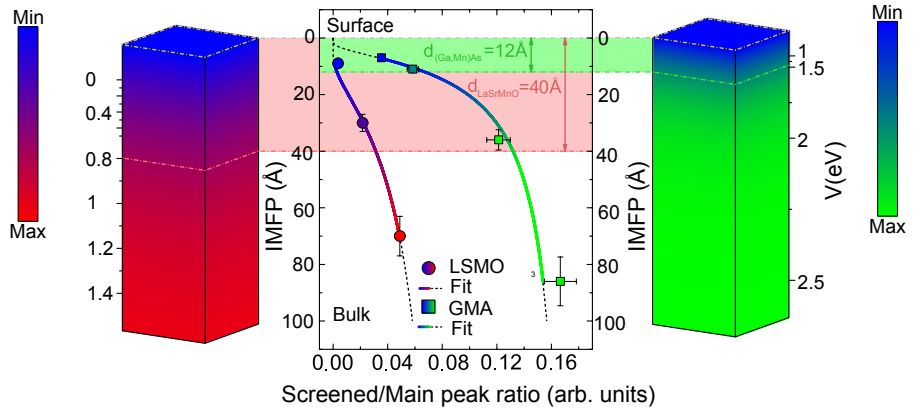

Figure 3.19: Summary picture of the information extracted by the procedure of quantification of the cross-over thickness. Details in text.

Fig. 3.19 sums up the result of our procedure. In the central panel the relative amplitude of the LBES is plotted as scatter points for the LSMO/LSAT strain-relaxed sample (circles) and the GMA sample (squares). The vertical error bar is calculated, as in Fig. 2, to be the 10% of the absolute value of the IMFP. The horizontal uncertainty is calculated

by means of error propagation from the uncertainty on the parameters of the peak fitting functions.

The solid curves show the fitted functions with Eq. 3.10, dashed in the region outside the datapoints. The light green (red) shaded area defines the cross-over thickness for GMA (LSMO) i.e. the value of the B parameter obtained from each fit. The parallepipeda at the side of the central panel represent schematically the solid: they are coloured with a gradient that reproduces the relative intensity of the LBES in GMA (LSMO) according to Eq. 3.10, with blue corresponding to zero and green (red) corresponding to the maximum value assumed by the function in the range 0-100 Å. The cross-over thickness is reported from the central panel. In each parallelepiped is reported the evolution of the hybridization parameter, as obtained from Fig. 3.18.

The observation of such a large cross-over thickness in LSMO unavoidably triggers the question: "why is it so large?". Clearly, our measurements do not give a certain answer.

However, it is first of all important to notice that our results must be compared with x-ray magnetic spectroscopy (Verna *et al.*, 2010) and transport measurements (Angeloni *et al.*, 2004) that reported altered magnetic and metallic character up to 30-50 Å away from the surface, not to mention the same measurement by Park and colleagues shown in Fig. 2.6, that still finds a significantly modified M(T) at the 50 Å probing depth of XMCD. For GMA, our result is consistent with the thickness of the depletion layer observed in (Sawicki *et al.*, 2010). The values that we observe are largely consistent with the ones observed in literature.

Secondly, our method provides a way to remove numerous extrinsic factors that have obscured its understanding in the past, allowing to design experiments that address specific mechanisms. In our case, we targeted strain, and found no clues of its relevance in the cross-over thickness at the free surface. Further experiments along these lines may single out the most significant interaction.

Summary of Part I

In this Part, the potentiality of HAXPES in exploring the electronic structure of strongly correlated materials is demonstrated on a system of high interest for spintronic application. The analysis of the Mn 2p presented in Sect. 3.2.1 at high primary photon energies (6 keV), allows to identify the low binding energy satellite that can be linked to the mobility of charges.

In the metallic phase, delocalized states appear close to the Fermi energy which are able to screen the core-hole charge produced in the photoemission process more efficiently than the transfer of charges from the ligand band. As discussed in Sect. 3.3.2, the intensity of the LBES can be attributed to the degree of hybridization of such coherent delocalized states with the ground state of the material. It is important to clarify that the hybridization considered here is not the unique fingerprint of metallic transport: in the complexity of this manganite, charge carriers can be moved with several different mechanisms and even when the material is above T_C, its transport characteristics are those of a badly conducting metal.

Such a specific probe can be used to study the effects of external parameters on the delicate equilibrium of the electronic structure. The simple inspection of the Mn 2p doublet at lower photon energies, and therefore probing shallower depths in the material, shows a significant reduction of the hybridization at the surface, leading to the disappearance of the LBES. Furthermore, it is clear that also other features at higher binding energies seem to evolve when probing different depths in the material. These structures are, however, broader and more difficult to separate as they are largely overlapped with the main line.

The picture of an enhanced localization is supported by the inspection of the band structure, which shows shifts of spectral weight towards lower binding energy closer to the surface. In particular, an enhancement of the intensity of the t_{2g} localized band is observed for the lowest photon energy spectrum. The comparison with the temperature effect study (at 6 keV primary photon energy) of Sect. 3.2.3 allows to conclude that the observed behaviour of the surface is not simply ascribable to a different temperature dependence of the topmost layers. In particular the confrontation of the Valence Band lineshape well

above the Curie temperature shows striking differences with the one observed for the smallest probing depth.

The difference between the valence band spectra below and above the Curie temperature allows to identify clearly the aforementioned shifts of spectral weight as in the metallic state an increased density of states is found at the top of the e_g band. The analysis of the Mn 2p doublet across the critical temperature shows that the LBES is largely enhanced by the emerging of long range ordering.

The analysis of circular dichroism in photoemission in Sect. 3.2.4 allows to identify the strong magnetic character of the LBES, that shows a large dichroic contrast. This again supports the picture of the LBES as arising from metallic states close to the Fermi energy as, given the half-metallic character of LSMO bandstructure, the effective screening mechanism can be mediated only by the majority electrons.

We then applied the wealth of information gathered from such spectroscopic study to the quantification of the size of the region with modified electronic hybridization. Building on a long standing effort to give effective modelling of the LBES in two materials, namely LSMO and GMA (Sect. 3.3.2), we could develop a reliable way of quantifying the hybridization corresponding to each spectrum measured at different photon energy.

Thanks to the recent progress in the description of the inelastic mean free path of high energy electrons in solids, we could attribute a precise probing depth to each different primary photon energy. This allowed us to give an hybridization profile as a function of the distance from the surface Sect. 3.3.3. Furthermore, we could fit the experimental data and identify the variation of the relative weight of the LBES.

Putting this information together, we employed an abrupt-step overlayer model to identify the thickness of the region in which the metallic properties are strongly modified. We obtain find (12 ± 1)Å for GMA and (40 ± 2)Å for LSMO, both are in good agreement with the literature.

Most importantly, however, the technique demonstrated in this work opens a new phase of the use of HAXPES measurement in the analysis if surfaces and buried interfaces, i.e. the availability of a combination of high resolution instrumentation, effective theoretical modelling and reliable fitting procedures that will enable quantification of the characteristics of the electronic structure.

The range of possible developments of this work is therefore rather wide. In direct continuity with the chosen systems, for example, there are several questions that remain unanswered:

1. Is the cross-over thickness of the metallic transport properties coincident with the one of the magnetic interactions or one is larger than the other?

2. What is the impact of the surface contamination on the cross-over thickness?

3. How does temperature affect it? Does the bulk-like region move closer tot the surface when the temperature is lowered?

4. Is it possible to go beyond the abrupt-step model and identify the functional dependence of the amplitude of the extra peak as a function of the probing depth?

Point 1. certainly addresses the difficult issue of disentangling transport and magnetic effects in the LBES. In a material in which these two characteristics are strongly intertwined, a way to investigate this subject is to use the powerful insight given by circular dichroism in HAXPES.

The effect of surface contamination (question 2.) may be studied by compared analysis of samples exposed to air and ones grown in-situ or transferred in vacuum.

As for point 3, a temperature study in the range used in Sect. 3.2.3 is already feasible at I09. The measurement at higher temperatures, requiring oxidizing gases to maintain the stoichiometry, is more challenging, but development of gas cells for ambient pressure HAXPES is under way and may offer interesting developments.

The last question is interesting because it takes the technique one step forward in the description of the electronic structure of complex materials. Overcoming the abrupt step model would mean individuating a different functional dependence of the mask function introduced in Eq. 3.8. It is then captivating to notice that, if one uses a smoother mask function with the same inflection point as the Heaviside step used here, the largest differences between the resulting observable attenuation functions for the LBES arise at the lowest probing depths. Lower probing depths correspond to lower photon energies, i.e. the range of operation of grooved monochromators, where the photon energy can easily be scanned in small steps. It would then be a feasible experiment to perform an analysis similar to the one described in this chapter, but acquiring a large number of spectra at lower photon energies. That would give solid ground to a less sketchy description of the relaxation of the electronic structure.

Part II

Dynamics of electronic correlation

Chapter 4

Dynamics of strongly correlated materials

> [...] a pulse of visible light seemed to be a rather blunt instrument when unleashed on a correlated electron system [...]. To skeptics, injecting photons, each delivering 1.5 eV of energy [...] was like detonating a nuclear device in a public library reading room.
>
> Joseph Orenstein, 2012

Correlations among electrons develop in a time scale that is also a fundamental characteristic of each material. The theoretical description of order parameters competing with each other to determine the ground state individuates mechanisms that have a specific set of elementary excitations. These, in turn, define a precise energy scale, schematically listed in Fig.4.1 a. As can be seen, such scales are rather diverse and span several orders of magnitude. Using the time-energy uncertainty relationship, it is possible to attribute a time-scale to each excitation.

It then becomes clear that, as close as the energies of different ground states may be, the time required to establish the lowest energy configuration will depend on the dominating interaction that drives it. The kinetics, observed in real time, of the formation of an ordered state can therefore help in disentangling the effect that produces such configuration from the ones that are competing with it.

Besides the applicative interest mentioned in the Introduction, therefore, there is a strong drive towards a deeper comprehension of the ordering mechanisms in TMOs by observing the formation of equilibrium states at very short time-scales.

The advancement in laser technology has, since the realization of Titanium-Sapphire regenerative amplifiers in the 1980s, made simpler the generation of infrared light pulses of high intensity with tens of femtosecond duration. This has pushed the boundary to timescales short enough that it is possible to describe the response of a solid as separate sets of excitations, which can be connected to a precise degree of freedom: orbital, spin, charge and lattice (4.1 b). The evolution of the system can be described by addressing

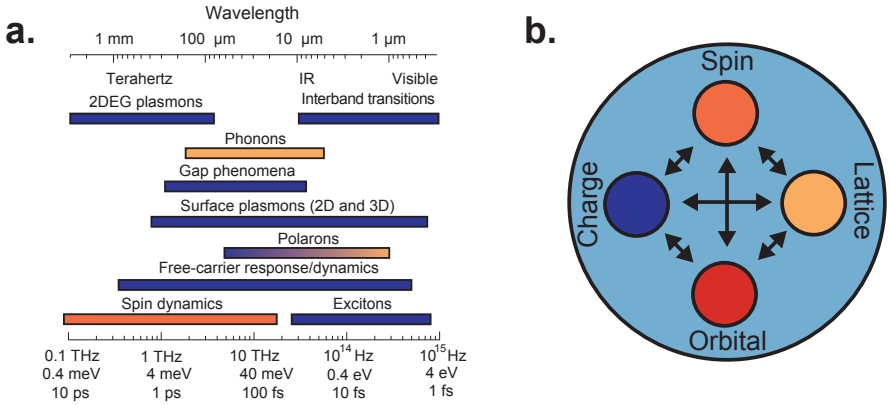

Figure 4.1: a. Typical fundamental excitations in complex materials, plotted against the corresponding energy, timescale and corresponding photon wavelength . Adapted from (Zhang and Averitt, 2014). b. Scheme of the mutually interacting charge, orbital, lattice and spin degrees of freedom that characterize the competing order in the ground state of correlated electron materials.

the rate at which the energy exchange between the different degrees of freedom (or within each one) develops.

4.1 The pump-probe method

The time-resolved investigation of solids in general, and of TMOs in particular, has mainly taken the form of a stroboscopic pump-probe method, shown schematically in Fig. 4.2. This strategy consists in exciting the material with an ultra-short, high intensity laser pulse, and then probing it with a second, lower intensity pulse of different wavelength such to provide a spectroscopic information.

The role of the first pulse is to push the system significantly out of equilibrium. For this reason, the pump pulse is often in the infrared range, as it is generally aimed at producing the lowest energy excitations. The amount of energy carried by the pump can be extremely large and can be expressed in number of absorbed photons *per single transition metal ion* and exceed unit values. The time duration of the pump pulse is a very important parameter: depending on the processes that an experiment aims to explore, it might be more interesting to induce a precise optically pumped excited state (and therefore use longer pulses), or states very far from equilibrium, that require extremely large peak power densities.

The pump pulse produces an abrupt step an selective excitation in the state of the material, and what follows is defined as the relaxation dynamics. To image it, the probe pulse must arrive at a controlled delay after the pump. This is realized, in most of the cases, by the implementation of controlled differences in the optical path of the laser light: thanks to the high precision with which mechanical motion can nowadays be realized, the

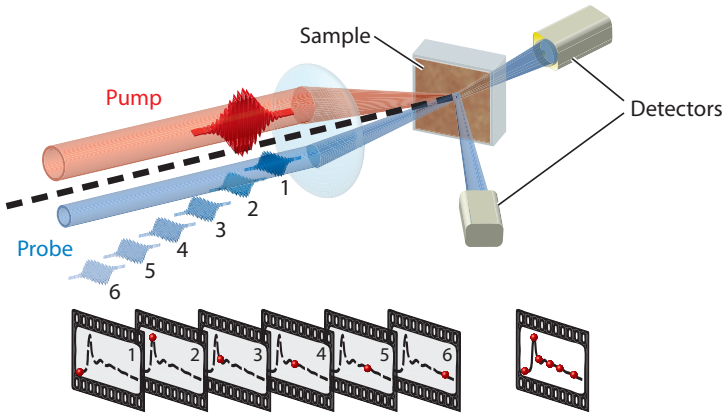

Figure 4.2: Schematic representation of a pump-probe experiment. An IR pulse (red) is used to excite the sample out of equilibrium. A second probe pulse (blue), often of different wavelength, reaches the sample at controlled delay. The probe pulse allows to measure the response of the material at a very precise instant. The experiment is repeated changing the delay in the time of arrival of the probe pulse (1-6), to image the full relaxation trace. From (Zhang and Averitt, 2014).

timing between the pulses can be tuned within femtoseconds. The time-duration of the probe pulse is also crucial to the experiment, as it needs to be much shorter than the relaxation process that is to be studied.

After shining the probe pulse, the system is left to cool down, allowing it to return to the thermodynamic ground state: the time left for recovery generally depends on the repetition rate of the source and can vary between microseconds to milliseconds. The excited state is then newly prepared by another pump pulse and the experiment, at a precise pump-probe delay is repeated until a sufficient statistics is achieved. Then the delay is changed and the successive point in the dynamical measurement is acquired.

Of the class of high power density experiments, the ones realized on solid state samples such as TMOs are among the ones that require the most careful evaluation of the pump intensity. Indeed, in order to probe highly non-equilibrium states, large pulse energies are required. On the other hand, however, since the target is non-renewable, it is necessary to avoid to overcome the permanent damage threshold. Furthermore, care has to be taken in order to avoid a temperature build-up in the sample: if the equilibrium state is not fully recovered at the arrival of the new pump pulse, the temperature will increase pulse after pulse until a balance between the residual heat and the thermal diffusion through the substrate reach an equilibrium. This process, which we will define *DC-heating* in the next, blurs the definition of the initial temperature of the sample before the pump-pulse: since in TMOs small changes in temperature might lead to different ground states, it is important to avoid it, or at least to have means to monitor the initial temperature and keep it under control.

Since the first experiments in the late 1980s, the field of time-resolved experiments has widened considerably, and obtained a wealth of exciting results. The advancement in the control of solid state laser generated short pulses of light that now span the THz (Zhang and Averitt, 2014) to Soft X-ray range (Popmintchev *et al.*, 2012), combined with the realization of Free Electron Lasers (Allaria *et al.*, 2013; Emma *et al.*, 2010; Tono *et al.*, 2013; Tiedtke *et al.*, 2009) has enabled the realization of a large number of different strategies. The use of two pulses of different wavelength allows to vary significantly the degrees of freedom of the material that are excited and the ones that are probed.

Without the intention of reviewing the field, a task beyond the scope of this thesis and fulfilled extensively by more experienced authors (Basov *et al.*, 2011; Zhang and Averitt, 2014; Giannetti *et al.*, 2016), we contextualize our work and the interest that it yields dividing the discussion in:

- *Pump control*: i.e. the set of experimental choices that are aimed at exciting specific degrees of freedom, and the consequent pieces of information that can be extracted from the dynamics.
- *Probe control*: i.e. the range of spectroscopic and structural techniques that have been applied to the investigation of correlated electron systems.

4.2 Controlling the pump

The control achieved in the optical manipulation of the pump pulse has enabled it to go significantly beyond its initial conception of a mean to drive the system somewhere out of equilibrium. As the understanding of dynamical processes in condensed matter systems increased, indeed, the pump assumed more and more the character of a precise instrument to guide the system in the complex free energy landscape of correlated electron materials.

Indeed, if one looks at the optical response of a correlated electron system, it is possible to note that there are specific features, of high interest in the control of the dynamics of transition metal oxides.

As shown in Fig. 4.3 a, following the concept of the band evolution suggested by DMFT in Sect. 1.2, we can describe the changes observed in the optical conductivity spectrum: as the U value increases, we move from metallic intra-band transitions, that show the characteristic sharp Drude peak, to transitions between the Lower Hubbard Band to the Upper Hubbard Band, producing a structure of 2W bandwidth with no low energy components (optical bandgap of U-W amplitude).

Between the two is possible to recognize regions in which intra-band transitions happen between the coherent and incoherent part, thus showing both Drude-like low energy excitations and structures at higher energies, that get closer and closer to U. In a Mott insulator, or a system very close to the MIT, it is therefore interesting to optically induce charge excitations by pumping at energies close to U, crossing the Mott gap and producing significant delocalization of charges. In many correlated electron systems, the value of U is in the units of eV range, thus corresponding to IR-visible pumping.

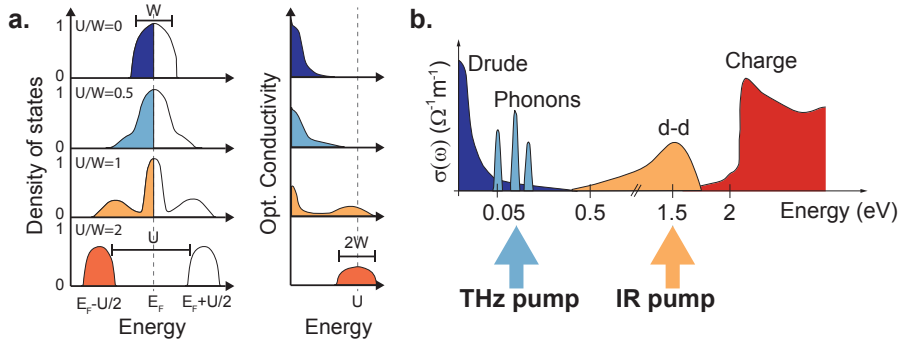

Figure 4.3: a. DMFT bandstructure and optical conductivity spectra of a correlated electron system as a function of the U/W ratio. As it can be seen, the system goes from a metallic Drude-response to an insulating one with the opening of an optical bandgap of amplitude U-W. b. Schematic representation of the optical conductivity spectrum of a correlated electron material close to the metal-insulator transition (from the metallic side). Both diagrams are adapted from (Singla, 2015).

The generation of large charge excitation has, for long time, been the most important way to excite a correlated electron system, and the triggering of other degrees of freedom has been largely probed as a consequence of IR-visible pumping. In the optical spectrum of a real system, however, a large number of other interactions are observable, such as IR-active phonons (shown in Fig. 4.3 b), spin-waves, or other excitations of the ordering parameters giving rise to the ground state.

Most of them, originating from lower energy interactions, are in the 100-10 meV range, and are studied in a new class of experiments using THz probe. While pumping in the IR generally involves transition between incoherent features of the spectrum, in the excitation of phonon, spin and charge oscillation modes, also the spatial coherence of the pump is a relevant parameter.

The use of the various parts of the of the spectrum, and namely IR-visible and THz, and the control of the spatial and temporal coherence of the pump has therefore become a very precise way of driving a correlated electron system through the phase space. In a way, a connection can be created with Chap. 2, where it is stated that the practical ways of controlling the ground state of TMOs were band filling and bandwidth tuning by acting on the tolerance factor.

Indeed, the optical excitation can be controlled to produce charge excitations, which, due to the generally different characteristic lifetime of electron and hole, may result in *photodoping* i.e. the transient change in the occupation of the bands. On the other hand, the resonant pumping of specific phonons, and specifically those associated with changing of the O-M-O bond angle, or breathing modes that affect the degeneracy of the e_g bands, may result in transient variation of the bandwidth.

Furthermore, for TMOs and especially in mixed valence compounds, the IR laser excitation is particularly effective in triggering inter-site charge excitations that couple

strongly with lattice ordering, resulting in a sudden polaron collapse. The polaron formation, either in the small form of doped manganites, or the cooperative mechanism of the TMO insulators, always tends to localize charges, producing generally insulating states. Upon sudden release of the polaron trapping, the interactions that tend to produce delocalized states can (transiently) take over, producing metallicity and ferromagnetism.

It is therefore clear that correlated electron systems offer a fascinating opportunity to explore and control the kinetics of solids in a complex energy landscape. It is possible to identify four classes of dynamics:

1. *Photoinduced variation of the thermodynamic state* (PIVTS): when the pump drives the system into a non-equilibrium state, that does not have a well defined thermodynamic potential. The state is then transient, and disappears within the relaxation time that characterizes the interaction dominating the formation of the ground state ordering. This kind of studies is aimed at deciphering the quasi-particle dynamics within a single thermodynamic phase.

2. *Photoinduced Phase Transition between Quasi-equilibrium Phases* (PIPT-QP): when the pump induces a phase transition that is observed also in the quasi-equilibrium phase diagram. Also this kind of states is transient and tends to relax to the initial state, often (but not always) following the quasi-equilibrium path, but allowing to identify the speed limits of its re-establishment.

3. *Photoinduced Phase Transition to a Hidden Phase* (PIPT-HP): when the pump produces an ultrafast transition to a state that is not thermodynamically accessible by quasi-static temperature variations.

4. *Coherent control of transient states*: where the presence of perturbing fields constrains the system to follow a particular path in the phase space.

Since the proposal of existence of hidden phases (Tokura, 2006), a large experimental effort has also been in the direction of exploring the creation of such configurations, leading to exciting results in superconductors (Fausti *et al.*, 2011), narrow bandwidth manganites (Zhang *et al.*, 2016; Ichikawa *et al.*, 2011; Polli *et al.*, 2007; Matsubara *et al.*, 2007, 2008) and layered dichalcogenides (Stojchevska *et al.*, 2014).

As will be discussed in Sect. 4.3, our work is aimed at opening a new way to investigate the dynamics of correlated electron materials. As this study constitutes one of the first steps towards the realization of time-resolved HAXPES experiments, the strategy we choose required that we avoided the complexity of strong phase competition, the presence of first order phase transitions and the ultrashort, tens-of-femtoseconds dynamics that hidden phases entail. We therefore focused more on PIVTS and PIPT-QP, in order to gain information on the interaction dominating the dynamics in our prototypical correlated material, LSMO. Addressing hidden and non-thermal phases is nonetheless the natural perspective of the work described here, as they can be realized with substantially the same materials and techniques employed in our study.

4.3 Controlling the probe

Most of the time resolved studies on correlated materials have been performed by means of optical spectroscopy (Basov *et al.*, 2011; Zhang and Averitt, 2014; Giannetti *et al.*, 2016, and references therein). The probe beam, either reflected or transmitted (or both as in Fig. 4.2) is, in that case, formed by pulses of light going from the visible to the THz range.

Indeed, as can be seen in Fig. 4.3, each individual feature of the spectrum can be attributed to specific excitations, ranging from the Drude sharp structure at long wavelength, which gives information on the low frequency conductivity, to the electronic inter-band charge excitations, passing by phonons, intra-band excitations, excitations between incoherent Hubbard features and hybridized states close to the Fermi energy.

All these features constitute important probes of the response of the solid and have been investigated extensively, with extremely sophisticated experimental strategies advantaging from the high degree of control achievable on high intensity optical pulses. The use of supercontinuum generation and broadband amplification, for example, has allowed to perform various form of single-shot spectroscopies, where a single pulse allows to measure a full optical spectrum of the system (Giannetti *et al.*, 2016).

A specific mention must be devoted to the optical technique that, manipulating the polarization state of the probe, enables to evaluate the macroscopic magnetization: the magneto-optical Kerr effect[1]. This technique has allowed a wealth of studies on the magnetic dynamics of manganites: the photoegeneration of ferromagnetism has been observed in $Pr_{1-x}Ca_xMnO_3$, $La_{1-x}Ca_xMnO_3$ and $Gd_{1-x}Sr_xMnO_3$ (Matsubara *et al.*, 2007, 2008; Liu *et al.*, 2001; Li *et al.*, 2013) both in the form of access to a hidden phase and as the PIPT to a quasi-equilibrium state. Furthermore, the evolution of the magnetic state in LSMO and LMO has been thoroughly studied with this technique (Averitt *et al.*, 2001; Ogasawara *et al.*, 2003; Lobad *et al.*, 2000a,b).

Since we know, from the studies discussed in Part I, that the dominating interaction in the correlated system of our choice is the ferromagnetic double exchange coupling, we performed a through time resolved MOKE analysis of the magnetic dynamics and we will therefore discuss in detail the technique, the methods and the experimental results in Chap. 5 and Chap. 6, respectively.

Nonetheless, as it will be confirmed by the results described in Chap. 6, all the optical techniques suffer of the indiscriminate sensitivity to low energy excitations of the solid. When the system is pumped with large energy densities, significant perturbation of the bands take place and it is often difficult to disentangle the effective variations of the electronic structure from bleaching effects (optical saturation of a particular transition), shifts of spectral weight or other disturbances of the signal.

[1]Magneto-optical Kerr effect corresponds, in reflection, to the transmission technique of Faraday rotation. MOKE is more often employed as a technique because ferromagnetic materials are often metallic and thus very little transparent to optical light (the high magnetic permeability often further shortens the skin depth with respect to non-magnetic metals).

4.3.1 High energy techniques

For this reason, and thanks to the developing fourth generation of light-sources, the Free-Electron Lasers, able to generate hundred to tens of femtoseconds hard X-ray pulses, the research community is now pioneering time-resolved high energy techniques, and applying them, among others, to the fascinating puzzles of correlated materials.

For example, pioneering studies have demonstrated the potentialities of time-resolved XANES in unravelling some of the characteristics of the photoinduced metallic phase of $Pr_{0.7}Ca_{0.3}MnO_3$ (PCMO) (Rini *et al.*, 2009).

A long standing work, developed by Beaud and colleagues, has used X-ray diffraction measuring superlattice peaks to study the dynamics of narrow bandwidth manganites LCMO (Beaud *et al.*, 2009) and PCMO (Beaud *et al.*, 2014), giving solid grounds to the aforementioned phenomenological Landau theory of phase transition, and individuating reliable order parameters that drive the dynamics (Esposito *et al.*, 2017).

Furthermore, resonant magnetic X-ray diffraction has allowed to probe the photoinduced collapse in magnetic correlations for the single-layered manganite $La_{0.5}Sr_{1.5}MnO_4$ (Först *et al.*, 2011; Ehrke *et al.*, 2011). Very recently also time-resolved Resonant Inelastic X-ray Scattering has been employed to highlight the role of dimensionality in magnetic correlation in Sr_2IrO_4 (Dean *et al.*, 2016).

Time-resolved photoelectron spectroscopy, instead, has a long history of time resolved implementation, as single photon photoemission can be realized as long as the photon energies are sufficient to overcome the work function and has therefore been realized since ultrashort optical pulses became available: 6 eV pulses can be easily generated by solid-state frequency upconversion in non-linear crystals of BBO, and even before that 3 eV pulses were employed to realize two-photon photoemission (Petek and Ogawa, 1997; Aeschlimann *et al.*, 1997; Winkelmann *et al.*, 2010; Chiang *et al.*, 2012; Ellguth *et al.*, 2015).

These techniques, despite having reported interesting results on several systems such as superconductors (Graf *et al.*, 2011) and topological insulators (Sobota *et al.*, 2012; Hajlaoui *et al.*, 2012), are however restricted to very limited regions of the Brilloun zone, due to small photon energy (Kirchmann *et al.*, 2010; Smallwood *et al.*, 2016, and references therein). Also the spatial information is difficult to interpret: largely material dependent, long IMFP and thus a complicated dependence on the surface contamination state complicate the understanding of the static spectra in the first place.

The extraordinary advantage of PES, as we mentioned earlier, is that it directly images the electronic structure and, in particular in its angularly resolved form, it can directly envision the momentum distribution of electrons in the solid, mapping the three dimensional structure of the Fermi surface and evaluating the details of direct and indirect gaps, probing the specific origin of electronic correlation. Its combination with a pump-probe routine yields a very powerful technique.

The technological advancement makes realistic the idea that in a single apparatus, the four degrees of freedom of the electron (the three components of the k-vector and the spin state) can be measured simultaneously even in out-of equilibrium condition,

possibly obtaining also site specific information through the Photoelectron Diffraction technique. A significant part in this revolution is the possibility of realizing shortly pulsed monochromatic soft x-ray pulses from table top lasers enabled by HHG sources which will be discussed in 8.1.

One of the first results of the application of such machines to correlated materials is, for example, the elegant study on the nature of gap opening in charge density wave layered dichalcogenides, which are classified as Peierls, Mott or Anderson insulator on the basis of the timescales of gap collapse at specific points of the ARPES spectra(Hellmann *et al.*, 2012). Femtosecond core-level PES based on Soft X-ray FEL has been applied to dichalcogenide systems successfully (Hellmann *et al.*, 2010).

As we have thoroughly demonstrated in Part I, however, another recent technique that has proven invaluable to investigate the electronic state of TMOs is HAXPES. With the complex panorama of possible dynamics that a TMO can access, a probe capable of directly assessing the electronic structure, together with chemical, magnetic and orbital sensitivity is surely needed to produce a clear picture of the system state even in non-equilibrium conditions.

4.3.2 Time-resolved HAXPES

Time-resolved HAXPES requires the generation of short pulses of hard X-ray photons that must be synchronized with an infrared laser pulse. At present, the sources that are able to produce picosecond to femtosecond pulses of hard x-rays are essentially two: synchrotron hard x-ray undulators and free electron lasers.

The synchrotron undulators can be employed in two ways. The first, and technologically more straightforward, is to exploit the syncrotron timestructure. Indeed, when each electron bunch accumulated in the ring passes through the undulator, it emits short burst of light whose duration is given by the length of the electron bunch. The bunch length is typically in the mm range, and the pulse duration is generally few tens of picoseconds.

If only one bunch is stored in the ring, it is possible to electronically synchronize the pump laser to the X-ray pulse and realize hard x-ray probe, IR-pump experiments. It is very rare, however, that in large scale facilities the operating mode is single bunch filling. Normally, hybrid filling is used instead, i.e. a part of the ring (say 3/4) is completely filled, while the remaining part hosts a single, isolated bunch, which generally carries a higher charge. The technical is then to separate the signal arising from the isolated bunch. The strategies that can be used will be discussed in Sect. 7.1.

This approach can be exploited, and as we will demonstrate yields promising results, but the time resolution is limited and it can detect electronic processes only when they are bottlenecked by some effect that slows them down, as it will be discussed in Sect. 5. Shorter pulses are obtained when the machines are operated in the so called *low-α mode*, where the bunch length is reduced and the time duration can be compressed to 3-4 ps.

The second strategy allows to enter the femtosecond regime, and consists in the so called *femtoslicing technique*. As the isolated bunch in hybrid filling travels through the undulator, an intense IR pulse is sent onto it. The IR produces an electric field that is large

enough to perturb the orbit of a small fraction (slice) of the bunch. The slice therefore emits a few tens femtosecond x-ray pulse that is slightly off axis from the emission of the remaining part of the bunch (Holldack *et al.*, 2014). The pulse can then be picked up by mirrors and delivered to the sample. This technique is effective on the reduction of the pulse duration, but it is intrinsically limited in intensity as the already limited amount of photons that can be extracted from a single bunch is further fractioned.

The most promising source, is instead the Free-Electron laser. In a free electron laser electron bunches are accelerated on a linear path, and first sent into a very long undulator (called the modulator). Here, the electron bunch interacts with the x-ray that it itself emits: the x-rays tend to modulate the spatial distribution of charges in the travelling direction. Whether initiated from a fluctuation (SASE (Emma *et al.*, 2010)), or seeded (Seeding (Allaria *et al.*, 2013) or Self-seeding (Amann *et al.*, 2012)), in a long enough modulator the bunch undergoes a net spatial charge redistribution called *microbunching*. The microbunches are positioned to match the wavelength of the emitted radiation: upon crossing a second undulator array (the radiator), they emit coherently, and the pulse length is given by the microbunch length, in the hundred femtoseconds range. The coherent emission builds up a large amount of photons, making the FELs the highest brilliance photon sources ever built.

FEL-based time-resolved HAXPES has been pioneered by the team based in SPring-8/SACLA campus and lead by Prof. M. Oura in collaboration with the Kiel University group under the direction of Prof. K. Rossnagel. Benefitting from the development achieved in Hamburg by the Kiel group together with W. Würth at the soft X-ray FLASH FEL, they discovered the paramount importance of single-shot detection to reduce the large FEL intensity fluctuations and arrival time jitter of SASE FEL, advancing the development of instrumentation to realize such experiments (Hellmann *et al.*, 2012; Oura *et al.*, 2014).

Nonetheless, in the first few beamtimes dedicated to HAXPES measurements, a significant hurdle was met, i.e. the formation of vacuum space-charge. As mentioned earlier, the FELs achieve their brilliance from the extremely high number of photons per pulse: the pulse energy can be in the several μJ to mJ range in the hard X-rays, blurring the intensity border between pump and probe (and indeed, a new class of experiments, those with X-ray pump, is now beginning to be explored (Ferrari *et al.*, 2016)). Nonetheless, if such high pulse energies are used, a large amount of photoelectrons is excited in the free space above the surface, all at almost the same time. Electrostatic repulsion within such an electron cloud then modifies strongly the kinetic energy of the photoelectrons and the HAXPES spectrum by shifting and broadening the peaks.

In a series of studies of the effects of space charge in $SrTiO_2$ (Oloff *et al.*, 2014, 2016a), they observed the effects of high energy per pulse in the probe, shown in Fig. 4.4 **a** for two different experimental energy resolutions. On the other hand, by measuring at low probe fluences, but high pump fluences, (Fig. 4.4 **b**), they also observe space charge effect, which due to the temporal evolution, can certainly be attributed to a second cloud of pump-generated photoelectrons, that arise from multiphoton photoemission (Aeschlimann *et al.*,

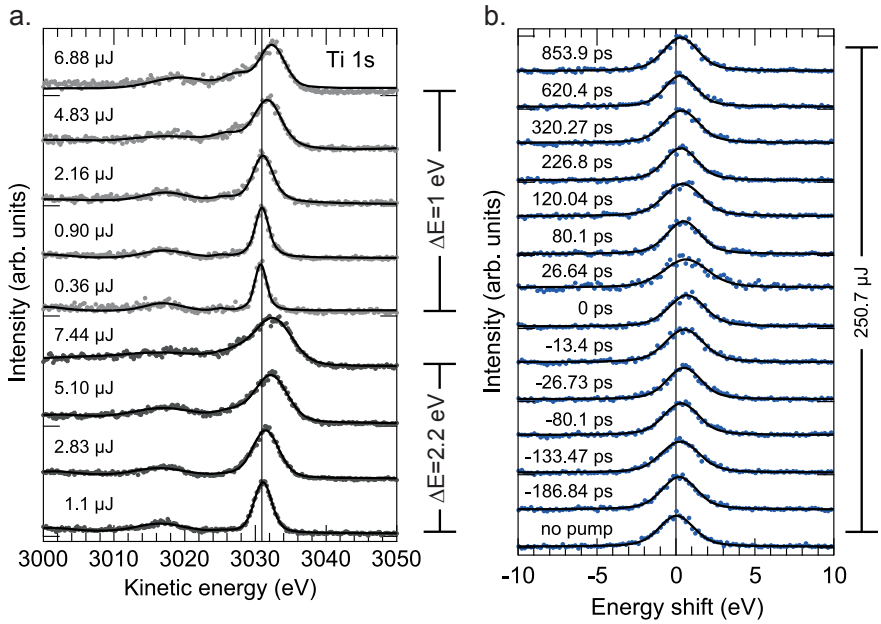

Figure 4.4: a. Evolution of the Ti 1s peak of electron-doped $SrTiO_2$ as a function of the probe pulse energy, measured at $h\nu = 8keV$ The light gray dots are measured at higher resolution (narrower analyser slits) corresponding to $\Delta E = 1\,eV$. Dark grey ones, at the same photon energy are measured with a more loose energy resolution of $\Delta E = 2.2\,eV$. From (Oloff *et al.*, 2014). b. Effects of space charge generated by the pump at high excitation densities of 250 μJ corresponding to 10 mJ/cm^2. The peak is the Ti 1s of the same sample pumped with $h\nu = 1.55\,eV$ photons and probed with $h\nu = 8\,keV$ HAXPES. The vertical line represents the position of the peak measured with the pump beam blocked (bottom spectrum). The different shifted spectra represent the various positive and negative delays. From (Oloff *et al.*, 2014).

1995; Sirotti *et al.*, 2014). To interpret their results, they develop a two charge clouds model, that consider classical many body interactions between disk-shaped clouds of pump-emitted electrons and probe-emitted ones, which reproduces well the experimental evidence.

Interestingly, by applying the model to probe-emitted clouds of different average energies, they find that the HAXPES regime, with average energies of keV in the probe-clouds, does not make their trajectories significantly stiffer, i.e. more resilient to shifts and broadening due to vacuum-space charge (Fig. 4.5 **a**).

On the other hand, they find that the elongated shape of the probe beam resulting from the grazing incidence geometry has a significant effect. Indeed, at grazing incidence the beam footprint is distributed on a wider area, resulting in a smaller photon (and therefore electron) density in the disk.

But even normalizing at the same photon density, the increase in the eccentricity of the elliptical disk reduces the Coulomb repulsive energy with respect to a disk, as shown in Fig. 4.5 **b**, where the space-charge shift is plotted as a function of the horizontal and vertical size.

All these results demonstrate that HAXPES has an upper limit in the number of photons per x-ray pulse that can be used. A schematic picture of rigid disk for the space charge cloud allows for a back-of-the-envelope calculation of the orders of magnitude (Oloff *et al.*, 2016b). The Coulomb energy of a uniformly charged circular disk is:

$$E_p = 6 \times 10^{-6} N/d\,[eV] \quad (4.1)$$

Where N is the number of electronic charges and d is the radius of the disk (in millimeters). It then becomes clear that, in order to keep the energy resolution in the hundred of meV range, E_p must be below this value, which is obtained, even with a large spotsize of 0.5 mm, by reducing the number of charges below 10^4 el/pulse. Considering a typical quantum efficiency of 10^{-2}, one has the maximum number of photons per pulse:

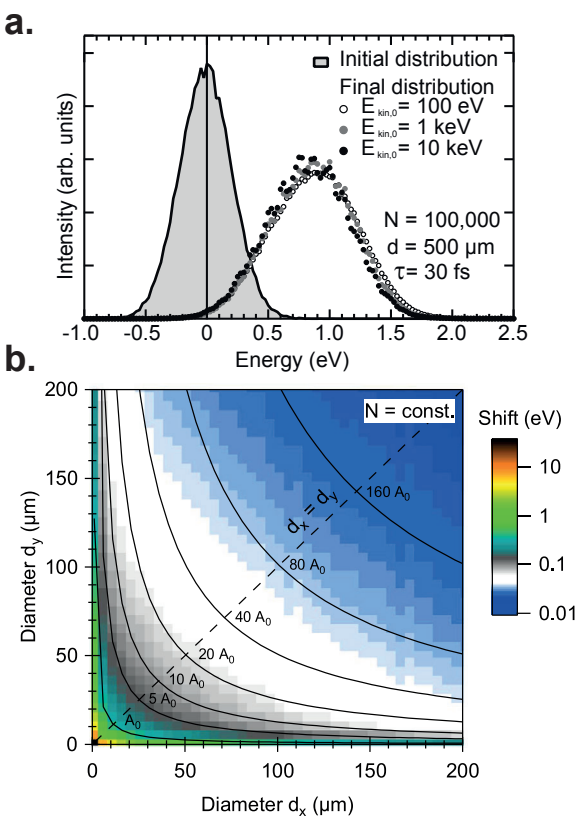

Figure 4.5: **a.** Effects of average kinetic energy of the space charge cloud on the shift and broadening of a sharp distribution (simulating an XPS peak). From (Oloff *et al.*, 2016b). **b.** Simulated shift of a peak of E=3 keV due to a space charge cloud of N=1000 charges generated in $\Delta t = 10\,fs$, as a function of horizontal and vertical spot size. Black curves indicate the regions with constant spot area. From (Oloff *et al.*, 2016a).

$$N_{max} \sim 10^6 \text{ ph/pulse} \quad (4.2)$$

If present day FELs, which have extremely low repetition rates (10-100 Hz) are attenuated below the photon threshold of Eq. 4.2, their flux drops in the 10^8-10^7.

The way to perform TR-HAXPES with present day FEL facilities seems therefore narrow, as even though it has been demonstrated to be feasible, each experiment must cope with very challenging statistics. An increase in the repetition rate would represent a significant improvement in the usable photon flux below the space charge threshold.

Nonetheless, it also has a limit: as correlated electron crystals are non-renewable targets, a lengthy recovery time is necessary to recover the initial state (at least 1 μs) and avoid DC-heating, giving also a rep. rate limit of 1 MHz. A plot of the existing and upcoming sources normalized to the usable photon flux (i.e. photons/s limited by Eq. 4.2) is shown in Fig. 4.6.

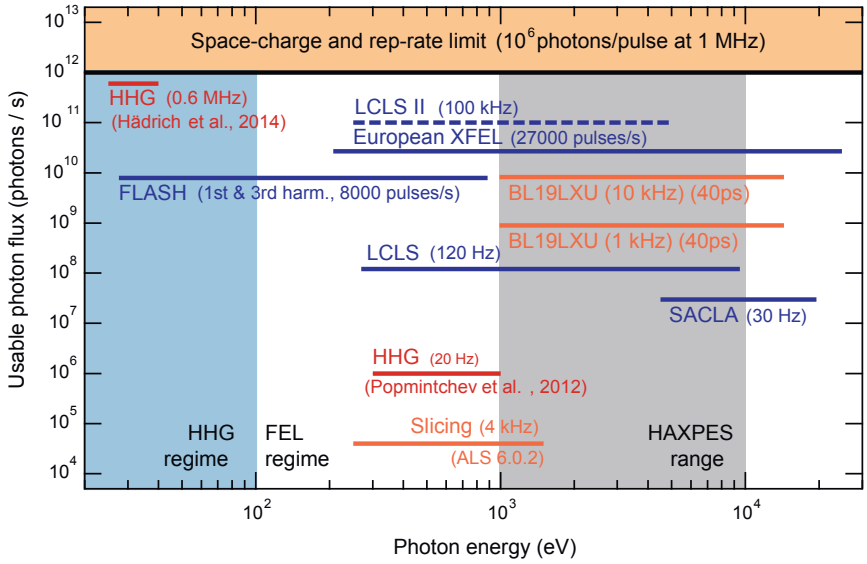

Figure 4.6: Comparison of the usable photon fluxes of several sources suitable for time-resolved photoelectron spectroscopy. Where the limit of 10^6 ph/pulse is not reached even for full power pulses, the maximum photon flux of the source is shown. For sources that can achieve the single pulse threshold, or higher, the photon flux is reported as 10^6 ph/pulse times the repetition rate. Not that the European XFEL, despite having on average, 27 kHz rep. rate, reaches peak values above the relaxation time threshold in bursts of 4.5 MHz. Note that the flux of BL19LXU, especially with the recent 10 kHz upgrade is, with relaxed time resolution, above most of the available FEL sources. Adapted from (Oloff *et al.*, 2016b).

The new generation of FELs under development in these years (X-FEL and LCLS II) seems promising, as both are aimed at higher repetition rates. However, the superconducting X-FEL timestructure seems also complicated to cope with: indeed, the pulses are delivered in 10 Hz bursts of 2700 pulses at 4.5 MHz rep rate. The short time between one pulse and the next within the burst (200 ns) may not allow for the complete recovery of the initial state. The pump laser would then have to be synchronized to 1 every 4-5 pulses, thus reducing the usable photon flux. The 100 kHz development of LCLS II seems to be the most promising for the realization of Time-Resolved Hard (and Soft) X-ray Photoelectron Spectroscopy as it is conceived at present[2].

[2]It is clearly possible that radical rethinking of photoemission experiments might lead to its realization

Alternative FEL schemes based on superconducting inverse Compton sources are being studied which could provide up to 10^8 photons per pulse at 1 MHz, regularly spaced, as it is being considered for the Milano EXPO source MARIX (Serafini *et al.*, 2016).

As we planned to study LSMO, that as will be discussed in 6 has a dynamic bottlenecked by its half metallic character, and thus slowed down to the hundreds of picoseconds, we could chose a different approach from Rossnagel and coworkers. We decided to relax the requirement of 100 fs time-resolution and instead employ 40 ps synchrotron pulses.

As can be seen in Fig. 4.6, this allowed us to operate with probably the highest statistics available for TR-HAXPES. We thus managed to measure with good statistics the Mn 2p peak despite its rather low cross section at the 8 keV energy that we used, and we could apply the robust understanding of the static features of this peak obtained in Part I to explore the dynamics of electronic and magnetic correlations in a prototypical TMO.

in high energy density regime, but, to the best of our knowledge, no such ideas have been put forward.

Chapter 5

Magnetization dynamics

Owning to the choice of LSMO, that is the manganite with the widest band, where the only dominant ordering parameter is the magnetization and the behaviour is the closest to a Heisenberg ferromagnet (Salamon and Jaime, 2001; Dagotto *et al.*, 2001; Krivoruchko, 2014), we were able to employ some of the methods developed within the framework of ultrafast magnetism. The investigation of the real-time response of the macroscopic magnetic momentum of itinerant 3d ferromagnets to ultrashort IR pumping has witnessed a significant effort from the scientific community due to its technological drive and intriguing physical questions. As a consequence, very effective ways of realizing magneto-optical experiments have been developed, and advanced methods to interpret data have been achieved.

In the next, we will thus review the most important concepts that are useful to understand the magnetic dynamics on the basis of particular features of the material band-structure.

5.1 Ultrafast magnetism

The field of ultrafast magnetism in metallic ferromagnets was literally triggered by the first observation of a sub-picosecond quench of the magneto-optical response of Ni thin films on an insulating substrate (Beaurepaire *et al.*, 1996), reported in Fig. 5.1 a. This observation met a great deal of interest as every previous attempt to address the dynamics of magnetic relaxation using short laser pulses had observed no effects up to the melting point of the samples (Agranat *et al.*, 1984; Vaterlaus *et al.*, 1990).

The only exception was a spin-resolved two-photon-photoemission experiment that could observe a 100 ± 80 ps relaxation in Gd (Vaterlaus *et al.*, 1991). In hindsight, after a wealth of high temporal resolution studies on Gd and the discovery of the complexity of its magnetic dynamics, this experiment represents a good example of how the choice of a material with a relatively slow dynamics allowed to pioneer its observation way ahead of time. It was indeed only in the late nineties that Ti:Sapphire regenerative amplifiers made intense, ultra-short infrared pulses easy to control and manipulate. The work by Vaterlaus and colleagues led to the first attempts of describing the microscopic mechanisms of demagnetization (Hübner and Bennemann, 1996) which elucidated with

remarkable clarity the mechanisms of interaction between the lattice and the spins, and which we will treasure in the next discussion.

As mentioned in the Introduction, an ultrafast optical control of magnetization offers an interesting way out of the magnetic trilemma in the realization of smaller, reliable and faster magnetic memory devices: the research field of ultrafast magnetism thus quickly flourished. Quite soon, the sudden demagnetization of Ni was confirmed by magnetic second harmonics generation (MSHG) experiments (Hohlfeld *et al.*, 1997), by two-photon photoemission spin-resolved analysis, shown in Fig. 5.1 b, (Scholl *et al.*, 1997), and by X-ray magnetic circular dichroism (XMCD) (Stamm *et al.*, 2007). The confirmation of the process by high energy spectroscopies is crucial, as the interpretation of optical data is extremely delicate on the shortest timescales, fact that was soon acknowledged by the community (Regensburger *et al.*, 2000; Koopmans *et al.*, 2000). This issue is discussed in Appendix A.

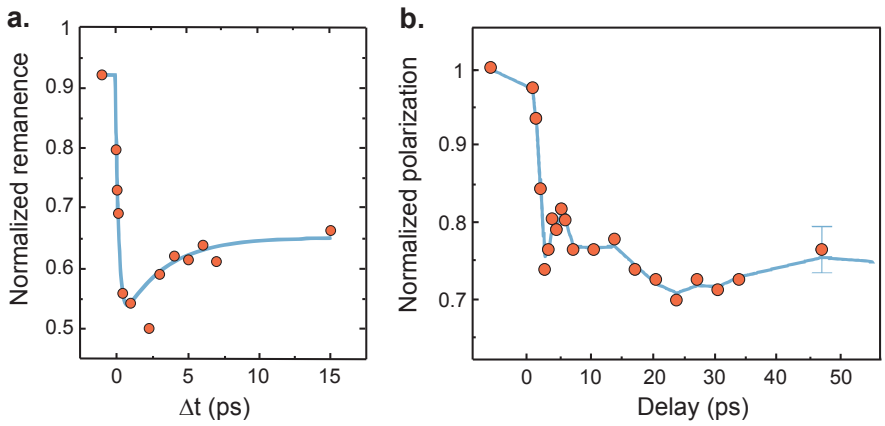

Figure 5.1: a. Time-Resolved longitudinal MOKE response of MgF_2-capped Ni(20nm) thin film upon excitation by 60 fs, 620 nm optical pulses at a fluence of 7mJ/cm². The signal is normalized to the signal measured in the absence of pump beam. The line is a guide to the eye. Adapted from (Beaurepaire *et al.*, 1996). b. Time-Resolved response of the polarization of the photoemitted electron of a Ni(1.2 nm)/Ag(100) thin film, excited with 170 fs, 400 nm optical pulses at few hundred μJ/cm². The signal is normalized to the signal measured in the absence of pump beam. The line is a guide to the eye. Adapted from (Scholl *et al.*, 1997).

Since then the study of ultrafast magnetism has been extended to numerous magnetic materials such as magnetic insulators, magnetic semiconductors, antiferromagnetic and ferrimagnetic systems (Kirilyuk *et al.*, 2010), observing several peculiar effects of great interest from the applicative point of view. A significant highlight, for example, is the observation of all-optical reversal of magnetization in the ferrimagnetic alloy GdFeCo (Stanciu *et al.*, 2007), and the recent achievement of switching in less than 20 ps in Cobalt-substituted yttrium iron garnet (YIG:Co), an optically transparent ferrimagnetic garnet (Stupakiewicz *et al.*, 2017).

Despite the number of interesting phenomena that have been observed, the mechanisms that produce ultrafast demagnetization are still object of intense discussion, mostly because ultrashort infrared excitation triggers a rich spectrum of processes influencing the spin dynamics. Together with the first observation of the ultrafast MOKE reduction, Beaurepaire et al. proposed a phenomenological model, called the three temperatures model (3TM), based on the separation of the excitations in three large classes. Each class corresponds to one of the degrees of freedom of the solid (Fig. 5.2 a): charge excitations (called more simply "electrons"), excitations of the lattice ("phonons"), and magnetic excitations ("spins").

This construction is rooted in the two temperature model (2TM) that had been successful in describing the optical reflectivity of metallic materials (Anisimov *et al.*, 1974). The extension to three temperatures was supported by an even prior demonstration of the separability of the specific heat of a magnet in electronic, phononic and magnetic (Hofmann *et al.*, 1956).

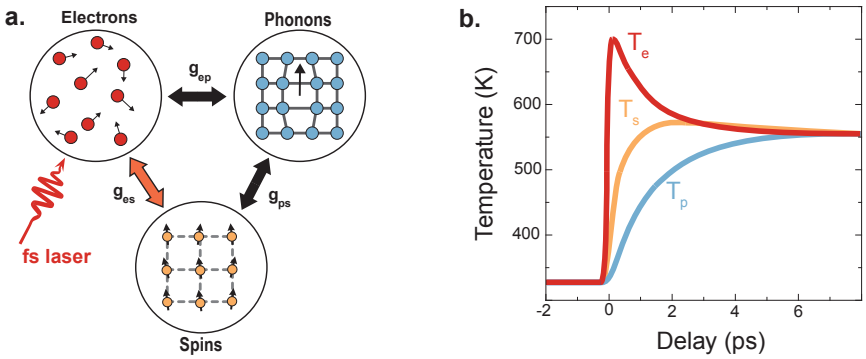

Figure 5.2: a. Division into three subsystems and flow of energy in the three temperatures model. Due to the ultrafast quenching of the magnetization, there must be an efficient channel to transfer energy albeit indirectly from the electronic system to the spins (marked in red). b. Graph of the expected dynamics of temperatures of the three systems. The electronic and spin temperatures follow each other quite closely at sub-ps timescales, while the lattice raises on a slower picosecond timescale. Adapted from (Schellekens, 2014).

These classes are considered as thermal reservoirs whose temperature (T_e,T_l,T_s) are assumed to be well defined. This is equivalent to instantaneous thermalization within each degree of freedom, and clearly is a strong assumption. Each reservoir has an heat capacity (C_e,C_l,C_s), and thus a system of coupled rate equations can be defined:

$$\begin{aligned} C_e(T_e)\dot{T}_e &= -G_{ep}(T_e - T_p) - G_{es}(T_e - T_s) + P(t) \\ C_p(T_p)\dot{T}_p &= -G_{ep}(T_p - T_e) - G_{ps}(T_p - T_s) \\ C_s(T_s)\dot{T}_s &= -G_{es}(T_s - T_e) - G_{ps}(T_s - T_p) \end{aligned} \tag{5.1}$$

Where G_{ep}, G_{es}, G_{ps} are phenomenological electron-phonon, electron-spin, phonon-spin interaction constants. $P(t)$ represents the time-dependent energy profile of the absorbed IR light from the laser, which includes the time profile of the optical pulse. By using realistic values of (C_e,C_l,C_s), combining transmission measurements to evaluate the electronic temperature and inverting the equilibrium M(T) curve to obtain T_s from the MOKE trace, it was possible to fit (G_{ep}, G_{es}, G_{ps}) and thus solve the system.

As shown in Fig. 5.2 b, this leads to a striking result: the temperature of the spin system seems to follow T_e much more closely than T_p. This results from a much smaller heat capacity of the spin system, but also from a very large value of G_{es}. This clearly indicates that there must be an efficient channel through which the kinetic excitations can be converted in magnetic ones.

The picture that emerges from the 3TM is therefore that the pump pulse excites the electrons producing vertical transitions, i.e. transferring negligible net angular and linear momentum to the electrons, but increasing their energy. This generates a strongly non-equilibrium distribution of electrons around the Fermi energy.

The electrons equilibrate instantly; clearly this is an approximation as it is known that distributions deviating from Fermi-Dirac persist for up to 400 fs (Rhie *et al.*, 2003), yet the fraction of non-thermal electrons reduces to very small percentages within few femtoseconds, thus the approximation is acceptable for schematic models (Fognini *et al.*, 2017).

The electronic system starts transferring energy to the spin system through an highly efficient channel: due to the small magnetic specific heat, the spin temperature closely follows the electronic one. As the two high temperature reservoirs start relaxing energy to the lattice, they cool down due to its large specific heat, while the lattice slowly warms up.

The magnetic system recovers part of the quench in such cooling, before the whole solid settles at a new meta-equilibrium temperature, that is then lowered on nanosecond timescales by cooling through the substrate.

The 3TM clearly has some shortcomings: primarily, it does not pinpoint a mechanism (or a class of mechanisms) giving rise to such ultrafast dynamics of the magnetic momentum; secondly, it does not pose specific constraints on the conservation of the total angular momentum, $\vec{J}$.

Several models have thus been proposed, mostly building up on three different frameworks:

1. the development of the rate equations of the 3TM, implementing a microscopic description of the relaxation channels

2. the modification of micromagnetic equations that describe the precessional dynamics, namely the Landau-Lifshitz-Gilbert equation, to include both transversal and longitudinal dynamics, in what is now called the Landau-Lifshitz-Bloch (LLB) equation (Garanin, 1997).

3. the inclusion of spin polarized transport effects (Battiato *et al.*, 2010; Fognini, 2014; Fognini *et al.*, 2017).

In the following discussion, we will concentrate on the models of the first type. Indeed, it has been demonstrated that the LLB treatment of the longitudinal relaxation dynamics pivots on the temperature evolution of a constant, whose dynamics can be mapped onto a type 1 approach (Atxitia and Chubykalo-Fesenko, 2011). The most important feature of the LLB approach is thus the accounting, in a single coherent description, of the diversity of the transversal and longitudinal dynamics: since we are interested only in the longitudinal relaxation (as we measured only one magnetization component at remanence), we will reduce the complexity by addressing the equivalent scalar problem of the longitudinal dynamics, in a type 1 model.

The approach of type 3 has emerged recently, and it is very interesting: upon strong optical pumping a large amount of electrons is excited in highly delocalized states, in particular in the elemental transition metals, where they move from 3d-like features to s- and p-like features in the bandstructure (Battiato *et al.*, 2010).

Obviously, the small linear momentum of an IR-photon cannot really punch electrons along the incidence direction: the picture is rather that a large, isotropic charge motion ensues but, while along the film plane such current does not give relevant effects[1], the broken symmetry of the vacuum/film and film/substrate interfaces do limit the expanding charge wave.

Large gap insulating substrates, or the interface with vacuum, supposedly act as reflecting surfaces, and give no net contribution to the magnetization dynamics. The interface with metallic or semiconducting under-layers, instead, gives rise to pulsed injection of carriers from the film. As the electrons and holes have different mean free paths in the exchange-split bands of the magnetic film, the carriers are spin-polarized and thus transfer a net magnetic momentum into the substrate.

The character of the current evolves with time passing from ballistic to diffusive: this mechanism is thus defined *super-diffusive spin currents* (SSC). If the substrate is metallic, there is no net charge flow, as the unpolarized carriers from the substrate compensate the ones injected in the film. Differently, in a semiconducting substrate, a complex dynamic of transient electric fields ensues, leading to a separation of the timescales of electron and hole propagation (Battiato and Held, 2016).

Other promising models have been proposed that consider diffusive spin-Seebeck currents ensuing from unbalances in the position of spin up and down chemical potential across the film thickness (Fognini *et al.*, 2017).

SSC have been proven to be effectively present in heterostructures (Melnikov *et al.*, 2011), and even in thick films of the same material where the spin-polarized carriers travel in unexcited regions of the material (Razdolski *et al.*, 2017). Despite in some cases considering only SSC is sufficient to account for the whole change of the magnetization

[1]Indeed, in an homogeneous film plane there are no significant variations of the electronic density of states, and therefore no net effects on the magnetization. Furthermore the spotsize of the pump and probe beam usually average onto areas too large to observe femtosecond transport effects.

signal, they must be a concurring mechanism to localized phenomena, as the magnetization quenching is also observed on insulating substrates and insulating magnets. In our case, our samples have a large extinction length at the pump-wavelength, and are grown on large band-gap insulators (STO or LSAT). They can thus be considered uniformly excited and in the condition in which SSC effects are minimized. We will thus concentrate on microscopic local mechanisms.

5.1.1 Microscopic Mechanisms

Most of the models proposed recently to describe the longitudinal dynamics of the magnetization vector builds are focused on a specific process, in the effort of addressing the dominant effect that drives the process, although it is very likely that many of them are present at once. Direct laser-interaction is debated, in particular considering laser induced spin-flips (Zhang *et al.*, 2009), or relativistic quantum electrodynamical processes (Bigot *et al.*, 2009), although being limited to the time-duration of the pulse (few tens of femtoseconds), they are hardly thought to be the mechanisms defining the timescale of the relaxation, which unfolds in hundreds of femtoseconds. The most interesting localized mechanism is Elliott-Yafet spin-flip scattering. Both electron-electron (Krauß *et al.*, 2009) or electron-phonon (Koopmans *et al.*, 2010) spin flip scattering mechanisms have been considered.

A simple consideration (Koopmans, 2007) suggests that the most favourable sink for the angular momentum is the lattice. The magnetic momentum is given by:

$$\vec{\mu} = \mu_B(\vec{L_e} + g\vec{S_e}) \tag{5.2}$$

where $g \approx 2$ is the gyromagnetic ratio of the electron. Including the exchange of angular momentum with the light photons, the total angular momentum of the system is:

$$\vec{J} = \vec{L_e} + \vec{S_e} + \vec{L_{ph}} + \vec{L_{IR}} \tag{5.3}$$

which must be conserved for the isolated system. Thus, if $\vec{\mu}$ is reduced, a redistribution of angular momentum in the right-hand side of Eq. 5.3. Let us consider a 3d transition metal in which, due to the quenching of the orbital momentum (Ashcroft and Mermin, 1976), $\vec{\mu} \approx \mu_B g\vec{S_e}$. Let us assume that, due to the laser excitation, the quenched spin angular momentum is transferred to $\vec{L_e}$ and that $\vec{L_{ph}}$ and $\vec{L_{IR}}$ do not participate. Then, because $g \approx 2$, the maximum reduction of the magnetic momentum would be of 50%, while the experimental evidence shows much larger demagnetizations. This was further supported by XMCD experiments (Stamm *et al.*, 2007).

A mechanism that describes a spin-flip interaction with transfer of angular momentum to the lattice is the Elliot-Yafet phonon assisted scattering. Indeed, in a solid, and in presence of spin orbit coupling (SOC), the Bloch states of the electron do not have a specific spin character, but are rather a linear combination of the type:

$$\psi_{\mathbf{k},\uparrow} = [a_{\mathbf{k}}(\mathbf{r})|\uparrow\rangle + b_{\mathbf{k}}(\mathbf{r})|\downarrow\rangle]e^{i\mathbf{k}\cdot\mathbf{r}} \tag{5.4}$$

It is this spin mixing that, when the electron scatters with an external potential allows for spin-flip scattering even if the external potential is spin conserving like the Coulomb interaction. In the Elliott-Yafet spin-flip scattering, the flipping probability a_{sf} is related to a parameter called *spin mixing*, defined as:

$$a_sf \propto \langle b^2 \rangle = avg[min(\langle \psi_k | \uparrow \rangle \langle \uparrow | \psi_k \rangle, \langle \psi_k | \downarrow \rangle \langle \downarrow | \psi_k \rangle)] \tag{5·5}$$

the average $avg[]$ is over the states involved in the scattering process around the Fermi level. When $\langle b^2 \rangle = 0$ the states are pure spin states, while when $\langle b^2 \rangle = 0.5$, they are completely mixed. The proportionality with a_{sf} is through a material-dependent constant.

Based on this concept, Koopmans and coworkers developed a model called the microscopic three temperatures model (M3TM) (Koopmans *et al.*, 2010; Schellekens, 2014). The scaffold of the model consists of the following steps:

1. Hamiltonians for the energy of the electronic, phononic and magnetic system are defined.
2. Hamiltonians for the interaction terms are defined. In this model, only electron-phonon scattering is assumed to be relevant. Therefore, there is a term describing spin-conserving scattering (proportional to $\sqrt{1 - a_{sf}}$), and a term for spin-flip scattering (proportional to $\sqrt{a_{sf}}$).
3. The transition rates are calculated using the Fermi golden rule
4. The energy transfer rates can thus be obtained, and a system of Boltzmann equations can be derived.

The interesting point of Koopman's model is that it builds a framework in which the exchanges of energy between the degrees of freedom are quantized, and angular momentum conservation is accounted for.

In the first application of the model, very strong assumptions were made in order to obtain an easily manageable set of equations. The density of states is considered to be constant and not modified by the large charge excitation. The spin system is modelled as a Weiss $S = 1/2$ localized spin system, and its specific heat is neglected. This is valid in a limited set of temperatures, i.e. far away from the low temperature large contribution of spin-wave effects, and the high temperature divergence close to T_C. The phononic system is modelled as a Debye set of oscillators, whose specific heat is assumed to be constant, which corresponds to the assumption of $T_p \gg T_D$ (the Debye temperature). This leads to a set of equations:

$$\begin{aligned} \gamma_e T_e \dot{T}_e &= -G_{ep}(T_e - T_p) + P(t) \\ C_p \dot{T}_p &= -G_{ep}(T_p - T_e) \\ \dot{m} &= R \frac{T_p}{T_C} m \left[1 - m \coth\left(m \frac{T_C}{T_e} \right) \right] \end{aligned} \tag{5.6}$$

The 2TM is thus decoupled from the magnetic evolution and only the normalized magnetization m is connected to both T_e and T_p. The magnetization dynamics is driven by a single free parameter: R, which contains a dependence from a_{sf}.

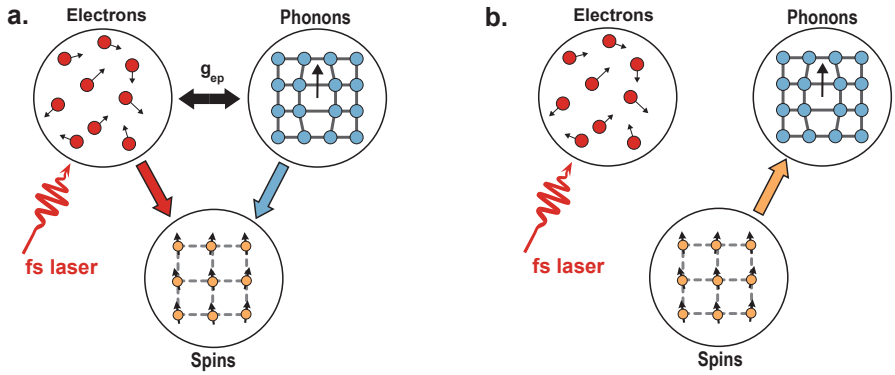

Figure 5.3: a. Flow of energy in the microscopic three temperature model. The assumption of negligible spin specific heat implies that only the temperatures of the electrons and phonons influence the spin temperature, and not the reverse. b. Transfer of angular momentum in the M3TM, in which it is quenched in the lattice. Adapted from (Schellekens, 2014).

Despite the strong assumptions, this model shows an interesting result: by using reasonable values for a_{sf}, the model allows for ultrafast dynamics, i.e. subpicosecond demagnetization in Ni and Co. Such a result is not obvious, as processes involving the excitation of lattice phonons have for long time been considered too slow to describe ultrafast demagnetization. The schematic model proposed by Koopmans also allowed to describe the two-step magnetization dynamics of Gd, although with more difficulty. As already mentioned, it was connected with the models used for the longitudinal relaxation dynamics in the LLB, and it was demonstrated to be consistent with the picture of prompt excitation of a magnon with orbital momentum quenching in the lattice (Carpene *et al.*, 2008; Piovera, 2014).

The scaffold of the model, however, is a structure open to further development, as it is demonstrated by its use in addressing the question of the nature of the excitations of the magnetic system. Indeed, the finite temperature characteristics can either be interpreted as a reduction of the magnetic momentum and thus of the exchange splitting of the bands (Stoner-like excitations), or as precession of localized spins which reduces their projection along the magnetization direction, while it averages out along transversal directions due to incoherence (Heisenberg-like excitations) (Schellekens, 2014).

Despite the fact that Stoner-like excitations are the most clearly connected with the scattering picture, plugging purely Stoner or purely Heisenberg excitations in the M3TM gives clearly more significant results for the Heisenberg case (Schellekens and Koopmans, 2013), mainly owing to the better description of the Curie temperature and M(T) curve. An implementation of the combined effects of the two mechanisms, always within the

M3TM framework, gave quite promising results, hinting at a feedback effect between magnetization reduction and band population imbalance that seems to further accelerate the process (Mueller *et al.*, 2013).

Very recently the power of spin-resolved photoemission has been applied to the issue, and hints of Stoner-like behaviour have been observed in the dynamics of the surface state of Gd (Andres *et al.*, 2015), while in Co the best description of the spectra was obtained purely within a Heisenberg picture (Eich *et al.*, 2017), although EUV light scattering seemed to suggest that Stoner excitations are present also in this material case (Turgut *et al.*, 2016).

5.2 Half-metallic ferromagnets

In the complex and mutating panorama of the efforts to describe the mechanisms at the basis of ultrafast demagnetization, there is an experiment that gives a solid piece of information on the electronic origin of this process: the study of the dynamics of half-metallic materials.

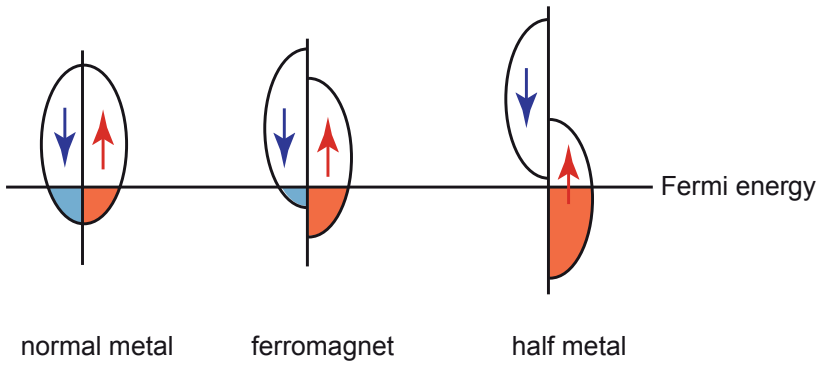

Figure 5.4: Cartoon picture of different classes of metal. In a simple metal the exchange interaction is too weak or absent, and the majority and minority bands cross the Fermi energy with identical DOS. In a ferromagnetic metal the exchange split bands cross the Fermi energy at different DOS, generating a net, unbalanced magnetic momentum. In an half-metal, one spin sub-band has a gap at the Fermi energy.

Half-metallic materials, first proposed as a new class of magnetic metals by deGroot and coworkers (de Groot *et al.*, 1983) are crystals in which the spin-resolved density of states (DOS) has a gap at the Fermi energy for only one sub-band. This means that the Fermi surface is formed completely of states with the same spin (Fig. 5.4). Since their discovery, these materials have received significant attention, as they give the possibility of transporting completely spin polarized currents, which is of extreme interest for spintronic applications. Clearly, such a peculiar feature in the electronic structure

gives to half-metallic materials a rich spectrum of subtle characteristics, whose discussion is anyway beyond the scope of this thesis and for which we refer to the in-depth analysis of Katsnelson and colleagues (Katsnelson *et al.*, 2008).

Half-metallicity is a property that appears in several classes of materials, of which the most numerous are Heusler alloys (both in $C1_b$ and $L2_1$ structures) and transition metal oxides, generally in the form of perovskites. The half-metals have been classified on the basis of the characteristics of the gap and the electronic mobility (Coey and Sanvito, 2004). Such a classification, however, must be taken with extreme caution as both the experimental and theoretical determination of half-metallicity is a rather difficult endeavour.

An example is, indeed, the discussion around the half-metallic character of LSMO. As discussed in Chap.2, considering double-exchange arguments, half-metallicity is expected. Theoretical description based on density functional theory calculations, however, with the use of the local density approximation, or the generalized gradient approximation, seemed to indicate the presence of minority states crossing the Fermi energy.

In spite of the total perfect spin polarization obtained in spin-resolved photoelectron spectroscopy experiments (Park *et al.*, 1998a), LSMO was classified as a "transport half-metal", in which minority states are present at the Fermi energy, but do not contribute to transport (Coey and Sanvito, 2004). Data from Andreev reflection and Meserwey-Tedorow technique were considered to be supporting this hypothesis (Nadgorny, 2007). However, it is known that DFT+LSDA tends to underestimate the gap in insulators.

Successive theoretical descriptions employing DMFT+GW (Kino *et al.*, 2003) or DMFT (Hariki *et al.*, 2016) have demonstrated an extremely wide (> 1 eV) band-gap both below and above the Fermi energy. On the experimental side, the difficulties in the realization of contact, interfaces and high purity films might have played a role, and indeed, recent measurements of the tunneling magnetoresistance in excess of 1800% (Bowen *et al.*, 2003) have brought Katsnelson and coworkers to ascribe LSMO to the class of full gap half-metals, the same as CrO_2 (Katsnelson *et al.*, 2008).

Our samples seem to confirm this, they yield record breaking TMR of up to 1900% (Werner *et al.*, 2011). In a recent experiment on the VESPA spin-ARPES instrument (Bigi *et al.*, 2017), we have observed spin resolved spectra analogous to the ones obtained by Park et al Park *et al.* (1998a), with a substantially fully spin polarized Fermi edge (Bigi *et al.*, 2018) and a clean (in-situ grown) well-ordered surface. As it will be discussed next, also the time resolved MOKE experiments support this view.

5.2.1 Dynamics of half-metallic ferromagnets

For what concerns the magnetic dynamics, the half-metals with a minority gap represent a bottlenecked system. Indeed, the absence of final states do not allow for low-energy excitations with spin-flip. In other words, one magnon excitations cannot be directly triggered. For ultrafast demagnetization experiments, then, the direct transfer of energy between the optically excited electrons and the spins is blocked, as shown in Fig. 5.5 a.

Due to the insulation of the spin system, the electronic temperature raise is first

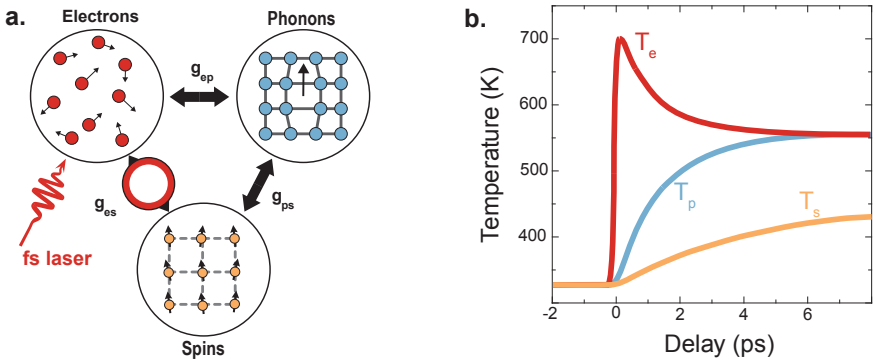

Figure 5.5: a. Flow of energy in a wide gap half-metallic material. Spin-flip excitations are suppressed, and thus the fast thermalization between spins and electrons. b. Dynamics of temperatures in the 3TM for a half-metallic system. The temperature of the magnetic system follows the increase of temperature of both electrons and lattice with a long delay, so that the solid can be considered at equilibrium but for the magnetic system. Adapted from (Müller *et al.*, 2009).

quenched in the lattice, and only when the crystal temperature starts to increase the spin system is warmed up slowly due to spin-lattice interaction as shown in Fig. 5.5 b.

It is thus possible to create a link between the duration of the demagnetization (τ_m) and the polarization (P) of the carriers at the Fermi energy: this has been realized in a series of through studies (Müller *et al.*, 2009; Mann *et al.*, 2012) involving a large number of half-metals of different classes and showing consistent results, depicted in Fig. 5.6.

In this diagram, the demagnetization time is plotted versus the estimated polarization of the carriers at the Fermi energy, which determines the availability of minority states for spin-flip scattering. It is clear that, as the polarization increases, the demagnetization time steeply rises, skipping more than three orders of magnitude from the classic ferromagnet Ni to the perfect half-metals CrO_2 and LSMO. In this picture, the Elliott-Yafet spin-flip scattering mechanisms provide a fast channel of demagnetization that is increasingly "choked" by the reducing minority DOS, and the dynamics is more and more defined by the spin-lattice interaction. In the region of the plane above the horizontal orange line, τ_m is so long that the spin and the electronic system can be considered isolated and the spin-flip scattering neglected. In the region below it a competition between the two mechanisms is present. The vertical orange line identifies the $P = 0.9$ value: at $P > 0.9$ no materials with intrinsic τ_m below the picosecond have been found. A wide set of narrow gap half-metals or pseudo-gap materials (which only have an extremely small number of minority states), are present in an intermediate region.

5.2.2 Microscopic mechanisms for demagnetization in half-metals

It is possible to give a schematic treatment of the hand-waving argument given in the previous section by going through the Fermi golden rule framework suggested by Koopmans,

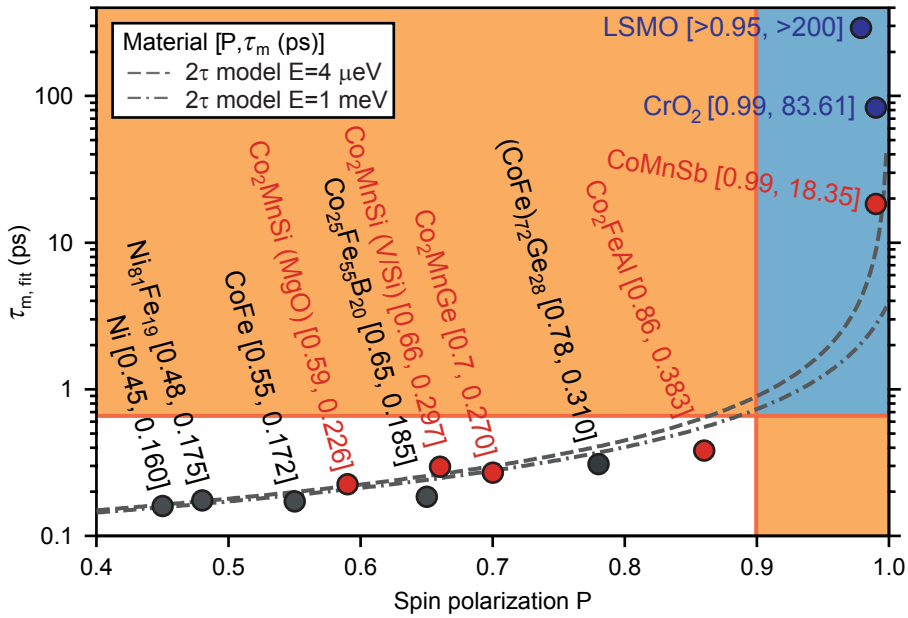

Figure 5.6: Polarization of the carriers at the Fermi energy versus demagnetization time in several ferromagnetic and half-metallic systems. Materials marked in red are Heusler compounds, the ones in gray are other magnetic alloys. The materials marked in blue are magnetic half-metallic oxides. In the white sector a competition between Eliott-Yafet spin-flip scattering and spin-lattice interaction defines the total τ_m. In the light blue sector the contribution of spin-flip scattering is negligible. The dashed and dot dashed curves are calculated with the microscopic model describe in the text for two different magnetic anisotropy energies. Adapted from (Mann *et al.*, 2012).

and following Müller Müller *et al.* (2009). Indeed, in a highly spin-polarized material the spin polarization can be expressed as:

$$P_n(E_F) = \frac{n_e^{\uparrow}(E_F) - n_e^{\downarrow}(E_F)}{n_e^{\uparrow}(E_F) + n_e^{\downarrow}(E_F)} \approx 1 - 2\frac{n_e^{\downarrow}(E_F)}{n_e^{\uparrow}(E_F)} \tag{5.7}$$

Since $n_e^{\downarrow}(E_F)$ is very small. If we assume that the density of states is constant in the neighbourhood of E_F in which the dynamics takes place, then we can write that the density of empty states for scattering is given by:

$$n_h^{\downarrow}(E_F) = \frac{n_e^{\uparrow}(E_F)}{2}(1 - P_n) \tag{5.8}$$

By considering the Fermi golden rule in the most schematic way, and neglecting the spin specific heat, the relaxation time due to the spin-flip scattering enters the rate equation:

$$\dot{\Delta N} = W_{\uparrow\downarrow} - W_{\downarrow\uparrow} = -\frac{\Delta N - N}{\tau_{es}} \tag{5.9}$$

where $\Delta N = N_e^{\uparrow}(E_F,t) - N_e^{\downarrow}(E_F,t)$ is the deviation from the equilibrium number of up and down electrons at the Fermi energy. Again in a schematic approximation it is possible to write:

$$W_{\uparrow\downarrow} \propto n_e^{\uparrow}(E_F) b^2 n_h^{\downarrow}(E_F) = \frac{n_e^{\uparrow}(E_F)^2}{2}(1-P_n)b^2 \tag{5.10}$$

where b^2 is the spin-mixing parameter averaged over the Fermi surface of eq. 5.5. By substituting into eq. 5.9, one can infer the relationship:

$$\tau_{es} = \frac{C_1}{1-P_n} \tag{5.11}$$

where C_1 is a constant accounting for all the constants involved in the scattering process.

On the other hand, the absence of final states for spin-flip scattering limits also the interaction of the lattice with the spins: the time reversed mechanism of the Elliot-Yafet scattering, i.e. a phonon-electron scattering that produces spin flip (or analogously, magnon excitation due to a phonon), is not possible. The only mechanism that allows the distribution of energy to the spin system is the "anisotropy fluctuation" proposed by Hübner et al. (Hübner and Bennemann, 1996) for Gd and confirmed by experiment on various half-metallic oxides (Ogasawara *et al.*, 2005). In this picture, in presence of magneto-crystalline anisotropy, the fluctuation of the lattice parameters due to phonons couple to the spins. An analysis, with the same scheme of the one developed here, but carried out with more formal rigour gives:

$$\tau_{sl} = \frac{1}{A_{\Theta_D}(T)|E_{\boxtimes}|^2} \tag{5.12}$$

Where $A_{\Theta_D}(T)$ is a parameter dependent on the initial temperature that is connected with the material Debye temperature (arising from the occupation of initial and final states in the Debye model), while $E_{\boxtimes}$ is the magnetic anisotropy energy. This energy is in the meV to μeV (per atom) range, that correspond to characteristic times in the 10 ps to ns range.

In the region where a competition between the two effects is present, one has to include both charateristic times, and sum them reciprocally. The curves in Fig. 5.6 are obtained by plotting:

$$\tau_m(P) = \frac{C_1}{C_1 A_{\Theta_D}(T)|E_{\boxtimes}|^2 + 1 - P} \tag{5.13}$$

at $C_1 = 0.1$ ps and $\tau_{sl} = 1$ ns (dashed curve, $E_{\boxtimes} = 4$ μeV/atom) or $\tau_{sl} = 3$ ps (dash-dotted curve, $E_{\boxtimes} = 1$ meV/atom).

It is thus clear that in the case of wide gap half-metallic materials (occupying the light blue region of Fig. 5.6), the magnetic dynamics it thus dominated by τ_{sl}, and slowed down to tens, or hundreds of picoseconds timescales. The evaluation of the contribution of τ_{es} is very sensitive to the polarization of the carriers at the Fermi energy, and has indeed been proposed as a method to evaluate half-metallicity (Müller *et al.*, 2009). However, in smaller band gap half-metals (such as some of the Heusler alloys) the temperature effects can be significant and need to be accounted. Recently a correction to the model presented

here has been developed (Mann *et al.*, 2012) which introduces a temperature dependent term that reduces the polarization.

Clearly, future developments of the modelling of ultrafast demagnatization will likely account more precisely for the details of the bandstructure. This will describe in a less abstract way the response of the reservoirs, thus encompassing naturally the half-metallic blocking effect. Hopefully, also a way to factor in the balance between local and non-local effects will allow to gain full insight in the faceted character of magnetic dynamics.

Given the half-metallic nature of LSMO, and the fact that it is characterized by a strong coupling between electronic delocalization and magnetic ordering, we decided to explore the dynamics of the appearance of electronic correlation as the magnetic order collapsed. As discussed here, the microscopic processes at the basis of ultrafast demagnetization in LSMO act on timescales suitable to observe this dynamics in a synchrotron-based experiment, with relaxed time resolution but reasonably high flux. Before performing the dynamical HAXPES experiment, however, we carried out a full MOKE characterization, in order to have a compass for the interpretation of the HAXPES data.

Chapter 6

Magneto-optical Kerr Effect experiments

> Simple it may be, but not ineffectual;
> rude, but not crude.
>
> John Kerr, 1898

Magneto-optical Kerr effect was discovered by Reverend John Kerr in 1877 in a series of experiments measuring the polarization of light reflected off the surface of a polished electromagnet pole (Qiu and Bader, 1999, and references therein), and earned him the Royal Medal in 1898. The discovery represented a significant breakthrough because it allowed to measure non-transparent media, that constitute a large class of magnetic materials.

The rotation of the polarization direction of optical light in presence of a magnetic field, observed by Faraday thirty years before, relied on refraction of light. Kerr discoveries provided a very effective, non-destructive tool to measure the average magnetization of magnetic surfaces.

The classical description came, as a derivation of the theory of the linear response, by hand of Voigt, building directly on Maxwell's explanation of the Faraday effect. A microscopic, quantum-mechanical description was instead developed by Argyres, that pinned down the interaction at its origin to specific transitions between exchange and spin-orbit split bands. Nowadays MOKE is a tool that has assumed countless declinations in different techniques.

Nonetheless, just as in its creators historical words, any time it is applied, great care must be taken to subtly interpret the results. For the sake of the discussion fluidity, however, we defer an in-depth analysis of the quantitative characteristics of the MOKE signal to Appendix A. There, we address the classical optics treatment of the Magneto-Optical Faraday and Kerr effect and give a qualitative microscopic description of the involved mechanisms. Subsequently, we derive the dependence of the dynamical optical signal, with particular attention to all the parameters that can induce non-magnetic dynamical effects and thus challenge the interpretation of data. In the next chapter, instead, we use these notions in the study of the dynamical evolution of the magnetization of LSMO after intense optical pumping.

6.1 Instrumentation

The set-up employed in the Kerr experiments was part of the laser laboratories of Regensburg university (Lehrstrul C. H. Back), in its last upgrade carried out by Dr. Stefan Günther (Günther, 2015), featuring an in-vacuum sample environment that allowed to study the sample in a wide temperature range (100-500 K). It is schematised in Fig. 6.1: in the following discussion the bold letter labelling to indicate the components is always intended as referred to this picture.

The pump laser diode (**a**) is a Continuous Wave Diode Pumped Solid State Millennia (Spectra Physics) delivering 15 W at 532 nm, with extremely low optical noise. It pumps the oscillator (**b**) and the regenerative amplifier (**d**) (sketched as a green beam). The oscillator is a Coherent MIRA 900 based on mode-locking in a Titanium Sapphire (Ti:Al_2O_3) cavity, that produces < 200 fs pulses at 76 MHz.

In the whole femtosecond laser system, an optimum between the bandwidth of the pulse and its time duration must be achieved, as the Fourier transform limit (or equivalently the time-energy indeterminacy for coherent states of photons) constrains the simultaneous minimization of these two values. From the experimental point of view, a narrow bandwidth is desirable both to avoid excessive chirping of the pulse through the optics, and to excite specific transitions both when pumping and when probing the system. On the other hand, a larger bandwidth allows for shorter pulses to be generated. In an ideal system (transform-limited), the bandwidth is kept at the minimum value that allows to achieve the desired pulse durations. In the case of the present set-up, the optimum is found at about 30 nm around the 800 nm wavelength, allowing for pulses of < 50 fs duration.

The oscillator delivers pulses of hundreds of femtoseconds duration to the regenerative amplifier REGA 9050. Before entering the amplifier, the pulse is chirped to a duration of 20 ps in a stretcher stage (**c**) in order to reduce the peak power on the optics. In the regenerative amplifier the pulse is injected by a Pockels cell into a second Ti:Al_2O_3 cavity where it runs twenty round trips before being ejected by a second Pockels cell. The time spent in the cavity by each pulse reduces the repetition rate to a maximum of 300 kHz, but it is tunable down to 10 kHz. The maximum pulse energy is about 6 μJ at 250 kHz.

After exiting the amplifier, the chirp of the pulse is then compensated in a compressing stage (**e**), reaching the minimum pulse duration of 55 fs. Here it can be monitored with an autocorrelator (**f**), that is feeded a small percentage of the beam (2%). After the compression, refractive optics are avoided as much as possible and focussing is mainly done with parabolic mirrors.

The beam is then sent in a BBO crystal (0.1 mm thick) allowing to produce the second harmonic of the beam at 400 nm that is used as a probe. The fundamental, that is used as a pump, is separated from the probe by an harmonic separator (**h**) and sent through a computer controlled delay line (**i**). The length of the optical path can be tuned with micrometer precision, controlling the delay between the pump and the probe with a resolution of about 1 fs. The pump beam is then modulated at few kHz by an optical

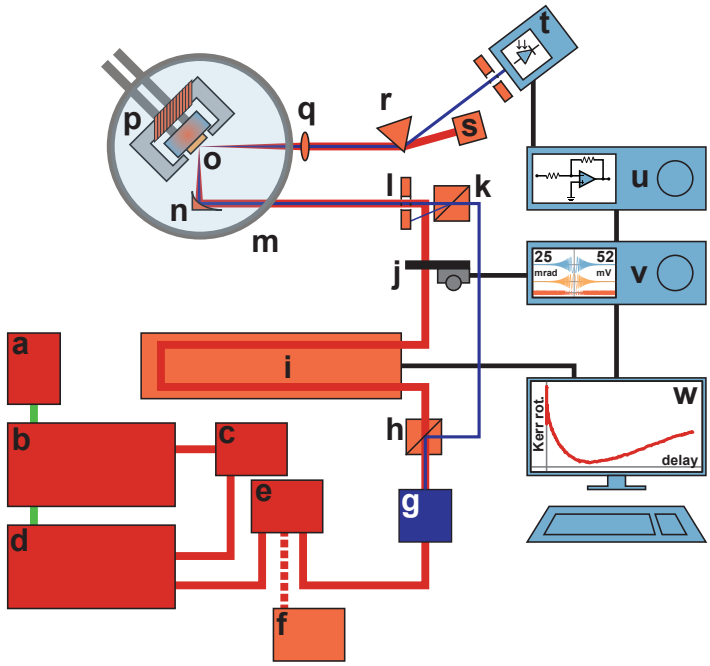

Figure 6.1: Schematic representation of the experimental set-up for the MOKE experiments. High-repetition rate, 70 fs pulses of 6 μJ at 800 nm wavelength are generated by the laser system (dark red boxes **a-e**). Then, the second harmonic is generated (dark blue box **g**), producing 70 fs pulses at 400 nm wavelength. A set of passive optics (orange and black boxes **h-l**) separate the fundamental (pump) and second harmonic (probe) beams, delay and modulate the pump and polarise the probe before recombining and delivering them to the vacuum chamber (grey ring **m**). In vacuum, a parabolic mirror (**n**) focuses the beam on the sample (**o**), whose magnetic state and initial temperature are regulated by the sample environment (**p**). A second set of optics (orange volumes **q-s**) collimates and separate the reflected beams, dumping the pump and directing the probe to the detection system (**t**). The signal is then handled by the detection chain (light-blue boxes **u-v**), and delivered to the control computer (**w**).

chopper (**j**), reflected on the edge of a plane mirror and sent into the vacuum chamber (**m**).

On the other hand, the probe beam is sent through a polariser. In order to avoid excessive chirping of the pulse, polarization is realized by a thin MgF crystal (**k**): the extraordinary beam propagates along the incident beam direction, while the faint[1] ordinary beam is blocked by an aperture (**l**). This yields a very high polarization ratio in the *s* direction (higher than 1:100000), while keeping the probe beam temporal broadening

[1]Second harmonic generation is a polarization dependent process, so the probe beam is already highly polarized in the *s* direction.

within 70 fs, that is taken as the ultimate time resolution of the experiment. The probe then passes close to the edge of the mirror on which the pump pulse is reflected, and the two beams, almost collinear, enter the vacuum chamber (**m**) through an UV grade quartz window.

The vacuum chamber is a steel cylinder with a top lid made of glass with a viton sealing. The base pressure, when pumped by an oil pump and two 70 l/s turbomolecular pumps is in the 10^{-8} mbar range. The vacuum is needed to cryogenically cool the sample without the risk of ice or dew formation and to heat it up without the risk of excessive oxidation. The two beams impinge on a 90ř off-axis parabolic mirror (**n**), that focusses them on the sample surface (**o**).

The sample temperature and magnetic state are controlled by the sample environment system (**p**). The temperature can be increased by direct heating through an high power Tungsten filament and reduced by an open cycle cryostat. A thermocouple on the sample side of the first copper block monitors the temperature and allows for stabilization loops by controlling the current in the filament. The magnetization is flipped by a computer-controlled electromagnet.

At this point the pulse duration doesn't need to be minimized any more and refractive optics can be used again. The reflected beams exit the chamber and are collimated by a lens (**q**). A prism (**r**) separates the pump from the probe. The pump is dumped (**s**), while the probe crosses an aperture and enters the detection system (**t**). In the case of the crossed polarisers configuration, polarimetry is performed by using a rotatable Glan-Thomson polariser and a simple diode. In the case of a balanced detection scheme, a Wollaston polariser with two diodes is employed. The on-board electronics of the diodes directly performs subtraction or summation (selectable through a switch) of the two voltage pulses.

The voltage pulse produced by the detection system is then preamplified (**u**), producing a -1 to 1 volt signal, that is then sent to a lock-in amplifier (**v**) synchronized with the chopper modulator (**j**). The modulation of the pump is used to exploit the huge improvement in sensitivity gained by the lock-in technique on the measurement of the pump effects. The signal is then sent to the computer (**w**).

The measurements are performed at remanence flipping the field at every delay. This inversion is a necessary part of the measurement routine, because, as discussed in Sect. A.1, Eq. A.1.6 in the crossed polarisers detection scheme the Kerr angle dynamics is summed to the diagonal reflectivity dynamics. In the balanced detection technique it is not strictly necessary, but it avoids the effects on the signal of imperfect balancing of the Wollaston angle. The I/O program thus displays during the measurement the point-by-point difference between the signals in the two magnetization directions, giving the demagnetization trace.

The recorded curve gives only $\Delta\vartheta(t)$. In order to normalize it, it is necessary to evaluate ϑ_0, the unperturbed Kerr angle. Clearly, in this case it is advantageous to transfer the sensitivity of the lock-in on the probe. Thus, the chopper (**j**) is rotated to cut the probe beam, the pump is dumped before the sample, and hysteresis are recorded. The

amplitude of the hysteresis at remanence is ϑ_0. If DC-heating is suspected, hysteresis are also recorded with the pump on the sample but at small negative delays and confronted. Clearly this procedure requires careful tracking of the preamplification factors and the lock-in scaling in order to have the delay trace and the normalization factor on the same scale. Measurement of the Kerr ellipticity are realized in an analogous way but placing a $\lambda/4$ waveplate before the detection system (**t**).

6.2 Results

Advantaging from the possibilities given by the set-up described above, we performed a study of the magnetization dynamics of LSMO samples, trying to cover the widest achievable set of parameters. We probed the dynamics at different initial temperatures, spanning a 150-320 K range, very close to the Curie temperature. We aimed at crossing the phase transition. We also measured at different pump fluences, spanning an order of magnitude (2-0.2 mJ/cm²)in the excitation density.

The experiment involved two of the samples (LSMO/STO and LSMO/LSAT) that were employed for the experiments of Part I, we thus refer, for the characterization, to Sect. 3.1.3. The two samples are in a different strain state, 1% tensile for LSMO/STO and strain relaxed for LSMO/LSAT.

6.2.1 Reflectivity

In a first batch of experiments we worked in the crossed polarisers configuration (See A). The probe is polarized in the *s* direction and the analyser polarization is oriented about 1° off the *p* direction. The pump was modulated at 800 Hz. As discussed in Sect. A.0.1, this detection scheme requires, in order to disentangle the magnetization and reflectivity dynamics, that two curves are recorded with opposite magnetization.

A typical result is shown in Fig. 6.2 **a**. The two curves are basically the raw data of a measurement at 150 K, with maximum fluence (2 mJ/cm²) of the LSMO/STO film. It is possible to distinguish the two curves obtained for the opposite magnetizations. The large difference between the two arising from the odd term upon magnetization reversal is superimposed to a significant dynamical variation of both signals. By summing them, the odd term is cancelled and the reflectivity curve is obtained (Fig. 6.2 **b**).

The reflectivity curves yield a great deal of information on the interaction of the electrons with the lattice, on the lattice itself and, in LSMO, in which the transport is strongly coupled with magnetism, indirectly on magnetic effects. It is thus worth to inspect the curves more closely.

Immediately after the arrival of the pulse, the reflectivity shows a sharp raise that reaches a maximum within 200 fs, and rapidly decays, equilibrating within 1.2 ps to an higher reflectivity value. Fig. 6.2 **c** shows a zoomed-in detail of the peak edge. This spike is originated directly by the large optical excitation of the delocalized electrons in the 3d bands. In particular, this particular photon energy is known to be preferentially absorbed by charge-transfer excitations between Mn 3+ and Mn 4+ sites (Okimoto *et al.*, 1997).

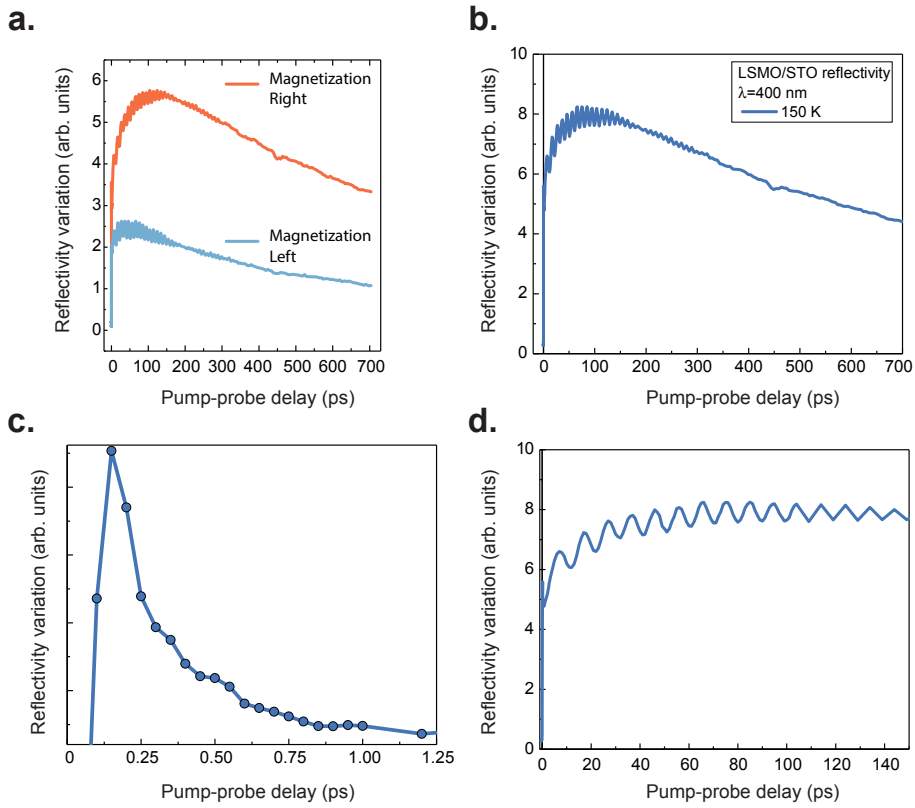

Figure 6.2: **a**. Raw signal of a typical measurement. Pump fluence 2 mJ/cm², LSMO/STO sample at 150 K initial temperature. **b**. Sum of the signals in panel **a**, giving the reflectivity dynamics over the full timescale studied. **c**. Enlargement of the short timescale region of panel **b**, showing the non-equilibrium charge spike. **d**. Enlargement of the intermediate timescales region, showing the coherent phonon oscillation.

At the maximum fluence we employed (2 mJ/cm²), the excitation density corresponds to about 10% of the Mn ites, an amount comparable to the doping level.

The rapid decay is usually considered, in studies of ordinary metallic samples, as a hint of the thermalization of the electrons with the lattice. In this case, it is certainly true that on this timescale the non-equilibrium distribution of the electrons cools down to an higher effective temperature and warms up the lattice. The equilibration time indeed results of 160 ± 70 fs by exponential fit between the peak edge and the flattening at 1.2 ps, and is scarcely variable as a function of sample temperature and strain state, pointing at a purely electronic, non-thermal character of the process.

Nonetheless, in the following we will gather increasing evidence that the optical excitation triggers a full scale rearrangement of the electronic structure, that covers much longer timescales. Indeed, right after the transient equilibrium reached at 1.2 ps, a new,

slower increase of the reflectivity takes over and is completed at about 100 ps. After such long time, the reflectivity starts to reduce as the sample cools down. This long-timescale reflectivity dynamics is a peculiar trait that has been observed in several CMR manganites such as PCMO, LCMO and LSMO (Lobad *et al.*, 2000a; Averitt *et al.*, 2001; McGill *et al.*, 2004).

Its origin can be traced back to the evolution of the optical spectrum of a correlated electron material sketched in Fig. 4.3. In the ideal correlated electron system that is derived from DMFT concept, as the bandstructure changes when crossing the metal-insulator transition, the optical absorption spectrum changes radically: the Drude spectral weight at lower energies, typical of intraband transitions in a metal, gradually disappears and an absorption band appears due to transitions between the LHB and UHB. Therefore, a large amount of spectral weight is transferred from lower to higher energies, and, due to the Kramers-Krönig integral relations, also the refraction index varies consistently, changing the reflectivity.

Upon ultrafast optical excitation, the system is then pushed closer to the MI phase transition and the electronic structure rearranges accordingly through the available channels giving rise to the so-called *Dynamical Spectral Weight Transfer* (DSWT). In the half-metallic manganites, the electronic structure rearrangement is bottlenecked by the slow magnetic response, giving rise to the hundred of picoseconds time-scale of the maximum in the DSWT. Indeed, this process proceeds on the same timescales as the evolution of the magnetic signal, and in the early days of the time-resolved measurements on correlated oxides it was indeed used as a probe of the magnetic dynamics. Its reliability, without supporting TR-MOKE data, has been questioned (McGill *et al.*, 2004).

In LCMO, which has narrower bands and above the Curie temperature shows a more marked insulating character, no significant DSWT is observed at 3 eV (Lobad *et al.*, 2000b). In the case of LSMO, two factors allow to see the effects of the DSWT at higher energies: the larger bandwidth[2] and the metallic character of the high temperature phase. Indeed, in LCMO, as the relevance of the absorption band at higher energies increases, the strong decrease of the Drude weight limits the effects of the integral character of the Kramers-Krönig relations to energies below 3 eV (Lobad *et al.*, 2000b). In LSMO, however, the Drude weight never disappears, allowing for the effects of the transition to be observable also at higher energies.

Interestingly, in LSMO optical spectrum, 1.5 eV is the inflection point between a region in which the spectral weight decreases close to T_C, and one in which it increases. The optical absorbivity thus shows minimal temperature variability. Pumping at this wavelength guarantees therefore constant excitation density.

At intermediate timescales, an interesting feature can be observed (Fig. 6.2 **d**). The oscillation that is superimposed to the reflectivity dynamics arises from the excitation of a coherent phonon, or, in other words of a shockwave travelling through the thickness of the film. The shockwave Doppler shifts the probe pulse, producing an interference in the

[2]Indeed, the width of the absorption peak is given by the joint density of states, combining the width of the initial band and the final band.

dynamical curve. The period of the oscillation is around 10 ps. From this, calculating that the round trip in the film thickness is about 80 nm, we obtain a speed of the shockwave of 8 nm/ps or 8000 m/s in an order of magnitude agreement with more accurate multi-wavelength studies (Ren *et al.*, 2007).

The apparent beating arises from the reduction of the sampling frequency: at 100 ps delay, the time step per acquisition is increased from 1 ps to 5 ps (corresponding to the minimum frequency to sample the oscillation for the Nyquist-Shannon theorem). The signal oscillation is phase shifted with respect to the sampling frequency, giving this aliasing effect.

Interestingly, the long persistance of the oscillation suggest that, for very long times, not even the lattice should be considered in thermodynamic equilibrium. Until such coherent component of the energy stored in the lattice is fully dissipated, indeed, one should not, in principle define a unique phononic temperature (Günther, 2015).

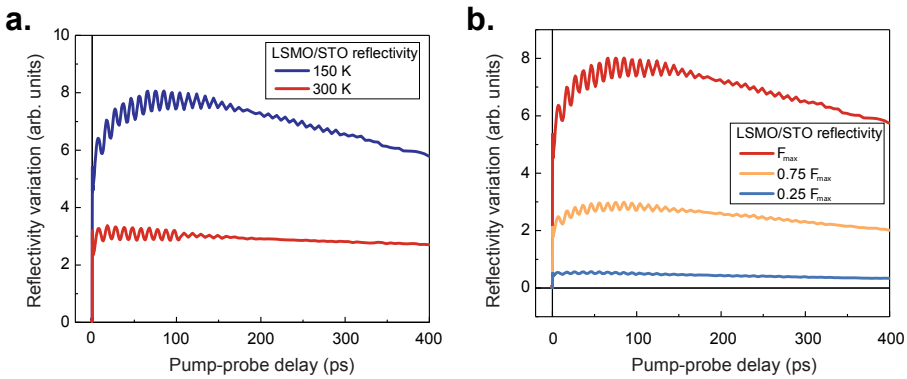

Figure 6.3: **a**. Temperature dependence of the reflectivity signal for the LSMO/STO sample at 300 K and 150 K, with maximum fluence. **b**. Fluence dependence at F_{max}, $0.75F_{max}$ and $0.1F_{max}$.

The magnetic origin of the DSWT can also be inferred from the influence of the initial sample temperature, shown in Fig. 6.3 **a**. Indeed, as the temperatures get closer to the Curie temperature, the pump-induced rearrangements of the electronic structure become smaller. At 300 K in the LSMO/STO sample, the reflectivity shows substantially a step increase, with only a small contribution of the DSWT at shorter times. The envelope of the coherent phonon decays on shorter timescales possibly due to softening of bulk phonon modes that allows to quench the coherent excitation more efficiently in incoherent excitations (Seikh *et al.*, 2004). Accordingly, the coherent phonon shifts slightly to longer periods.

When varying the fluence (Fig. 6.3 **b**), further evidence is gained on the DSWT: at hundreds of ps timescales, an increased excitation density can be considered as producing a larger ΔT in the electronic and lattice temperature. Thus, the DSWT becomes larger and larger as the laser fluence is increased, pushing the system towards the transition

temperature. Indeed, by reducing the fluence of one order of magnitude, a step-like component is observed, with minimal contribution of the DSWT.

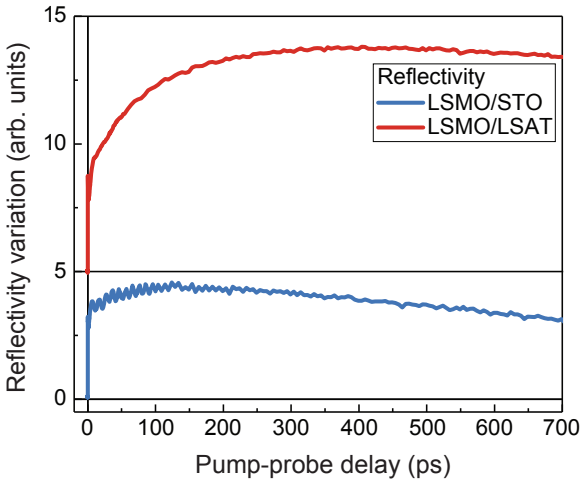

Figure 6.4: Reflectivity dynamics of LSMO/LSAT and LSMO/STO samples. Initial temperature 250K, maximum fluence. The curve of LSMO/LSAT has been shifted vertically for clarity.

Finally, we consider the strain dependence by observing the curves for the LSMO/STO and LSMO/LSAT. In the curves shown in Fig. 6.4, it is possible to see that the sample grown on LSAT has a significantly smaller contribution of the coherent phonon, due to its strain relaxed state. The rest of the dynamics is qualitatively analogous to the one observed on STO, despite the fact that the DSWT and the reflectivity variation seem to be larger, quantitative confrontation is not reliable as, between the two samples, a slight re-optimization of the laser was performed gaining a 3% in average power. As can be seen, even slight variation of the pump fluence lead to large effects in the reflectivity dynamics: precise assessment of the variation of reflectivity, while certainly interesting, would require dedicated experiments that are beyond the scope of this work. Given the added complication of a large coherent phonon contribution, we decided to concentrate the following magnetic Kerr analysis on the strain relaxed LSMO/LSAT.

6.2.2 Ellipticity and rotation

When passing to study the dynamics of the difference between the two signals of Fig. 6.2 **a**, however, we observed a very rapid reduction of the Kerr rotation, followed by an inversion of the signal at short timescales, so that the value of $\Delta\vartheta/\vartheta_0$ became positive. Subsequently, a long-timescale quench set in, producing the largest demagnetization. Since in LSMO there are no ferrimagnetic components, the response of the system puzzled us.

We thus decided to carry out a full ellipsometric study on the LSMO/LSAT sample, by employing the balanced detection technique (See A). With the same configuration of the experimental system, we substituted the analyser and the photodiode with a Wollaston polarizer and two balanced diodes. By adding or removing a quarter waveplate we could switch between the ellipticity and rotation measurement, evaluating the full complex Kerr angle.

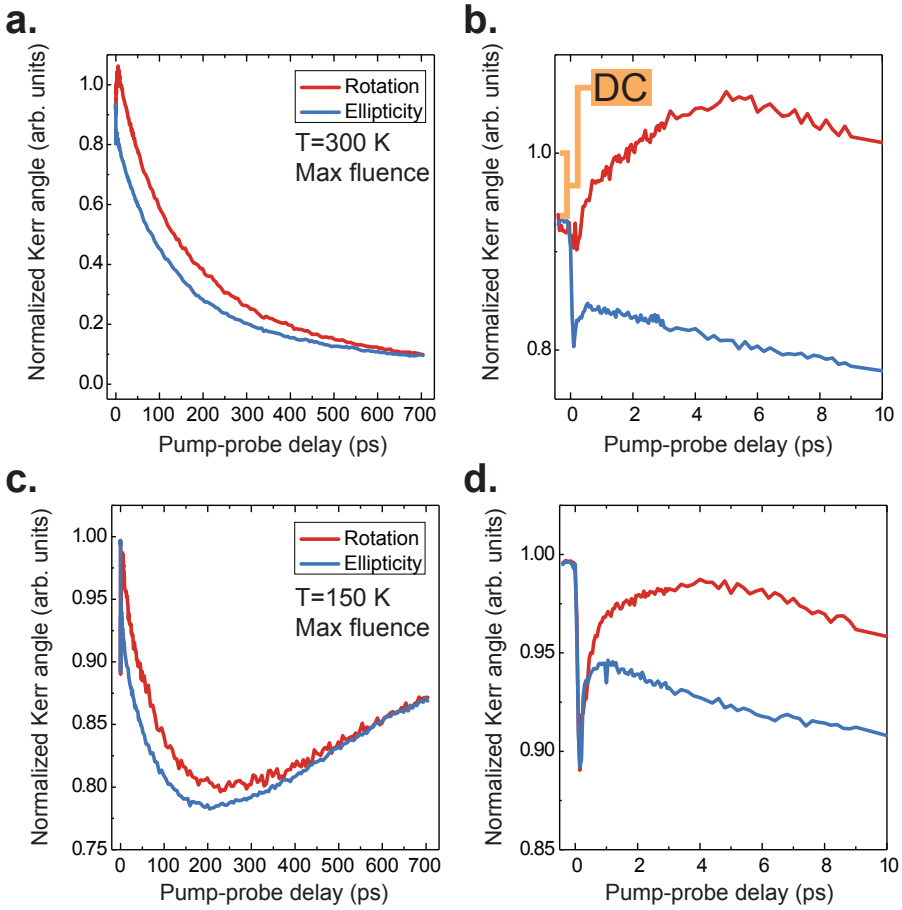

Figure 6.5: **a** Long timescale dynamics of Kerr rotation and ellipticity in LSMO/LSAT sample at room temperature, with maximum pump fluence. **b**. Zoomed-in short timescales region, evidencing opposite dynamics arising from stray effects of the diagonal elements of the dielectric tensor. In orange is evidenced the effect of residual heat between one pump pulse and the successive. **c**. Same as panel **a**, but with initial sample temperature of 150 K. **d**. Same as panel **b** but with initial sample temperature 150 K. The DC heating effect is reduced due to the flattening of the M(T) curve at lower temperatures.

In Fig. 6.5 the results of the study are shown. It is easy to notice that the ellipticity and the rotation variation remain different between each other for very long time after the optical excitation, thus breaking the relationship expected for the optimal condition A.1.5. The Kerr rotation or ellipticity thus do not represent individually the magnetic dynamics, as they are differently influenced by the dynamics of the multiplying Fresnel coefficient.

The curves have been measured at the maximum fluence. In this first analysis, we

recorded the normalization hysteresis at the two temperatures by blocking the pump beam and modulating the probe to evaluate $\vartheta_0(T)$ and $\eta_0(T)$. The curves are then normalized to obtain $\Delta\vartheta(t,T)/\vartheta_0(T)$ and $\Delta\eta(t,T)/\eta_0(T)$. In order to better appreciate the reduction of the magnetization dependent signal, the curves were shifted by adding one: if Eq. A.1.5 were applicable, values smaller than one would represent demagnetization. This customary, and used in ultrafast magnetism studies to make immediately clear whether, under photoexcitation, the magnetization increases, is quenched to zero, or switches to negative values.

Due to this choice, at negative time delays, the curve at 300 K does not reach one (Fig. 6.5 **b**). This is recognisable as a DC heating effect: with respect to the $\vartheta_0(T)$ and $\eta_0(T)$ measurements performed with the pump blocked, the dynamical curves do not allow full recovery of the initial temperature, *de facto* shifting the initial temperature a few degrees. This effect is more evident at higher temperatures, as the steepness of the $M(T)$ curve increases: a small shift of T produces larger reduction of M closer to T_c. The curve in Fig. 6.5 **d** are thus much closer to one. In the next, this problem will be avoided by normalizing to the values at negative delays in presence of the pump, thus removing the small temperature shift due to DC-heating.

At time zero, both curves undergo a sudden reduction, more evident at lower temperature. Then, ellipticity and rotation evolve differently: the rotation starts to increase and even increases above the initial value at room temperature. The increase completes within 6 ps and then the long decrease sets in. The ellipticity instead recovers for much shorter times, going from sub-picosecond at 300 K to 1.2 ps at 150 K, and with a much smaller amplitude. Then, also for ellipticity, the long reduction starts. The difference accumulated in the first 6 ps is then slowly reduced and the two curves are almost parallel for the following dynamics.

Such a persisting difference between the rotation and ellipticity has been observed in CMR manganites (McGill *et al.*, 2004) and in the half-metallic oxide CrO_2 (Carpene *et al.*, 2013). It is clear that the presence of stray effects of ε_{xx} plays a significant role in the first picoseconds. The investigation of the magnetization dynamics in LSMO can thus proceed in two directions:

- Attempt to analyse the ellipsometry data, trying to disentangle, or at least individuate clearly, the effects of charge dynamics in the evolution of the Kerr angle. This shall be discussed in Sect. 6.3.1.

- Basing on the fact that we are mostly interested in the long timescale collapse of the magnetization dynamics, choose one parameter (ellipticity or rotation) and perform comparative studies of the long timescale dynamics. As Shown in Fig. 6.5**a** and **c**, indeed, the two curves substantially mirror each other while slowly recovering the initial difference.

6.2.3 Fluence and temperature

We thus reconfigured the system in the crossed polarizer configuration, that allows for a higher signal-noise ratio, and decided to study the ellipticity signal on the LSMO/LSAT sample at maximum fluence. In order to have suitable normalization, the value of $\eta_0(T)$ as a function of the initial substrate temperature was recorded, shown in Fig. 6.6 **a**. Then we measured the demagnetization traces for a large number of initial temperatures. The obtained curves, each one normalized to the corresponding value of $\eta_0(T)$, are shown in Fig. 6.6 **b**.

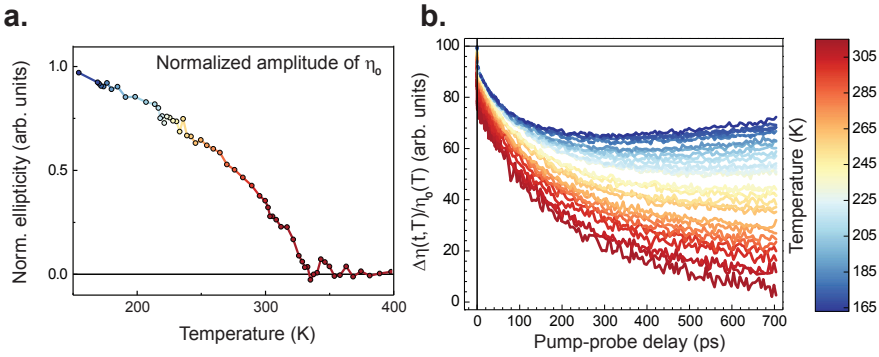

Figure 6.6: **a**. Normalized value of $\eta_0(T)$. The value at 150 K that defines the scaling has been retrieved from the SQUID curve of Fig. 3.4 **c**. **b**. Relative variation of the ellipticity as a function the initial temperature. The colouring of the curves is consistent to panel **a**, indicating the sample initial temperature.

From the inspection of Fig. 6.6, it is possible to notice that the reduction of the ellipticity reaches a minimum at about 200-250 ps for the lowest temperatures. After such minimum dissipation through the substrate allows to cool the sample back to the initial temperature, and the curve takes an upward turn. The position of such minimum shifts with the initial temperature, moving out of the measurable interval around 245 K. This arises from an increase of characteristic time of the magnetic fluctuations in proximity of the phase transition and is called *critical slow-down*. This phenomenon has been observed and studied in a large number of magnetic materials, particularly in CMR oxides (Kise *et al.*, 2000; Liu *et al.*, 2001; Ogasawara *et al.*, 2003, 2005). It is a mechanism that can be explained with scaling laws bothered from the quasi-equilibrium theory of phase transitions, and it will be further discussed in 6.3.3.

Furthermore, it is possible to notice that the amplitude of the relative quench increases with larger temperatures. As it will be further discussed in the next sections, indeed, it is safe to assume that, at these timescales, the effect of the pump pulse is to shift the magnetic system forward on the M(T) curve, diving it closer to the phase transition. When the system is warmed up, approaching the Curie temperature, the same temperature shift produces a larger relative demagnatization, as is observable in the highest temperature curves.

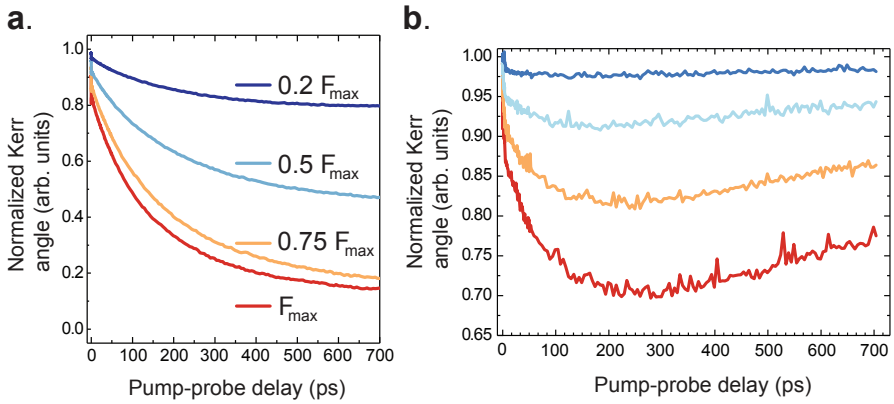

Figure 6.7: **a**. Room temperature variation of the ellipticity as a function of the pump fluence for LSMO/LSAT sample. **b**. Same as panel **a**, but at 150 K.

Finally, to further investigate the long timescale evolution of the ellipticity, we studied the dependence of its collapse as a function of the pump fluence, as reported in Fig. 6.7. We reduced the incident fluence by a factor $3/4, 1/2$ and $1/5$ at four temperatures (150 K, 200 K, 250 K and 300 K). In almost all the cases, the long timescale demagnetization is observed. At the highest fluences and at 300 K the maximum amplitude of $\Delta\eta$ is close to saturation in a complete disappearence of the signal. Only at the lowest temperature and lowest fluence, the long timescale dynamics does not appear to be present, and oly the small charge step dominates the evolution. This is consistent with the observations at much lower fluences (200 μJ/cm^2) in millimetre-sized crystals by (Ogasawara *et al.*, 2003).

6.3 Discussion

The amount of data that can be obtained by optical measurements is rather rich, but their interpretation is subtle. In the following discussion, the reliability of the signal as a probe of the magnetic dynamics is firstly addressed, giving reliable grounds for further analysis of the data. Then, we study the amplitude of the variation of the ellipticity as a function of temperature and fluence, extracting information on the variation of the temperature of the magnetic system in various regimes. Finally, by addressing the timescales of such magnetization, we obtain evidence of the mechanism driving the quench and of the universality class of magnetic interaction in LSMO.

6.3.1 Disentangling magnetization dynamics

Once the broken identity between the dynamics of the Kerr rotation and the ellipticity is individuated, the first necessary step that must be undertaken in order to analyse the

ellipsometric data is the calculation of the modulus of the complex Kerr angle:

$$|\Theta(t)| = \sqrt{\vartheta^2(t) + \eta^2(t)} \tag{6.1}$$

It is only this quantity that allows to disentangle the effects associated to the diagonal and off-diagonal elements of the dielectric tensor. The dependence of Eq. A.0.12 holds indeed for the whole complex angle. Thus, when separating ϑ and η, different dependences from the imaginary and complex part of ε_{xx} emerge, giving different functional dependences of the corresponding Fresnel coefficient. By calculating $|\Theta|$, instead, a unique dependance from the square modulus of the Fresnel coefficient is retrieved. The result of the calculation of $\Delta|\Theta(t)|/|\Theta_0|$ at two temperatures is shown in Fig. 6.8.

At both temperatures, the Kerr angle long timescale dynamics is qualitatively identical to the separate dynamics of rotation or ellipticity observed in Fig. 6.5. At shorter timescales, the apparent increase observed in the rotation signal is cancelled: an ultrafast downwards spike is recovered on ultra-short timescales, the same of the reflectivity increase peak of Fig. 6.2 **c**. The recovery is almost complete in the room temperature curve, while it leaves the system with a small initial step in the low temperature case.

We can compare these results with the ones obtained by Carpene and colleagues (Carpene *et al.*, 2013) that realized an ellipsometric study on the half-metallic oxide CrO_2. Combining the measurement of Kerr angle, ellipticity in the s and p configuration with accurate reflectometry (in the tilted sp and ps polarizations), they are able to employ numerical procedures and extract the four independent components $\mathfrak{Re}(\varepsilon_{xx}(t))$, $\mathfrak{Im}(\varepsilon_{xx}(t))$, $\mathfrak{Re}(\varepsilon_{xy}(t))$ and $\mathfrak{Re}(\varepsilon_{xy}(t))$. Using heavily smoothed data to avoid divergences in the inversion of the relationships, they find that $\mathfrak{Re}(\varepsilon_{xx}(t))$ ($\mathfrak{Im}(\varepsilon_{xx}(t))$) shows a step-like increase (decrease), followed by a constant trend. By feeding these two in the modulus of the Fresnel coefficient they find that the dynamics attributable to ε_{xx} consists indeed of the initial step.

On the other hand, the dependance of ε_{xy} on the magnetization gives to its modulus a long timescale component, reflected in the dynamics of $|\Theta|$. They also find that while the dynamics of ϑ and η in general differs between s and p geometry, the dynamics of $\Theta_{s,p}$ is identical, due to the unitary ratio of the reflectivities in the two configurations at any delay.

Clearly, in our case, given the temperature variation of the electronic structure close to the phase transition, the variation of the Fresnel coefficient would also have a temperature dependence, explaining the negligible charge step at room temperature but its presence at 150 K. However, due to the analogy between the fundamental charateristics of the bandstructure of the LSMO and CrO_2, we can qualitatively interpret the initial spike and the persistent initial step as arising from the dynamics of ε_{xx}, while our thesis that the long timescale dynamics is due to spin-lattice demagnetization gains significant strength.

6.3.2 Amplitude of the total quench: temperature and fluence variation

Further evidence of the magnetic origin of the long timescale demagnetization can be obtained by analysis of the amplitude of the maximum quench as a function of the initial

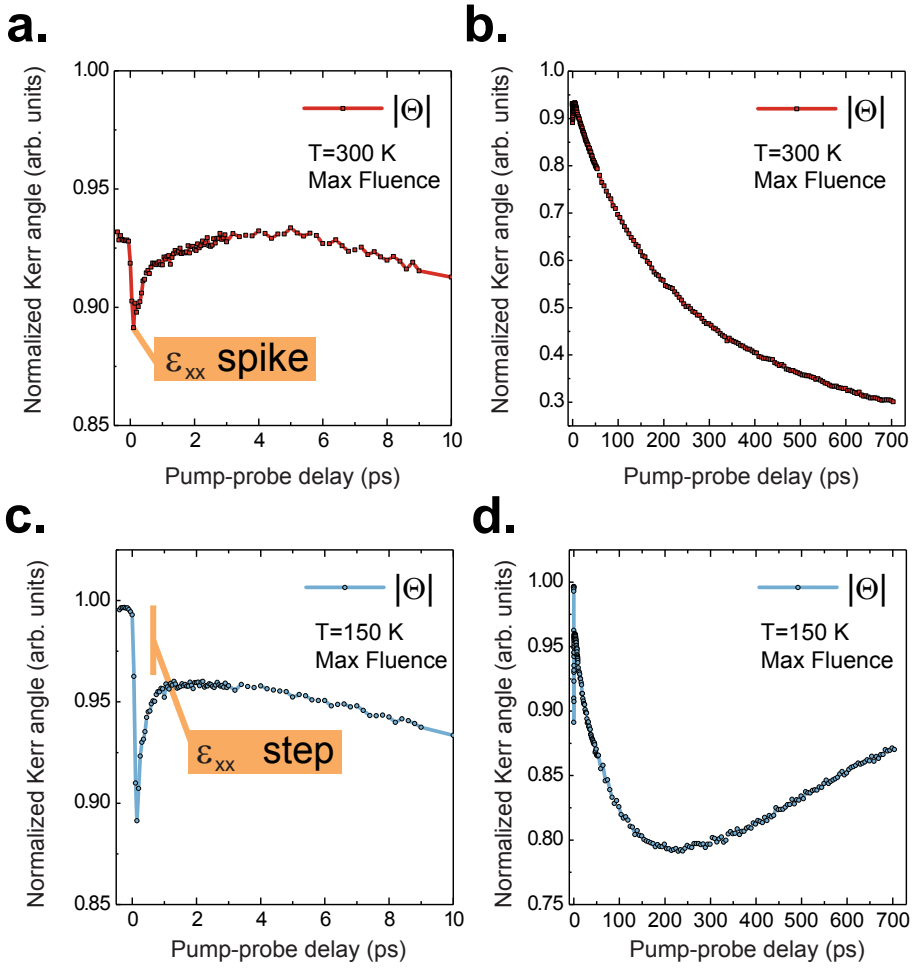

Figure 6.8: **a**. Short timescale dynamics of the modulus of the complex Kerr angle at room temperature, maximum fluence. The ultrafast spike is recovered completely, before the long timescale dynamics sets in. **b**. Long timescale dynamics, in the same conditions as panel **a**. c. Short timescale dynamics of the modulus of the Kerr angle at maximum fluence, 150 K initial temperature. At these temperatures the ultrafast spike is not recovered completely, and a persistent step offsets the long-timescale dynamics. **d**. Long timescale dynamics in the same conditions of panel **c**.

sample temperature. In Fig. 6.9 **a** are shown two curves: the first represents the value of $\eta(T)$ at negative delays normalized to the maximum value $\eta(150K)$. The second is formed by the values of $\eta(\tau_{max}, T)$ at which the curves of Fig. 6.6 **b** reach the maximum demagnetization.

Point-by-point difference of these two curves gives the one in Fig. 6.9 **b**, quantifying the absolute amplitude of the magnetization as a function of the initial temperature. The non-linear evolution , with the vanishing amplitude close to T_C indicates that the long

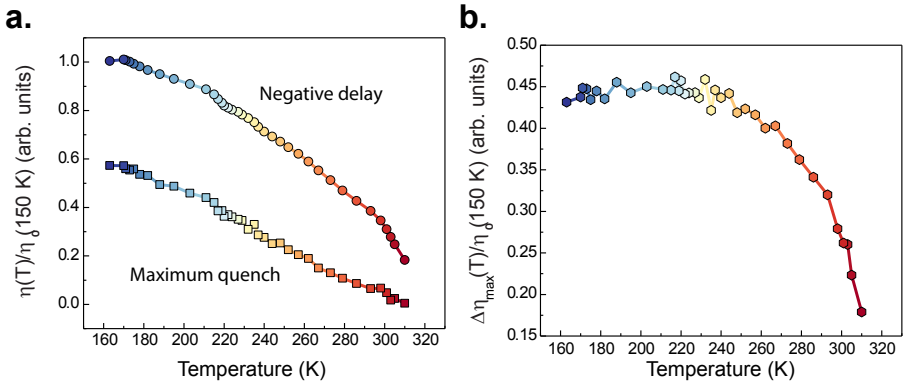

Figure 6.9: **a** Normalized ellipticity signal at negative delays (circles) and at maximum demagnetization (squares) as a function of the initial sample temperature. LSMO/LSAT sample, maximum fluence. **b** Amplitude of the demagnetization step in the same conditions, obtained as the difference between the two curves in panel **a**.

timescale reduction is of magnetic origin. Indeed, it can be tied to finite temperature shifts (ΔT) along the M(T) curve.

In the weak excitation limit, one can expect to observe a finite difference linearisation of the type:

$$\Delta\eta(\tau_{max}, T) = \frac{\mathrm{d}M(T)}{\mathrm{d}T}\Delta T \tag{6.2}$$

the curve thus should peak before T_c, reaching a sharp maximum and decaying rapidly to zero both at higher and lower temperatures. This has indeed been observed in LSMO crystals under 200 μJ/cm^2 fluence excitation (Ogasawara *et al.*, 2003, 2005).

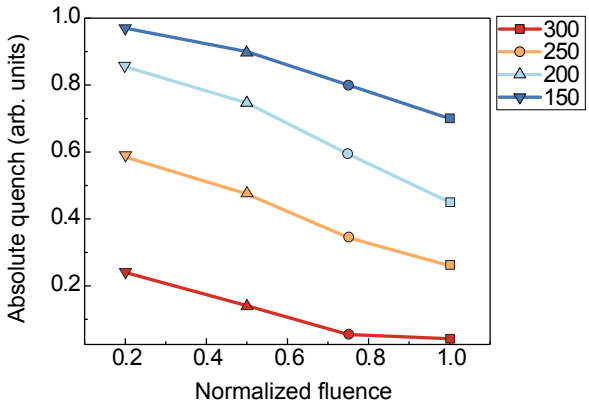

Figure 6.10: Variation of the minimum value of $\eta(t, T)$ with fluence for the LSMO/LSAT sample.

In the strong excitation limit, the finite ΔT_s shifts can be large, and the linearisation is no longer valid. At initial temperatures close to T_C, the application of a temperature shift provokes complete collapse of the small residual magnetization, resulting in a small absolute quench. As the temperature is decreased, the absolute quench follows the M(T) as long as the temperature shift is no longer sufficient to quench M completely. At this point a maximum is reached, and the shifts are between temperatures at which M(T) is finite.

Given the large ΔT, after the maximum, the initial temperature is in a region of the curve in which M(T) increases slowly, while the final temperature is where M(T) increases steeply. Thus, by further reducing the initial temperature, the absolute quench slowly decreases.

In the present case, the maximum of the curve in Fig. 6.9 **b** is around 230 K, that, given a T_C of 330 K corresponds to large temperature shifts: $\Delta T = 100K$. This is confirmed by the simpler analysis sketched in Fig. 6.9 **a**: the quench observed furthest from saturation (at 160 K) is of the 42%. By looking at the negative delay curve, the shift needed to reach 58% of the 150 K value is also of 100 K.

The curve of Fig. 6.9 thus not only adds evidence to the attribution of the long timescale variation of η as a magnetic effect, but it allows to identify the excitation regime and to quantify the temperature variation of the spin system.

The analysis of the amplitude of the quench can be extended to the different fluence regimes. In Fig. 6.10 $\eta(\tau_{max}, T, F)$ is shown for four different fluences and four different temperatures. At the two highest temperatures the change in slope at the highest fluence is due to the complete collapse of the magnetization induced by the large ΔT. The linear trend observed in the lower temperatures is due to the flattening of the $\Delta\eta(\tau_{max}, T)$ curve in this region.

At lower fluences instead, the effect of the ε_{xx} step is visible in a net change of slope of the lowest temperature curve. The higher temperature ones show close to linear relationships.

6.3.3 Critical slow-down

To further deepen our discussion, we can extend the analysis to the characteristic timescale of the demagnetization. As mentioned in Sect. 5.2.2, we expect that the mechanism dominating the dynamics of LSMO is spin-phonon coupling through anisotropy fluctuations. Given the weak anisotropy observed in LSMO (001) of 13-5 kJ/m^3 (Steenbeck and Hiergeist, 1999), corresponding to 5-2 μeV, gives 0.64-4 ns when substituted into Eq. 5.12 at room temperature, in full consistency with the present results.

Within this simple picture, the increase in the characteristic time of the demagnetization at long timescales observed in Fig. 6.6 **b** is qualitatively expected: as the initial temperature becomes closer to T_C the magnetic anisotropy energy decreases (Steenbeck and Hiergeist, 1999). As τ_{sl} has an inverse dependence from the anisotropy energy, it is thus expected that it increases.

Furthermore, in the vicinity of the Curie temperature, the process is further slowed down by the divergence of the spin specific heat. This can be treated with the methods employed to analyse critical behaviour in the proximity of the phase transition.

Koopmans' M3TM model allows to give an estimate of the dependence of τ from T. Given that the third equation of Eq. 5.6 describes directly $\dot{m}(t)$, they estimate the characteristic time in the vicinity of T_C as the amplitude of the total magnetization quench divided by the initial demagnetization speed. By expanding the Brillouin function around T_C and the equation of the magnetic dynamics around $t = 0$, they obtain (Schellekens,

2014):

$$\tau = \frac{1}{2R(1 - T/T_C)} \tag{6.3}$$

thus an inverse power relationship, holding for a spin 1/2 system way above its Debye temperature.

In our case, LSMO is best approximated in the Heisenberg mean field by S=2, and the Debye temperature is above the Curie temperature (Salamon and Jaime, 2001). The predictions of the Koopmans model cannot be straightforwardly applied, even supposing that the complex electronic structure with the long-lived non-equilibrium states demonstrated previously can be approximated by the constant DOS at equilibrium assumed in the M3TM.

In order to analyse the critical behaviour of a complex oxide such as LSMO, there is a much more powerful instrument that can be applied: the dynamical scaling theory. Indeed, as a result of the extension in the time domain of the renormalization group theory to the Ginzburg-Landau Hamiltonian for the order parameters (Hohenberg and Halperin, 1977), the charateristic timescale of the fluctuations τ is described by:

$$\tau \propto |T - T_C|^{-z\nu} \tag{6.4}$$

Where ν is the correlation length exponent defined from the spatial correlation length $\xi \propto |T - T_C|^{-\nu}$, while z is the dynamic exponent (Singh *et al.*, 2016).

These exponents define universality classes and can be calculated theoretically with numerous techniques, yielding a high generality. In particular, they have been calculated for the Heisenberg Model, yielding $z\nu = 1.38 \pm 0.04$ (Peczak and Landau, 1990) and for the double exchange model, obtaining $z\nu = 1.35 \pm 0.01$ (Fernandes *et al.*, 2005), and thus suggesting their belonging to a unique universality class. On the other hand, 2D Ising model calculations gave values of $z\nu \approx 2.165$ (Ito, 1993), thus clearly attributing it to another universality class.

In order to compare our results with the theoretical expectations, it was necessary to perform an exponential fitting. Indeed, as mentioned earlier, the minimum of the curves in Fig. 6.6 **b** shifts rapidly out of the range covered by our delay line, and it is not possible to evaluate its position directly. Each curve has therefore been fitted with the law:

$$\Delta\eta(t,T)/\eta_0(T) = A(T) \cdot e^{-t/\tau(T)} + C \tag{6.5}$$

in a time range that goes from $t = 10ps$ to the minimum of $\Delta\eta(t,T)/\eta_0(T)$. The results of the batch fitting are shown in Fig. 6.11.

At low temperatures the values of τ, close to 50 ps, slowly increase. This might be linked to the progressive reduction of the anisotropy. Around 305 K, the curve takes a net upward turn. It is in this region that the criticality exponents can be fit. We use the function:

$$\tau(T) = \frac{A}{|T - T_C|^{-z\nu}} \tag{6.6}$$

with A and $z\nu$ as fit parameters.

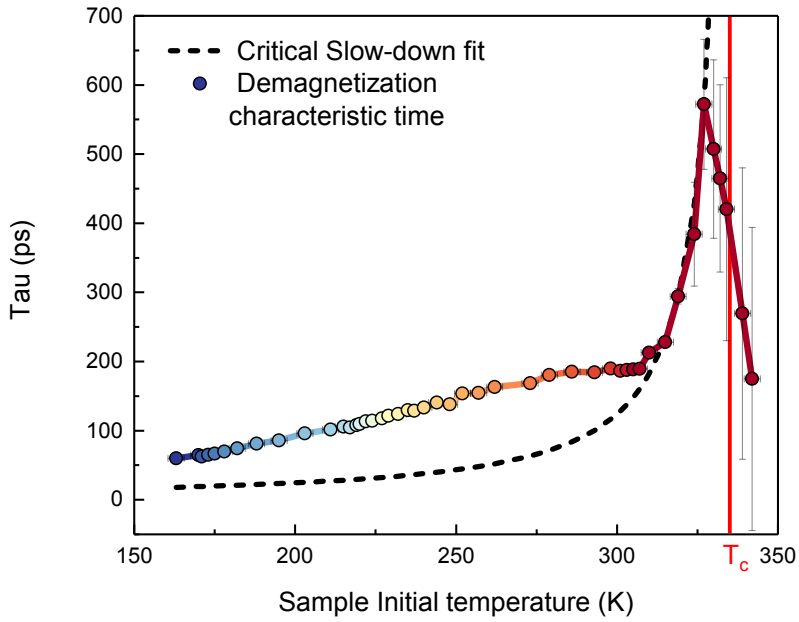

Figure 6.11: Fitted characteristic time of the Kerr ellipticity quench from the curves of Fig. 6.6 **b** (circles). The vertical error bars are given by the standard deviation of the fit. Due to increasingly small signal, the error bars at the temperatures closer to T_C are larger. The dashed line represents the critical exponent fit. The vertical red bar shows the Curie temperature obtained from Fig. 6.6 **a**.

The fitting converged, attaining an acceptable chi square value[3], in the range 305-327 K, obtaining $z\nu = 1.28 \pm 0.16$. The obtained curve is shown as a dashed line in Fig. 6.11. It is clear that the number of experimental data points that can be used in the fit is extremely limited. However, it is encouraging to notice the full consistency with the theoretical prediction for a double exchange system in three dimensions and with results of similar experiments on several half-metallic transition metal oxides such as Sr_2FeMoO_6 (Kise *et al.*, 2000), LCMO (Liu *et al.*, 2001), LSMO (Ogasawara *et al.*, 2003, 2005).

The analysis presented here of the divergence of τ in this system should therefore be interpreted on two levels:

- Focussing on the specific case of this manganite, and connected to the main topic that is being unfolded in the present discussion, it completes the evidence that LSMO is a true half-metallic ferromagnet whose magnetic dynamics is consistent with a 3D double exchange model. The dynamics is slowed down by the half-metallicity that blocks spin-flip excitations, thus isolating the spin system. Only

[3]The Chi square value was 0.43, well below 10.6, the value sufficient to reject the null hypothesis at P=5%.

the anisotropy fluctuations allow the transfer of energy to the lattice leading to the observed long timescales. In these conditions, the divergence of τ appears to be at least qualitatively describable by the power law derived by the dynamical scaling theory, thus in the domain of equilibrium thermodynamics. Certainly the accumulation of a larger number of data points in the critical region would allow to pin down more firmly a quantitative result.

- On a more general level, this result adds to previous investigations in displaying the powerful insight provided by advanced pump-probe experiments in the investigation of critical phenomena. It certainly guarantees a way to access the dynamical evolution of variables on extremely short timescales, allowing to test theories at the cross-over between equilibrium and non-equilibrium dynamics. This would allow to tackle the problem of ultrafast phase transitions from the point of view of statistical physics. Extending, for example, this approach to topologically non-trivial symmetry breaking mechanisms such as charge density wave (Yusupov *et al.*, 2010) or vortex formation (Zurek, 1985; Griffin *et al.*, 2012), could allow to probe the dynamics of topological defect formation by Kibble-Zurek mechanism (del Campo and Zurek, 2014) or even beyond it (Meier *et al.*, 2017).

Chapter 7

Time-resolved HAXPES experiments

As demonstrated in Chap. 6 the extraction of reliable data and the derivation of solid conclusions by use of optical techniques is a rather delicate operation. Especially in the case of the complex electronic structure of correlated electron materials, where the rearrangements of the bandstructure close to the Fermi energy can be critical, the extreme sensitivity of the optical techniques to a wide spectrum of low energy excitations mixes the processes of interest with other dynamical effects. In the quest for a technique in which the sensitivity is more sharply focussed, or at least appears to be treatable by a low-parameter analysis, we thus resorted to time-resolved HAXPES, in order to probe the electronic-magnetic correlation in LSMO at the picosecond time-scale suggested by MOKE. By building on the widely consistent dataset of advanced spatial (Part I) and accurate temporal characterization (Chap. 6), we move onto the next step building on a solid ground. In this Chapter we will therefore discuss how, by employing the HAXPES technique, we ventured in the direct observation of the dynamics of electronic correlation.

7.1 Instrumentation

Thanks to the pioneering work of the team led by Prof. Rossnagel, together with the local group of Prof. Oura, it is possible to realize HAXPES experiments at the physics beamline BL19LXU. Since the beamline has already been described in Sect. 3.1.2, its main features are resumed only briefly here for the convenience of the reader.

BL19XU is a beamline of the SPring-8 synchrotron radiation facility in Japan. Exploiting an extremely long undulator (25 m) and one of the highest energy third generation light sources in the world, it reaches extremely high brilliances in the hard X-ray ($\approx 2 \times 10^{14} ph/s$ at 14 keV), allowing for the realization of a variety of photon-hungry experiments. After the front-end, a liquid nitrogen cooled Si (111) monochromator realizes the first photon energy selection. In HAXPES experiments, it is followed by a Si (444) channel cut monochromator and an horizontal refocussing mirror system, which also rejects higher harmonics. The endstation features a cryogenically cooled, five axes manipulator, and a Scienta R4000-10kV electron energy analyser.

Beamline set-up for time resolved measurements

The implementation of the pump-probe technique relies on the exploitation of the synchrotron time-structure. The "full filling pattern" of SPring-8 is called *A-mode*. In this configuration, the machine emits low intensity pulses of light at a very high frequency: 203 bunches are accumulated in the ring, with a 4.8 μs round trip period, corresponding to a 42 MHz repetition rate. In BL19LXU long undulator, this produces pulses of 5×10^6 photons, equally separated by 23.6 ns.

In order to perform infrared pump-hard X-ray probe experiments, a *hybrid filling* mode is needed. The total accumulated current is maintained identical to the "full filling" mode by injecting a large number of high charge bunches in only a fraction of the ring, while a bunch with even larger charge is isolated by significant dark gaps. In the case of the present experiment, we exploited one of the *H-filling* runs of Spring-8, where about 1/3 of the ring was closely packed with bunches (at 11 ns interval, even shorter than A-mode), while a single bunch was isolated by 1.5 μs dark gaps.

Each of the bunches in the dense train had 1.2 times the charge of a A-mode bunch, while the isolated one was enhanced by a factor of ten. With this configuration, the changing of the time-structure does not change the available intensity for non-time resolved experiments, and the hybrid filling modes can be operated rather often: the H-mode is available 4 times a year at Spring-8.

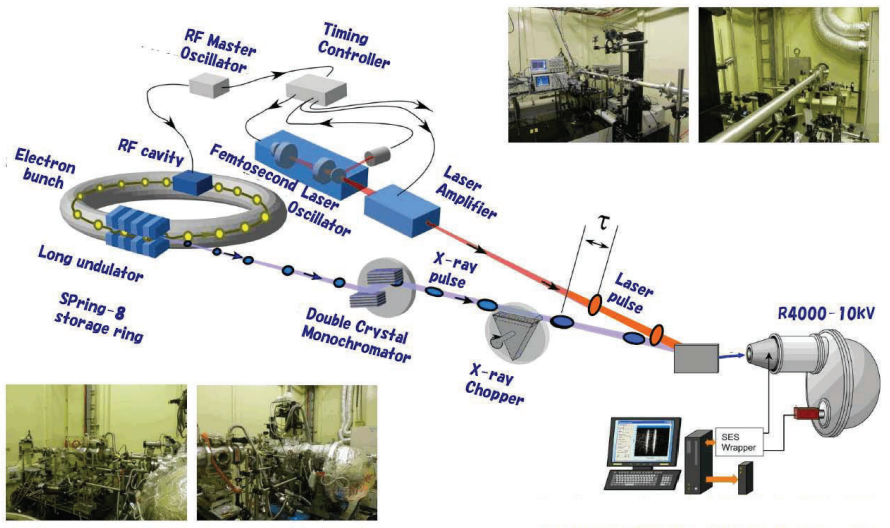

Figure 7.1: Scheme of BL19LXU, evidencing the most important features for the Time-resolved measurements. Adapted from (Chainani and Oura, 2014).

To realize an experiment in the pump-probe mode, it is necessary to ensure that two criteria are met. Firstly, the laser system must be synchronized with the synchrotron pulses. Secondly, the signal generated by the isolated pulse, which is at short delay from

the pump, must be separated from the dense pulse train.

These criteria bring us to the differences from the set-up of the beamline described in Sect. 3.1.2. As already covered there, indeed, the first hutch of the beamline hosts the channel-cut monochromator and the refocussing optics, while the third encloses the experimental endstation. In the second, instead, it is hosted an infrared laser system, depicted in blue in Fig. 7.1, the timing system and the X-ray chopper.

The ultrafast optical laser is a commercial Spectra Physics system: a Millennia 532 nm diode laser pumps a Tsunami oscillator and a Spitifire amplifier. The oscillator generates pulses of less than 100 fs at a repetition rate of 80 MHz in the nJ energy range. The pulses are then amplified by the Spitfire up to several mJ, with durations of about 130 fs. The oscillator is connected to a synchronization electronics that picks a trigger signal from a master oscillator. This system is in turn connected with the radiofrequency cavities that regulate the timing of X-ray pulses. The time delay can be controlled by electronically retarding the laser oscillator trigger, operation that can be performed with picosecond accuracy.

A small part of the beam is separated for real time diagnostics, while the rest is transported to the experimental chamber by a system of optics outside of the vacuum chambers. After a final focussing mirror, the beam crosses a set of square slits that define it into a square spot of uniform intensity. The infrared beam enters the chamber at an angle of 45° from the synchrotron beam, in the direction of the electron energy analyser. The system is able to deliver up to 4 mJ/cm² at a repetition rate of 1 kHz.

The repetition rate is clearly a strong limiting factor of the TR-HAXPES experiments, as discussed in Sect. 4.3.2. Indeed, the use of a single pulse, and the further reduction to 1 kHz due to the laser, reduce the usable flux by about five orders of magnitude, to about 10^9 photons/s. This is indeed the direction in which further upgrades of the beamline are pointing: very recently the same laser set-up has been modified to reach 10 kHz repetition rate, increasing significantly the photon flux.

To implement the second criterion, an X-ray chopper is used. It consists of a thin disk of pure aluminium of 20 cm diameter with a narrow diametral groove (about 200 μm wide, 1 mm deep). The disc is attached to a stepper motor with an extremely regular rotation speed, i.e. a picosecond jittering noise between the trigger signal received from the master oscillator and the crossing of a mechanical reference switch.

The chopper is aligned with the beam by a set of high precision stepper motors, that allow to precisely position the centre of motion in the axis of the beam. Only when the narrow channel is aligned with the beam path, the X-rays can be transmitted downstream. At 1 kHz rotation speed, the shutter is open for 300 ns. By synchronising the rotation to the passing time of the isolated pulse, the remaining dense pulse is chopped, allowing to retrieve the single pulse signal. The chopper can be easily moved away from the beam and back in without losing synchronization, by means of a low-backlash vertical translation motor.

In Fig. 7.2, the principle of operation of the beamline is recapped in a time scheme. The synchrotron is filled with one isolated pulse an a 1/3 train, which cycle trough the

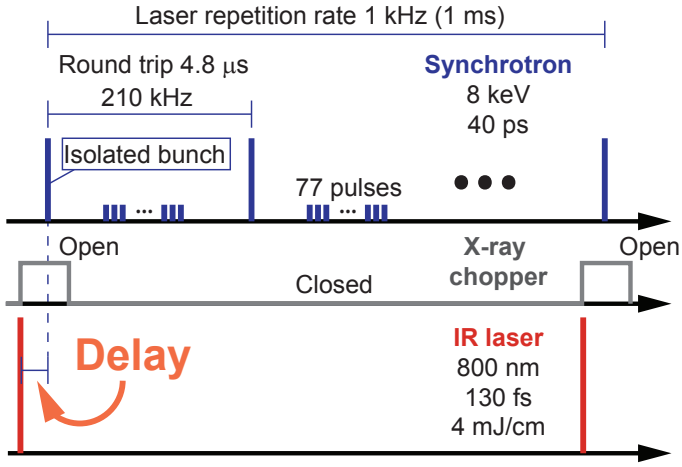

Figure 7.2: Time chart of the operation of BL19XU showing the synchrotron time structure (blue), the gating via the X-ray chopper (dark grey), and the pulses from the IR laser (red). The delay (orange) is controlled by an electronic timing electronics. Adapted from (Chainani and Oura, 2014).

undulator at the round trip frequency (208 kHz). The X-ray chopper is opened to let pass only one in 208 isolated pulses, to match the repetition rate of the laser, which is synchronized and sent to the chamber with a controlled delay τ.

In the experimental chamber, the pump and probe beams are overlapped spatially at the sample position by using a YAG crystal. The crystal is visualized by a set of high magnification cameras oriented at different angles, that allow to check the spatial alignment. The focussed X-ray beam is much smaller than the several hundreds of microns of the area excited by the laser, so that small misalignments, or small positional drifts of either beam, do not result in the probe footprint reaching an unpumped area.

Given the great difficulty in realizing a system that can determine the coincidence of photons with such a diverse energy, a rough temporal overlap is realized by inserting a fast break-junction silicon photodiode in the beam path. The rise time of the photodiode is about 100 ps.

The temporal superposition is thus achieved by overlapping the rising peaks of the two pulses, which results in a 100 ps jittering uncertainty. A more precise definition of the zero delay must be achieved by observation of the pump-induced effects in the HAXPES lineshapes by scanning around the coarse zero in small steps.

This leaves space for systematic errors in the determination of the onset of dynamical effects. Recently, a routine based on fitting of the Si 1s peak shifts due to surface photovoltage has been implemented. It allows to define the time-zero position with picosecond precision, but it is quite time expensive. The possibility of individuating rapidly and precisely the temporal overlap of such largely different photon energies is certainly still

an open technological challenge.

7.2 Approach and results

Owing to the reduced flux of the pump-probe routine, several precautions had to be taken in order to achieve maximum statistics and statistical consistency. The sample was cooled to the minimum temperature of the cryostat, 50 K, in order to enhance the intensity and energy separation of the LBES from the main peak structure. In these conditions, an energy resolution of $\Delta E = 500eV$ is sufficient to clearly resolve and characterize the LBES.

Consequently, several combinations of the pass energy and the width of the entrance slits of the R4000-10keV scienta analyzer were tried, in order to achieve the highest count-rate while maintaining acceptable energy resolution. The optimum was obtained at P.E. $= 200eV$, $Slits = 1.5mm$, which gave $\Delta E = 480eV$. Despite these precautions, the count rate remained rather low, with about 100 counts/s on the main feature of the Mn $2p_{3/2}$ peak. It became thus necessary to integrate for long times, in the scale of several hours.

At such low count rates, the details of the detection scheme become relevant. Indeed, the Scienta R4000-10keV uses a multichannel plate amplifier followed by a phosphor screen, that is read out by a CCD camera. This configuration, that is extremely effective in most of the applications, has one of its shortcomings in the high dark noise of the CCD camera. When a small signal is integrated for long times, the dark noise continuously builds up a background, flattening the dynamic range of the signal. To compensate this distortion, it became necessary to make confrontation between signals with the same statistical characteristics.

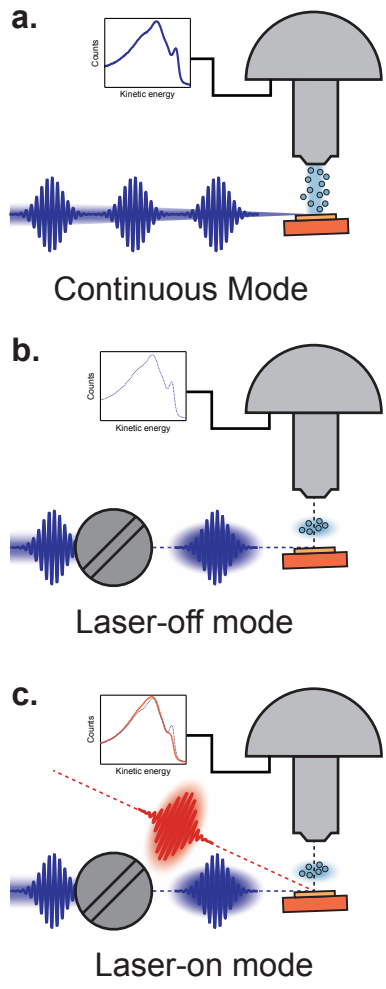

Figure 7.3: **a**. **Static mode**: the X-ray beam is not chopped. **b**. **Laser-off mode**: the beam is chopped but the pump laser is blocked. **c**. **Laser on mode**: The beam is chopped and the IR laser is shone on the sample.

We therefore operated in three modes, sketched in Fig. 7.3. The "static mode" represented in Fig. 7.3 **a**, is implemented by removing the chopper from the beam. The

counts reach almost 10^6 cts/s, and the equilibrium spectra of the sample can be recorded. If the pump laser was switched on in these conditions, its short lived effect would be hidden by the higher statistics of unpumped signals. This mode has been used for the preliminary equilibrium characterization, and, by turning on the pump-laser, to check if any DC-heating effects are present. At this repetition rate, no temperature build-up was observed.

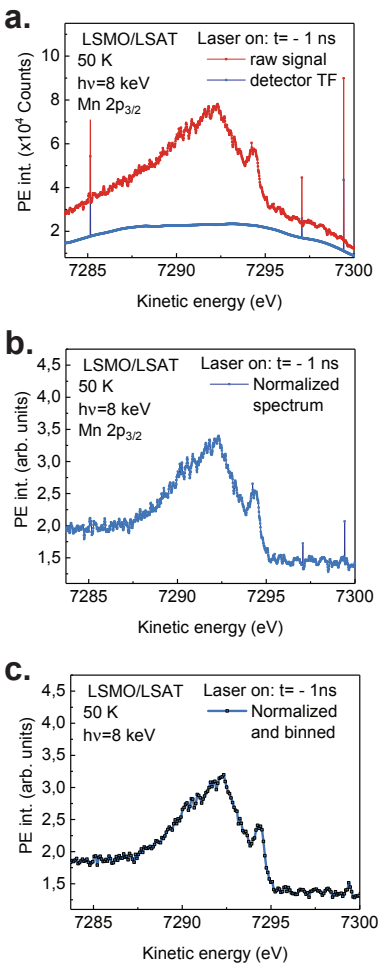

Figure 7.4: **a**. Raw signal (Red) and detector transfer function (DTF, blue). The sample is at 50 K and delay is - 100 ps. **b**. Result of the division of the signal by the DTF. **c**. Result of the binning procedure with bins 250 meV wide.

The "laser off" mode in Fig. 7.3 **b**, serves as a reliable confrontation: the equilibrium Mn $2p_{3/2}$ peak is measured in absence of the pump-laser with the same counting rate of the pump-probe experiment. This type of measurement was repeated several times throughout the experiment, in order to check the effects of sample damage or intensity variations. Finally, the "laser on" mode corresponds to the proper pump-probe experiment. Any difference from the "laser off" spectrum must be induced by the pump.

When a photoelectron spectrum is acquired, energy dispersive analysers usually operate in "swept mode": the potentials of the electrostatic lenses are ramped and only a small region at the centre of the detector is acquired. This allows homogeneous data acquisition and the removal of warping effects in the acquisition chain, but has a rather large time consumption. In order to maximize the acquisition time, we instead operated in "fixed mode". In this configuration the part of interest of the spectrum (in our case he Mn 2p 3/2) is fitted into the CCD window of energies, and the potentials are left unchanged for the whole acquisition.

Clearly, such choice exposes to aberrations of the electronic lenses, inhomogeneities of the phosphor screen, damaged regions and hotspots in the CCD sensor. Furthermore, the CCD pixel size leads to a sampling of the spectrum at energy intervals much smaller than physical resolution thus adding to the noise. These issues can however be solved by careful handling of the signal, as illustrated in Fig. 7.4.

In Fig. 7.4 **a** the raw signal of a laser-on measurement at negative delays is shown.

The presence of a convex shaped warping of the baseline, together with several hotspots is evident. We thus moved the energy window a few eV away, where the "static" spectra showed a flat background, and measured the transfer function of the detector, with which we would normalize the pump-probe spectra. To avoid adding noise in the normalization process, we fitted the shape of the transfer function by a high order polynomial, adding the measured hot-spot points at the end. The result of the division is shown in Fig. 7.4 **b**. It is clear that the baseline is now flattened to its physical shape.

To address the issue of oversampling, we designed a special binning routine: the spectrum is divided in energy intervals that are closer to the energy resolution (in Fig. 7.4 **c** it is shown for 200 meV steps) and the average between the points in that interval is calculated, resulting in a single point in the "binned spectrum". Note that this is not a smoothing procedure: the features of the spectrum are not blurred by a moving average. We instead reduce, on a physically solid basis, the noise resulting from oversampling.

By applying all the aforementioned precautions, we successfully measured time resolved HAXPES spectra at two negative delays (-900 ps and -100 ps), at zero, at two positive short delays (100 ps and 300 ps), and at two positive long delays (1.1 ns and 3.1 ns). On a LSMO/LSAT sample, which was characterized as in 3.1.3, and had consistent structural, electrical and spectroscopic parameters. The results of each long acquisition is shown in Fig. 7.5 **a**. The spectra have undergone the data processing described above, followed by a linear background removal and normalization to the area. In Fig. 7.5 **b** the curves at selected delays are shown with highlighted differences from the laser off spectrum.

At negative delays, the spectra are substantially identical to the laser off spectrum. The small variations between the curves can be taken as the error band on the spectral lineshape. The first delay at which we observed a modified lineshape was defined "time zero". The trend in the demagnetization timescales observed for the MOKE signal suggests that at low temperatures, τ is in the few tens of picoseconds timescales. We thus expect that our positioning of the zero value may have a systematic error below 50 ps.

It is however evident, even in Fig. 7.5 **a**, that the electronic hybridization is suddenly quenched by the pump pulse. The changing of the peak structure follows a complex dynamical behaviour. At zero delay the peak shows a significantly reduced LBES, but no significant changes of the HBES, which would accompany an equilibrium increase of temperature. At positive delays, the Mn $2p_{3/2}$ shows an increased intensity in the HBES and a completely quenched LBES. At longer delays, both peaks slowly recover, with slightly larger spectral weight left for the HBES.

These measurements were repeated in three separate beamtimes at BL19XU, and consistent results have been obtained on different replica samples of nominally identical composition, confirming reproducibility.

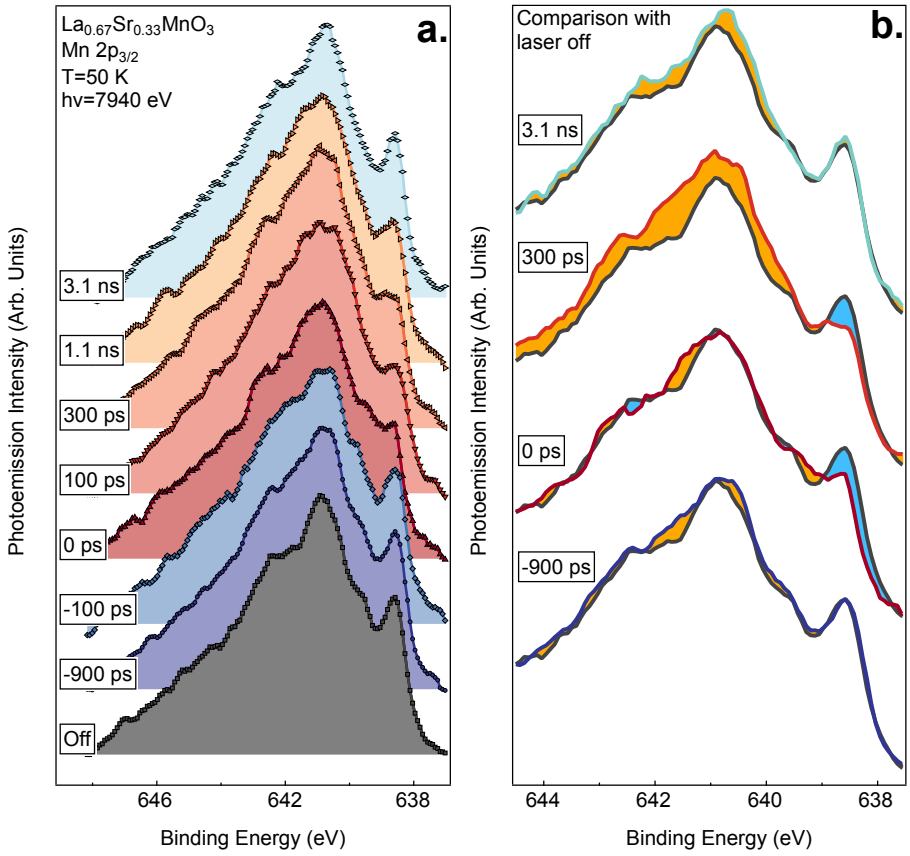

Figure 7.5: **a**. Time Resolved HAXPES spectra of the LSMO/LSAT sample measured at 50 K, with 8 keV photon energy. The black curve is acquired in the laser off mode, negative delays are in blue, positive delays range from red (shortest) to green (longest). The curves are vertically shifted for clarity. **b**. Selected curves from in panel **a**, each one compared with the black "laser off" curve. The fill-to-next curve shading is blue when the "laser on" curve is smaller than "laser off", yellow when it's bigger.

7.3 Discussion

We can assess qualitatively the evolution of the system by comparing the traces measured at short positive delays with the ones observed for the quasi-equilibrium temperature variations discussed in Chap. 3.3.1.

In Fig. 7.6 **a**, it is therefore shown the difference between the lowest temperature reached in the quasi-equilibrium measurements and room temperature. Due to its strong connection with the magnetization, the peak shows little evolution at temperatures lower than 150 K, thus the quasi-equilibrium spectrum at 150 K can qualitatively be confronted

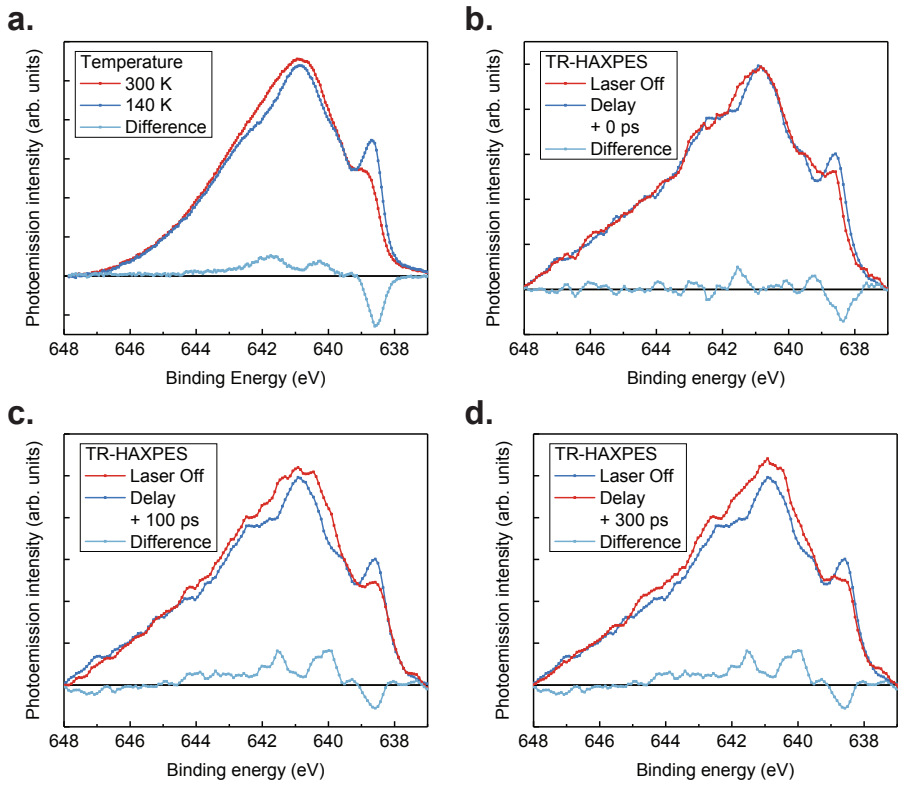

Figure 7.6: **a**. Quasi-equilibrium curves from Chap. 3.2.3. Measured at I09 on the same LSMO/LSAT sample, with energy resolution of $\Delta E = 200meV$. **b**. "Laser off", "laser on" and difference curves at 0 ps delay. Initial sample temperature: 50 K. **c**. Same as in panel **b**, but at 100 ps delay. **d**. Same as in panel **b**, but at 300 ps delay.

with the laser-off at 50 K.

The choice of the quasi-equilibrium high temperature spectrum, besides the qualitative agreement, is dictated by a rough estimate of the temperature shifts, extrapolating the results of Sect. 6.3.2. As can be seen in Fig. 6.10, the trend of the amplitude of the maximum Kerr ellipticity variation at medium-high fluences and low temperatures is substantially linear. It is therefore possible to convert the total quench variation in a total temperature variation with the simple scheme of Fig. 6.9 **a**, obtaining shifts of 52, 76 and 100 K respectively. By extrapolating to the high fluences used here, we obtain a temperature shift of 200 K, which, starting from the 50 K initial temperature, puts the pumped spectrum in the 250-300 K range. Clearly this estimate is highly approximated due to the large extrapolation steps, but it somewhat adds strength to the choice of 300 K for the high temperature spectrum.

In comparing Fig. 7.6 **a** with the other panels (**b**,**c** and **d**), the reduction of the detector dynamical range at lower intensities is evident: the curvature at high binding energies

due to metallicity is flattened to an almost linear slope. Furthermore, the difference in resolution is clear in the width of both the main peak and the satellite. In this qualitative comparison, attention should be turned more to the amplitude of the LBES and HBES variation than to the fine details of the structure widths.

As it can be seen, the spectra in panels **c** and **d** are clearly qualitatively comparable to the quasi-equilibrium ones: in the difference spectra the HBES shows a distinctive two edged structure, while the LBES is reduced. On the other hand, in panel **b** a different structure is observed, with the HBES substantially unchanged, while the LBES is already significantly quenched.

The results of the HAXPES measurements can be collected together in two time traces showing the variations in amplitude of the LBES and HBES as a function of the delay. Integration of the difference spectra in the two regions of the LBES (639-641 eV) and HBES (641-646.5) at each delay gives the two curves of Fig. 7.6 **b** and **c**. The vertical error bars are obtained by the integral of the difference between laser off and the most negative delay: the absolute value of their deviation from zero gives an estimate of the uncertainty on the integrals due to the measurement noise. The horizontal error bars are instead given by the probe pulse duration of 40 ps. The two curves clearly show mirroring dynamics, except for the fact that the HBES varies with a delay from the LBES, as expected from Fig. 7.6.

The analysis of the dynamical evolution of the Mn $2p_{3/2}$ peak thus shows a picture consistent with the one obtained from the Kerr measurements, but points more directly to the collapse of electronic hybridization.

By optical infrared pumping the electronic system is excited at short timescales. The hot electron distribution relaxes very rapidly by transferring heat to the lattice on the scale of few hundreds of femtoseconds to one picosecond, as suggested by the optical reflectivity measurements. At this point the system has a high electronic temperature and an increasing lattice temperature as the internal degrees of freedom of the lattice system equilibrate.

This triggers a long lived rearrangement of the electronic structure, as the system moves towards the phase transition. As delocalization is achieved in LSMO by the double exchange mechanism, it is unavoidably tied to the magnetic order, whose collapse is slowed down by the blocking of small energy magnetic excitations (spin-flip or one-magnon). The bandstructure remains therefore out of equilibrium for very long times, to the point that the 40 ps synchrotron pulse is able to detect a non-thermal lineshape of the Mn $2p_{3/2}$. This can be linked to the observation of different dynamics for the Kerr rotation and ellipticity, which show the largest discrepancy in the first 50-70 ps (Fig. 6.5 **c**).

After 100 ps, the electronic structure is equilibrated: the Kerr ellipticity and rotation are substantially closer to each other, and the HAXPES spectra recover the equilibrium shape. The system is quenched for a few hundred picoseconds, and then the recovery by substrate cooling begins, taking place in the nanosecond timescale.

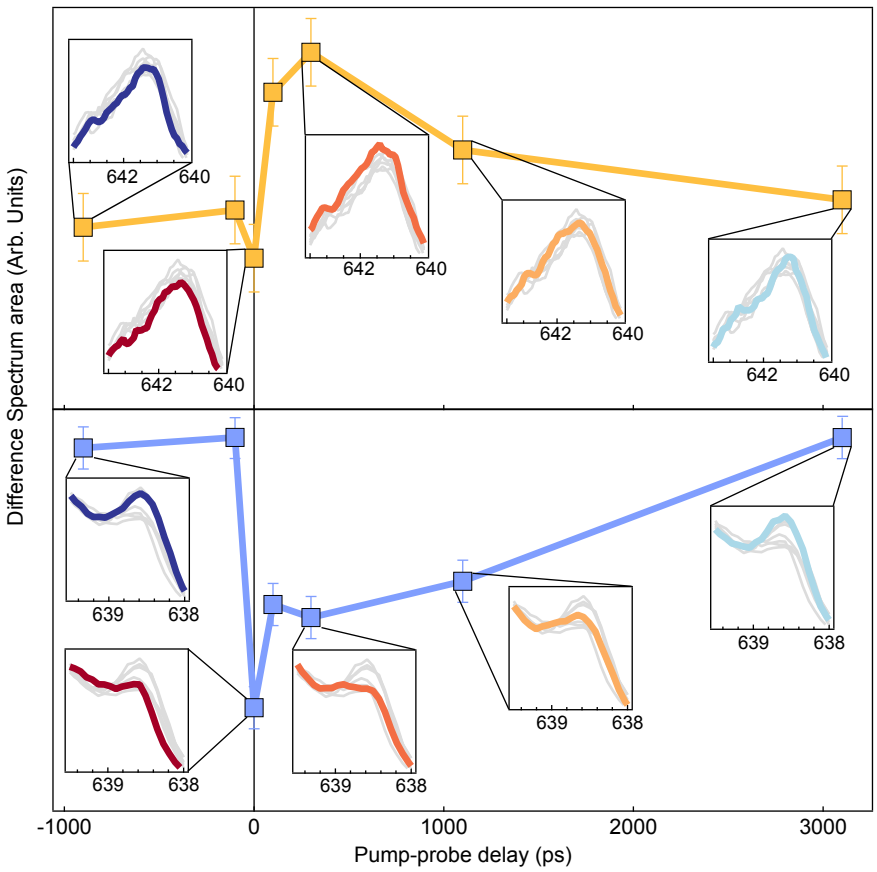

Figure 7.7: Top panel: evolution of the integral of the difference spectra in the HBES region. Bottom: evolution of the integral of the difference spectra in the LBES region. The insets show the HAXPES lineshapes in the corresponding regions (thin gray curves). Selected delays are highlighted by the thicker coloured line.

Summary of Part II

In this Part, the characteristic timescales of the relaxation of the electronic structure of LSMO samples is explored, combining TR-MOKE and TR-HAXPES measurements. LSMO represents an excellent candidate to begin the exploration of the dynamics of correlated electron materials, because its metallic phase is dominated by the delocalization due to the double exchange interaction. The complexity of phase competition and electronic disordering is thus reduced to a minimum. As a consequence of this, the magnetic response of LSMO is the closest to an Heisenberg ferromagnet that can be achieved in doped manganites (Salamon and Jaime, 2001), thus simplifying the picture of its magnetic characteristics. This gives the possibility of comparing the results to several interpretative tools developed in the field of ultrafast magnetism, thus allowing to achieve a more sound interpretation of experiments.

We studied the optical response of LSMO to shortly-pulsed infrared excitation. We measured films in two different strain states, namely relaxed and 1% tensile (due to, respectively, growth on a LSAT and STO substrate). As we aimed at exploring the PIVTS and PIPT-QP dynamics, we spanned the widest range achievable in terms of initial temperature (150 K - 400 K), and in terms of pump fluence (0.6-3mJ/cm^2).

The observation of the reflectivity dynamics (Sect. 6.2.1) yielded important information, as the characteristic spike indicating the sudden raise in the electronic temperature is observed. The electrons then lose energy by equilibrating with the lattice, with a characteristic time of 160 ± 70 fs, thus completing the process within 1.2 ps. This time-scale is weakly dependent on the temperature, supporting the idea that the observed spike is due to hot electrons.

As the temperature of the lattice is suddenly increased, however, it triggers a long-lived rearrangement of the electronic structure, due to the bottlenecked collapse of the double exchange coupling and thus the crossing (or the approaching) of the phase transition. In the reflectivity this translates in the DSWT, a further increase at the probe wavelength of 400 nm, due to the increase in spectral weight of high energy features at the expense of the Drude peak. Its temperature dependence clarifies its connection with the critical temperature.

In the tensile strained sample we detect a periodic modulation of the reflectivity that can be explained as a coherent shock-wave travelling through the thickness of the film. The moving surface Doppler-shifts the reflected probe beam, thus producing the interferential periodic behaviour. The period of the modulation is in an order of magnitude agreement with the speed of sound in LSMO, as measured with a more accurate multi-wavelength study (Ren *et al.*, 2007).

Such a long persistence of the coherent oscillation is interesting on an applicative side, as it suggest the possibility of manipulating precisely variations in the strain state of the sample. It would, for example, be interesting to explore the possibility of quenching the oscillation by a second, timed pump pulse. It may be possible not only to activate an effect on extremely short time-scales, but also to de-activate it, a characteristic which is highly sought after, but rarely found. Even if the magnetic or transport properties of LSMO were not to be influenced drastically by such effect, as suggested by our results, it would then be possible to interface it with other materials with larger piezo-response.

On the other hand, it also raises a more fundamental question on which times are necessary to consider the phonon system internally equilibrated, as until the coherent vibration is completely damped, there is a persisting dissipation of energy to the incoherent vibrations. This complicates significantly the interpretation of data, and we thus chose to focus on the strain relaxed sample, where the shock-wave effects are hardly visible, leaving the exploration of such interesting feature to future dedicated work.

The measurement of the magneto-optical response evidenced significant discrepancies between the dynamics of the ellipticity and the rotation signal, that persisted for several hundreds of picoseconds, as reported in Sect. 6.2.2. An in-depth analysis of the dynamical MOKE signal supports the attribution of such difference to significant evolution of the optical constants, leading to a time-dependance of the Fresnel coefficient that multiplies the measured component of $\vec{M}$ to give the complex Kerr angle. This is in agreement with the picture of the electronic structure undergoing significant rearrangement on long time-scales that derives from the presence of the DSWT in the reflectivity curves.

The ellipticity and rotation traces can be combined to give the modulus of the complex Kerr angle (Sect. 6.3.1). This observable has a more clear-cut dependence from the modulus of the Fresnel coefficient and the modulus of magnetization, allowing for confrontation with other studies (Carpene *et al.*, 2013), and thus qualitative labelling of the two phases of the MOKE dynamics. The sharp decrease that is rapidly recovered, either completely (closer to T_C) or partially (further below T_C), can be identified as an effect of the dynamics of the diagonal elements of the dielectric tensor, influencing strongly the evolution of the Fresnel coefficient at the shortest delays. At longer delays, instead, the evolution of the signal is dominated by the change in amplitude of the magnetization.

At the longest timescales we detect the long characteristic times typical of half-metallic materials. The demagnetization is indeed completed in times longer than 200 ps, in agreement with the results of (Müller *et al.*, 2009). This allows for the application of half-metallic magnetization dynamics as described in Sect. 5.2.1 and Sect. 5.2.2, in the limiting case of particularly weak anisotropy. At the shortest timescales, the MOKE

signal is blinded by charge effects, and it is not possible to draw conclusions on the magnetization dynamics in an highly non-equilibrium electronic configuration.

As confirmed in Sect. 6.3.1, the dynamics of Kerr ellipticity and rotation shows the same features at long timescales as the modulus of the complex Kerr angle. It is thus possible to perform comparative analysis, even quantitatively, of the sole ellipticity signal as a function of the fluence and the sample initial temperature (Sect. 6.2.3). The analysis of the amplitude of the total variation of the magnetization (maximum quench) can be consistently carried out in a picture of constant, large variations in the spin temperature, that move the the system closer to (or above) the Curie temperature. A quantitative analysis allows to estimate the maximum variation of temperature to be around 100 K at the maximum fluence. The variation of the amplitude as a function of the fluence can also be coherently explained as arising from shifts in temperature of the spin system.

The characteristic time of the long demagnetization can be studied. In general, a slowing down of the demagnetization process can be expected, both because as T_C is approached the anisotropy energy decreases and the spin system becomes increasingly thermally insulated, and because in the vicinity of the criticality the spin specific heat diverges. An effective way to assess quantitatively this problem is to borrow from the renormalization group theory that defines precise critical laws for the dimensionality and type of magnetic interaction. Our result is fully consistent with the critical behaviour of a three dimensional double-exchange ferromagnet.

By changing the probe to the HAXPES Mn $2p_{3/2}$ satellite feature whose static characteristics were deeply scrutinized in Part I, we obtain two significant advantages. The first is that no intrinsic effects can blur or even completely obnubilate the effect of interest, as we address a precise final state of an high energy interaction. The second is that we challenge the problem of the relaxation of a sudden excitation by directly looking at the electronic hybridization in the crystal. We are thus reversing the perspective with respect to the optical measurements that are sensitive to the macroscopic magnetic ordering. The hundreds of picosecond timescale of the processes allows to perform the experiments in a synchrotron, thus advantaging of what is at present the largest flux available for time-resolved HAXPES experiments.

The observation of the HAXPES lineshapes as a function of the pump-probe delay is performed in a comparative way (Sect. 7.2) to rule out any effect due to the broader resolution and the reduced dynamical range available as an effect of the limited count rate. The Mn $2p_{3/2}$ line is measured in the same conditions, but with the pump laser blocked can be confronted with the negative time delays, confirming that the equilibrium state at the lowest initial temperature is achieved in both cases and no DC-heating is present. The first spectrum with modified lineshape is labelled as "zero ps" delay. After time zero, the low binding energy structure is quenched at the 100 ps and 300 ps delays. The successive delays of 1 ns and 3 ns show a recovery to the initial lineshape.

On the other hand, the high binding energy structure, that is observed to vary in quasi-static changes of temperature (Sect. 3.3.1), seems to follow the dynamics of the LBES symmetrically, except for the point at 0 ps delay. The strongest result of this

study is therefore that dynamics of the electronic hybridization follows the long timescale dynamics of the demagnetization. The photoexcited system is effectively bottlenecked and, although the electronic temperature is increased suddenly, the thermal insulation of the magnetic ordering preserves the electronic hybridization for long time. Only when the increase of temperature of the lattice quenches the magnetic order, the electronic hybridization is suppressed. The HAXPES spectra become then comparable to the ones observed at temperatures closer to T_C.

Only the 0 ps delay seems to show a significant discrepancy between the dynamics of the two substructures of the peak. Representing a single point in the delay series, it must be interpreted with caution. As a part of the series it certainly defines the beginning of the peak shape evolution as precisely as allowed by the 40 ps pulse, and substantiates the claim that delays in the order of 100 ps are necessary to go from a non-equilibrium spectrum to a quenched equilibrium lineshape.

Further interpretation of its individual shape would be speculative, as none of the spectra calculated for equilibrium states suggests reasons why the dynamics of the LBES and HBES could be decoupled (Sect. B). It would therefore be necessary to develop a modelling of the response of the solid that is able to account for its non-equilibrium condition. A starting point could be the connection with the long-lived discrepancy between the Kerr rotation and ellipticity, which is maximal at short timescales. Naturally this is only an argument based on the similarity of timescales and qualitative relation to dynamical rearrangement of the electronic structure. Further experimental evidence and modelling work would surely be beneficial.

The work presented here demonstrates how the application of HAXPES in the time domain can give important information on the evolution of the electronic structure of complex oxides, overcoming the surface issues that limits the standard forms of photoemission and describing clearly the evolution of the electronic structure. There are thus several interesting directions in which these results can be developed.

The most desirable progress is clearly improving the temporal resolution. Yet, as discussed in Sect. 4.3.2, the availability of sources is rather limited. Owing to the limitation in the maximum number of photons per pulse due to the space charge and in the maximum repetition rate due to DC-heating, it appears that only high repetition rate Free Electron Lasers could achieve sufficient average flux.

Another possibility, with much higher accessibility and feasibility, is provided by Inverse Compton Scattering sources (Serafini *et al.*, 2016), that produce hard X-rays pulses by electron-photon scattering. These sources can operate in the kHz to tens of MHz range and produce hard X-ray pulses (3 keV - MeV). The number of photons per pulse goes from below to above the space charge limit (10^5-10^8 ph/pulse), and the pulse duration can be in the hundred of femtoseconds range. Increasing the temporal resolution would allow to deepen the comprehension of the non-equilibrium state of materials.

A second development, that might be achievable with the technology presented in this study, would be the further exploration of the fascinating properties of correlated electron materials under photoexcitation. By complicating the free energy landscape

with narrower bandwidth materials, it is possible to attempt the photocontrol of phase competition. A particularly appealing experiment is the sudden release of carriers trapped in cooperative polaronic phase of LCMO, thus accessing the magnetically ordered and conducting hidden phase, which gave spectacular results when investigated in THz experiments (Zhang *et al.*, 2016).

Time resolved HAXPES might also be employed in the study of coherent vibration of the lattice, that can have a profound impact on the response of these materials. This class of experiments can be realized by choosing a pump energy that is resonant with a particular IR-active phonon (Singla, 2015). An even more refined mean of pump tailoring is the transient grating mechanism, where two pump pulses are made to interfere on the sample surface, producing a spatially periodic arrangement of pumped and un-pumped regions. This approach has been applied to the excitation of charge density waves in Cuprates (Torchinsky *et al.*, 2013).

Part III

Towards shorter time interval and length scales

Chapter 8

SPRINT laboratory

> [...] the time dreamers of SPRINT laboratory.
>
> G. Rossi, 2017

On account of several of the points emerged in Part II, it is clear that the real-time investigation of the dynamics of solids requires understanding of the trigger mechanisms of the evolution towards equilibrium order parameters, and the methods to address it are rapidly progressing. In this thesis, we came across numerous complex phenomena that call for pump-probe experiments to be properly addressed, such as the multi-faceted character of the dynamics of magnetization (Chap. 5), the fundamental understanding of the interactions driving ordering in correlated electron materials, and the optical triggering of quantum phase transitions (Chap. 4).

We also demonstrated how the technique of photoelectron spectroscopy allows for a different perspective from optical experiments, which is especially useful in the case of the bandstructure of correlated electron materials, where optical experiments are challenged by significant dynamical rearrangements the DOS. We therefore directed our efforts in the development of instrumentation and methods to contribute to the expansion of the field with such a complementary perspective.

In parallel with the pioneering of pump-probe HAXPES, we thus designed and built a laboratory for the realization of time-resolved photoelectron spectroscopy with soft X-rays, advantaging of the extraordinary potentialities of frequency upconversion unlocked by high power femtosecond laser sources. The Spin Polarized Research Instrument in the Nanoscale and Time domain (SPRINT) laboratory is open to users in the framework of the NFFA-Trieste project, a novel facility to be added to the single-access-point network of facilities across Europe (NFFA-Europe).

NFFA-SPRINT aims to fulfil two parallel objectives:

1. Apply the powerful insight of time-resolved soft X-ray photoemission to explore the non-equilibrium bandstructure of solids (Smallwood *et al.*, 2016), with particular attention to systems in which the spin degree of freedom plays a crucial role in

the ordering of the material. The instrumentation is thus oriented to the measurement of the electronic structure of the solid by angularly resolved photoelectron spectroscopy, and to the measurement of the magnetic state of the material, by the direct means of spin polarimetry.

2. Bridge the gap, in terms of scientific problems and of experimental approaches between synchrotron-based equilibrium spectroscopy and FEL-based high-energy density spectroscopy. For this reason, the laboratory is located in the experimental hall of Fermi Free Electron Laser, but powered by an dedicated laser source. Proof-of-principle experiments and instruments can thus be tested with the flexibility of this sandbox set-up, avoiding the competition due to single beamline operation, that arches over all the fields of FEL-based science. The same endstation (SPRINT-Ultraspin) is designed to be also connected to FEL sources, once the necessity and the ability to assess high excitation densities is demonstrated.

Indeed, the scientific community has developed a robust competence in realizing photoemission experiments with continuous sources such as Helium discharge lamps and continuous wave lasers, or quasi-continuous sources such as synchrotrons and laser oscillators. The machines for the realization of equilibrium advanced photoelectric experiments are progressing at an increasingly rapid pace and achieving extremely high resolutions and efficiencies. But when photoemission is attempted in FELs, which achieve even higher brilliances but concentrating exorbitant peak fluxes in extremely short times, the vacuum space charge effect and the intrinsically multi-hit detection force a radical rethinking of the experiments. Observables that are robust against the stochastic effects of space charge must be individuated, and detection schemes must be devised so that large peak photoelectron currents can be detected.

8.1 Sources and instrumentation

A facility with such objectives must rely on a photon source of extreme adaptability in terms of repetition rate, energy per pulse, and wavelength tunability. We thus resorted to high repetition rate high harmonics generation (HHG) from a gas jet (Lindner *et al.*, 2003; Chen *et al.*, 2009; Heyl *et al.*, 2012). A wealth of laboratories based on this kind of sources has recently flourished (Buss *et al.*, 2017; Plötzing *et al.*, 2016; Carley *et al.*, 2012; Crepaldi *et al.*, 2017; Locher *et al.*, 2014), although only few reach adequately high pulse repetition rates (>100 kHz) and are designed as facilities open to users (Turcu *et al.*, 2009).

8.1.1 The high harmonics generation process

The HHG process, observed for the first time in its modern form by McPherson and coworkers (McPherson *et al.*, 1987), consists of a non linear process. By focussing an optical or infrared laser with high peak power (above $10^{14}\ W/cm^2$) on a low density inert gas, indeed, the generation of odd harmonics of the fundamental wavelength with

very high order (above the 17th) was observed. While simple considerations pivoting on the inversion symmetry of gases explained the fact that no even harmonics are produced, the intensity of the highest harmonics orders was not understandable in terms of the perturbative models used then.

An in-depth discussion of the complex non-linear mechanism at the basis of this phenomenon is beyond the scope of this thesis, and we will thus resort to the simplest picture (Popmintchev *et al.*, 2010), illustrated in Fig. 8.1. The process, which in more advanced models is considered as a unique coherent process, is here broken down in three steps.

A mono-atomic gas is assumed for simplicity. When the large electric field of the optical or infrared fundamental pulse perturbs the atom, the outer shell electrons can be ejected by strong field ionization. The ionized atoms can be a very large fraction of the gas, up to several percent. The fundamental field drives the electron away from the ion, but as the optical cycle is completed, the field reverses its spatial direction. The electron is then driven back to the ionized atom. In the process, the electron absorbs a large number of photons, and when it recombines with the ion it emits an high energy photon at an odd harmonic of the fundamental.

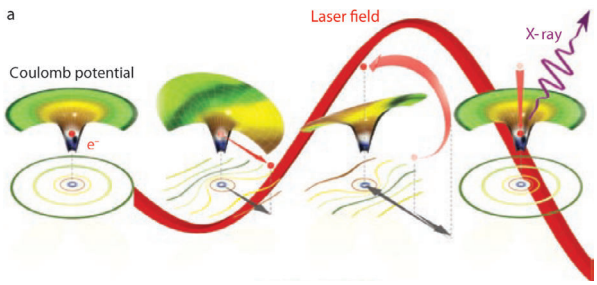

Figure 8.1: Schematic representation of the three step model of HHG. From (Popmintchev *et al.*, 2010).

Clearly, in the simplicity of this picture, the importance of the coherence of the driving field is somewhat hidden by the single-particle picture. It anyway allows to understand the simple formula that defines the "cut-off" energy after which the intensity of the harmonics drops rapidly:

$$h\nu_{cutoff} = I_p + 3.17U_p \approx I_L\lambda_L^2 \tag{8.1}$$

Where I_p is the gas ionization potential and U_p is the ponderomotive energy, i.e. the average energy of an electron in an electric field of intensity I_L and wavelength λ_L. The last term of the equality shows that very high energies can be reached by driving the gas with sufficient intensity.

The preservation of the coherent superposition of the fundamental and the harmonics within the interaction region, called *macroscopic phase-matching*, is necessary for the realization of the addictive superposition of single atom emission. There are indeed several factors that prevent the **k**-vector of the harmonics from being identical (modulo 2π) to the **k**-vector of the fundamental in the whole interaction region, and at any time t. In general, four important factors are identified (Heyl *et al.*, 2012): a single atom dipole phase arising from the complex character of the polarisability, a geometrical term due to the divergence in the fundamental produced by focussing, a term due to dispersion in the neutral gas, and one due to dispersion in the ionized plasma. These quantities have different signs. This can be exploited to compensate them reciprocally in the interaction

region.

Several strategies are used to realise the phase matching. If very large pulse power can be achieved (in the order of several mJ/pulse), it is not necessary to focus strongly the fundamental to achieve sufficient power density. The geometrical dephasing is thus small, low densities of gas allow to tune precisely the refraction indices even in long interaction regions. This configuration is achieved with low repetition rate (< 1kHz) Ti:Al_2O_3 lasers, and the use of gas cells or hollow optical fibers.

If higher repetition rates are sought after, instead, another approach is necessary. Indeed, state of the art commercial lasers are generally limited to few tens of watts, thus resulting in sub-mJ pulses at several hundred kHz. In these conditions, a tight focussing geometry is required to achieve sufficient power densities. The fundamental spot is focussed to achieve a few tens of microns beam waist, thus reaching the strong ionization threshold. As a consequence, the geometrical phase becomes significant and larger variations of the gas and plasma index of refraction are needed to compensate for it. The gas pressure must be increased up to the bar range. In these conditions though, the gas and plasma are strongly absorptive, and the region of interaction must be limited. The tight focussing geometry is therefore realized by concentrating the fundamental on an high pressure jet expanding in vacuum from a narrow capillary nozzle.

It is this geometry that allows to realize HHG even with high repetition rate Yb:KGW lasers (Lorek *et al.*, 2014; Boullet *et al.*, 2009). These ultrafast regeneratively amplified lasers have extremely high stability, and very reliable tunability of the repetition rate in the kHz to MHz range. They thus combine the elasticity desired for the SPRINT laboratory project to reliability, ensuring efficient operation of the facility.

8.1.2 Beamline design

The system for the generation of the soft X-rays via the HHG process, and the subsequent optics required to prepare the radiation for the transmission in the experimental chamber form a proper compact beamline, sketched in Fig. 8.2. The SPRINT laboratory is a facility combined in a twin-beamline laboratory with Elettra Time-resolved photoelectron spectroscopy facility T-REX.

Laser source

The laser source **LS** is the work-horse of the laboratory. It is a commercial PHAROS 20 W Yb:KGW fiber laser, provided by Lightconversion. It encloses, in a compact single casing, the oscillator, the pump diodes, the regenerative amplification cavity. The cavity achieves maximum peak power at a repetition rate of 50 kHz, delivering pulses of 400 μJ energy and 290 fs duration at 1030 nm wavelength (**IR**), corresponding to peak power around 1 GW/pulse.

Increasing the repetition rate reduces linearly the energy per pulse, as the maximum average power in the cavity is anyhow limited to 20 W. The repetition rate can be increased up to 1 MHz. To achieve repetition rates below 50 kHz, a set of Pockels cells

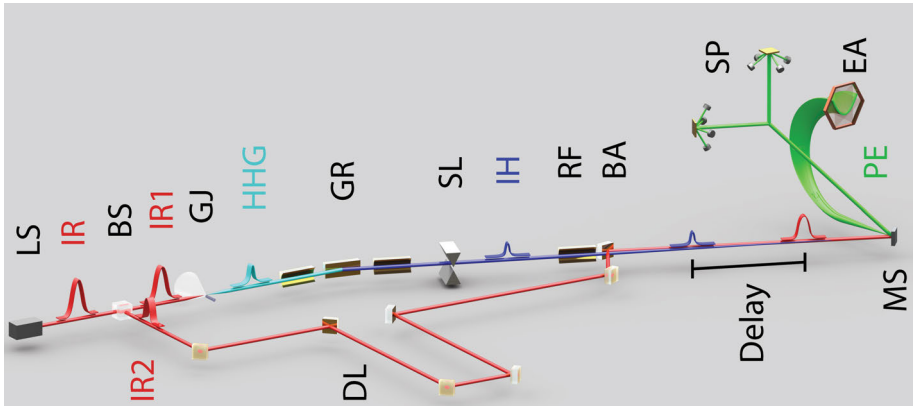

Figure 8.2: Scheme of the SPRINT lab laser beamline. The laser source (**LS**) delivers 400μJ, 300 fs pulses (**IR**) at λ=1030nm at 50 kHz. After a beam-splitter (**BS**) the pulses (**IR1**) are tightly focused in a gas jet (**GJ**) to produce HHG. A single harmonic (**IH**) is then isolated with a monochromator (**GR**+**SL**) and focused (**RF**) in the endstation. A part of the infrared beam (**IR2**) is separated with a beamsplitter (**BS**) and sent through a delay line (**DL**) to implement a quasi-collinear (**BA**) pump-probe measurement scheme. The probe, absorbed by the sample (**MS**), ejects photoelectrons (**PE**), detectable by the Mott polarimeter (**SP**) or energy analyser (**EA**).

is used as a pulse-divider, allowing to drop some of the pulses. The energy per pulse therefore does not increase below 50 kHz, and the average power decreases. The system is capable of single pulse operation.

The pulse duration can also be changed, by chirping the output up to 10 ps. The PHAROS system is designed for "turn-key" operation: an highly integrated software controls the feedback loops to achieve the desired mode of operation, that the user demands by simply choosing the relevant parameters. Security protocols to safeguard the integrity of the optics are also implemented. The PHAROS also features an high power and positional stability in a temperature controlled low humidity environment.

A second laser system can be used to perform high peak power, low repetition rate (FEL-like) experiments. It is a 1 kHz, 8 mJ/pulse, 100 fs Ti:Al_2O_3 doubly amplified laser system, Coherent Legend Elite DUO.

The output of the PHAROS system can then be directly extracted, or driven in a pair of high power optical parametric amplifiers. These systems generate the second harmonic of the fundamental with high efficiency, produce white-light supercontinuum in a non-linear crystal and amplify a selectable wavelength of the white-light by exploiting dispersion and synchronization. This process results in an almost continuously (5 nm steps) tunable wavelength conversion with more than 10% efficiency. The two Lightconversion ORPHEUS-HP and ORPHEUS-ONE cover, respectively, the ranges 630-2600 nm and 1340-4000 nm. They can be used to tailor both the energy of the pump and the probe, allowing to span a wide spectrum of possible excitations.

Generation of harmonics

The beam is splitted (**BS**) in a part dedicated to the generation of harmonics (**IR1**) and one dedicated to the formation of the pump (**IR2**) the ratio is usually 90% to 10%, but it can be changed. The pump pulse is sent through a delay line (**DL**), and realigned with the HHG beam by a specially shaped straight-edge mirror (**BA**) before entering the experimental chamber and impinging on the sample. The second beam enters the beamline vacuum system from an anti-reflective window, accessing the generation chamber. The chamber contains a short focal length lens (f=10 cm). This produces a 40 μm gaussian beam waist, leading to a peak intensity of $10^{14} W/cm^2$ at 1 GW/pulse.

The tight focussing geometry requires however an effective gas jet (**GJ**) delivery and control. In the case of the SPRINT beamline, a glass capillary nozzle with a very sharp tip (70 μm internal diameter and 100 μm external diameter) is positioned in the vicinity of the laser focus by a micrometre precision manipulator. The whole interaction region is enclosed in a case that is directly pumped (via an in-vacuum high diameter tube feedthrough) by a 350 m^3/h primary pump. The case is open to the vacuum only through pumping inductances in the direction of the laser beam. The chamber itself is pumped by a 2000 l/s magnetically levitated pump, and a 35 m^3/h primary scroll. The redundant pumping has been designed to allow operation even in high backing pressures of the nozzle (up to 10 bar), and to reduce the pressure as close to the laser focus as possible, in order to avoid x-ray absorption.

Monochromatization

The harmonics are then propagated through a pinhole, and enter the monochromator chamber (**GR**). Here they are isolated by a single grating monochromator that conserves the time duration of the pulse. Indeed, due to the effect of diffraction of a soft X-ray beam from a grating, the pulse can be temporally stretched by several hundreds of femtoseconds: each ray diffracted at the same order by two adjacent grooves is delayed by one wavelength, resulting in up to 1 ps broadening in high density gratings.

A solution to this problem comes from the work of Frassetto and colleagues (Frassetto *et al.*, 2011), that developed a single-grating monochromator in which the grooves are parallel to the plane of propagation of light. In this configuration, the front of each harmonic is not tilted, and rays of the same energy travel the same optical path.

To maximize the efficiency, these optics are operated in the off-plane geometry: an entrance toroidal mirror collimates the beam and deviates the rays to impinge on the grating surface. The harmonics of different energy are dispersed in the direction perpendicular to the beam propagation plane. By rotating the grating along the optical axis of the system, the desired spectral range is reflected on a second toroidal mirror, which focuses horizontally the radiation.

In the focus is placed a set of vertical slits (**SL**) that selects a narrow bandwidth. It must be noted, however that the resolution of this kind of monochromators is rather poor: they serve only to isolate a specific harmonic, while it is the intrinsic linewidth that

determines the final photon energy resolution.

In SPRINT beamline, the monochromator is actually formed by a set of five different gratings and three mirrors. Indeed, it also acts as a switch that deviates the soft X-ray beam in the two endstations attached to the source. The entrance mirror is common, but two gratings send the beam to the T-REX branchline, while the other three deliver it to SPRINT laboratiry endstation: Ultraspin.

The three gratings have 150 gr/mm, 400 gr/mm and 1200 gr/mm and are aimed at covering, respectively, the ranges 8-30 eV, 30-50 eV, 50-100 eV with resolution $\Delta E \approx 2eV$, sufficient to separate the harmonics. The isolated harmonics (**IH**) are then measured in intensity in a dedicated chamber where a channeltron can be inserted in the beam and the photocurrent measured.

On August 18, 2017, the plasma was first generated in the Argon gas jet, as shown in Fig. 8.3. Few days later, on August 25, 2017, sharp peaks in the emission could be detected on the channeltron current as the 400 l/mm grating was angularly scanned. The first part of the beamline is thus operating and characterization work is under way to optimize the emission. Given the characteristics of a similar set-up, described in (Lorek *et al.*, 2014), we expect the achievement of similar fluxes, in the order of 10^{10}-10^{9} ph/s per harmonic.

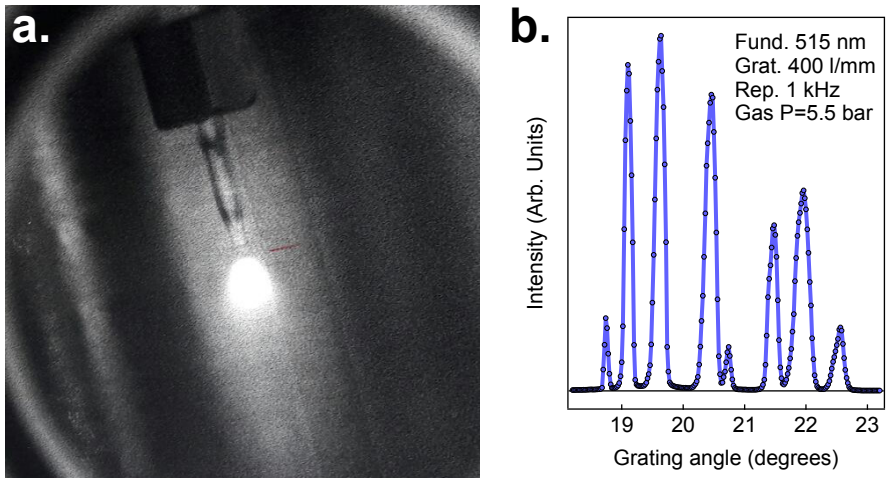

Figure 8.3: a. Photograph of the capillary gas nozzle. The white cloud in front of it is formed by the plasma of Argon atoms ionized by the fundamental beam. b. First scan of the harmonics emission at backing pressure P=5.5 bar, repetition rate 1kHz. The mid-range 400 l/mm grating is angularly scanned.

Transport and endstation

When the channeltron is removed, the harmonic can propagate to a refocusing mirror (**RF**) that compensates the horizontal divergence due to focussing on the slits. The beam

then grazes the edge of the beam alignment mirror (**BA**) and propagates quasi-collinearly to the pump beam onto the sample (**MS**) in the endstation.

Ultraspin endstation is formed by two spherical UHV chambers. Its status during off-line commissioning is described in detail in (Pincelli, 2014; Pincelli *et al.*, 2016). For the sake of the fluidity of the discussion we will report here only the most important characteristics.

The first chamber is dedicated to preparation and basic characterization of samples with the standard techniques of surface science: ion bombardment, annealing at various temperatures, LEED, Auger Electron Spectroscopy, evaporation of metallic thin films. The second one is devoted to advanced experiments with photoemission. It hosts a Vectorial Compact Classical Mott detector (Petrov *et al.*, 2003), that measures the spin polarization (**SP**) of the secondary electrons (Pincelli *et al.*, 2016), and a Scienta SES 2002 electron energy analyser (**EA**). For static measurements, an high brightness Helium discharge lamp is operative.

Each of the main parts of this chamber is object of a separate project to advance its functionality:

- The spin detector has undergone a revolution in its detection electronics, realizing a machine capable of spanning both the heavily multi-hit regime of FEL-like experiments and single electron counting modes of synchrotron-like regimes. As it is somehow an example of the objectives of the laboratory, it will be discussed in a deeper detail in Sect. 8.2.

- The electron energy analyser is object of a two steps long term project in which the phosphor screen + CCD detection scheme currently operating will be first replaced by a delay-line detector, which has much lower dark noise. This can be beneficial to low S/N experiments with the HHG source, such as the detection of small features of the valence. Subsequently the possibility of acceleration and direct CCD detection will be explored, further improving the dynamical range of the instrument.

- The sample manipulator has been developed to provide an advanced and effective sample environment. It features three stages: one cryogenically cooled, with four independent electrical contacts. The second is a modular block, compatible with several possible designs of sample mounting devices, including the ones commercially available from Ferrovac GmbH. Finally the third one spans higher than room temperatures in the range of 500-600 K. An in-vacuum transferable system has been designed in order to mount magnetic samples directly on the poles of an electromagnet, thus closing the magnetic field lines in high permittivity materials. This will allow measurements with free electrons even under applied magnetic fields.

The laboratory is furthermore equipped with several advanced optical set-ups. The generation up to the fifth harmonic of the 1030 nm fundamental of the PHAROS allows to deliver in the vacuum chamber UV pulses of 206 nm, i.e. 6 eV photons (or 257.5 nm, i.e. 4.8 eV from the fourth harmonic). As a complementary technique, we plan

on implementing a TR-MOKE measurement set-up, that operates on the samples in the experimental UHV chamber. In the laser hutch, an all-optical transient grating set-up has started operation recently, developed by R. Cucini.

8.2 Development of a multi-hit spin detector

The development of this instrument is motivated by the fascinating physical problem of the complex dynamics of magnetic materials introduced in Chap. 5. In the progress of understanding the intricate set of individual mechanisms that ensue in an out of equilibrium magnet, many different processes have been proposed, ranging from spin-photon interactions to super-diffusive spin currents. Yet, as we have shown in Chap. 6 and in Appendix A, the interpretation of TR-MOKE data at shorter timescales is rather difficult, and requires complex measures and a sophisticated interpretative work. Furthermore, the discovery of longitudinal transport mechanisms either in the approach of superdiffusive spin-transport (Battiato *et al.*, 2010) or the diffusive model proposed by Fognini and coworkers (Fognini, 2014; Fognini *et al.*, 2017), has singled out the relevance of spatial inhomogeneities in these mechanisms.

We thus strived to apply the high degree of control that photoemission allows both on the spatial and temporal dimensions to the comprehension of magnetic dynamics at shorter timescales and at smaller depths in the solid. To do so, we developed an instrument that is intrinsically capable of operating with pulsed sources, namely with high peak photoelectron currents and with possible strong shot-to-shot fluctuations. Furthermore, we needed to address an observable that is resilient against the effects of vacuum space-charge.

8.2.1 Spin-polarization of the secondary cascade: a robust quantity

The pioneering work by Fognini and colleagues (Fognini *et al.*, 2014b,a) showed how the polarization of the secondary electrons in the lowest kinetic energy region of the spectrum is partially reduced, but not cancelled, even in high excitation density regimes. The polarization of the secondary electrons arises from a spin filtering mechanism. The low energy electrons have different IMFPs in a ferromagnetic material, depending on their spin state. Indeed, mainly due to the exchange interaction, the spin-resolved DOS of a ferromagnetic material is different for spin majority and minority electrons in the vicinity of the Fermi energy. This gives a different phase space for the scattering processes, thus yielding different lifetimes and IMFPs (Zhukov *et al.*, 2006). The differences in IMFPS can be quite large, with the majority up to 7 times larger than the minority (van Dijken *et al.*, 2002).

Schematically, as the low kinetic energy electrons, that have undergone numerous scattering processes, reach the surface barrier, the majority spin state (with longer $\mathrm{IMFP}_{\uparrow}$) is transmitted without further interaction. The minority state travels a shorter $\mathrm{IMFP}_{\downarrow}$ length and is depolarized. The majority electrons exit the solid and the minority depolarize again. At the end of such process, the emerging population of majority electrons is

larger than the minority, and a spin polarized signal is measured. Owing to the fact that it arises from a process iterated until the extreme surface, the information is retrieved from an small effective depth that is sometimes referred as *spin relaxation length*. Accurate measurements by Ta overlayer deposition (accounting also for the interface effects) put it at 5 Å for Fe (Paul *et al.*, 1991).

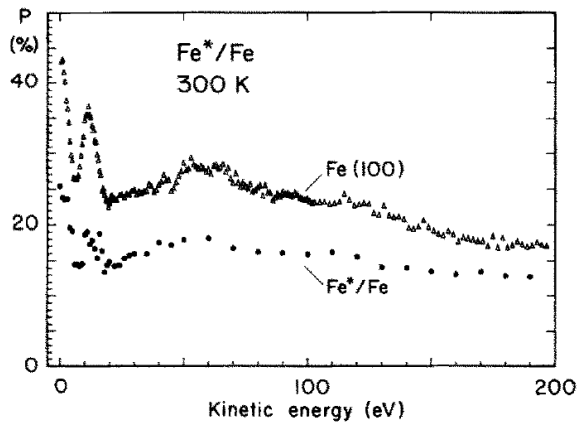

Figure 8.4: Spectrum of the spin polarization of the secondary electrons emitted from Fe. The bottom curve shows the deduced polarization of the iron crystal with suppressed polarization in the last layer. From (Paul *et al.*, 1991).

The measurement of the polarization of the secondary electrons is thus seen as a direct way to assess the magnetization of the surface of metallic materials. Its insensitivity to the space charge issue arises from the fact that the polarization of the secondary electrons does indeed reach the highest values at the lowest energies, but it is present (to still significant extent) across the whole spectrum (Fig. 8.4). In presence of vacuum space charge, the amount of low energy electrons accepted in the detector lenses is reduced, as they are pushed off-trajectory by Coulomb repulsion. The high energy part of the spectrum is thus still accepted, and it still carries a significant, exchange filtered polarization. In FEL based experiments (Fognini *et al.*, 2014b), no deterioration of the signal was observed until pulses of 20 μJ/cm^2 were used, and even at 400 μJ/cm^2 the absolute reduction of the signal was less than 10 %.

8.2.2 Importance of the detection scheme

In developing an instrument to address the spin polarization of the secondary electrons in high charge density regimes, we had to optimize the choice of the detection mechanism. The resolution of electron's spin degree of freedom has fascinated scientists ever since its introduction (Uhlenbeck and Goudsmith, 1926). However, since it has been demonstrated that Stern-Gerlach magnetic separation cannot be realized with electrons (Kessler, 1976), it was necessary to resort to spin-dependent scattering mechanisms of much lower efficiency. Several of them have been attempted, resulting in a vast possibility of choice in the instrument design.

The first to be used was high energy incoherent Mott scattering (Mott, 1929), in a sophisticated double scattering experiment (Shull *et al.*, 1943). This process is based on the relativistic spin-orbit effect, that becomes evident in incoherent scattering when the Coulomb contribution is minimized, i.e. at large scattering angles. In this kind of

measurements, the photoemitted electron beam is accelerated to impinge normally on a thin polycrystalline high Z target (e.g. Gold) target, and asymmetries are detected by counting the scattered electrons at symmetrical large angles (Fig. 8.5):

$$A = \frac{N_l - N_r}{N_l + N_r} \tag{8.2}$$

The asymmetry can be connected to the initial beam polarization component normal to the scattering plane by a coefficient, the *Sherman function*, that depends on the scattering energy and the detection angle.

$$P_\perp = \frac{1}{S} A \tag{8.3}$$

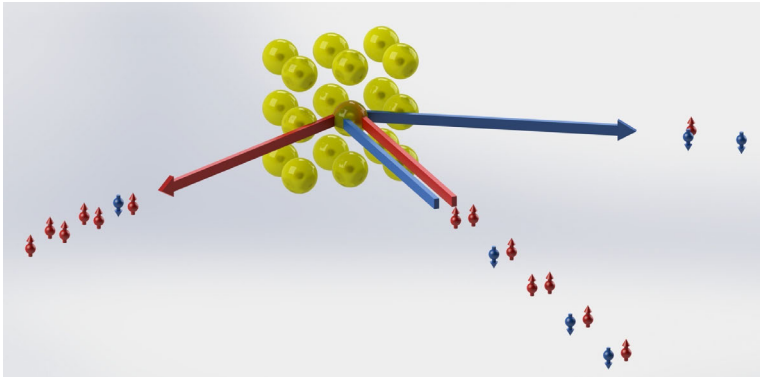

Figure 8.5: Cartoon scheme of Mott spin selective scattering. The yellow spheres represent the atoms of a gold scattering target. The small blue and red spheres stand for the spin up and down electrons. The coloured arrows show the directions of prevalent scattering of the corresponding spins.

The Shermann function defines the ability of the detector of separating spins, tends to increase with energy and has a maximum at 120° scattering angle. It can be calculated theoretically in the single atom limit, but in real polarimeters an *effective Sherman function* (S_{eff}) is obtained by calibration, accounting for multiple scattering effects. A relevant parameter for the evaluation of the efficiency of a spin detector is the *figure of merit* (ε):

$$\varepsilon = \frac{I}{I_0} S_{eff} \tag{8.4}$$

where I is the photoelectron current reaching the electron counters, while I_0 is the primary current impinging on the target. ε is considered as a quantifier of the statistical efficiency of the machine, because it appears in the calculation of the absolute error (ΔP) on a polarization measurement (Pincelli *et al.*, 2017a):

$$\Delta P = \frac{1}{\sqrt{N_0 \varepsilon}} \tag{8.5}$$

where it increases the error (in general $\varepsilon << 1$) with respect to the Poissonian uncertainty in counting N_0 electrons (as it would be in a spin-integrated spectrum).

Since the first experiments, spin detectors have been the object of constant evolution, as successive generations of physicists tackled the problem. For a detailed account of the successive developments of spin detectors, we refer to (Kessler, 1976; Gay and Dunning, 1992; Jozwiak, 2008; Dil, 2009; Schönhense *et al.*, 2015, and references therein). The detectors based on Mott scattering evolved to reach their maximum $\varepsilon = 6 \times 10^{-4}$, in a compact instrument, able to measure two components of the polarization vector simultaneously (Petrov *et al.*, 2003).

However, with the rising of advanced methods for surface preparation, a revolution came for the spin detectors when the low energy scattering begun to be used. Exploiting atomically ordered surfaces to produce the LEED specular reflection, the factor $\frac{I}{I_0}$ in ε was boosted by two orders of magnitude. Exploiting exchange interaction in reflection off a passivated Fe surface (Tillmann *et al.*, 1989; Bertacco *et al.*, 1998; Winkelmann *et al.*, 2008; Okuda *et al.*, 2011; Bigi *et al.*, 2017), or spin-orbit effect in the diffraction from 5d transition metals such as W (Kirschner and Feder, 1979; Feder, 1981; Kutnyakhov *et al.*, 2015), Ir (Kutnyakhov *et al.*, 2013), or Au passivated Ir (Kirschner *et al.*, 2013). In this case, using the LEED (00) beam, a single spin filtered beam is reflected. To evaluate asymmetry, one of the external parameters is changed, may it be the magnetization of Fe, a change in the scattering energy or an axial rotation of the Ir crystal.

Recently, the attention has been drawn on the enormous advantage of massive parallel acquisition, allowed by the availability of large Ir and W crystals of high crystalline quality (Schönhense *et al.*, 2015). In a flare, the collaboration between the groups in ETH Zurich, Universitat Mainz and MPI Halle advanced rapidly the technology of electron spectrometers. Recently an impressive machine has been demonstrated that measures the in-plane angular distribution, the energy distribution and the spin polarization simultaneously. It de-facto micro-tomographs the electronic structure in the five dimensional space of the electron degrees of freedom. The figure of merit was re-defined acquisition wise as:

$$\varepsilon = N_{pts} \times \frac{I}{I_0} S_{eff} \tag{8.6}$$

where N_{pts} is the number of independent points that can be acquired simultaneously. Whopping numbers up to $\varepsilon = 10^2$ have become possible.

Yet, these machines are limited to work as far as possible from the intrinsic space charge effects, which stochastically (and therefore irreversibly) blur the spectral features (Schönhense *et al.*, 2015). Application at low repetition rate FELs in pump probe experiments requires progress in the direction of high vacuum charge densities. We thus choose to reduce the information to the attainable one in a high pulse energy experiment, transmitting directly the electrons to the spin polarimeter with only a broad band-pass (0-100 eV) energy filter, and no momentum resolution.

Furthermore, we factored in the effects of relative fluctuations in the source intensity (γ), both in continuous and single-shot acquisition. Amplified sources, such as FELs

(especially SASE or self-seeding) or high pulse energy, low repetition rate HHG sources, have rather large shot-to-shot fluctuations, up to several tens per cent.

Continuous sources, when taken to very high brilliances, produce high average photoelectron fluxes at the detector (N_e). In these conditions, even small γ produce photoelectron flux fluctuations (γN_e) that are larger than the Poisson counting error $1/\sqrt{N_e}$, and are thus detectable.

The use of a spin polarimeter reduces N_e, but does not change γ. Furthermore, it evaluates small ($10^{-4} - 10^{-3}$) imbalances in a scattering process dominated by the Coulomb interactions, and introduction of intensity noise can be disruptive. We find (Pincelli *et al.*, 2017a) that, in these conditions, the spin-mirror polarimeters suffer a disadvantage, because due to their intrinsically one-beam detection geometry, they have to evaluate the electron flux at two different times to retrieve asymmetry. This exposes them to the intensity fluctuation noise. Dual-beam detectors such as Mott detectors, despite the lower efficiency, are instead always normalized to the total intensity entering the detector.

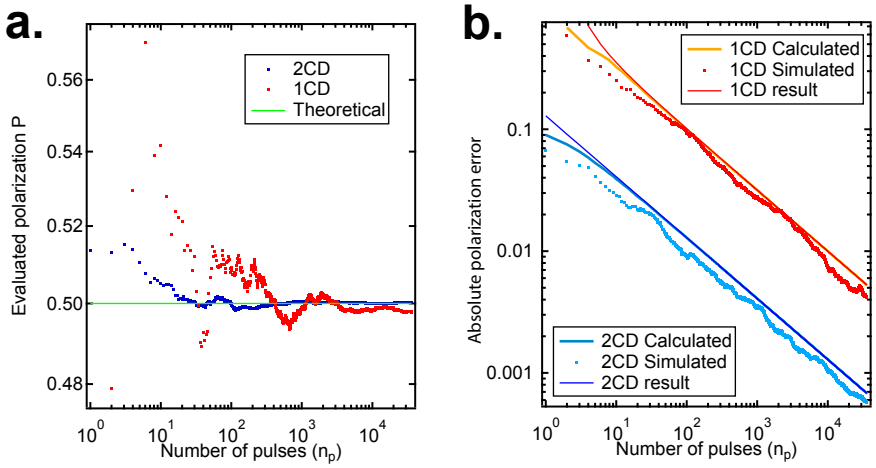

Figure 8.6: a. The result of a simulated measurement of a 50% polarization ($P^{true} = 0.5$) with a one-beam (1CD, red) and two-beams (2CD, blue) detectors as a function of the number of averaged pulses. b. The results of a simulated run on 1CD and 2CD detector. In this case, we used $n_p = 36000$, corresponding to 1h acquisition at 10Hz, $\bar{N}_e = 100000$. For 1CD, $\gamma = 0.1$, $S_{\text{eff}} = 0.36$,$\varepsilon_V = 1 \times 10^{-2}$. For 2CD $\varepsilon_M = 6 \times 10^{-4}$. $N_{sim} = 100$. The solid red and dark blue line show the non-approximated calculation of the initial expression, the light blue and orange the results of our approximation for large n_p, and the dots the simulated measurements.

By simple application of the theory of propagation of independent errors we demonstrated (Pincelli *et al.*, 2017a) that, by measuring n_p pulses each containing $\bar{N}_e$ electrons

on average, the error on the weighted average value with a two-beam detector is:

$$\Delta P_{\perp}(n_p) \approx \left(\frac{1}{n_p \bar{N}_e \varepsilon_{2B}} \right)^{1/2} \tag{8.7}$$

while for a single-beam:

$$\Delta P_{\perp}(n_p) \approx \left[\frac{1}{n_p} \left(\frac{1}{\bar{N}_e \varepsilon_{1B}} + \frac{\gamma^2}{S_{eff}^2} \right) \right]^{1/2} \tag{8.8}$$

the increase in the error is evident, as the quantities are all positive. Even accounting for the higher ε_{1D} than ε_{2D}, we obtain that the error for the two-beam detector is almost three times smaller in typical operation. Statistical simulations, shown in Fig. 8.6 support our view. Assessment of all the three components of the polarization vector further favour this choice as in a one-beam detector γ appears three times for the full vectorial evaluation. For this reason, we chose to upgrade a vectorial compact Mott detector for multi-hit acquisition.

Chapter 9

Testing and first results

> With this kind of instruments, you have to be a perfectionist.
>
> Vladimir N. Petrov, 2014

An high scattering energy Mott detector is well suited for multi-hit detection also because of its electron counters. Indeed, in the Classical Compact Mott detector, the electrons are detected by Silicon Barrier detectors, a rather unusual system in condensed matter electron spectrometry, borrowed from β-ray spectroscopy of nuclear and particle physics. Due to the significantly lower energies, channeltrons followed by charge amplifiers, or multichannel plates followed by phosphor screens and CCDs (or by delay-line detectors) are normally employed.

A Silicon Surface Barrier (SSB) detector is essentially a pn-junction with a thin, heavily p-doped top electrode, which is polarized in deep reverse bias. The depletion region is thus extended through the whole thickness of the wafer. When electrons impinge on the top surface with sufficient energy, they cross the p-doped "blind layer". In the depletion region, they lose their energy by creating a cascade of electron-hole pairs. These are separated by the depletion field, and collected by the electrodes. Summation and amplification allow to determine the particle initial energy with broad resolution (4-6 keV).

For particle physics, the 50 keV of scattering energy used in Mott detectors are a rather small value: the SSBs have to be realized with especially thin p-doped layers in this application. This is realized by doping the silicon via ion implantation in what is called a Passivated Implanted Planar Silicon detector (PIPS). This allows for $< 50nm$ top electrodes, enabling the detection of electrons with energies $> 30keV$. The silicon barrier detectors are chosen for two main reasons:

1. They allow for compact and low operating voltage detection. As the first part of the detection chain is floating at 50 kV, geometrical constraints and difficulties in power transmission due to isolation make these very desirable features.

2. They allow to select, via discrimination of the amplitude of the charge pulse, the elastically scattered electrons, thus reducing the multiple scattering background.

Considering the narrow difference between the minimum detection energy (30 keV) and the energy of scattering (50 keV), which is only 3-4 times the resolution, Fognini et al. (Fognini, 2014) proposed that the detectors could be used in multi-hit mode, by measuring the charge build-up in the detector. Indeed, and as will be shown in Sect. 9.2, one can attribute an amplitude to the charge pulse of a single electron (A_{1e}), averaged across the 20 keV passing band, weighted with the energy distribution after Mott scattering.

When operating in multi-hit mode, the amplitude of the charge build-ups can be distributed in integer multiples of A_{1e}. The central value of the distribution gives the total number of electrons that have entered the PIPS in a single pulse. The team in ETH Zurich thus developed an high sampling frequency electronics that is able to measure the amplitude of the charge build-up and save it in real time, allowing them to perform the pioneering experiments at FLASH FEL discussed above.

In continuity with their work, and in collaboration with them, we pushed this concept one step further. Thanks to the expertise of the laboratory of instrumentation and detectors led by Dr. G. Cautero in Elettra Sincrotrone, we developed an advanced detection system, based on high bandpass, low noise charge sensitive amplifiers and analog to digital converters. The on board electronics, floating at 50 kV is controlled by an FPGA integrated circuit that communicates with the acquisition computer via optical fibres. The programmable on-board FPGA allows for the desired extreme adaptability of the machine, that can run in:

1. Single electron-counting mode, i.e. the one that is optimally applied with continuous sources. The charge amplification is software selectable between three values (50 fC/V, 500 fC/V, 5 pC/V). The single charge pulses are discriminated with software selectable levels. Discrimination is actually realized with a series of conditions beyond the simple threshold, to ensure noise suppression and multi-hit separation. The number of counts acquired in a gating window is transferred to the computer.

2. Multi-hit mode, i.e. the mode best applied with pulsed, high intensity sources. The charge build-up after multiple electron absorption in the PIPS is measured. No pulse shaping is applied, and instead the FPGA analyses in real time the pulses, determining baseline, peak height and area of each single pulse. The peak height, or its integral, is transferred to the computer.

3. Full-acquisition mode, i.e. the same as the multi-hit mode, but no on-line data analysis is performed and the entire ADC output time-traces are transferred to the computer for offline analysis.

9.1 Testing the electronics

In a first commissioning phase with the collaboration of Prof. V. N. Petrov, described in (Pincelli, 2014), the instrument was set into operation, its electron optics was revised, modified and tuned to optimal transmission and positional stability using an electron gun. In the same conditions, optimal and reliable measurement of a polarization signal

was achieved. The noise on the polarization measurements was limited to the one arising from counting statistics (Eq. 8.7). The electron gun was then gated, and a prototype of the electronics was tested with microsecond pulses (Pincelli *et al.*, 2016). In all the subsequent measurements, we used an effective Sherman function $S_{eff} = 0.1$.

The endstation was then moved to the SPRINT beamline, and a full-scale testing became possible. We used the fifth harmonic of the PHAROS fundamental, at 206 nm, 6.0 eV. The first experiments were performed in single electron counting mode, by raising the repetition rate of the PHAROS to 200 kHz and attenuating (with a half-waveplate and a polarizer) the fifth harmonic until a count rate of 100k Counts/s was achieved. This is the working point of the system, where the linearity of the PIPS gives to each one the same response. The fact that only one electron every two pulses reaches each PIPS guarantees that there are a sufficiently small number of multi-hits, but that the statistics is sufficiently high (Weber, 2012).

9.1.1 Single electron counting tests

The tests were performed by confronting measurements on a clean surface of Cu(111), taken as a "zero reference", a film of LSMO(40nm)/STO(001), and a film of Fe(43nm)/MgO(001). They are shown in Fig. 9.1 **a**. The Cu(111) single crystal was sputtered in two cycles of 20 min at 1 keV in 5×10^{-6} mbar Argon. The LSMO/STO sample was transferred in air from the CLUSTER/MBE growth chamber at the NFFA-APE beamline facility in the Elettra hall, where it had been grown by A. Y. Petrov (see, for characterization reference Chap. 3.1.3). No surface cleaning procedures were performed, due to the risk of stoichiometry disproportionation. The Fe/MgO sample was grown by MBE in CLUSTER/MASK chamber by G. Vinai on a clean (1.5 h 1000 K 10^{-6} mbar oxygen annealing) MgO substrate. It was transferred with an UHV shuttle chamber. Pressure never went above 1×10^{-9} mbar even during transfer. Again, no surface preparation procedures were performed.

Each measurement is performed by applying a pulsed magnetic field and then measuring at remanence. The field is then reversed and the spin polarization (SP) is measured again. The two measurements are then summed with opposite signs and divided by two, in order to cancel non magnetic effects. This is repeated for long acquisitions to both achieve a high statistical confidence and to control the stability of the experiment[1]. As the detector is equipped with two pairs of PIPS, identifying two orthogonal quantization axes, the two in-plane components of the polarization are measured simultaneously: the one parallel to the external field H ($P_{\parallel}$), and the one perpendicular to it ($P_{\perp}$).

It is clear, from Fig. 9.1, that the measurements on Cu yield a reliable zero, on both channels. The measurement on LSMO/STO shows a small polarization (2.2% $P_{\parallel}$)

[1]The first concern is naturally the stability of surface polarization. Furthermore, at such low kinetic energies any small issue in the electrical connections, and even very small charging of any neighbouring surface can have significant effects on the trajectories. The fact that an accelerating field is present between the sample and the first lens of the detector, however, reduced this issue. We thus could avoid charging effects.

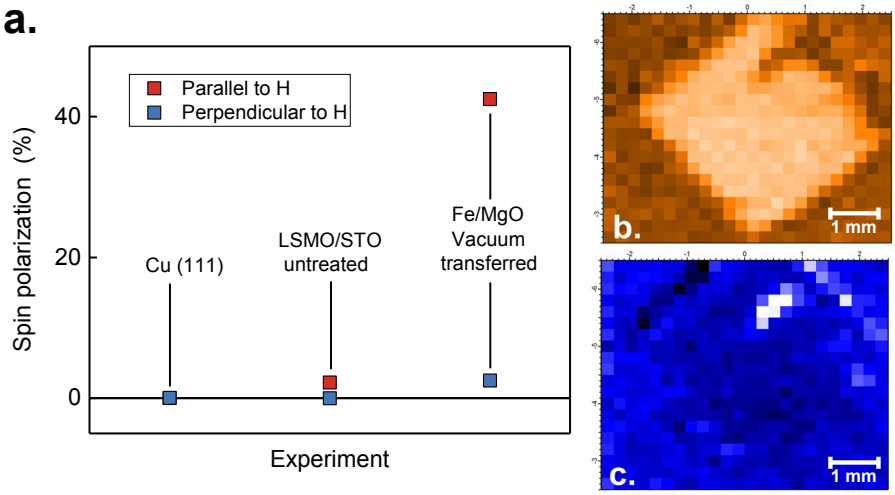

Figure 9.1: a. First measurements of the spin polarization of the secondary electrons under 206 nm laser excitation. The samples are a Cu(111) single crystal, LSMO(40 nm)/STO(001) and Fe(43nm)/MgO(001) each point represents a different experiment. The statistical error bars are smaller than the symbols. **b**. Topographic map of the spin polarization $P_{\parallel}$ component. **c**. Topographic map of the $P_{\perp}$ component. The dark (bright) spot observed in **b** (**c**) is not present in the spin integrated map, and has been identified as a domain.

that might be the faint residual of its magnetic state. However, the possible presence of small stray magnetic fields prevents us from trusting such small values, despite the high statistical confidence. Further work, with in-vacuo sample transfer, low temperatures and more efficient closure of the magnetic circuit are needed, and under way.

The measurement on Fe/MgO shows a very large value of $P_{\parallel}$ (42.5%). The magnetic easy axis, where the remanent magnetization lays, has indeed been approximately aligned in the direction of the field by rotating the MgO crystal of 45° with respect to the horizontal. The small signal observed in $P_{\perp}$ must again be considered with caution owing to possible stray field effects, but it could be easily explained as a slight misalignment of the easy axis with the horizontal direction.

The signal is very large, so that topographic spin polarization maps could be obtained (Fig. 9.1 **b** and **c**). This measurement was performed without applying any field and demonstrates the high polarization contrast achievable in a single measurement. On the top right side of the film a domain is oriented along the vertical easy axis. Application of the field unpinned it, and it was not observed again. It is clearly possible to achieve higher lateral resolution than the present $200 \times 200 \mu m$ by focussing the laser spot more tightly and running the raster scan in smaller steps. $1 \mu m$ steps are in principle possible, but $10 \mu m$ is a safer assumption.

9.1.2 Multi-hit tests

The large polarization signal obtained from the Fe/MgO free surface showed unexpected robustness in vacuum. This allowed us to run the first effective tests of the instrument in strongly multi-hit regime by relying on a stable polarization signal. We thus reduced the repetition rate of the laser to achieve maximum fluence and studied the detector response as a function of the pulse energy (Fig.9.2).

We chose the pulse energies so that we could have an effective reference point. The first value (50 nJ) is the same pulse energy that gave the optimal single-electron counting rate. We could thus be sure that single-electron events dominated in that regime.

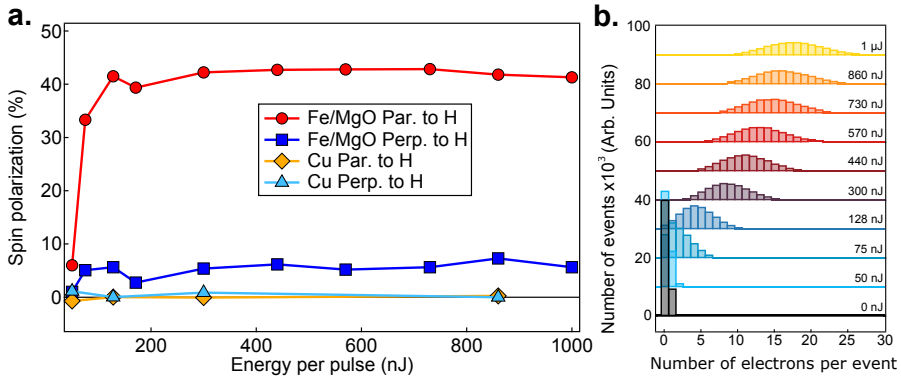

Figure 9.2: **a**. Measurement of the spin polarization signal of the Cu (111) crystal and the Fe/MgO film as a function of the pulse energy of the UV, 206 nm laser. **b** Histogram sorting the frequencies of observation of n-electron events as a function of the pulse energy. The shift of the distribution centres towards many electrons events is clear.

Panel **a** shows the amplitude of the polarization signal as a function of the pulse energy, for the Fe/MgO sample and for the Cu crystal. The asymmetries are evaluated by detecting the total amplitude of each charge spike. Cu measurements show reliably that no excessive spurious effects produce signals in our instrument. At medium pulse energies, the Fe/MgO sample shows approximately the same values of asymmetry observed in single electron counting.

At higher pulse energies, a small inflection seems to appear, showing hints of the space charge effect proposed by Fognini et al. (Fognini *et al.*, 2014b). Yet, we plan on further extending the curve in order to reliably confirm the result, because of the significant error in the pulse energy determination in the UV range.

At the lowest fluence, the polarization is reduced. This is an instrumental issue, as the prototype charge amplifiers were set to too small amplification. The peak detection algorithm was then triggered by noise, and mixed the small amount of one-electron events with zero-electron events.

This is evident in panel **b**. Here, the amplitudes of the spikes have been sorted in a frequency histogram. The width of the bin corresponds to the amplitude of a single

electron charge pulse, obtained by fitting the un-binned distribution at the lowest pulse energy. The first histogram (black) shows the distribution of heights observed in a dark run, with the UV laser blocked: only noise and few dark counts appear in the distribution. At the lowest pulse energy, the detection barely (but detectably) differs from noise.

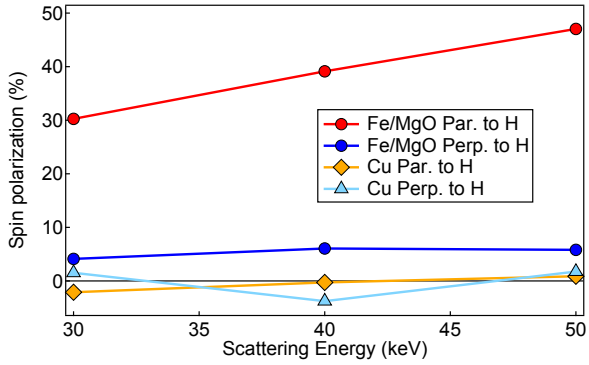

Figure 9.3: Variation of the polarization signal as a function of the scattering energy in the multi-hit operation mode, with 128 nJ pulses of the 206 nm UV Laser.

By further increasing the pulse energy, zero-electron events are no longer relevant and the amplitudes distribute increasingly symmetrically around a central value. We reach a maximum central value (per single channel) of approx. 17 e/pulse, thus demonstrating reliable electron counting even in the multi-hit regime. The lower pulse energy issue can be solved by measuring the two parts of the curve with different amplifications and then normalizing the signals, thus extending the dynamic range of the instrument.

This multi-hit detection scheme clearly does not reject the multiply scattered electrons, as the discrimination level scheme does. However, the close-by entrance energy barrier filters out most of the inelastically scattered electrons. We thus tried to understand if, by reducing the scattering energy to values closer to the minimum threshold, we would achieve higher scattering efficiencies.

Fig. 9.3 shows that, instead, the measured polarization decreases. This clearly arises from the reduction of the single-atom Sherman function with energy (Gellrich and Kessler, 1991). We thus can conclude that the non-discriminated inclusion of the inelastically scattered electrons does not significantly reduce the Sherman function, but allows to count bright pulses of electrons, allowing for highly improved efficiency.

9.2 Preliminary measurements and open projects

We conclude this part by discussing some of the first results that might chime with the motif of this thesis, relating to the techniques addressing spatially and temporally the electronic structure of complex solids.

Exploiting the control over the laser wavelength unlocked by the OPA, we attempted to tune the energy of the UV beam around the photoemission threshold. The output 1030 nm beam of the PHAROS was thus feeded into the ORPHEUS-HP OPA, converting it into 630nm-2600nm wavelength, tunable in steps of 5 nm. We employed the range of maximum efficiency: 1032-800 nm, where the converted power is around the 10%. We

then picked up the OPA output and used it to generate the fourth harmonic in a set-up with broad-band crystals.

The evolution of the signal with changing photon energy is shown in Fig. 9.4. By reducing the photon energy, the total spin polarization increased to extremely large values (up to 77%), in agreement with previous results (Eib and Reihl, 1978).

We are aware that this kind of measurements requires delicate interpretation and high degree of control on the experimental parameters, as evidenced by the accurate work done on the matter from the late 70s to the 90s (see, for example (Kisker and Carbone, 1992, and references therein)).

Our data are at the moment too immature to speculate on details of the variations of the polarization: the changing of the photon energies required realignment of the crystals and re-optimizations of the intensity, and electrons of meV energies are extremely sensitive to any electric and magnetic disturbance. It does not surprise, therefore, that the repeated point at 5 eV shows a different value of the spin-polarization, suggesting that there are sources of noise other than statistical.

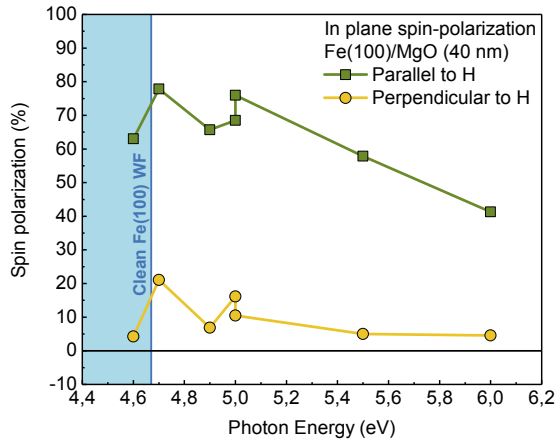

Figure 9.4: Spin polarization of the photoemitted yield as a function of the photon energy, decreasing close to the work function of the material.

Yet, it is clear that the polarization of Fe/MgO increases to very high values. As the photon energy decreases, the kinetic energy of the electrons is decreases and their IMFP increases significantly, while the photon absorption length shortens. Following the lines of previous works, we are lead to the picture of a decreasing relative spectral weight of inelastically scattered secondary electrons in favour of the elastic electrons. This is supported by the observations of polarization inversion in Ni (Clauberg *et al.*, 1981), due to the increased sensitivity to the population of the minority spin band. This would substantially increase the probing depth of the spin polarization measurement from the short spin relaxation depth to the longer IMFP of elastic electrons.

Precise studies with over-layers and the whole set of photon energies offered by the combination of OPA and HHG might allow us to individuate a crossover point from the inelastic cascade-dominated regime and the regime dominated by elastic electrons. This would give us an interesting instrument to explore the characteristics of magnetic systems in different near-surface regions. Experiments either in single or multi-hit mode implementing the pump-probe scheme might add the time resolution to the achievable

information. The ultrafast surface magnetometer foreseen by Landolt in 1986 (Landolt, 1986) might be closer today.

The first unanswered question that we may address with the possibilities offered by this set-up brings us back to the dynamics of LSMO. In Part II, indeed, we neglected the effects of possible spin currents ensuing within the film on the basis of the fact that no charge transfer can happen through the interfaces with vacuum and with the large band-gap insulator. Furthermore, MOKE averages over the full thickness of the film, and 8 keV HAXPES addresses the homogeneous bulk region. On the other hand, we have shown in Part I that within 4 nm from the surface, the electronic structure, is indeed different. This creates an inhomogeneity where the spin currents might be of relevance. We thus would like to understand if it is possible to perturb the top layer by photoexcitation, thus transiently activating new functionalities.

Chapter 10

Concluding remarks

In **Part I**, I employ HAXPES and PES to demonstrate highly precise spatial control of the distance from the surface at which the spectral information is retrieved. I perform an accurate study of the low binding energy satellite (LBES) of the Mn 2p peak at different primary photon energies and polrizations. Combining it with measurements at different temperatures, I clarify the LBES sensitivity to electronic hybridization and long range magnetic order. By using schematic but effective theoretical modelling of the electronic structure and of the photoemission process itself, I am able to directly quantify the evolution of electronic correlation as a function of the distance from the surface. I can then define the cross-over thickness of the region in which the properties are modified by the interruption of the crystal.

The system at the focus of my interest is the strongly correlated transition metal oxide, $La_{1-x}Sr_xMnO_3$, that is promising for spintronics application owing to its half metallic character and the display of colossal magnetoresistance. I compare the retrieved length scale with the one measured on another compound of high interest in spintronics, the diluted magnetic semiconductor (Ga,Mn) As. I find largely different scales in the two materials: $z^c_{LSMO} = 4.0 \pm 0.2nm$ and $z^c_{GMA} = 1.2 \pm 0.1nm$. For LSMO I also measured three different substrate induced strain states (1% in plane tensile, relaxed, 1% in plane compressive), and found no detectable influence on the cross-over thickness. Further investigation is needed to understand the mechanisms leading to such differences, and I propose several directions along which further experiments can be carried out.

In **Part II**, I extend the investigation of $La_{1-x}Sr_xMnO_3$ to the time domain, probing the bulk region in an infrared pump - HAXPES probe experiment. I am able to observe how the relaxation of the energy pumped by photoexcitation. Comparing with a large dataset of magneto-optical measurements, I can conclude that the emergence of electronic correlation is due to the collapse of the double exchange interaction, coupled with magnetic ordering. The collapse of magnetization is however bottlenecked by the half-metallic bandstructure, that slows it by forbidding spin-flip excitations. Only coupling via the weak magneto-crystalline anisotropy allows the quenching of magnetic ordering, thus delaying the electronic correlation of several hundreds ps. I also conclude by presenting possible developments of this work.

In **Part III** (Chap. 10-11) I address the development of instrumentation and methods for the realization of spin and time resolved photoemission in the soft X-rays with an HHG source, thus targeting shorter timescales and shallower probing depths in magnetic and spintronic materials. I describe the structure of a new generation laboratory, designed to bridge the development of techniques, the experimental strategies and the scientific questions from the well established equilibrium spectroscopy to the largely unexplored study of out-of-equilibrium dynamics. In particular, I highlight the development and testing of an apparatus for the measurement of the spin-polarization of the secondary electrons. This instrument has been chosen, upgraded and tested in order to operate in a heavily multi-hit regime, i.e. to be able to detect photoelectrons reliably also when they are emitted in short, high peak current pulses. I conclude by presenting some preliminary results, that show the efficiency and the potentialities of such apparatus.

Appendices

Appendix A

Magneto-optical Kerr signal

The most straightforward way to address the Kerr and Faraday effect is the picture used by Maxwell. Indeed, to explain the Faraday rotation of polarization, he decomposed linearly polarized light into a combination of left- and right-circularly polarized waves. These two form a natural set of eigenmodes of electromagnetic wave propagation in a magnetic field or magnetic medium as they have the same symmetry under time reversal. The eigenvalues, however, are different between the two modes. Thus, the two components of the initially linearly polarized wave acquire a phase difference and give, in the transmitted wave, combine to form again a linearly polarized wave with a polarization direction rotated by some angle ϑ_F called the Faraday angle. In most of the cases, not only the phase velocity is different, but also the absorption index. The transmitted beam does not have, consequently, perfectly linear polarization, but it acquires a Faraday ellipticity ε_F.

These two effects have clearly consequences also in the polarization of the reflected beam, due to the boundary conditions of the wave reflection from the surface. Thus, the effects of magnetization can be seen in a rotation by a Kerr angle ϑ_K and a Kerr ellipticity η_K also in the reflected beam, allowing to measure non-transparent materials.

More precisely (Qiu and Bader, 1999), the 3×3 dielectric tensor of a crystalline medium:

$$\tilde{\varepsilon} = \begin{pmatrix} \varepsilon_{xx} & \varepsilon_{xy} & \varepsilon_{xz} \\ \varepsilon_{yx} & \varepsilon_{yy} & \varepsilon_{yz} \\ \varepsilon_{zx} & \varepsilon_{zy} & \varepsilon_{zz} \end{pmatrix} \tag{A.0.1}$$

can be written in a combination of a symmetric and antisymmetric form: $\varepsilon_{ij} = (\varepsilon_{ij} + \varepsilon_{ji})/2 + (\varepsilon_{ij} - \varepsilon_{ji})$. The symmetric part can be then diagonalized by rotating the coordinates. By assuming isotropy of the refraction index one can consider the diagonal part as constant (ε). It is then possible to write:

$$\tilde{\varepsilon} = \varepsilon \begin{pmatrix} 1 & iQ_z & -iQ_y \\ -iQ_z & 1 & iQ_x \\ iQ_y & -iQ_x & 1 \end{pmatrix} \tag{A.0.2}$$

Where the three off-diagonal components are defined by exploiting the symmetry of the dielectric tensor to reduce the dimensionality, so that they can be included in $\mathbf{Q} =$

$(Q_x, Q_y, Q_z) = i(\varepsilon_{yz}, -\varepsilon_{xz}, \varepsilon_{xy})$, called the Voigt vector. Then the eigenmodes of propagation in the medium are easily found, and have eigenvalues:

$$\begin{cases} n_L = \sqrt{\varepsilon}(1 - \frac{1}{2}\mathbf{Q} \cdot \hat{k}) \\ n_R = \sqrt{\varepsilon}(1 + \frac{1}{2}\mathbf{Q} \cdot \hat{k}) \end{cases} \tag{A.0.3}$$

Where $\hat{k}$ is the versor of the light propagation direction. The Voigt vector is a vector of complex numbers. The two refraction indexes thus contain both the dispersive (real) and the absorptive part (imaginary). The Faraday angle can be obtained by calculating the phase difference acquired by a path of length L in the medium:

$$\Theta_F = \frac{\pi L}{\lambda}(n_L - n_R) = -\frac{\pi L \sqrt{\varepsilon}}{\lambda}\mathbf{Q} \cdot \hat{k} \tag{A.0.4}$$

As it can be seen, the Faraday rotation depends on the anti-symmetrical part of the dielectric tensor. The Onsager's relations state that, to preserve time-reversal symmetry, each swap of the indexes in the tensor of the response parameters must correspond to a change in sign in their dependency from observables odd under time-reversal symmetry. In the case of the dependence of ε from external electric and magnetic fields, this translates into: $\varepsilon_{ij}(E, H) = \varepsilon_{ji}(E, -H)$. Expansion of ε up to the linear terms in E and H makes clear that the antisymmetric part of ε ($\mathbf{Q}$) depends on $\mathbf{H}$ in general and on $\mathbf{M}$ in magnetic materials. An analogous argument holds for the Kerr effect.

It must be clearly kept in mind that the Faraday and Kerr angles are in general sensitive to any observable that can generate time reversal symmetry breaking, and that the magnetic field is only a special case. When the system is adiabatically driven out of equilibrium, the quasi-static thermodynamic approach is broken and reversibility is not guaranteed. As discussed in the following, the understanding of the MOKE response at very short timescales is an open research field.

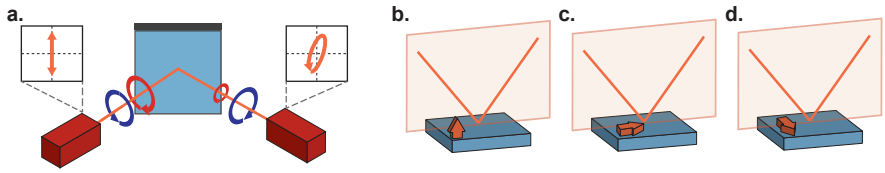

Figure A.1: a. Scheme representing the basic mechanism of the MOKE rotation: the linear incident polarization can be decomposed in two opposite circularly polarized components. Upon reflection, they undergo a phase shift and different absorption, so that the outgoing polarization is elliptical, with rotated axis. b. Scheme of the polar-MOKE configuration. c. Scheme of the longitudinal MOKE configuration. d. Scheme of the transversal MOKE-configuration. Adapted from (Schellekens, 2014).

In order to deepen the discussion of MOKE keeping it on a reasonable level of complexity, it is important to consider the experimental configurations in which it is realized.

Indeed, the restriction to a particular geometry allows to further reduce the dimensionality of the problem. Three classes of geometries are usually considered with respect to the position of the magnetization vector with respect to the plane of incidence of light and the material surface. In the *polar* geometry **M** lays in the incidence plane and is perpendicular to the surface (Fig. A.1 b), in the *longitudinal* geometry **M** is both in the scattering and in the surface plane (Fig. A.1 c), in the *transversal* geometry **M** is perpendicular to the scattering plane, but lays in the surface plane (Fig. A.1 d). The discussion, for the sake of simplicity, will be limited to the transversal geometry, as it is the one that was employed in the experiments.

In this configuration, the dielectric tensor of Eq. A.0.1 can be rewritten as:

$$\tilde{\varepsilon} = \begin{pmatrix} \varepsilon_{xx} & 0 & \varepsilon_{xz} \\ 0 & \varepsilon_{xx} & 0 \\ -\varepsilon_{xz} & 0 & \varepsilon_{xx} \end{pmatrix} \tag{A.0.5}$$

Where isotropy is assumed ($\varepsilon_{xx} = \varepsilon_{yy} = \varepsilon_{zz}$). By imposing the boundary conditions at the surface, together with Snell's law at a reflection angle of 45°, it is possible to find:

$$\Theta^L_{s,p} = \vartheta^L_{s,p} + i\eta^L_{s,p} = f_{s,p}(\varepsilon_{xx}) \times \varepsilon_{xz} \tag{A.0.6}$$

Where the s and p indexes reflect the fact that the light polarization is perpendicular to the incidence plane (*senkrecht*, s) or parallel to it (*parallel*, p). The + and − signs correspond to these two cases, respectively.

In order to explicit the dependence on the components of the magnetization in the effective experimental configuration, it is necessary to evaluate the Fresnel coefficients in reflection accounting also for the conditions at the surface for the magnetic vector. Also in this case, considerations on the geometry are important for the reduction of the dimensionality of the problem. If we consider a solid with sufficient thickness to give negligible transmission, then it is possible to restrict the discussion to the incident and reflected beam, described by two component vectors. Each component of the vector quantifies the projection of the EM wave electric field vector in the incidence plane (p), or perpendicular to it (s). In the Jones formalism the reflection from the sample surface is described by a matrix product:

$$P^r = \begin{pmatrix} E^r_s \\ E^r_p \end{pmatrix} = M \begin{pmatrix} E^i_s \\ E^i_p \end{pmatrix} = MP^i \tag{A.0.7}$$

where M is the matrix of the Fresnel reflection coefficients:

$$M = \begin{pmatrix} r_{ss} & r_{sp} \\ r_{ps} & r_{pp} \end{pmatrix} \tag{A.0.8}$$

the subscripts indicate, respectively which reflected and incident component of the polarization each coefficient refers to. Thus:

$$P^r = \begin{pmatrix} r_{ss}E^i_s + r_{sp}E^i_p \\ r_{sp}E^i_s + r_{pp}E^i_p \end{pmatrix} \tag{A.0.9}$$

One can then define the two Kerr angles:

$$\begin{cases} \Theta_s = \vartheta_s + i\eta_s = \dfrac{r_{ps}}{r_{ss}} \\ \\ \Theta_p = \vartheta_p + i\eta_p = \dfrac{r_{sp}}{r_{pp}} \end{cases} \tag{A.0.10}$$

If one assumes that the interface is formed with vacuum ($n \approx 1$), that in the optical region the relative magnetic permeability of the medium is close to unit ($\mu \approx 1$) and that the angle of incidence is 45°, the general expression of the Fresnel coefficients can be reduced to give Θ_s:

$$\Theta_s = \frac{r_{ps}}{r_{ss}} = -\frac{i\sqrt{2}\varepsilon_{xx}\left(m_y + m_z\sqrt{2\varepsilon_{xx}-1}\right)Q}{\sqrt{2\varepsilon_{xx}-1}(\varepsilon_{xx}+\sqrt{2\varepsilon_{xx}-1})(1+\sqrt{2\varepsilon_{xx}-1})} \tag{A.0.11}$$

where the factor Q is a complex number that is called the magneto-optical constant and that is material and wavelength dependent. If the magnetization has no out-of-plane components:

$$\Theta_s = \frac{r_{ps}}{r_{ss}} = -\frac{i\sqrt{2}\varepsilon_{xx}m_y Q}{\sqrt{2\varepsilon_{xx}-1}(\varepsilon_{xx}+\sqrt{2\varepsilon_{xx}-1})(1+\sqrt{2\varepsilon_{xx}-1})} = f(\varepsilon_{xx}) \times m_y \tag{A.0.12}$$

At equilibrium, therefore, there is a direct proportionality between the total Kerr angle and the in-plane component of the magnetization that lies in the scattering plane.

From the band-structure point of view, MOKE arises from the simultaneous presence of spin-orbit interaction and exchange splitting. Indeed, the optical light produces transitions between filled states in the bandstructure to empty states above the Fermi energy. Generally, such states have a specific orbital character, and are split by the spin-orbit interaction. Therefore, light with finite angular momentum ($L_z = \pm 1$) produces transitions between p character features in the bandstructure to very specific regions in the spin-orbit split 3d bands.

The 3d bands, however, are also split by a large exchange shift: for a precise photon energy, the majority and minority spins thus find different density of states. The states with identical orbital character, to which transitions are allowed by the selection rules are indeed shifted by the exchange interaction more than one eV further for one of the two spin states. The absorptive part of the dielectric function has, therefore, off-diagonal components that are dependent on the magnetization. The dispersive part shows analogous behaviour as can be obtained by applying the Kramers-Kronig relations.

As previously explained, such dependencies translate in a magnetization dependent complex rotation angle Θ. As can be inferred from this argument, the Kerr angle must have a photon energy dependence. Varying the wavelength of light, indeed, favours transitions between different regions of the bandstructure. This is indeed the aim of Kerr spectroscopy, of which two examples are shown in Fig. A.2.

It is important to address accurately the photon energy at which the Kerr angle is measured, and to combine them with calculations in order to recognize the optical

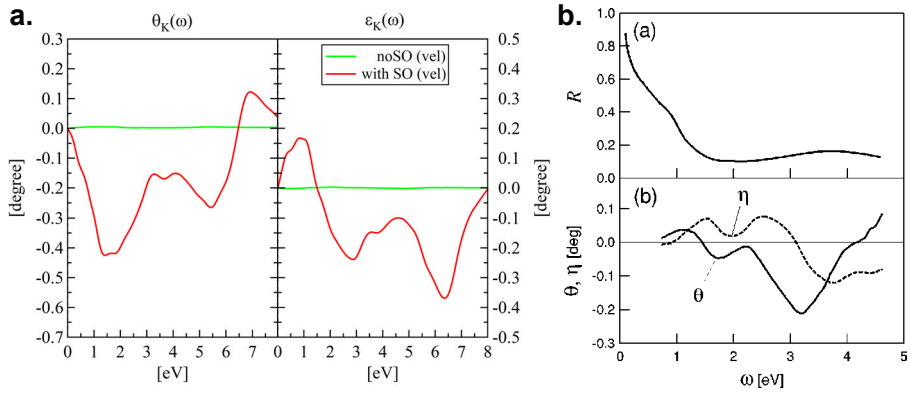

Figure A.2: a. Calculated Kerr spectra of bcc Iron. The panels from left to right show the Kerr rotation and ellipticity, respectively. The green curves represent DFT calculations with YAMBO code in which the spin-orbit coupling constant has been artificially set to zero. The red curves represent converging calculations with finite SOC and exchange splitting. From YAMBO webpage. b. Top panel: Reflectivity spectrum of LSMO single crystal, optimally doped. Bottom panel: Kerr spectroscopy of the same sample, with separated curves for rotation (solid) and ellipticity (dashed). From (Ogasawara *et al.*, 2003).

transitions responsible of the features in the Kerr spectrum. For example, it is known that the structures appearing in the Kerr spectrum of LSMO (Fig. A.2 b) in the range 1.5-2 eV are due to a plasma-edge enhancement originating in the diagonal term $f(\varepsilon_{xx})$. Thus, probing the Kerr rotation makes it more sensitive to changes in ε_{xx} than in ε_{xy}, thus not a reliable source of information on the magnetization. On the other hand, the feature at 3 eV can be attributed to charge transfer transitions from the oxygen O 2p states to the Mn 3d empty states, which have the symmetry discussed above and a small ε_{xx} contribution. This photon energy is thus a reliable probe of the magnetization and we choose it for our experiment.

A.0.1 Detection of Kerr rotation and ellipticity

The detection of the Kerr rotation can be performed in a variety of ways, and in the experiments discussed in the following we employed the *crossed-polarizer configuration* and the *balanced detection configuration*.

Crossed polarisers configuration

The simplest realization of the MOKE experiment consists in polarizing the incident light with a first optical element, called the *polariser* (P), reflecting the light off the sample surface at a precise angle, and placing a second polarizing element called *analyser* (A) in the optical path before the light-sensitive detector. The Jones matrix formalism can then be employed. By defining the state of the light after the polarizer as $P^i = (1, 0)$, we

choose the s-polarization configuration. Then the Jones matrix of the reflection from the sample surface is:

$$M = r_{ss} \begin{pmatrix} 1 & r_{sp}/r_{ss} \\ r_{ps}/r_{ss} & r_{pp}/r_{ss} \end{pmatrix} = \sqrt{R} \begin{pmatrix} 1 & r_{sp}/r_{ss} \\ \Theta & r_{pp}/r_{ss} \end{pmatrix} \tag{A.0.13}$$

Where R is the s-polarization total reflectivity. The Jones matrix for the analyser, tilted of an angle α with respect to the polariser axis is:

$$A = \begin{pmatrix} \cos^2\alpha & -\cos\alpha\sin\alpha \\ -\cos\alpha\sin\alpha & \sin^2\alpha \end{pmatrix} \tag{A.0.14}$$

The final wave is given by:

$$P^r = AM \begin{pmatrix} 1 \\ 0 \end{pmatrix} \tag{A.0.15}$$

The intensity on the detector is given by $P^r P^{r*}$, which gives:

$$I = R\left(\cos^2\alpha + (\vartheta^2 + \eta^2)\sin^2\alpha + \vartheta\sin 2\alpha\right) \tag{A.0.16}$$

As both ϑ and η are small, the quadratic term is neglected. ϑ is obtained by choosing α close to $\pi/2$, so that:

$$I = R(2\vartheta\beta + \beta^2) \tag{A.0.17}$$

where $\beta = \alpha - \pi/2$. The optimum between the reduction of the background deriving from the term in β^2 and an excessive reduction of the signal is usually achieved experimentally. By inserting a quarter waveplate in the beam, the incident polarization is changed to circular and the intensity signal is proportional to η. By measuring with opposite directions of $\mathbf{M}$ and subtracting the signals, one removes from the value of Θ all non-magnetic contributions.

Balanced detection configuration

An improvement of the crossed polarisers technique is the use of balanced detection schemes. In this case, the analyser is substituted by a birifringent crystal, that separates the the incoming beam into two components (called the *ordinary* and *extraordinary* rays). Each component is then detected by a photodiode, and the two voltage signals are subtracted. Due to the need for geometrical symmetry in the mechanical realization, usually a Wollaston prism is used, that bends the ordinary and extraordinary rays of the same (but opposite) angles off-axis. One then has:

$$I = I^p - I^s = R\left[\left(\cos^2\alpha - \sin^2\alpha\right)\left(\vartheta^2 + \varepsilon^2 - 1\right) + 4\vartheta\sin\alpha\cos\alpha\right] \tag{A.0.18}$$

where α is the angle between the polarization of the extraordinary ray and the s-polarization direction (normal to the light scattering plane). By setting $\cos^2\alpha - \sin^2\alpha = \tan 2\alpha = 0$, i.e. $\alpha = 1/2\,\arctan(\vartheta/2)$, one isolates the ϑ dependence. Analogously to the case of the crossed polarisers, the measurement of the ellipticity can be realized by inserting a quarter waveplate in the reflected beam.

A.1 Dynamical effects in MOKE

Building on the definitions given for the equilibrium MOKE, it is now possible to consider the mathematical consequences of implementing the MOKE in an out-of-equilibrium configuration. Clearly, one expects that $\Theta = \Theta(t)$ and $\mathbf{M} = \mathbf{M}(t)$, and that it is possible to individuate a relationship between them. However, when the ferromagnetic material is excited by the pump pulse, a large redistribution of the charges takes place, making the whole dielectric tensor time dependent. In general, each independent component has a specific dynamics, and several of the assumptions that have been employed at equilibrium to extract the magnetization dependence of the Kerr angle are no longer valid. To avoid misinterpretation of the data, it is thus necessary to carefully address the consequences of such effects.

In general, it is possible to write, phenomenologically (Koopmans, 2003):

$$\Theta(t) = G(t) + \sum_{i=x}^{z} F_i(t) M_i(t) \tag{A.1.1}$$

where the complex quantities G and F are generalized Fresnel coefficients. The second term on the right-hand side is the linearisation in $\mathbf{M}$, which we assume to be still valid. As obtained in Eq. A.0.12, by choice of the geometry and considering the characteristics of the material, in the present case only m_y is relevant:

$$\Theta_s(t) = G(t) + F_{s,y}(t) M_y(t) \tag{A.1.2}$$

The variation in the Kerr angle induced by the pump is considered in the small perturbations limit by differentiating. Indicating the initial equilibrium values by a subscript "0", it is possible to write:

$$\Delta\Theta_s(t) = \Delta G(t) + \Delta F_{s,y}(t) \cdot M_{0,y} + \Delta M_y(t) \cdot F_{s,0,y} \tag{A.1.3}$$

The Δ precedes the variations from equilibrium. This means that, in general, the variation of Θ does not describe directly the evolution of the magnetization.

In the optimal case is obtained if during the time-resolved experiment the orientation of the magnetization vector remains constant. Otherwise, measuring only one component, it is difficult to distinguish the effective longitudinal dynamics from the transversal precession that projects the same modulus over different components. Furthermore, if $G(t) = G_0$ and $F(t)_{s,y} = F_{s,0,y}$, i.e. the Fresnel coefficients are constant:

$$\Theta_s(t) = G_0 + F_{s,0,y} M(t) \tag{A.1.4}$$

In this case, then, differentiating as in Eq. A.1.3, considering Eq. A.0.6 and normalizing to the initial value, one obtains the important relationship:

$$\frac{\Delta\vartheta(t)}{\vartheta_0} = \frac{\Delta\eta(t)}{\eta_0} = \frac{\Delta m_y(t)}{m_{y,0}} \tag{A.1.5}$$

The choice of m_y obviously yields no loss of generality for this identity. The important message of Eq. A.1.5 is that, if the ellipticity and the rotation have identical dynamics, the optimal conditions are met: the variation of the Fresnel coefficients is negligible and the dynamics of the magnetization is described by the evolution of ϑ or η.

Reversing the statement, if the first two terms of Eq. A.1.5 are not equal for any t, it means that the Fresnel coefficients are contributing to the dynamics and influencing the Kerr signal. The discussion can be branched in two parts, considering the effects of $G(t)$, which are easier to remove experimentally, and the effects of $F(t)$.

A.1.1 Even symmetry charge dynamics effects

The main source of non-magnetic dynamical signal is the dynamics of the reflectivity, that in turn depends only on the diagonal terms of the dielectric tensor, $\varepsilon_{xx} = n^2$. As a rule of thumb, the reflectivity changes in an optically perturbed metal due to the fact that a large number of hot carriers is suddenly excited in the bandstructure, promptly modifying the low energy optical conductivity and producing significant shifts of spectral weight at many wavelengths.

It is thus reasonable to expect that the reflectivity R used in the previous discussion has a temporal dependence in a pump-probe experiment, i.e. $R = R(t)$. If the result obtained in Eq. A.0.17 is differentiated to evaluate the pump-induced change:

$$\Delta I(t) = 2R_0\beta\Delta\vartheta(t) + \beta^2\Delta R(t) \tag{A.1.6}$$

stopping at the leading order in Θ. Generally, $\Delta R(t)/R_0$ is much smaller than $\Delta\vartheta/\vartheta_0$, thus normalization reduces the effects of reflectivity dynamics, together with the second order in β. Especially at shorter timescales, when the system is strongly out of equilibrium, the reflectivity effects can be significant. The strategy to avoid this issue consists in recording two traces of $\Delta I(t)$ with opposite sign of m_y and subtract them: as $R(t)$ depends only on ε_{xx}, is even under magnetization reversal, and its effect is cancelled. By converse, summing the curves with positive sign gives $2R(t)$, cancelling magnetic effects.

In the case of the balanced detection, when the system is exactly at balance (setting $\alpha = 1/2\arctan(1/2\vartheta_0)$ in Eq. A.0.18), the subtraction that removes effects of ε_{xx} is performed electronically in the signal detection and the signal does not depend on the reflectivity variations. In a way analogous to the reversal of m_y in the crossed polarizer configuration, electronically summing the signals of the diodes gives the diagonal reflectivity variation ΔR.

A.1.2 Odd symmetry charge dynamics effects

Even when all the experimental precautions to remove the effects of reflectivity variations are taken, there still is a second quantity that can depend on ε_{xx}, the Fresnel coefficients that appear multiplicatively in Eq. A.1.3. These cannot be removed by subtracting measurements with opposite magnetization. Indeed, they depend on ε_{xx} and are thus

even under changes in sign of m_y, but are multiplied by it: the factor $\Delta F_{s,y}(t)m_{0,y}$ has thus the same symmetry as $F_{s,0,y}\Delta m_y(t)$.

This is an issue that has been signalled very early in the history of ultrafast magnetism: just four years after Beaurepaire's experiment, the realization of Magnetic Second Harmonics Generation (MSHG) experiments (Regensburger *et al.*, 2000) on Ni films proved that the MSHG signal can be dominated by the dynamics of ε_{xx}. Furthermore, in a MOKE experiment on a complex wedged sample (Koopmans, 2003), several discrepancies were observed between the evolution of $\vartheta(t)$ and η. Experiments on thicker Ni, Fe and CoPt films, instead did not find large differences (Carpene *et al.*, 2013; Guidoni *et al.*, 2002). Ab-initio studies (Oppeneer and Liebsch, 2004) were also dedicated to the matter, coming to the conclusion that charge dynamics can indeed affect the MOKE signal at ultra-short timescales, and must be accounted in the extraction of the signal. Since then, a large number of different techniques have been applied in order to remove spurious contributions obscuring the magnetization dynamics: the different temperature dependence of the two factors (Koopmans, 2003), and detailed ellipsometric analysis to disentangle the contributions (Carpene *et al.*, 2013, 2015; Razdolski *et al.*, 2017).

Another interesting study is that of Zhang and coworkers (Zhang *et al.*, 2009), that describe both the magnetic and optical response of a nickel film with the common time-dependent density matrix. Solving its dynamics by resolution of nearly half a million Liouville equations allows to extract the non-equilibrium magnetization and dielectric polarization vector. Plotting $\mathfrak{Im}(M_{xy})$ versus $\mathfrak{Im}(P_{xy})$ produces a diagram that, at equilibrium, should have trajectories only laying in the planes diagonal. When the dynamics is started by a short laser pulse, however, the trajectories stray significantly off-diagonal, demonstrating large dephasing between the magnetic and optical response. The amplitude of such dephasing does not seem to depend strongly on the laser intensity, but on the time duration of the pulse (is larger for shorter pulses). The photon energy also play a role, in order to choose the region in which the responses of the two vectors are individually as consistent as possible. The dephasing suggested by Zhang corresponds to the picture of the other authors that have addressed the ellipticity study (Carpene *et al.*, 2013; Razdolski *et al.*, 2017), and is linked, by an identity of timescale argument, to the charge dephasing time suggested by Bigot (Bigot, 2001) to be the microscopic origin of the difference between rotation and ellipticity.

The recent discovery of the relevance of non-local effects in magnetization dynamics offers a new perspective to look at the contrasting results obtained in apparently analogous conditions. As we now know that in the perturbed film significant charge and spin dynamics ensue, we know that we mus look beyond the local characteristics of the sample. The presence of a metallic or insulating substrate, the use of optically thin or thick films can all redistribute charge and spins in the probing region of MOKE. This new concept is further supported by the recent observation (Wieczorek *et al.*, 2015) that the measurement of ellipticity and rotation have a different probing depth in the material.

The inclusion of such complexity in the interpretation of the MOKE signal makes it difficult to confront with theoretical interpretations and in particular ab-initio calculations.

It is thus necessary that experimental methods are developed to isolate the magnetization dynamics from the MOKE signal. Some of the strategies will be discussed in relation with the interpretation of the data, in Sect. 6.3.1. Naturally, as mentioned in the Introduction, these difficulties are also a pressure towards the realization of complementary techniques that probe more directly the state of the spin system.

Appendix B

The high binding energy structure

The attentive reader might have noticed that in the theoretical calculations of Fig. 3.17 at the high binding energy side of the poorly screened peak the evolution with hybridization is seemingly opposite with respect to the one observed as a function of the photon energy in Fig. 3.6 and as a function of the temperature in Fig. 3.10. Indeed, the theoretical spectrum at $V^* = 0$ eV shows a sizeable shoulder, while the highly hybridized spectrum at $V^* = 1.176$ eV shows a barely distinguishable hump. In the experimental spectra, by converse, a distinguishable structure appears at the larges probing depths and in the lowest temperature states, namely in the more strongly hybridized conditions. The HBEF structure cannot be resolved at the lowest probing depths an at high temperatures, giving substantially a single poorly screened peak.

The inconsistency is only apparent, however, and arises by the fact that the presence of Mn 4+ ions is not accounted for in that calculation. It is indeed possible to calculate the spectrum of the Mn 4+ in the oxygen octahedron within the classical CM. As shown in Fig. B.1 **a**, the peak largely overlaps with the poorly screened structure of the Mn 3+, complicating the picture.

As a rough approximation to understand the evolution of the HBEF, it is possible to sum it with each of the Mn 3+ spectra. In Fig. B.1 **b**, this is done by combining the spectra with stoichiometric coefficients, 0.33 for Mn 4+ and 0.67 for Mn 3+. The peaks are then convolved to a Gaussian with half-maximum width of 0.25 eV, the experimental resolution. This blurs slightly the three edged poorly screened peak that forms by simple summation. By looking at panel **b**, it is now clear why the vanishingly hybridized regimes do not show a net high binding energy shoulder, while it is evident in highly hybridized ones.

We conclude by clarifying the connection between the LBES and the HBEF. If one separates the ECM Mn 3+ spectrum in its components arising from the different initial states, as in Fig. B.2, it is immediately clear.

It is indeed evident that the 3d5C component has significant spectral weight even in the region of the main peak. The substructure from which the LBES and the HBEF originate is the same, although it appears with opposite sign in the variation versus temperature owing to the effects of Mn 4+ in the normalization. It is on this basis that

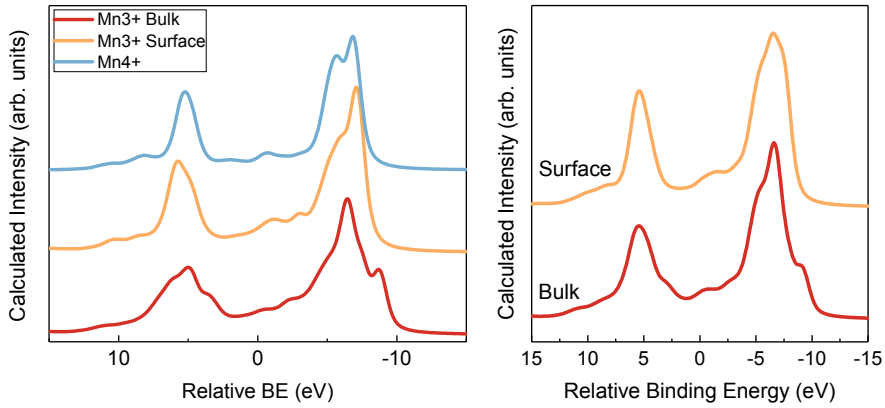

Figure B.1: a. Spectra of Mn 3+ for surface and bulk calculated with the ECM, and Mn 4+ calculated with the CM. The surface spectrum has $V^* = 0$ eV, while the bulk one $V^* = 1.176$. b. Spectra of the surface and the bulk obtained by combining Mn 3+ and Mn 4+ spectra.

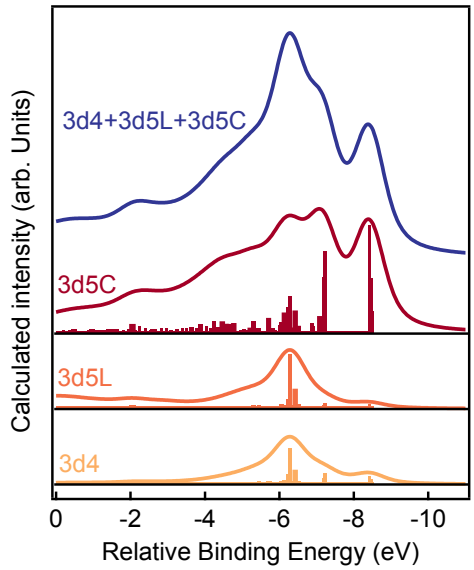

Figure B.2: Spectrum of Mn 3+ divided in its three initial state components: the ground state 3d4, the charge transfer from the ligand hole 3d5L and the charge transfer from the sharp structure, 3d5C. Note that if $V^* \neq 0$, also the 3d4 and 3d5L initial states can project (with a small probability) in the 3d5C final state, giving a small contribution to the LBES.

we claim that at equilibrium there is no reason for the HBEF to be different from the LBES.

Bibliography

M. Aeschlimann, M. Bauer, S. Pawlik, W. Weber, R. Burgermeister, D. Oberli, and H. C. Siegmann (1997), "Ultrafast Spin-Dependent Electron Dynamics in fcc Co," Physical Review Letters **79** (25), 5158–5161.

M. Aeschlimann, C. A. Schmuttenmaer, H. E. Elsayed-Ali, R. J. D. Miller, J. Cao, Y. Gao, and D. A. Mantell (1995), "Observation of surface enhanced multiphoton photoemission from metal surfaces in the short pulse limit," The Journal of Chemical Physics **102** (21), 8606–8613.

M. B. Agranat, S. I. Ashitkov, A. B. Granovskii, and G. I. Rukman (1984), "Interaction of picosecond laser pulses with the electron, spin, and phonon subsystems of nickel," Zh. Eksp. Teor. Fiz **86** (1376), 10.

E. Allaria, D. Castronovo, P. Cinquegrana, P. Craievich, M. Dal Forno, M. B. Danailov, G. D'Auria, A. Demidovich, G. De Ninno, S. Di Mitri, B. Diviacco, W. M. Fawley, M. Ferianis, E. Ferrari, L. Froehlich, G. Gaio, D. Gauthier, L. Giannessi, R. Ivanov, B. Mahieu, N. Mahne, I. Nikolov, F. Parmigiani, G. Penco, L. Raimondi, C. Scafuri, C. Serpico, P. Sigalotti, S. Spampinati, C. Spezzani, M. Svandrlik, C. Svetina, M. Trovo, M. Veronese, D. Zangrando, and M. Zangrando (2013), "Two-stage seeded soft-X-ray free-electron laser," Nature Photonics **7** (11), 913–918.

J. Amann, W. Berg, V. Blank, F.-J. Decker, Y. Ding, P. Emma, Y. Feng, J. Frisch, D. Fritz, J. Hastings, Z. Huang, J. Krzywinski, R. Lindberg, H. Loos, A. Lutman, H.-D. Nuhn, D. Ratner, J. Rzepiela, D. Shu, Yu Shvyd'ko, S. Spampinati, S. Stoupin, S. Terentyev, E. Trakhtenberg, D. Walz, J. Welch, J. Wu, A. Zholents, and D. Zhu (2012), "Demonstration of self-seeding in a hard-X-ray free-electron laser," Nature Photonics **6** (10), 693–698.

P. W. Anderson (1959), "New Approach to the Theory of Superexchange Interactions," Physical Review **115** (1), 2–13.

P. W. Anderson (1961), "Localized Magnetic States in Metals," Physical Review **124** (1), 41–53.

P. W. Anderson, and H. Hasegawa (1955), "Considerations on Double Exchange," Physical Review **100** (2), 675–681.

B. Andres, M. Christ, C. Gahl, M. Wietstruk, M. Weinelt, and J. Kirschner (2015), "Separating Exchange Splitting from Spin Mixing in Gadolinium by Femtosecond Laser Excitation," Physical Review Letters **115** (20), 207404.

M. Angeloni, G. Balestrino, N. G. Boggio, P. G. Medaglia, P. Orgiani, and A. Tebano (2004), "Suppression of the metal-insulator transition temperature in thin La0.7Sr0.3MnO3 films," Journal of Applied Physics **96** (11), 6387–6392.

S. I. Anisimov, B. L. Kapeliovich, and T. L. Perelman (1974), "Electron emission from metal surfaces exposed to ultrashort laser pulses," Zh. Eksp. Teor. Fiz **66** (2), 375–377.

N.W. Ashcroft, and N.D. Mermin (1976), *Solid state physics* (Saunders College).

U. Atxitia, and O. Chubykalo-Fesenko (2011), "Ultrafast magnetization dynamics rates within the Landau-Lifshitz-Bloch model," Physical Review B **84** (14), 144414.

R. D. Averitt, A. I. Lobad, C. Kwon, S. A. Trugman, V. K. Thorsmolle, and A. J. Taylor (2001), "Ultrafast Conductivity Dynamics in Colossal Magnetoresistance Manganites," Physical Review Letters **87** (1), 017401.

A. Awan, H. Truong, and R. J. Lancashire (2017), "CrystalFieldTheory," in *Inorganic Chemistry*, Chemistry LibreTexts (University of California Davis).

M. N. Baibich, J. M. Broto, A. Fert, F. Nguyen Van Dau, F. Petroff, P. Etienne, G. Creuzet, A. Friederich, and J. Chazelas (1988), "Giant magnetoresistance of (001)Fe/(001)Cr magnetic superlattices," Phys. Rev. Lett. **61**, 2472–2475.

D. N. Basov, Richard D. Averitt, Dirk van der Marel, Martin Dressel, and Kristjan Haule (2011), "Electrodynamics of correlated electron materials," Reviews of Modern Physics **83** (2), 471–541.

M. Battiato, K. Carva, and P. M. Oppeneer (2010), "Superdiffusive spin transport as a mechanism of ultrafast demagnetization," Physical Review Letters **105** (2), 027203.

M. Battiato, and K. Held (2016), "Ultrafast and Gigantic Spin Injection in Semiconductors," Physical Review Letters **116** (19), 196601.

M. Baumgartner, K. Garello, J. Mendil, C. O. Avci, E. Grimaldi, C. Murer, J. Feng, M. Gabureac, C. Stamm, Y. Acremann, S. Finizio, S. Wintz, J. Raabe, and P. Gambardella (2017), "Spatially and time-resolved magnetization dynamics driven by spin–orbit torques," Nature Nanotechnology **151**, 1–8.

P. Beaud, A. Caviezel, S. O. Mariager, L. Rettig, G. Ingold, C. Dornes, S.-W. Huang, J. A. Johnson, M. Radovic, T. Huber, T. Kubacka, A. Ferrer, H. T. Lemke, M. Chollet, D. Zhu, J. M. Glownia, M. Sikorski, A. Robert, H. Wadati, M. Nakamura, M. Kawasaki, Y. Tokura, S. L. Johnson, and U. Staub (2014), "A time-dependent order parameter for ultrafast photoinduced phase transitions," Nature Materials **13** (10), 923–927.

P. Beaud, S. L. Johnson, E. Vorobeva, U. Staub, R. A. De Souza, C. J. Milne, Q. X. Jia, and G. Ingold (2009), "Ultrafast Structural Phase Transition Driven by Photoinduced Melting of Charge and Orbital Order," Physical Review Letters **103** (15), 155702.

E. Beaurepaire, J.-C. Merle, A. Daunois, and J.-Y. Bigot (1996), "Ultrafast Spin Dyna-

mics in Ferromagnetic Nickel," Physical Review Letters **76** (22), 4250–4253.

G. Berner, A. Müller, F. Pfaff, J. Walde, C. Richter, J. Mannhart, S. Thiess, A. Gloskovskii, W. Drube, M. Sing, and R. Claessen (2013), "Band alignment in $LaAlO_3/SrTiO_3$ oxide heterostructures inferred from hard x-ray photoelectron spectroscopy," Physical Review B **88** (11), 115111.

R. Bertacco, M. Merano, and F. Ciccacci (1998), "Spin dependent electron absorption in Fe(001)-p(1x1)O: A new candidate for a stable and efficient electron polarization analyzer," Applied Physics Letters **72** (16), 2050–2052.

R. Bertacco, A. Tagliaferri, M. Riva, L. Signorini, M. Cantoni, A. Cattoni, F. Ciccacci, B. A. Davidson, F. Maccherozzi, I. Vobornik, and G. Panaccione (2008), "Surface electronic and magnetic properties of La2/3Sr1/3MnO3 thin films with extended metallicity above the Curie temperature," Physical Review B **78**, 035448.

H. Bethe (1928), "Theorie der beugung von elektronen an kristallen," Annalen der Physik **392** (17), 55–129.

M. Bibes, Ll. Balcells, S. Valencia, J. Fontcuberta, M. Wojcik, E. Jedryka, and S. Nadolski (2001), "Nanoscale Multiphase Separation at La2/3Sr1/3MnO3/srtio3 Interfaces," Physical Review Letters **87** (6), 067210.

M. Bibes, and A. Barthelemy (2007), "Oxide spintronics," IEEE Transactions on Electron Devices **54** (5), 1003–1023, arXiv: 0706.3015.

Mark C. Biesinger, Brad P. Payne, Andrew P. Grosvenor, Leo W. M. Lau, Andrea R. Gerson, and Roger St. C. Smart (2011), "Resolving surface chemical states in XPS analysis of first row transition metals, oxides and hydroxides: Cr, Mn, Fe, Co and Ni," Applied Surface Science **257** (7), 2717–2730.

C. Bigi, P. K. Das, D. Benedetti, F. Salvador, D. Krizmancic, R. Sergo, A. Martin, G. Panaccione, G. Rossi, J. Fujii, and I. Vobornik (2017), "Very efficient spin polarization analysis (VESPA): new exchange scattering-based setup for spin-resolved ARPES at APE-NFFA beamline at Elettra," Journal of Synchrotron Radiation **24** (4), 750–756.

C. Bigi, T. Pincelli, P. Orgiani, A. Verna, A. Petrov, J. Fujii, I. Vobornik, F. Offi, and G. Panccione (2018), "To be published," .

J.-Y. Bigot (2001), "Femtosecond magneto-optical processes in metals," Comptes Rendus de l'Académie des Sciences - Series IV - Physics **2** (10), 1483–1504.

J.-Y. Bigot, M. Vomir, and E. Beaurepaire (2009), "Coherent ultrafast magnetism induced by femtosecond laser pulses," Nature Physics **5** (7), 515–520.

G. Binasch, P. Grünberg, F. Saurenbach, and W. Zinn (1989), "Enhanced magnetoresistance in layered magnetic structures with antiferromagnetic interlayer exchange," Physical Review B **39** (7), 4828–4830.

F. Bloch (1928), *Uber die Quantenmechanik der Elektronen in Kristallgittern* (Springer).

K. Bobowski, M. Gleich, N. Pontius, C. Schüssler-Langeheine, C. Trabant, Marko Wietstruk, B. Frietsch, and M. Weinelt (2017), "Influence of the pump pulse wavelength on the ultrafast demagnetization of Gd(0 0 0 1) thin films," Journal of Physics: Condensed Matter **29** (23), 234003.

J. H. de Boer, and E. J. W. Verwey (1937), "Semi-conductors with partially and with completely filled 3 d -lattice bands," Proceedings of the Physical Society **49** (4S), 59.

Giovanni Borghi, Michele Fabrizio, and Erio Tosatti (2009), "Surface Dead Layer for Quasiparticles Near a Mott Transition," Physical Review Letters **102** (6), 066806.

J. Boullet, Y. Zaouter, J. Limpert, S. Petit, Y. Mairesse, B. Fabre, J. Higuet, E. Mével, E. Constant, and E. Cormier (2009), "High-order harmonic generation at a megahertz-level repetition rate directly driven by an ytterbium-doped-fiber chirped-pulse amplification system," Optics letters **34** (9), 1489–1491.

M. Bowen, M. Bibes, A. Barthélémy, J.-P. Contour, A. Anane, Y. Lemaître, and A. Fert (2003), "Nearly total spin polarization in La2/3Sr1/3MnO3 from tunneling experiments," Applied Physics Letters **82** (2), 233–235.

Luis Brey (2007), "Electronic phase separation in manganite-insulator interfaces," Physical Review B **75** (10), 104423.

S. Brivio, M. Cantoni, D. Petti, and R. Bertacco (2010), "Near-room-temperature control of magnetization in field effect devices based on La0.67Sr0.33MnO3 thin films," Journal of Applied Physics **108** (11), 113906.

F. Y. Bruno, J. Garcia-Barriocanal, M. Varela, N. M. Nemes, P. Thakur, J. C. Cezar, N. B. Brookes, A. Rivera-Calzada, M. Garcia-Hernandez, C. Leon, S. Okamoto, S. J. Pennycook, and J. Santamaria (2011), "Electronic and Magnetic Reconstructions in La0.7Sr0.3MnO3/SrTiO3 Heterostructures: A Case of Enhanced Interlayer Coupling Controlled by the Interface," Physical Review Letters **106** (14), 147205.

J. H. Buss, J. Maklar, F. Joucken, H. Wang, Y. Xu, S.-K. Mo, A. Lanzara, and R. A. Kaindl (2017), "Ultrafast extreme-ultraviolet ARPES studies of electronic dynamics in two-dimensional materials," (International Society for Optics and Photonics) p. 101020I.

A. del Campo, and W. H. Zurek (2014), "Universality of phase transition dynamics: Topological defects from symmetry breaking," International Journal of Modern Physics A **29** (08), 1430018.

R. Carley, K. Döbrich, B. Frietsch, C. Gahl, M. Teichmann, O. Schwarzkopf, P. Wernet, and M. Weinelt (2012), "Femtosecond Laser Excitation Drives Ferromagnetic Gadolinium out of Magnetic Equilibrium," Physical Review Letters **109** (5), 057401.

E. Carpene, F. Boschini, H. Hedayat, C. Piovera, C. Dallera, E. Puppin, M. Mansurova, M. Münzenberg, X. Zhang, and A. Gupta (2013), "Measurement of the magneto-optical response of Fe and CrO2 epitaxial films by pump-probe spectroscopy: Evidence for spin-charge separation," Physical Review B **87** (17), 174437.

E. Carpene, H. Hedayat, F. Boschini, and C. Dallera (2015), "Ultrafast demagnetization of metals: Collapsed exchange versus collective excitations," Physical Review B **91** (17), 174414.

E. Carpene, E. Mancini, C. Dallera, M. Brenna, E. Puppin, and S. De Silvestri (2008), "Dynamics of electron-magnon interaction and ultrafast demagnetization in thin iron films," Physical Review B **78** (17), 174422.

A. Chainani, and M. Oura (2014), "Real-time observation of photoinduced valence-transitions in mixed-valence compounds by means of hard X-ray photoelectron spectroscopy," , 1–27.

M.-C. Chen, M. R. Gerrity, S. Backus, T. Popmintchev, X. Zhou, P. Arpin, X. Zhang, H. C. Kapteyn, and M. M. Murnane (2009), "Spatially coherent, phase matched, high-order harmonic EUV beams at 50 kHz," Optics Express **17** (20), 17376–17383.

C.-T. Chiang, A. Winkelmann, J. Henk, F. Bisio, and J. Kirschner (2012), "Spin-selective pathways in linear and nonlinear photoemission from ferromagnets," Physical Review B **85** (16), 165137.

R. Clauberg, W. Gudat, E. Kisker, and E. Kuhlmann (1981), "Spin polarized threshold-photoemission from Ni(110) with transverse sample magnetization," Zeitschrift für Physik B Condensed Matter **43** (1), 47–54.

J. M. D. Coey, and S. Sanvito (2004), "Magnetic semiconductors and half-metals," Journal of Physics D: Applied Physics **37** (7), 988.

A. Crepaldi, S. Roth, G. Gatti, C. A. Arrell, J. Ojeda, F. van Mourik, P. Bugnon, A. Magrez, H. Berger, M. Chergui, and M. Grioni (2017), "Time-resolved ARPES at LACUS: Band Structure and Ultrafast Electron Dynamics of Solids," CHIMIA International Journal for Chemistry **71** (5), 273–277.

Elbio Dagotto, Takashi Hotta, and Adriana Moreo (2001), "Colossal magnetoresistant materials: the key role of phase separation," Physics Reports **344** (1), 1–153.

M. P. M. Dean, Y. Cao, X. Liu, S. Wall, D. Zhu, R. Mankowsky, V. Thampy, X. M. Chen, J. G. Vale, D. Casa, Jungho Kim, A. H. Said, P. Juhas, R. Alonso-Mori, J. M. Glownia, A. Robert, J. Robinson, M. Sikorski, S. Song, M. Kozina, H. Lemke, L. Patthey, S. Owada, T. Katayama, M. Yabashi, Yoshikazu Tanaka, T. Togashi, J. Liu, C. Rayan Serrao, B. J. Kim, L. Huber, C.-L. Chang, D. F. McMorrow, M. Först, and J. P. Hill (2016), "Ultrafast energy- and momentum-resolved dynamics of magnetic correlations in the photo-doped Mott insulator Sr_2IrO_4," Nature Materials **15** (6), 601–605.

S. van Dijken, X. Jiang, and S. S. P. Parkin (2002), "Spin-dependent hot electron transport in $Ni_{81}Fe_{19}$ and $Co_{84}Fe_{16}$ films on GaAs(001)," Physical Review B **66** (9), 094417.

J. H. Dil (2009), "Spin and angle resolved photoemission on non-magnetic low-dimensional systems," Journal of Physics: Condensed Matter **21** (40), 403001.

M. Dobrowolska, K. Tivakornsasithorn, X. Liu, J. K. Furdyna, M. Berciu, K. M. Yu, and W. Walukiewicz (2012), "Controlling the Curie temperature in (Ga,Mn)As through location of the Fermi level within the impurity band," Nature Materials **11** (5), 444–449.

C. Domb (1986), *Phase Transitions and Critical Phenomena*, Phase Transitions and Critical Phenomena No. v. 19 (Elsevier Science).

H. Ehrke, R. I. Tobey, S. Wall, S. A. Cavill, M. Först, V. Khanna, Th. Garl, N. Stojanovic, D. Prabhakaran, A. T. Boothroyd, M. Gensch, A. Mirone, P. Reutler, A. Revcolevschi,

S. S. Dhesi, and A. Cavalleri (2011), "Photoinduced Melting of Antiferromagnetic Order in La0.5Sr1.5MnO3 Measured Using Ultrafast Resonant Soft X-Ray Diffraction," Physical Review Letters **106** (21), 217401.

W. Eib, and B. Reihl (1978), "Spin Polarization of Photoelectrons and Itinerant Magnetism in Iron," Physical Review Letters **40** (25), 1674–1676.

S. Eich, M. Plötzing, M. Rollinger, S. Emmerich, R. Adam, C. Chen, H. C. Kapteyn, M. M. Murnane, L. Plucinski, D. Steil, B. Stadtmüller, M. Cinchetti, M. Aeschlimann, C. M. Schneider, and S. Mathias (2017), "Band structure evolution during the ultrafast ferromagnetic-paramagnetic phase transition in cobalt," Science Advances **3** (3), e1602094.

M. Ellguth, C. Tusche, and J. Kirschner (2015), "Optical Generation of Hot Spin-Polarized Electrons from a Ferromagnetic Two-Dimensional Electron Gas," Physical Review Letters **115** (26), 266801.

P. Emma, R. Akre, J. Arthur, R. Bionta, C. Bostedt, J. Bozek, A. Brachmann, P. Bucksbaum, R. Coffee, F.-J. Decker, Y. Ding, D. Dowell, S. Edstrom, A. Fisher, J. Frisch, S. Gilevich, J. Hastings, G. Hays, Ph Hering, Z. Huang, R. Iverson, H. Loos, M. Messerschmidt, A. Miahnahri, S. Moeller, H.-D. Nuhn, G. Pile, D. Ratner, J. Rzepiela, D. Schultz, T. Smith, P. Stefan, H. Tompkins, J. Turner, J. Welch, W. White, J. Wu, G. Yocky, and J. Galayda (2010), "First lasing and operation of an Ångstrom-wavelength free-electron laser," Nature Photonics **4** (9), 641–647.

Y. Erlich, and D. Zielinski (2017), "DNA fountain enables a robust and efficient storage architecture," Science **355** (6328), 950–954.

V. Esposito, M. Fechner, R. Mankowsky, H. Lemke, M. Chollet, J. M. Glownia, M. Nakamura, M. Kawasaki, Y. Tokura, U. Staub, P. Beaud, and M. Först (2017), "Nonlinear electron-phonon coupling in doped manganites," Physical Review Letters **118** (24), 247601.

M. Först, R. I. Tobey, S. Wall, H. Bromberger, V. Khanna, A. L. Cavalieri, Y.-D. Chuang, W. S. Lee, R. Moore, W. F. Schlotter, J. J. Turner, O. Krupin, M. Trigo, H. Zheng, J. F. Mitchell, S. S. Dhesi, J. P. Hill, and A. Cavalleri (2011), "Driving magnetic order in a manganite by ultrafast lattice excitation," Physical Review B **84** (24), 241104.

C. S. Fadley (2016), "Hard X-ray Photoemission: An Overview and Future Perspective," in *Hard X-ray Photoelectron Spectroscopy (HAXPES)*, Springer Series in Surface Sciences (Springer, Cham) pp. 1–34.

D. Fausti, R. I. Tobey, N. Dean, S. Kaiser, A. Dienst, M. C. Hoffmann, S. Pyon, T. Takayama, H. Takagi, and A. Cavalleri (2011), "Light-Induced Superconductivity in a Stripe-Ordered Cuprate," Science **331** (6014), 189–191.

R. Feder (1981), "Spin-polarised low-energy electron diffraction," Journal of Physics C: Solid State Physics **14** (15), 2049.

H. A. Fernandes, J. R. Drugowich de Felício, and A. A. Caparica (2005), "Short-time behavior of a classical ferromagnet with double-exchange interaction," Physical Review B **72** (5), 054434.

E. Ferrari, C. Spezzani, F. Fortuna, R. Delaunay, F. Vidal, I. Nikolov, P. Cinquegrana, B. Diviacco, D. Gauthier, G. Penco, P. R. Ribič, E. Roussel, M. Trovó, J.-B. Moussy, T. Pincelli, L. Lounis, M. Manfredda, E. Pedersoli, F. Capotondi, C. Svetina, N. Mahne, M. Zangrando, L. Raimondi, A. Demidovich, L. Giannessi, G. De Ninno, M. B. Danailov, E. Allaria, and M. Sacchi (2016), "Widely tunable two-colour seeded free-electron laser source for resonant-pump resonant-probe magnetic scattering," Nature Communications **7**, ncomms10343.

A. Fognini, T. U. Michlmayr, G. Salvatella, C. Wetli, U. Ramsperger, T. Bähler, F. Sorgenfrei, M. Beye, A. Eschenlohr, N. Pontius, C. Stamm, F. Hieke, M. Dell'Angela, S. de Jong, R. Kukreja, N. Gerasimova, V. Rybnikov, A. Al-Shemmary, H. Redlin, J. Raabe, A. Föhlisch, H. A. Dürr, W. Wurth, D. Pescia, A. Vaterlaus, and Y. Acremann (2014a), "Ultrafast reduction of the total magnetization in iron," Applied Physics Letters **104** (3), 032402.

A. Fognini, T. U. Michlmayr, A. Vaterlaus, and Y. Acremann (2017), "Laser-induced ultrafast spin current pulses: a thermodynamic approach," Journal of Physics: Condensed Matter **29** (21), 214002.

A. Fognini, G. Salvatella, T. U. Michlmayr, C. Wetli, U. Ramsperger, T. Bähler, F. Sorgenfrei, M. Beye, A Eschenlohr, N. Pontius, C. Stamm, F. Hieke, M. Dell'Angela, S. de Jong, R. Kukreja, N. Gerasimova, V. Rybnikov, H Redlin, J. Raabe, A. Föhlisch, H. A. Dürr, W. Wurth, D. Pescia, A. Vaterlaus, and Y. Acremann (2014b), "The role of space charge in spin-resolved photoemission experiments," New Journal of Physics **16** (4), 043031.

A. W. Fognini (2014), *ULTRAFAST DEMAGNETIZATION: AN ELECTRONIC POINT OF VIEW*, Ph.D. thesis (Eidgenössische Technische Hochschule Zürich), phD Thesis.

X. Fong, Y. Kim, K. Yogendra, D. Fan, A. Sengupta, A. Raghunathan, and K. Roy (2016), "Spin-transfer torque devices for logic and memory: Prospects and perspectives," IEEE Transactions on Computer-Aided Design of Integrated Circuits and Systems **35** (1), 1–22.

F. Frassetto, C. Cacho, C. A. Froud, I. C. E. Turcu, P. Villoresi, W. A. Bryan, E. Springate, and L. Poletto (2011), "Single-grating monochromator for extreme-ultraviolet ultrashort pulses," Optics Express **19** (20), 19169–19181.

J. C. Fuggle, M. Campagna, Z. Zolnierek, R. Lässer, and A. Platau (1980), "Observation of a Relationship between Core-Level Line Shapes in Photoelectron Spectroscopy and the Localization of Screening Orbitals," Physical Review Letters **45** (19), 1597–1600.

J. Fujii, B. R. Salles, M. Sperl, S. Ueda, M. Kobata, K. Kobayashi, Y. Yamashita, P. Torelli, M. Utz, C. S. Fadley, A. X. Gray, J. Braun, H. Ebert, I. Di Marco, O. Eriksson, P. Thunström, G. H. Fecher, H. Stryhanyuk, E. Ikenaga, J. Minár, C. H. Back, G. van der Laan, and G. Panaccione (2013), "Identifying the Electronic Character and Role of the Mn States in the Valence Band of (Ga,Mn)As," Physical Review Letters **111** (9), 097201.

J. Fujii, M. Sperl, S. Ueda, K. Kobayashi, Y. Yamashita, M. Kobata, P. Torelli, F. Borg-

atti, M. Utz, C. S. Fadley, A. X. Gray, G. Monaco, C. H. Back, G. van der Laan, and G. Panaccione (2011), "Identification of Different Electron Screening Behavior Between the Bulk and Surface of (Ga,Mn)As," Physical Review Letters **107** (18), 187203.

A. Fujimori (1992), "Electronic structure of metallic oxides: Band-gap closure and valence control," Journal of Physics and Chemistry of Solids Special Issue Elecronic Structure and Fermiology of High-Tc Superconductors, **53** (12), 1595–1602.

D. A. Garanin (1997), "Fokker-Planck and Landau-Lifshitz-Bloch equations for classical ferromagnets," Physical Review B **55** (5), 3050–3057.

T. J. Gay, and F. B. Dunning (1992), "Mott electron polarimetry," Review of Scientific Instruments **63** (2), 1635–1651.

A. Gellrich, and J. Kessler (1991), "Precision measurement of the Sherman asymmetry function for electron scattering from gold," Physical Review A **43** (1), 204–216.

P. G. de Gennes (1960), "Effects of Double Exchange in Magnetic Crystals," Physical Review **118** (1), 141–154.

C. Giannetti, M. Capone, D. Fausti, M. Fabrizio, F. Parmigiani, and D. Mihailovic (2016), "Ultrafast optical spectroscopy of strongly correlated materials and high-temperature superconductors: a non-equilibrium approach," Advances in Physics **65** (2), 58–238.

J. Graf, C. Jozwiak, C. L. Smallwood, H. Eisaki, R. A. Kaindl, D.-H. Lee, and A. Lanzara (2011), "Nodal quasiparticle meltdown in ultrahigh-resolution pump-probe angle-resolved photoemission," Nature Physics **7** (10), 805–809.

S. M. Griffin, M. Lilienblum, K. T. Delaney, Y. Kumagai, M. Fiebig, and N. A. Spaldin (2012), "Scaling Behavior and Beyond Equilibrium in the Hexagonal Manganites," Physical Review X **2** (4), 041022.

R. A. de Groot, F. M. Mueller, P. G. van Engen, and K. H. J. Buschow (1983), "New Class of Materials: Half-Metallic Ferromagnets," Physical Review Letters **50** (25), 2024–2027.

L. Guidoni, E. Beaurepaire, and J.-Y. Bigot (2002), "Magneto-optics in the Ultrafast Regime: Thermalization of Spin Populations in Ferromagnetic Films," Physical Review Letters **89** (1), 017401.

S. Günther (2015), *Ultrafast probing of the magnetic order parameter*, Ph.D. thesis (Fakultät für Physik der Universität Regensburg), phD Thesis.

M. Hajlaoui, E. Papalazarou, J. Mauchain, G. Lantz, N. Moisan, D. Boschetto, Z. Jiang, I. Miotkowski, Y. P. Chen, A. Taleb-Ibrahimi, L. Perfetti, and M. Marsi (2012), "Ultrafast Surface Carrier Dynamics in the Topological Insulator Bi2te3," Nano Letters **12** (7), 3532–3536.

T. Hara, M. Yabashi, T. Tanaka, T. Bizen, S. Goto, X. M. Maréchal, T. Seike, K.i Tamasaku, T. Ishikawa, and H. Kitamura (2002), "The brightest x-ray source: A very long undulator at SPring-8," Review of Scientific Instruments **73** (3), 1125–1128.

A. Hariki, A. Yamanaka, and T. Uozumi (2016), "Orbital- and spin-order sensitive nonlocal screening in Mn 2p X-ray photoemission of La 1-x Sr x MnO 3," EPL (Europhysics

Letters) **114** (2), 27003.

S. Hellmann, M. Beye, C. Sohrt, T. Rohwer, F. Sorgenfrei, H. Redlin, M. Kalläne, M. Marczynski-Bühlow, F. Hennies, M. Bauer, A. Föhlisch, L. Kipp, W. Wurth, and K. Rossnagel (2010), "Ultrafast Melting of a Charge-Density Wave in the Mott Insulator 1T-TaS2," Physical Review Letters **105** (18), 187401.

S. Hellmann, T. Rohwer, M. Kalläne, K. Hanff, C. Sohrt, A. Stange, A. Carr, M. M. Murnane, H. C. Kapteyn, L. Kipp, M. Bauer, and K. Rossnagel (2012), "Time-domain classification of charge-density-wave insulators," Nature Communications **3**, ncomms2078.

J. Hemberger, A. Krimmel, T. Kurz, H.-A. Krug von Nidda, V. Yu. Ivanov, A. A. Mukhin, A. M. Balbashov, and A. Loidl (2002), "Structural, magnetic, and electrical properties of single-crystalline La1-xSrxMnO3 (0.4<x<0.85)," Physical Review B **66** (9), 094410.

C. M. Heyl, J. Güdde, A. L'Huillier, and U. Höfer (2012), "High-order harmonic generation with μJ laser pulses at high repetition rates," Journal of Physics B: Atomic, Molecular and Optical Physics **45** (7), 074020.

D. J. Higley, K. Hirsch, G. L. Dakovski, E. Jal, E. Yuan, T. Liu, A. A. Lutman, J. P. MacArthur, E. Arenholz, Z. Chen, G. Coslovich, P. Denes, P. W. Granitzka, P. Hart, M. C. Hoffmann, J. Joseph, L. Le Guyader, A. Mitra, S. Moeller, H. Ohldag, M. Seaberg, P. Shafer, J. Stöhr, A. Tsukamoto, H.-D. Nuhn, A. H. Reid, H. A. Dürr, and W. F. Schlotter (2016), "Femtosecond X-ray magnetic circular dichroism absorption spectroscopy at an X-ray free electron laser," Review of Scientific Instruments **87** (3), 033110.

K. Hirano, K. Izumi, T. Ishikawa, S. Annaka, and S. Kikuta (1991), "An x-ray phase plate using bragg-case diffraction," Japanese Journal of Applied Physics **30** (3A), L407.

T. Hishida, K. Ohbayashi, M. Kobata, E. Ikenaga, T. Sugiyama, K. Kobayashi, M. Okawa, and T. Saitoh (2013a), "Empirical relationship between x-ray photoemission spectra and electrical conductivity in a colossal magnetoresistive manganite La1-xSrxMnO3," Journal of Applied Physics **113** (23), 233702.

T. Hishida, K. Ohbayashi, and T. Saitoh (2013b), "Hidden relationship between the electrical conductivity and the Mn 2p core-level photoemission spectra in La1-xSrxMnO3," Journal of Applied Physics **113** (4), 043710.

J. A. Hofmann, A. Paskin, K. J. Tauer, and R. J. Weiss (1956), "Analysis of ferromagnetic and antiferro-magnetic second-order transitions," Journal of Physics and Chemistry of Solids **1** (1), 45–60.

P. C. Hohenberg, and B. I. Halperin (1977), "Theory of dynamic critical phenomena," Reviews of Modern Physics **49** (3), 435–479.

J. Hohlfeld, E. Matthias, R. Knorren, and K. H. Bennemann (1997), "Nonequilibrium Magnetization Dynamics of Nickel," Physical Review Letters **78** (25), 4861–4864.

K. Holldack, J. Bahrdt, A. Balzer, U. Bovensiepen, M. Brzhezinskaya, A. Erko, A. Eschenlohr, R. Follath, A. Firsov, W. Frentrup, L. Le Guyader, T. Kachel, P. Kuske, R. Mitzner, R. Müller, N. Pontius, T. Quast, I. Radu, J.-S. Schmidt, C. Schüßler-

Langeheine, M. Sperling, C. Stamm, C. Trabant, and A. Föhlisch (2014), "FemtoSpeX: a versatile optical pump/soft X-ray probe facility with 100 fs X-ray pulses of variable polarization," Journal of Synchrotron Radiation **21** (5), 1090–1104.

T. Holstein (1959), "Studies of polaron motion: Part II. The "small" polaron," Annals of Physics **8** (3), 343–389.

K. Horiba, M. Taguchi, A. Chainani, Y. Takata, E. Ikenaga, D. Miwa, Y. Nishino, K. Tamasaku, M. Awaji, A. Takeuchi, M. Yabashi, H. Namatame, M. Taniguchi, H. Kumigashira, M. Oshima, M. Lippmaa, M. Kawasaki, H. Koinuma, K. Kobayashi, T. Ishikawa, and S. Shin (2004), "Nature of the Well Screened State in Hard X-Ray Mn 2p Core-Level Photoemission Measurements of La1-xSrxMnO3 Films," Physical Review Letters **93** (23), 236401.

J. Hubbard (1963), "Electron correlations in narrow energy bands," Proc. R. Soc. Lond. A **276** (1365), 238–257.

W. Hübner, and K. H. Bennemann (1996), "Simple theory for spin-lattice relaxation in metallic rare-earth ferromagnets," Physical Review B **53** (6), 3422–3427.

S. Hüfner (2003), *Photoelectron Spectroscopy - Principles and Applications*, 3rd ed., Advanced Texts in Physics (Springer-Verlag Berlin Heidelberg).

H. Ichikawa, S. Nozawa, T. Sato, A. Tomita, K. Ichiyanagi, M. Chollet, . Guerin, N. Dean, A. Cavalleri, S. Adachi, T. Arima, H. Sawa, Y. Ogimoto, M. Nakamura, R. Tamaki, K. Miyano, and S. Koshihara (2011), "Transient photoinduced 'hidden' phase in a manganite," Nature Materials **10** (2), 101–105.

M. Imada, A. Fujimori, and Y. Tokura (1998), "Metal-insulator transitions," Rev. Mod. Phys. **70**, 1039–1263.

V. I. Irkhin, and M. I. Katsnelson (1994), "Half-metallic ferromagnets," Physics-Uspekhi **37** (7), 659.

T. Ishikawa, K. Tamasaku, and M. Yabashi (2005), "High-resolution X-ray monochromators," Nuclear Instruments and Methods in Physics Research Section A: Accelerators, Spectrometers, Detectors and Associated Equipment Proceedings of the Workshop on Hard X-ray Photoelectron Spectroscopy, **547** (1), 42–49.

N. Ito (1993), "Non-equilibrium relaxation and interface energy of the Ising model," Physica A: Statistical Mechanics and its Applications **196** (4), 591–614.

S. Jin, M. McCormack, T. H. Tiefel, and R. Ramesh (1994), "Colossal magnetoresistance in La-Ca-Mn-O ferromagnetic thin films (invited)," Journal of Applied Physics **76** (10), 6929–6933.

M. Johnson, and R. H. Silsbee (1985), "Interfacial charge-spin coupling: Injection and detection of spin magnetization in metals," Phys. Rev. Lett. **55**, 1790–1793.

C. M. Jozwiak (2008), *A New Spin on Photoemission Spectroscopy*, Ph.D. thesis (University of California, Berkeley).

T. Jungwirth, J. Wunderlich, V. Novák, K. Olejník, B. L. Gallagher, R. P. Campion, K. W. Edmonds, A. W. Rushforth, A. J. Ferguson, and P. Němec (2014), "Spin-dependent phenomena and device concepts explored in (Ga,Mn)As," Reviews of Modern Physics

86 (3), 855–896.

O. Jürgensen (2015), *Extended Hubbard Models for Ultracold Atoms in Optical Lattices*, Ph.D. thesis (Fakultät für Mathematik, Informatik und Naturwissenschaften Fachbereich Physik der Universität Hamburg), phD Thesis.

M. I. Katsnelson, V. Yu. Irkhin, L. Chioncel, A. I. Lichtenstein, and R. A. de Groot (2008), "Half-metallic ferromagnets: From band structure to many-body effects," Reviews of Modern Physics **80** (2), 315–378.

Joachim Kessler (1976), "Introduction," in *Polarized Electrons*, Texts and Monographs in Physics (Springer, Berlin, Heidelberg) pp. 1–6.

H. Kino, F. Aryasetiawan, I. Solovyev, T. Miyake, T. Ohno, and K. Terakura (2003), "GW study of half-metallic electronic structure of La0.7sr0.3mno3," Physica B: Condensed Matter Proceedings of the 23rd International Conference on Low Temperature Physics, **329** (Part 2), 858–859.

P. S. Kirchmann, L. Perfetti, M. Wolf, and U. Bovensiepen (2010), "Femtosecond Time- and Angle-Resolved Photoemission as a Real-time Probe of Cooperative Effects in Correlated Electron Materials," in *Dynamics at Solid State Surfaces and Interfaces*, edited by U. Bovensiepen, H. Petek, and M. Wolf (Wiley-VCH Verlag GmbH & Co. KGaA) pp. 475–497, dOI: 10.1002/9783527633418.ch20.

A. Kirilyuk, A. V. Kimel, and T. Rasing (2010), "Ultrafast optical manipulation of magnetic order," Reviews of Modern Physics **82** (3), 2731–2784.

J. Kirschner, and R. Feder (1979), "Spin Polarization in Double Diffraction of Low-Energy Electrons from W(001): Experiment and Theory," Physical Review Letters **42** (15), 1008–1011.

J. Kirschner, F. Giebels, H. Gollisch, and R. Feder (2013), "Spin-polarized electron scattering from pseudomorphic Au on Ir(001)," Physical Review B **88** (12), 125419.

T. Kise, T. Ogasawara, M. Ashida, Y. Tomioka, Y. Tokura, and M. Kuwata-Gonokami (2000), "Ultrafast Spin Dynamics and Critical Behavior in Half-Metallic Ferromagnet: Sr2FeMoO6," Physical Review Letters **85** (9), 1986–1989.

E. Kisker, and C. Carbone (1992), "Chapter 12 Spin- and Angle-Resolved Photoemission from Ferromagnets," in *Studies in Surface Science and Catalysis*, Angle-Resolved Photoemission, Vol. 74, edited by S. D. Kevan (Elsevier) pp. 469–508, dOI: 10.1016/S0167-2991(08)61782-6.

K. Kobayashi (2016), "HAXPES Applications to Advanced Materials," in *Hard X-ray Photoelectron Spectroscopy (HAXPES)*, Springer Series in Surface Sciences (Springer, Cham) pp. 467–531.

K. Kobayashi, M. Yabashi, Y. Takata, T. Tokushima, S. Shin, K. Tamasaku, D. Miwa, T. Ishikawa, H. Nohira, T. Hattori, Y. Sugita, O. Nakatsuka, A. Sakai, and S. Zaima (2003), "High resolution-high energy x-ray photoelectron spectroscopy using third-generation synchrotron radiation source, and its application to Si-high k insulator systems," Applied Physics Letters **83** (5), 1005–1007.

B. Koopmans (2003), "Laser-Induced Magnetization Dynamics," in *Spin Dynamics in*

Confined Magnetic Structures II, Topics in Applied Physics (Springer, Berlin, Heidelberg) pp. 256–323.

B. Koopmans (2007), "Time-resolved Kerr-effect and Spin Dynamics in Itinerant Ferromagnets," in *Handbook of Magnetism and Advanced Magnetic Materials* (John Wiley & Sons, Ltd) dOI: 10.1002/9780470022184.hmm313.

B. Koopmans, M. van Kampen, J. T. Kohlhepp, and W. J. M. de Jonge (2000), "Ultrafast Magneto-Optics in Nickel: Magnetism or Optics?" Physical Review Letters **85** (4), 844–847.

B. Koopmans, G. Malinowski, F. Dalla Longa, D. Steiauf, M. Fähnle, T. Roth, M. Cinchetti, and M. Aeschlimann (2010), "Explaining the paradoxical diversity of ultrafast laser-induced demagnetization," Nature Materials **9** (3), 259–265.

Gabriel Kotliar, and Dieter Vollhardt (2004), "Strongly Correlated Materials: Insights From Dynamical Mean-Field Theory," Physics Today **57** (3), 53–59.

M. Krauß, T. Roth, S. Alebrand, D. Steil, M. Cinchetti, M. Aeschlimann, and H. C. Schneider (2009), "Ultrafast demagnetization of ferromagnetic transition metals: The role of the Coulomb interaction," Physical Review B **80** (18), 180407.

V. N. Krivoruchko (2014), "The Griffiths phase and the metal-insulator transition in substituted manganites (Review Article)," Low Temperature Physics **40** (7), 586–599.

R. L. Kronig, and W. G. Penney (1931), "Quantum mechanics of electrons in crystal lattices," Proceedings of the Royal Society of London A: Mathematical, Physical and Engineering Sciences **130** (814), 499–513, http://rspa.royalsocietypublishing.org/content/130/814/499.full.pdf .

K. Kubo (1972), "A Quantum Theoy of Double Exchange. II. The Green Function of a Hole." Journal of the Physical Society of Japan **33** (4), 10.1143/JPSJ.33.929.

K. Kubo, and N. Ohata (1972), "A Quantum Theory of Double Exchange. I," Journal of the Physical Society of Japan **33** (1), 21–32.

D. Kutnyakhov, H. J. Elmers, G. Schönhense, C. Tusche, S. Borek, J. Braun, J. Minár, and H. Ebert (2015), "Specular reflection of spin-polarized electrons from the W(001) spin-filter crystal in a large range of scattering energies and angles," Physical Review B **91** (1), 014416.

D. Kutnyakhov, P. Lushchyk, A. Fognini, D. Perriard, M. Kolbe, K. Medjanik, E. Fedchenko, S. A. Nepijko, H. J. Elmers, G. Salvatella, C. Stieger, R. Gort, T. Bähler, T. Michlmayer, Y. Acremann, A. Vaterlaus, F. Giebels, H. Gollisch, R. Feder, C. Tusche, A. Krasyuk, J. Kirschner, and G. Schönhense (2013), "Imaging spin filter for electrons based on specular reflection from iridium (001)," Ultramicroscopy Eighth International Workshop on LEEM/PEEM, **130** (Supplement C), 63–69.

G. van der Laan (2015), "Zen and the art of dichroic photoemission," Journal of Electron Spectroscopy and Related Phenomena Special Anniversary Issue: Volume 200, **200** (Supplement C), 143–159.

M. Landolt (1986), "High-resolution magnetic measurements at surfaces with spin polarized electrons," Applied Physics A **41** (1), 83–89.

T. Li, A. Patz, L. Mouchliadis, J. Yan, T. A. Lograsso, I. E. Perakis, and J. Wang (2013), "Femtosecond switching of magnetism via strongly correlated spin-charge quantum excitations," Nature **496** (7443), 69–73.

F. Lindner, W. Stremme, M. G. Schätzel, F. Grasbon, G. G. Paulus, H. Walther, R. Hartmann, and L. Strüder (2003), "High-order harmonic generation at a repetition rate of 100 kHz," Physical Review A **68** (1), 013814.

X. J. Liu, Y. Moritomo, A. Nakamura, H. Tanaka, and T. Kawai (2001), "Critical behavior of a photodisordered spin system in doped manganite," Physical Review B **64** (10), 100401.

A. I. Lobad, R. D. Averitt, C. Kwon, and A. J. Taylor (2000a), "Spin/lattice interaction in colossal magnetoresistance manganites," Applied Physics Letters **77** (24), 4025–4027.

A. I. Lobad, A. J. Taylor, C. Kwon, S. A. Trugman, and T. R. Gosnell (2000b), "Laser induced dynamic spectral weight transfer in La0.7Ca0.3MnO3," Chemical Physics **251** (1), 227–236.

R. Locher, M. Lucchini, J. Herrmann, M. Sabbar, M. Weger, A. Ludwig, L. Castiglioni, M. Greif, M. Hengsberger, L. Gallmann, and U. Keller (2014), "Versatile attosecond beamline in a two-foci configuration for simultaneous time-resolved measurements," Review of Scientific Instruments **85** (1), 013113.

V. Lollobrigida (2016), *Strongly correlated electron materials: a core level photoelectron spectroscopy investigation*, Ph.D. thesis (Scuola Dottorale in Matematica e Fisica, Universitá degli Studi Roma Tre), phD Thesis.

E. Lorek, E. W. Larsen, C. M. Heyl, S. Carlström, D. Paleček, D. Zigmantas, and J. Mauritsson (2014), "High-order harmonic generation using a high-repetition-rate turnkey laser," Review of Scientific Instruments **85** (12), 123106.

Yu Lu, X. W. Li, G. Q. Gong, Gang Xiao, A. Gupta, P. Lecoeur, J. Z. Sun, Y. Y. Wang, and V. P. Dravid (1996), "Large magnetotunneling effect at low magnetic fields in micrometer-scale epitaxial La0.67Sr0.33MnO3 tunnel junctions," Physical Review B **54** (12), R8357–R8360.

F. Maccherozzi, G. Panaccione, G. Rossi, M. Hochstrasser, M. Sperl, M. Reinwald, G. Woltersdorf, W. Wegscheider, and C. H. Back (2006), "Influence of surface treatment on the magnetic properties of Ga1-xMnxAs thin films," Physical Review B **74** (10), 104421.

F. Maccherozzi, M. Sperl, G. Panaccione, J. Minár, S. Polesya, H. Ebert, U. Wurstbauer, M. Hochstrasser, G. Rossi, G. Woltersdorf, W. Wegscheider, and C. H. Back (2008), "Evidence for a Magnetic Proximity Effect up to Room Temperature at Fe/(Ga,Mn)As Interfaces," Physical Review Letters **101** (26), 267201.

Andreas Mann, Jakob Walowski, Markus Münzenberg, Stefan Maat, Matthew J. Carey, Jeffrey R. Childress, Claudia Mewes, Daniel Ebke, Volker Drewello, Günter Reiss, and Andy Thomas (2012), "Insights into Ultrafast Demagnetization in Pseudogap Half-Metals," Physical Review X **2** (4), 041008.

F. Massee, S. de Jong, Y. Huang, W. K. Siu, I. Santoso, A. Mans, A. T. Boothroyd,

D. Prabhakaran, R. Follath, A. Varykhalov, L. Patthey, M. Shi, J. B. Goedkoop, and M. S. Golden (2011), "Bilayer manganites reveal polarons in the midst of a metallic breakdown," Nature Physics **7** (12), 978–982.

M. Matsubara, Y. Okimoto, T. Ogasawara, S. Iwai, Y. Tomioka, H. Okamoto, and Y. Tokura (2008), "Photoinduced switching between charge and orbital ordered insulator and ferromagnetic metal in perovskite manganites," Physical Review B **77** (9), 094410.

M. Matsubara, Y. Okimoto, T. Ogasawara, Y. Tomioka, H. Okamoto, and Y. Tokura (2007), "Ultrafast Photoinduced Insulator-Ferromagnet Transition in the Perovskite Manganite Gd0.55Sr0.45MnO3," Physical Review Letters **99** (20), 207401.

S. A. McGill, R. I. Miller, O. N. Torrens, A. Mamchik, I-Wei Chen, and J. M. Kikkawa (2004), "Dynamic Kerr Effect and the Spectral Weight Transfer of the Manganites," Physical Review Letters **93** (4), 047402.

A. McPherson, G. Gibson, H. Jara, U. Johann, Ting S. Luk, I. A. McIntyre, Keith Boyer, and Charles K. Rhodes (1987), "Studies of multiphoton production of vacuum-ultraviolet radiation in the rare gases," JOSA B **4** (4), 595–601.

Q. N. Meier, M. Lilienblum, S. M. Griffin, K. Conder, E. Pomjakushina, Z. Yan, E. Bourret, D. Meier, F. Lichtenberg, E. K. H. Salje, N. A. Spaldin, M. Fiebig, and A. Cano (2017), "Global Formation of Topological Defects in the Multiferroic Hexagonal Manganites," Physical Review X **7** (4), 041014.

A. Melnikov, I. Razdolski, T. O. Wehling, E. Th. Papaioannou, V. Roddatis, P. Fumagalli, O. Aktsipetrov, A. I. Lichtenstein, and U. Bovensiepen (2011), "Ultrafast transport of laser-excited spin-polarized carriers in Au/Fe/MgO(001)," Physical Review Letters **107** (7), 076601.

A. J. Millis (1996), "Cooperative Jahn-Teller effect and electron-phonon coupling in La1-xAxMnO3," Physical Review B **53** (13), 8434–8441.

A. J. Millis, R. Mueller, and Boris I. Shraiman (1996), "Fermi-liquid-to-polaron crossover. II. Double exchange and the physics of colossal magnetoresistance," Physical Review B **54** (8), 5405–5417.

S.-K. Mo, J. D. Denlinger, H.-D. Kim, J.-H. Park, J. W. Allen, A. Sekiyama, A. Yamasaki, K. Kadono, S. Suga, Y. Saitoh, T. Muro, P. Metcalf, G. Keller, K. Held, V. Eyert, V. I. Anisimov, and D. Vollhardt (2003), "Prominent Quasiparticle Peak in the Photoemission Spectrum of the Metallic Phase of V2O3," Physical Review Letters **90** (18), 186403.

S. Mobilio, F. Boscherini, and Meneghini C., Eds. (2015), *Synchrotron Radiation* (Springer-Verlag Berlin Heidelberg).

N. F. Mott (1929), "The scattering of fast electrons by atomic nuclei," Proceedings of the Royal Society of London. Series A **124** (794), 425–442, http://rspa.royalsocietypublishing.org/content/124/794/425.full.pdf+html .

N. F. Mott, and H. Jones (1945), *The Theory of the Properties of Metals and Alloys*, The International Series of Monographs on Physics (Dover Publications).

N. F. Mott, and R. Peierls (1937), "Discussion of the paper by de boer and verwey," Proceedings of the Physical Society **49** (4S), 72.

B. Y. Mueller, A. Baral, S. Vollmar, M. Cinchetti, M. Aeschlimann, H. C. Schneider, and B. Rethfeld (2013), "Feedback Effect during Ultrafast Demagnetization Dynamics in Ferromagnets," Physical Review Letters **111** (16), 167204.

G. M. Müller, J. Walowski, M. Djordjevic, G.-X. Miao, A. Gupta, A. V. Ramos, K. Gehrke, V. Moshnyaga, K. Samwer, J. Schmalhorst, A. Thomas, A. Hütten, G. Reiss, J. S. Moodera, and M. Münzenberg (2009), "Spin polarization in half-metals probed by femtosecond spin excitation," Nature Materials **8** (1), 56–61.

J. A. Mundy, Y. Hikita, T. Hidaka, T. Yajima, T. Higuchi, H. Y. Hwang, D. A. Muller, and L. F. Kourkoutis (2014), "Visualizing the interfacial evolution from charge compensation to metallic screening across the manganite metal-insulator transition," Nature Communications **5**, ncomms4464.

B. Nadgorny (2007), "The case against half-metallicity in La 0.7 Sr 0.3 MnO 3," Journal of Physics: Condensed Matter **19** (31), 315209.

Naoyuki Nakagawa, Harold Y. Hwang, and David A. Muller (2006), "Why some interfaces cannot be sharp," Nature Materials **5** (3), 204–209.

T. Ogasawara, M. Matsubara, Y. Tomioka, M. Kuwata-Gonokami, H. Okamoto, and Y. Tokura (2003), "Photoinduced spin dynamics in La0.6Sr0.4MnO3 observed by time-resolved magneto-optical Kerr spectroscopy," Physical Review B **68** (18), 180407.

T. Ogasawara, K. Ohgushi, Y. Tomioka, K. S. Takahashi, H. Okamoto, M. Kawasaki, and Y. Tokura (2005), "General Features of Photoinduced Spin Dynamics in Ferromagnetic and Ferrimagnetic Compounds," Physical Review Letters **94** (8), 087202.

Nagao Ohata (1973), "A Quantum Theory of Double Exchange. III. Spin Wave in a Double-Exchange Ferromagnet," Journal of the Physical Society of Japan **34** (2), 343–345.

H. Ohno, A. Shen, F. Matsukura, A. Oiwa, A. Endo, S. Katsumoto, and Y. Iye (1996), "(Ga,Mn)As: A new diluted magnetic semiconductor based on GaAs," Applied Physics Letters **69** (3), 363–365.

A. Ohtomo, and H. Y. Hwang (2004), "A high-mobility electron gas at the LaAlO3/SrTiO3 heterointerface," Nature **427** (6973), 423–426.

J. Okabayashi, A. Kimura, O. Rader, T. Mizokawa, A. Fujimori, T. Hayashi, and M. Tanaka (1998), "Core-level photoemission study of Ga1-xMnxAs," Physical Review B **58** (8), R4211–R4214.

Y. Okimoto, T. Katsufuji, T. Ishikawa, T. Arima, and Y. Tokura (1997), "Variation of electronic structure in La1-xSrxMnO3($0 \leq x \leq 0.3$) as investigated by optical conductivity spectra," Physical Review B **55** (7), 4206–4214.

T. Okuda, K. Miyamaoto, H. Miyahara, K. Kuroda, A. Kimura, H. Namatame, and M. Taniguchi (2011), "Efficient spin resolved spectroscopy observation machine at Hiroshima Synchrotron Radiation Center," Review of Scientific Instruments **82** (10), 103302.

L.-. Oloff, A. Chainani, M. Matsunami, K. Takahashi, T. Togashi, H. Osawa, K. Hanff, A. Quer, R. Matsushita, R. Shiraishi, M. Nagashima, A. Kimura, K. Matsuishi, M. Yabashi, Y. Tanaka, G. Rossi, T. Ishikawa, K. Rossnagel, and M. Oura (2016a), "Time-resolved HAXPES using a microfocused XFEL beam: From vacuum space-charge effects to intrinsic charge-carrier recombination dynamics," Scientific Reports **6**, srep35087.

L.-P. Oloff, M. Oura, A. Chainani, and K. Rossnagel (2016b), "Femtosecond Time-Resolved HAXPES," in *Hard X-ray Photoelectron Spectroscopy (HAXPES)*, Springer Series in Surface Sciences (Springer, Cham) pp. 555–568.

L.-P. Oloff, M. Oura, K. Rossnagel, A. Chainani, M. Matsunami, R. Eguchi, T. Kiss, Y. Nakatani, T. Yamaguchi, J Miyawaki, M. Taguchi, K. Yamagami, T. Togashi, T. Katayama, K. Ogawa, M. Yabashi, and T. Ishikawa (2014), "Time-resolved HAXPES at SACLA: probe and pump pulse-induced space-charge effects," New Journal of Physics **16** (12), 123045.

P. M. Oppeneer, and A. Liebsch (2004), "Ultrafast demagnetization in Ni: theory of magneto-optics for non-equilibrium electron distributions," Journal of Physics: Condensed Matter **16** (30), 5519.

P. Orgiani, A. Yu. Petrov, R. Ciancio, A. Galdi, L. Maritato, and B. A. Davidson (2012), "Evidence of direct correlation between out-of-plane lattice parameter and metal-insulator transition temperature in oxygen-depleted manganite thin films," Applied Physics Letters **100** (4), 042404.

M. Ossiander, F. Siegrist, V. Shirvanyan, R. Pazourek, A. Sommer, T. Latka, A. Guggenmos, S. Nagele, J. Feist, J. Burgdörfer, R. Kienberger, and M. Schultze (2017), "Attosecond correlation dynamics," Nature Physics **13** (3), 280–285.

M. Oura, L.-P. Oloff, A. Chainani, K. Rossnagel, M. Matsunami, R. Eguchi, T. Kiss, T. Yamaguchi, Y. Nakatani, J. Miyawaki, K. Yamagami, M. Taguchi, T. Togashi, T. Katayama, K. Ogawa, M. Yabashi, T. Gejo, K. Myojin, K. Tamasaku, Y. Tanaka, T. Ebihara, and T. Ishikawa (2014), "Electron Dynamics Probed by Time-Resolved Hard X-ray Photoelectron Spectroscopy," Transactions of the Materials Research Society of Japan **39** (4), 469–473.

G. Panaccione, M. Altarelli, A. Fondacaro, A. Georges, S. Huotari, P. Lacovig, A. Lichtenstein, P. Metcalf, G. Monaco, F. Offi, L. Paolasini, A. Poteryaev, O. Tjernberg, and M. Sacchi (2006), "Coherent Peaks and Minimal Probing Depth in Photoemission Spectroscopy of Mott-Hubbard Systems," Physical Review Letters **97** (11), 116401.

J.-H. Park, E. Vescovo, H.-J. Kim, C. Kwon, R. Ramesh, and T. Venkatesan (1998a), "Direct evidence for a half-metallic ferromagnet," Nature **392** (6678), 794–796.

J.-H. Park, E. Vescovo, H.-J. Kim, C. Kwon, R. Ramesh, and T. Venkatesan (1998b), "Magnetic Properties at Surface Boundary of a Half-Metallic Ferromagnet $La_{0.7}Sr_{0.3}MnO_3$," Physical Review Letters **81** (9), 1953–1956.

B.D. Patterson, R. Abela, H-H. Braun, R. Ganter, B. Pedrini, M. Pedrozzi, S. Reiche, and M. van Daalen, Eds. (2010), *Ultrafast Phenomena at the Nanoscale: Science op-*

portunities at the SwissFEL X-ray Laser (Paul Scherrer Institut, Switzerland).

O. Paul, S. Toscano, K. Totland, and M. Landolt (1991), "The spatial origin of the spin-polarization of secondary-electron emission from Fe," Surface Science **251** (Supplement C), 27–30.

E. Pavarini, F. Anders, E. Koch, and M. Jarrell (2012), *Correlated electrons*, Tech. Rep. PreJuSER-136393 (Forschungszentrum Jülich GmbH).

P. Peczak, and D. P. Landau (1990), "Monte Carlo study of critical relaxation in the 3d Heisenberg model," Journal of Applied Physics **67** (9), 5427–5429.

R. Peng, H. C. Xu, M. Xia, J. F. Zhao, X. Xie, D. F. Xu, B. P. Xie, and D. L. Feng (2014), "Tuning the dead-layer behavior of La0.67Sr0.33MnO3/SrTiO3 via interfacial engineering," Applied Physics Letters **104** (8), 081606.

D. Pesquera, A. Barla, M. Wojcik, E. Jedryka, F. Bondino, E. Magnano, S. Nappini, D. Gutiérrez, G. Radaelli, G. Herranz, F. Sánchez, and J. Fontcuberta (2016), "Strain-Driven Orbital and Magnetic Orders and Phase Separation in Epitaxial Half-Doped Manganite Films for Tunneling Devices," Physical Review Applied **6** (3), 034004.

D. Pesquera, G. Herranz, A. Barla, E. Pellegrin, F. Bondino, E. Magnano, F. Sánchez, and J. Fontcuberta (2012), "Surface symmetry-breaking and strain effects on orbital occupancy in transition metal perovskite epitaxial films," Nature Communications **3**, ncomms2189.

H. Petek, and S. Ogawa (1997), "Femtosecond time-resolved two-photon photoemission studies of electron dynamics in metals," Progress in Surface Science **56** (4), 239–310.

A. Yu. Petrov, X. Torrelles, A. Verna, H. Xu, A. Cossaro, M. Pedio, J. Garcia-Barriocanal, G. R. Castro, and B. A. Davidson (2013), "Surface Octahedral Distortions and Atomic Design of Perovskite Interfaces," Advanced Materials **25** (29), 4043–4048.

V. N. Petrov, V. V. Grebenshikov, B. D. Grachev, and A. S. Kamochkin (2003), "New compact classical 40 kV Mott polarimeter," Review of Scientific Instruments **74** (3), 1278–1281.

Piero Pianetta, and Ingolf Lindau (2016), "HAXPES at the Dawn of the Synchrotron Radiation Age," in *Hard X-ray Photoelectron Spectroscopy (HAXPES)*, Springer Series in Surface Sciences (Springer, Cham) pp. 43–63.

S. Picozzi, C. Ma, Z. Yang, R. Bertacco, M. Cantoni, A. Cattoni, D. Petti, S. Brivio, and F. Ciccacci (2007), "Oxygen vacancies and induced changes in the electronic and magnetic structures of La0.66Sr0.33MnO3: A combined ab initio and photoemission study," Physical Review B **75** (9), 094418.

T. Pincelli (2014), *Towards Spin-resolved/Time-resolved Photoelectron Spectroscopy at the fs time scale: construction and commissioning of the ULTRASPIN apparatus*, Master's thesis (Dipartimento di Scienze Matematiche, Fisiche e Naturali, Universitá di Modena e Reggio Emilia), masters Thesis.

T. Pincelli, F. Grasselli, V. N. Petrov, P. Torelli, and G. Rossi (2017a), "Performance of photoelectron spin polarimeters with continuous and pulsed sources: from storage rings to free electron lasers," Journal of Synchrotron Radiation **24** (1), 175–187.

T. Pincelli, V. Lollobrigida, F. Borgatti, A. Regoutz, B. Gobaut, C. Schlueter, T.-L. Lee, D. J. Payne, M. Oura, K. Tamasaku, A. Y. Petrov, P. Graziosi, F. Miletto Granozio, M. Cavallini, G. Vinai, R. Ciprian, C. H. Back, G. Rossi, M. Taguchi, H. Daimon, G. van der Laan, and G. Panaccione (2017b), "Quantifying the critical thickness of electron hybridization in spintronics materials," Nature Communications **8**, ncomms16051.

T. Pincelli, V. N. Petrov, G. Brajnik, R. Ciprian, V. Lollobrigida, P. Torelli, D. Krizmancic, F. Salvador, A. De Luisa, R. Sergo, A. Gubertini, G. Cautero, S. Carrato, G. Rossi, and G. Panaccione (2016), "Design and optimization of a modular setup for measurements of three-dimensional spin polarization with ultrafast pulsed sources," Review of Scientific Instruments **87** (3), 035111.

C. Piovera (2014), *Ultrafast laser-induced dynamics in ferromangets: towards the control of the spin order from the femtosecond to the sub-nanosecond time scale*, Ph.D. thesis (Dipertimento di Fisica, Universitá degli Studi di Milano), phD Thesis.

M. Plötzing, R. Adam, C. Weier, L. Plucinski, S. Eich, S. Emmerich, M. Rollinger, M. Aeschlimann, S. Mathias, and C. M. Schneider (2016), "Spin-resolved photoelectron spectroscopy using femtosecond extreme ultraviolet light pulses from high-order harmonic generation," Review of Scientific Instruments **87** (4), 043903.

D. Polli, M. Rini, S. Wall, R. W. Schoenlein, Y. Tomioka, Y. Tokura, G. Cerullo, and A. Cavalleri (2007), "Coherent orbital waves in the photo-induced insulator/metal dynamics of a magnetoresistive manganite," Nature Materials **6** (9), 643–647.

T. Popmintchev, M.-C. Chen, P. Arpin, M. M. Murnane, and H. C. Kapteyn (2010), "The attosecond nonlinear optics of bright coherent X-ray generation," Nature Photonics **4** (12), 822–832.

T. Popmintchev, M.-C. Chen, D. Popmintchev, P. Arpin, S. Brown, S. Ališauskas, G. Andriukaitis, T. Bal čiunas, O. D. Mücke, A. Pugzlys, A. Baltu ška, B. Shim, S. E. Schrauth, A. Gaeta, C. Hernández-García, L. Plaja, A. Becker, A. Jaron-Becker, M. M. Murnane, and H. C. Kapteyn (2012), "Bright Coherent Ultrahigh Harmonics in the keV X-ray Regime from Mid-Infrared Femtosecond Lasers," Science **336** (6086), 1287–1291.

Z. Q Qiu, and S. D Bader (1999), "Surface magneto-optic Kerr effect (SMOKE)," Journal of Magnetism and Magnetic Materials **200** (1), 664–678.

I. Radu, C. Stamm, N. Pontius, T. Kachel, P. Ramm, J.-U. Thiele, H. A. Dürr, and C. H. Back (2010), "Laser-induced generation and quenching of magnetization on FeRh studied with time-resolved x-ray magnetic circular dichroism," Physical Review B **81** (10), 104415.

D. C. Ralph, and M. D. Stiles (2008), "Spin transfer torques," Journal of Magnetism and Magnetic Materials **320** (7), 1190–1216.

I Razdolski, A Alekhin, U Martens, D Bürstel, D Diesing, M Münzenberg, U Bovensiepen, and A Melnikov (2017), "Analysis of the time-resolved magneto-optical kerr effect for ultrafast magnetization dynamics in ferromagnetic thin films," Journal of Physics: Condensed Matter **29** (17), 174002.

H. Regensburger, R. Vollmer, and J. Kirschner (2000), "Time-resolved magnetization-induced second-harmonic generation from the Ni(110) surface," Physical Review B **61** (21), 14716–14722.

D. Reinsel, J. Gantz, and J. Rydning (2017), "Data age 2025: The evolution of data to life-critical. an IDC white paper, sponsored by Seagate," Data Age 2025: The Evolution of Data to Life-Critical. An IDC White Paper, sponsored by Seagate.

Y. H. Ren, M. Trigo, R. Merlin, Venimadhav Adyam, and Qi Li (2007), "Generation and detection of coherent longitudinal acoustic phonons in the La0.67Sr0.33MnO3 thin films by femtosecond light pulses," Applied Physics Letters **90** (25), 251918.

H.-S. Rhie, H. A. Dürr, and W. Eberhardt (2003), "Femtosecond Electron and Spin Dynamics in Ni/W(110) Films," Physical Review Letters **90** (24), 247201.

M. Rini, Y. Zhu, S. Wall, R. I. Tobey, H. Ehrke, T. Garl, J. W. Freeland, Y. Tomioka, Y. Tokura, A. Cavalleri, and R. W. Schoenlein (2009), "Transient electronic structure of the photoinduced phase of Pr0.7Ca0.3MnO3 probed with soft x-ray pulses," Physical Review B **80** (15), 155113.

L. M. Rodriguez-Martinez, and J. P. Attfield (1996), "Cation disorder and size effects in magnetoresistive manganese oxide perovskites," Physical Review B **54** (22), R15622–R15625.

T. Saitoh, A. E. Bocquet, T. Mizokawa, H. Namatame, A. Fujimori, M. Abbate, Y. Takeda, and M. Takano (1995), "Electronic structure of La1-xSrxMnO3 studied by photoemission and x-ray-absorption spectroscopy," Physical Review B **51** (20), 13942–13951.

J. Salafranca, and L. Brey (2006), "Disorder-induced first order transition and Curie temperature lowering in ferromagnetic manganites," Physical Review B **73** (21), 214404.

M. B. Salamon, and M. Jaime (2001), "The physics of manganites: Structure and transport," Reviews of Modern Physics **73** (3), 583–628.

S. Sasaki (1994), "Analyses for a planar variably-polarizing undulator," Nuclear Instruments and Methods in Physics Research Section A: Accelerators, Spectrometers, Detectors and Associated Equipment **347** (1), 83–86.

M. Sawicki, D. Chiba, A. Korbecka, Y. Nishitani, J. A. Majewski, F. Matsukura, T. Dietl, and H. Ohno (2010), "Experimental probing of the interplay between ferromagnetism and localization in (Ga,Mn)As," Nature Physics **6** (1), 22–25.

A. J. Schellekens (2014), *Manipulating spins: novel methods for controlling magnetization dynamics on the ultimate timescale*, Ph.D. thesis (Department of Physics, Technische Universiteit Eindhoven), phD Thesis.

A. J. Schellekens, and B. Koopmans (2013), "Comparing Ultrafast Demagnetization Rates Between Competing Models for Finite Temperature Magnetism," Physical Review Letters **110** (21), 217204.

D. G. Schlom, J. H. Haeni, J. Lettieri, C. D. Theis, W. Tian, J. C. Jiang, and X. Q. Pan (2001), "Oxide nano-engineering using MBE," Materials Science and Engineering: B

87 (3), 282–291.

C. Schlueter, P. Orgiani, T.-L. Lee, A. Yu. Petrov, A. Galdi, B. A. Davidson, J. Zegenhagen, and C. Aruta (2012), "Evidence of electronic band redistribution in La0.65Sr0.35MnO3-delta by hard x-ray photoelectron spectroscopy," Physical Review B **86** (15), 155102.

A. Scholl, L. Baumgarten, R. Jacquemin, and W. Eberhardt (1997), "Ultrafast Spin Dynamics of Ferromagnetic Thin Films Observed by fs Spin-Resolved Two-Photon Photoemission," Physical Review Letters **79** (25), 5146–5149.

G. Schönhense, K. Medjanik, and H.-J. Elmers (2015), "Space-, time- and spin-resolved photoemission," Journal of Electron Spectroscopy and Related Phenomena Special Anniversary Issue: Volume 200, **200** (Supplement C), 94–118.

Md Motin Seikh, Chandrabhas Narayana, L. Sudheendra, A. K. Sood, and C. N. R. Rao (2004), "A Brillouin scattering study of La 0.77 Ca 0.23 MnO 3 across the metal/insulator transition," Journal of Physics: Condensed Matter **16** (24), 4381.

A. Sekiyama, T. Iwasaki, K. Matsuda, Y. Saitoh, Y. Ônuki, and S. Suga (2000), "Probing bulk states of correlated electron systems by high-resolution resonance photoemission," Nature **403** (6768), 396–398.

L. Serafini, D. Alesini, N. Bacci, N. Bliss, K. Cassou, C. Curatolo, I. Drebot, K. Dupraz, A. Giribono, V. Petrillo, L. Palumbo, C. Vaccarezza, A. Variola, and F. Zomer (2016), "High intensity X/γ photon beams for nuclear physics and photonics," EPJ Web of Conferences **117**, 05002.

C. G. Shull, C. T. Chase, and F. E. Myers (1943), "Electron polarization," Phys. Rev. **63**, 29–37.

F. Siek, S. Neb, P. Bartz, M. Hensen, C. Strüber, S. Fiechter, M. Torrent-Sucarrat, V. M. Silkin, E. E. Krasovskii, N. M. Kabachnik, S. Fritzsche, R. D. Muiño, P. M. Echenique, A. K. Kazansky, N. Müller, W. Pfeiffer, and U. Heinzmann (2017), "Angular momentum–induced delays in solid-state photoemission enhanced by intra-atomic interactions," Science **357** (6357), 1274–1277.

R. Singh, K. Dutta, and M. K. Nandy (2016), "Critical dynamics of a nonlocal model and critical behavior of perovskite manganites," Physical Review E **93** (5), 052132.

R. Singla (2015), *Measuring correlated electron dynamics on few femtoseconds time scale*, Ph.D. thesis (Department Physik der Universität Hamburg), phD Thesis.

J. Sinova, and I. Žutić (2012), "New moves of the spintronics tango," Nature Materials **11** (5), 368–371.

F. Sirotti, N. Beaulieu, A. Bendounan, M. G. Silly, C. Chauvet, G. Malinowski, G. Fratesi, V. Véniard, and G. Onida (2014), "Multiphoton k-resolved photoemission from gold surface states with 800-nm femtosecond laser pulses," Physical Review B **90** (3), 035401.

Fausto Sirotti, Giancarlo Panaccione, and Giorgio Rossi (1995), "Atom-specific surface magnetometry," Physical Review B **52** (24), R17063–R17072.

C. L. Smallwood, R. A. Kaindl, and A. Lanzara (2016), "Ultrafast angle-resolved pho-

toemission spectroscopy of quantum materials," EPL (Europhysics Letters) **115** (2), 27001.

J. A. Sobota, S. Yang, J. G. Analytis, Y. L. Chen, I. R. Fisher, P. S. Kirchmann, and Z.-X. Shen (2012), "Ultrafast Optical Excitation of a Persistent Surface-State Population in the Topological Insulator Bi2Se3," Physical Review Letters **108** (11), 117403.

A. Sommerfeld (1928), "Zur elektronentheorie der metalle auf grund der fermischen statistik," Zeitschrift für Physik **47** (1), 1–32.

S. R. Spurgeon, P. V. Balachandran, D. M. Kepaptsoglou, A. R. Damodaran, J. Karthik, S. Nejati, L. Jones, H. Ambaye, V. Lauter, Q. M. Ramasse, K. K. S. Lau, L. W. Martin, J. M. Rondinelli, and M. L. Taheri (2015), "Polarization screening-induced magnetic phase gradients at complex oxide interfaces," Nature Communications **6**, ncomms7735.

C. Stamm, T. Kachel, N. Pontius, R. Mitzner, T. Quast, K. Holldack, S. Khan, C. Lupulescu, E. F. Aziz, M. Wietstruk, H. A. Dürr, and W. Eberhardt (2007), "Femtosecond modification of electron localization and transfer of angular momentum in nickel," Nature Materials **6** (10), 740–743.

C. D. Stanciu, F. Hansteen, A. V. Kimel, A. Kirilyuk, A. Tsukamoto, A. Itoh, and Th. Rasing (2007), "All-Optical Magnetic Recording with Circularly Polarized Light," Physical Review Letters **99** (4), 047601.

K. Steenbeck, and R. Hiergeist (1999), "Magnetic anisotropy of ferromagnetic La0.7(Sr,Ca)0.3MnO3 epitaxial films," Applied Physics Letters **75** (12), 1778–1780.

L. Stojchevska, I. Vaskivskyi, T. Mertelj, P. Kusar, D. Svetin, S. Brazovskii, and D. Mihailovic (2014), "Ultrafast Switching to a Stable Hidden Quantum State in an Electronic Crystal," Science **344** (6180), 177–180.

A. Stupakiewicz, K. Szerenos, D. Afanasiev, A. Kirilyuk, and A. V. Kimel (2017), "Ultrafast nonthermal photo-magnetic recording in a transparent medium," Nature **542** (7639), 71–74.

M. Suzuki, Y. Inubushi, M. Yabashi, and T. Ishikawa (2014), "Polarization control of an X-ray free-electron laser with a diamond phase retarder," Journal of Synchrotron Radiation **21** (3), 466–472.

Motohiro Suzuki, Naomi Kawamura, and Tetsuya Ishikawa (2003), "Application of optical scanner to switching of x-ray photon helicities at kHz range," Review of Scientific Instruments **74** (1), 19–22.

M. Taguchi, and G. Panaccione (2016), "Depth-Dependence of Electron Screening, Charge Carriers and Correlation: Theory and Experiments," in *Hard X-ray Photoelectron Spectroscopy (HAXPES)*, Springer Series in Surface Sciences (Springer, Cham) pp. 197–216.

Y. Takata, M. Yabashi, K. Tamasaku, Y. Nishino, D. Miwa, T. Ishikawa, E. Ikenaga, K. Horiba, S. Shin, M. Arita, K. Shimada, H. Namatame, M. Taniguchi, H. Nohira, T. Hattori, S. Södergren, B. Wannberg, and K. Kobayashi (2005), "Development of hard X-ray photoelectron spectroscopy at BL29xu in SPring-8," Nuclear Instruments and Methods in Physics Research Section A: Accelerators, Spectrometers, Detectors

and Associated Equipment Proceedings of the Workshop on Hard X-ray Photoelectron Spectroscopy, **547** (1), 50–55.

H. Tanaka, Y. Takata, K. Horiba, M. Taguchi, A. Chainani, S. Shin, D. Miwa, K. Tamasaku, Y. Nishino, T. Ishikawa, E. Ikenaga, M. Awaji, A. Takeuchi, T. Kawai, and K. Kobayashi (2006), "Electronic structure of strained La0.85Ba0.15MnO3 thin films with room-temperature ferromagnetism investigated by hard x-ray photoemission spectroscopy," Physical Review B **73** (9), 094403.

S. Tanuma, C. J. Powell, and D. R. Penn (2011), "Calculations of electron inelastic mean free paths. IX. Data for 41 elemental solids over the 50 eV to 30 keV range," Surface and Interface Analysis **43** (3), 689–713.

A. Tebano, C. Aruta, S. Sanna, P. G. Medaglia, G. Balestrino, A. A. Sidorenko, R. De Renzi, G. Ghiringhelli, L. Braicovich, V. Bisogni, and N. B. Brookes (2008), "Evidence of Orbital Reconstruction at Interfaces in Ultrathin La0.67Sr0.33MnO3 Films," Physical Review Letters **100** (13), 137401.

K. Tiedtke, A. Azima, N. von Bargen, L. Bittner, S. Bonfigt, S. Düsterer, B. Faatz, U. Frühling, M. Gensch, Ch Gerth, N Guerassimova, U. Hahn, T. Hans, M. Hesse, K. Honkavaar, U. Jastrow, P. Juranic, S. Kapitzki, B. Keitel, T. Kracht, M Kuhlmann, W. B. Li, M. Martins, T. Núñez, E. Plönjes, H. Redlin, E. L. Saldin, E. A. Schneidmiller, J. R. Schneider, S Schreiber, N. Stojanovic, F. Tavella, S. Toleikis, R. Treusch, H. Weigelt, M. Wellhöfer, H. Wabnitz, M. V. Yurkov, and J Feldhaus (2009), "The soft x-ray free-electron laser FLASH at DESY: beamlines, diagnostics and end-stations," New Journal of Physics **11** (2), 023029.

D. Tillmann, R. Thiel, and E. Kisker (1989), "Very-low-energy spin-polarized electron diffraction from Fe(001)," Zeitschrift für Physik B Condensed Matter **77** (1), 1–2.

Y. Tokura (2006), "Photoinduced Phase Transition: A Tool for Generating a Hidden State of Matter," Journal of the Physical Society of Japan **75** (1), 011001.

K. Tono, T. Togashi, Y. Inubushi, T. Sato, T. Katayama, K. Ogawa, H. Ohashi, H. Kimura, S. Takahashi, K. Takeshita, H Tomizawa, S. Goto, T. Ishikawa, and M. Yabashi (2013), "Beamline, experimental stations and photon beam diagnostics for the hard x-ray free electron laser of SACLA," New Journal of Physics **15** (8), 083035.

D. H. Torchinsky, F. Mahmood, A. T. Bollinger, I. Božović, and N. Gedik (2013), "Fluctuating charge-density waves in a cuprate superconductor," Nature Materials **12** (5), 387–391.

P. Torelli, M. Sacchi, G. Cautero, M. Cautero, B. Krastanov, P. Lacovig, P. Pittana, R. Sergo, R. Tommasini, A. Fondacaro, F. Offi, G. Paolicelli, G. Stefani, M. Grioni, R. Verbeni, G. Monaco, and G. Panaccione (2005), "Experimental setup for high energy photoemission using synchrotron radiation," Review of Scientific Instruments **76** (2), 023909.

Sven Tougaard (1997), "Universality Classes of Inelastic Electron Scattering Cross-sections," Surface and Interface Analysis **25** (3), 137–154.

I. C. E. Turcu, E. Springate, C. A. Froud, C. M. Cacho, J. L. Collier, W. A. Bryan,

G. R. A. J. Nemeth, J. P. Marangos, J. W. G. Tisch, R. Torres, T. Siegel, L. Brugnera, J. G. Underwood, I. Procino, W. R. Newell, C. Altucci, R. Velotta, R. B. King, J. D. Alexander, C. R. Calvert, O. Kelly, J. B. Greenwood, I. D. Williams, A. Cavalleri, J. C. Petersen, N. Dean, S. S. Dhesi, L. Poletto, P. Villoresi, F. Frassetto, S. Bonora, and M. D. Roper (2009), "Ultrafast science and development at the Artemis facility," p. 746902.

E. Turgut, D. Zusin, D. Legut, K. Carva, R. Knut, J. M. Shaw, C. Chen, Z. Tao, H. T. Nembach, T. J. Silva, S. Mathias, M. Aeschlimann, P. M. Oppeneer, H. C. Kapteyn, M. M. Murnane, and P. Grychtol (2016), "Stoner versus Heisenberg: Ultrafast exchange reduction and magnon generation during laser-induced demagnetization," Physical Review B **94** (22), 220408.

G. E. Uhlenbeck, and S. Goudsmith (1926), "Spinning electrons and the structure of spectra," Nature **117**, 264–265.

A. A. Ünal, A. Parabas, A. Arora, J. Ehrler, C. Barton, S. Valencia, R. Bali, T. Thomson, F. Yildiz, and F. Kronast (2017), "Laser-driven formation of transient local ferromagnetism in FeRh thin films," Ultramicroscopy 10.1016/j.ultramic.2017.03.024.

A. Vaterlaus, T. Beutler, and F. Meier (1991), "Spin-lattice relaxation time of ferromagnetic gadolinium determined with time-resolved spin-polarized photoemission," Physical Review Letters **67** (23), 3314–3317.

A. Vaterlaus, D. Guarisco, M. Lutz, M. Aeschlimann, M. Stampanoni, and F. Meier (1990), "Different spin and lattice temperatures observed by spin-polarized photoemission with picosecond laser pulses," Journal of Applied Physics **67** (9), 5661–5663.

M. van Veenendaal (2006), "Competition between screening channels in core-level x-ray photoemission as a probe of changes in the ground-state properties of transition-metal compounds," Physical Review B **74** (8), 085118.

M. A. van Veenendaal, and G. A. Sawatzky (1993), "Nonlocal screening effects in 2p x-ray photoemission spectroscopy core-level line shapes of transition metal compounds," Physical Review Letters **70** (16), 2459–2462.

A. Verna, Bruce A. Davidson, Y. Szeto, A. Yu. Petrov, A. Mirone, A. Giglia, N. Mahne, and S. Nannarone (2010), "Measuring magnetic profiles at manganite surfaces with monolayer resolution," Journal of Magnetism and Magnetic Materials Proceedings of the Joint European Magnetic Symposia, **322** (9), 1212–1216.

Dieter Vollhardt, Krzysztof Byczuk, and Marcus Kollar (2012), "Dynamical Mean-Field Theory," in *Strongly Correlated Systems*, Springer Series in Solid-State Sciences (Springer, Berlin, Heidelberg) pp. 203–236.

J. Walowski, and M. Münzenberg (2016), "Perspective: Ultrafast magnetism and THz spintronics," Journal of Applied Physics **120** (14), 140901.

A. Weber (2012), *Ultrafast spindynamics in ferromagnetic thin films*, phd.

R. Werner, A. Yu. Petrov, L. Alvarez Miño, R. Kleiner, D. Koelle, and B. A. Davidson (2011), "Improved tunneling magnetoresistance at low temperature in manganite junctions grown by molecular beam epitaxy," Applied Physics Letters **98** (16), 162505.

J. Wieczorek, A. Eschenlohr, B. Weidtmann, M. Rösner, N. Bergeard, A. Tarasevitch, T. O. Wehling, and U. Bovensiepen (2015), "Separation of ultrafast spin currents and spin-flip scattering in Co/Cu(001) driven by femtosecond laser excitation employing the complex magneto-optical Kerr effect," Physical Review B **92** (17), 174410.

A. Winkelmann, C.-T. Chiang, F. Bisio, W.-C. Lin, J. Kirschner, and H. Petek (2010), "Higher Order Photoemission from Metal Surfaces," in *Dynamics at Solid State Surfaces and Interfaces*, edited by U. Bovensiepen, H. Petek, and M. Wolf (Wiley-VCH Verlag GmbH & Co. KGaA) pp. 33–51, dOI: 10.1002/9783527633418.ch2.

A. Winkelmann, D. Hartung, H. Engelhard, C.-T. Chiang, and J. Kirschner (2008), "High efficiency electron spin polarization analyzer based on exchange scattering at Fe/W(001)," Review of Scientific Instruments **79** (8), 083303.

J. Woicik, Ed. (2016), *Hard X-ray Photoelectron Spectroscopy (HAXPES)*, 1st ed., Springer Series in Surface Sciences (Springer International Publishing).

U. Wurstbauer, M. Sperl, M. Soda, D. Neumaier, D. Schuh, G. Bayreuther, J. Zweck, and W. Wegscheider (2008), "Ferromagnetic GaMnAs grown on (110) faced GaAs," Applied Physics Letters **92** (10), 102506.

T. Yajima, Y. Hikita, and H. Y. Hwang (2011), "A heteroepitaxial perovskite metal-base transistor," Nature Materials **10** (3), 198–201.

Z. Yang, C. Ko, and S. Ramanathan (2011), "Oxide Electronics Utilizing Ultrafast Metal-Insulator Transitions," Annual Review of Materials Research **41** (1), 337–367.

R. Yusupov, T. Mertelj, V. V. Kabanov, S. Brazovskii, P. Kusar, J.-H. Chu, I. R. Fisher, and D. Mihailovic (2010), "Coherent dynamics of macroscopic electronic order through a symmetry breaking transition," Nature Physics **6** (9), 681.

J. Zaanen, G. A. Sawatzky, and J. W. Allen (1985), "Band gaps and electronic structure of transition-metal compounds," Physical Review Letters **55** (4), 418–421.

C. Zener (1951), "Interaction between the d-Shells in the Transition Metals. II. Ferromagnetic Compounds of Manganese with Perovskite Structure," Physical Review **82** (3), 403–405.

G. P. Zhang, W. Hübner, G. Lefkidis, Y. Bai, and T. F. George (2009), "Paradigm of the time-resolved magneto-optical Kerr effect for femtosecond magnetism," Nature Physics **5** (7), 499–502.

J. Zhang, and R. D. Averitt (2014), "Dynamics and Control in Complex Transition Metal Oxides," Annual Review of Materials Research **44**, 19–43.

J. Zhang, X. Tan, M. Liu, S. W. Teitelbaum, K. W. Post, F. Jin, K. A. Nelson, D. N. Basov, W. Wu, and R. D. Averitt (2016), "Cooperative photoinduced metastable phase control in strained manganite films," Nature Materials **15** (9), 956–960.

V. P. Zhukov, E. V. Chulkov, and P. M. Echenique (2006), "Lifetimes and inelastic mean free path of low-energy excited electrons in Fe, Ni, Pt, and Au: Ab initio GW+T calculations," Physical Review B **73** (12), 125105.

R. Zimmermann, R. Claessen, F. Reinert, P. Steiner, and S. Hüfner (1998), "Strong hybridization in vanadium oxides: evidence from photoemission and absorption

spectroscopy," Journal of Physics: Condensed Matter **10** (25), 5697.

W. H. Zurek (1985), "Cosmological experiments in superfluid helium?" Nature **317** (6037), 505.

List of publications

1. **T. Pincelli**, R. Cucini, A. Verna, V. Lollobrigida, F. Borgatti, M. Oura, K. Tamasaku, H. Osawa, T.L. Lee, C. Schlueter, S. Günther, C.H. Back, M. Dell'Angela, A. Yu. Petrov, F. Sirotti, R. Ciprian, V. Dediu, I. Bergenti, P. Graziosi,F. Miletto Granozio, Y.Tanaka, T. Ueta, M. Yoshida, K. Tanaka, H. Daimon, G. Rossi, M. Taguchi & G. Panaccione *Revealing the role of delocalized electrons in ultrafast magnetic relaxation of half metallic manganites*, in preparation.

2. **T. Pincelli**, V. Lollobrigida, F. Borgatti, A. Regoutz, B. Gobaut, C. Schlueter, T.-L. Lee, D.J. Payne, M. Oura, K. Tamasaku, A.Y. Petrov, P. Graziosi, F. Miletto Granozio, M. Cavallini, G. Vinai, R. Ciprian, C.H. Back, G. Rossi, M. Taguchi, H. Daimon, G. van der Laan & G. Panaccione *Quantifying the critical thickness of electron hybridization in spintronics materials*, Nature Communications, 8, 16051, (2017).
Doi: 10.1038/ncomms16051

3. R. Costantini, **T. Pincelli**, A. Cossaro, A. Verdini, A. Goldoni, S. Cichoň, M. Caputo, M. Pedio, G. Panaccione, M.G. Silly, F. Sirotti, A. Morgante & M. Dell'Angela *Time resolved resonant photoemission study of energy level alignment at donor/acceptor interfaces*, Chemical Physics Letters, xxx, xx-xxxx, (2017). In press.
Doi: 10.1016/j.cplett.2017.04.033.

4. E. Ferrari, C. Spezzani, F. Fortuna, R. Delaunay, F. Vidal, I. Nikolov, P. Cinquegrana, B. Diviacco, D. Gauthier, G. Penco, P. R. Ribič, E. Roussel, M. Trovò, J.-B. Moussy, **T. Pincelli**, L. Lounis, M. Manfredda, E. Pedersoli, F. Capotondi, C. Svetina, N. Mahne, M. Zangrando, L. Raimondi, A. Demidovich, L. Giannessi, G. De Ninno, M. Boyanov Danailov, E. Allaria & M. Sacchi *Element Selective Probe of the Ultra-Fast Magnetic Response to an Element Selective Excitation in Fe-Ni Compounds Using a Two-Color FEL Source*, Photonics, **4**, 6 (2017). Doi: 10.3390/photonics4010006.

5. **T. Pincelli**, F. Grasselli, V. N. Petrov, P. Torelli & G. Rossi *Performance of photoelectron spin polarimeters with continuous and pulsed sources: from storage rings to free electron lasers*, Journal of Synchrotron Radiation, **24**, 175 (2017).
Doi: 10.1107/S1600577516017513.

6. R. Ciprian, P. Torelli, A. Giglia, B. Gobaut, B. Ressel, G. Vinai, M. Stupar, A. Caretta, G. De Ninnoa, **T. Pincelli**, B. Casarina, G. Adhikary, G. Sberveglieri, C. Baratto & M. Malvestuto, *New strategy for magnetic gas sensing*, Royal Society of Chemistry Advances, **6**, 83399 (2016).
Doi: 10.1039/C6RA18213E.

7. **T. Pincelli**, V. N. Petrov, G. Brajnik, R. Ciprian, V. Lollobrigida, P. Torelli, D. Krizmancic, F. Salvador, A. De Luisa, R. Sergo, A. Gubertini, G. Cautero, S. Carrato, G. Rossi & G. Panaccione *Design and optimization of a modular setup for measurements of three-dimensional spin polarization with ultrafast pulsed sources*, Review of Scientific Instruments, **87**, 035111 (2016).
Doi: 10.1063/1.4943255.

8. E. Ferrari, C. Spezzani, F. Fortuna, R. Delaunay, F. Vidal, I. Nikolov, P. Cinquegrana, B. Diviacco, D. Gauthier, G. Penco, P. R. Ribič, E. Roussel, M. Trovò, J.-B. Moussy, **T. Pincelli**, L. Lounis, M. Manfredda, E. Pedersoli, F. Capotondi, C. Svetina, N. Mahne, M. Zangrando, L. Raimondi, A. Demidovich, L. Giannessi, G. De Ninno, M. Boyanov Danailov, E. Allaria & M. Sacchi *Widely tunable two-colour seeded free-electron laser source for resonant-pump resonant-probe magnetic scattering*, Nature Communications, **7**, 10343 (2016).
Doi: 10.1038/ncomms10343.

Acknowledgements

May you build a ladder to the stars
And climb on every rung
May you stay
Forever young

Bob Dylan, *Forever young*, 1974

This thesis represents the landmark conclusion of an over four year long work within the group of NFFA-Trieste. It has been a period of continuous growth, whose extent and importance I could feel especially clearly on the tips of my fingers during this last phase of writing. I thus take the chance of this space to express my gratitude, with all my heart, to all the people who accompanied me in this process. I was not joking when I chose their phrases as epigraphs of some of my chapters. It is this human, live, spoken and heard side of science that I have discovered in this PhD and in whose importance I now believe profoundly.

Firstly, I would like to express my sincere thankfulness to my advisor Prof. G. Rossi for the support of my Ph.D study and related research. There is is no way to overstate the importance and the number of opportunities I was given to realize my research and to grow as a scientist. But on an even more important level, I hope that his example of gentle and inspiring leadership is shaped into my character, and that, given opportunity at any level, I will do my best in that direction. He motivates us extraordinarily by being the first to relentlessly put effort and care on the proceeding of our investigations. He finds the time, even at unruly hours, to read, understand, advise and guide our studies.

His passion for scientific discussion and his razor-sharp logic fire up my enthusiasm for argumentation, that else would dull under the frustration of everyday difficulties. He taught me to enjoy the adventurous side of being a scientist, with its world-wide travelling and roller-coaster of emotions, with my daring hypotesis sometimes landing on a fulfilling confirmation, sometimes crashing in utter contradiction. I consider myself privileged for having had him as advisor and mentor for my Ph.D study.

This thesis would not have been possible without my Co-supervisor Dr. G. Panaccione. It is him that had to put up day by day with my undirected and raw desire to understand. He gently bent and addressed it in an orderly fashion, helping me to spend effort in effective directions. He inspired my growth with patience, accepting that the dialectic would start with me deciding to do things my own way, and finish with me reaching the conclusion that he was right in the first place. When needed, he applied pressure in fair amount, so that I could be faced with stimulating challenges. He showed me the essentiality of aesthetics and elegance in science, not only in its graphical representation, but most importantly in the ideas and their handling. He also taught me much on how to manage the relationships with the varied categories of people (and even more varied individual characters) that one can meet in experimental physics research. Not to mention that he makes fantastic cakes.

I also would like to thank Dr. P. Torelli and Dr. I. Vobornik, the scientists in charge of the two headed NFFA-APE beamline facility for their friendliness, their kindness and their all-round availability. They allowed me to share their knowledge and experience in scientific discussion and to access the instrumentation they manage despite the tight schedule of use. They also endured the trouble of hosting, in a facility that was in the middle of massive upgrades, also the first phases of the development of Ultraspin endstation.

I also want to acknowledge Dr. P. Orgiani for sharing his vast knowledge in lengthy discussions, for providing me with references and guiding me in lining a narrow path in the complex landscape of transition metal oxides. He and his wife Dr. R. Ciancio also helped me in sorting out issues with the measurements of surface roughness by SEM analysis. I'd like to show gratitude also to Dr. Martina Dell'Angela and Prof. Fausto Sirotti for clarifying many of the intricacies of time resolved experiments. Prof. F. Offi and Dr. F. Borgatti gave me important advice on how to handle XPS data.

I would like to thank Prof. V. N. Petrov for teaching me how to handle a Mott spin-polarimeter: they are rebellious instruments, that require discipline, patience and sacrifice to be tamed. I would like to give many thanks to Dr. J. Fujii for his kindness and patience: there is an impressive amount of science in the development of instrumentation, and he is an encyclopaedic resource for that. I would like to thank Dr. G. Cautero and his team, especially R. Sergo, Dr. G. Brajnik and Dr. C. Dri, not only for guaranteeing unthinkable advancement of the electronics of the spin polarimeter, but for their continuous display of energy and inventive, that greatly inspires optimism. I would also like to thank F. Cilento and his team, D. Kopić, A. Sterzi and D. Payne for their important work in the development of the HHG beamline.

During these years, the team of the NFFA-Trieste facility has been something more than a workplace of amazing possibilities. It has also been a circle of friends, where I could feel really surrounded by trust and support. I don't know if I have to thank them more for their invaluable scientific suggestion and contributions, or for their equally precious friendship: Dr. G. Vinai, Dr. B. Gobaut, Dr. A. Yu. Petrov, Dr. V. Lollobrigida, Dr. C. Castàn-Guerrero, Dr. V. Buonanni, Dr. R. Singla, C. Bigi, F. Motti.

I am profoundly grateful to Dr. R. Cucini, who taught me much about laser systems and optical measurements and A. Fondacaro that has changed the SPRINT-Laboratory from a student's work into proper state of the art research facility. Both have helped me immensely and are nothing short than dear friends.

I would like to acknowledge also the scientists in other facilities that made this research possible, Dr. T.-L. Lee and Dr. C. Schleuter (now at DESY Lightsource in Hamburg) at I09 of Diamond Lightsource; Dr. A. Regoutz and Dr. D. Payne of Imperial College London; Prof. M. Oura, Dr. M. Suzuki, Prof. Y. Tanaka, Dr. H. Osawa of SPring-8 RIKEN synchrotron radiation facility; Dr. M. Taguchi of Nara Institute of Science and Technology and Prof. G. Van der Laan of Diamond Lightsource. I also thank Prof. C. H. Back and especially Dr. S. Günther of Regensburg Universität for allowing me to perform the TR-MOKE measurements, when the latter was just few days away from his thesis defense.

I want to acknowledge F. Grandi and F. Grasselli that have lived with me in our house in Trieste for the whole period (the former) or part of it (the latter). They have been an awesome company and, for what I can understand, they are theoretical physicists of great level. It is with them that the craziest scientific discussions, spanning over days, making one miss the bus (or many), happening deep in the night, forgetting to eat or drink. It is also their merit if most of the times my enthusiasm is bridled in mathematical rigour. It has been an amazing adventure, and we are set off for many more.

I want to thank my family for encouraging me through all of these years, and always providing me with the warmest love, affection and unwavering support.

Finally, I cannot help but to be profoundly grateful to Caterina, although she would not want me to be. There's no way to overstate the support that she and L. gave me.